The Impact of a High-Salt Diet on Macrophage Development and Function in the Gut and Liver of Mice

Dissertation

zur

Erlangung des Doktorgrades (Dr. rer. nat.)

der

Mathematisch-Naturwissenschaftlichen Fakultät

der

Rheinischen Friedrich-Wilhelms-Universität Bonn

vorgelegt von

Aya Rafea Nasr

aus As-Suwayda, Syria

Bonn 2025

Angefertigt mit Genehmigung der Mathematisch-Naturwissenschaftlichen Fakultät der
Rheinischen Friedrich-Wilhelms-Universität Bonn

Gutachterin/Betreuerin: Prof. Dr. Elvira Mass

Gutachter: Prof. Dr. Waldemar Kolanus

Tag der Promotion: 29.10.2025

Erscheinungsjahr: 2025

Table of Contents

Abbreviations

Abbreviation	Full Name
Acta2	Actin Alpha 2
AGRN	Agrin
Apoa4	Apolipoprotein A4
Atxn2	Ataxin 2
Bank1	B Cell Scaffold Protein with Ankyrin Repeats 1
BM	Bone Marrow
BMP	Bone Morphogenetic Protein signaling
Bmpr1b	Bone Morphogenetic Protein Receptor Type 1B
BSA	Bovine Serum Albumin
Cacna1d	Calcium Voltage-Gated Channel Subunit Alpha1 D
CADM	Cell Adhesion Molecule
CCL	C-C Motif Chemokine Ligand
Cdh19	Cadherin 19
CDH	Cadherin
CDh5	Cadherin 5
CD	Control
PTPRC	Protein Tyrosine Phosphatase Receptor Type C
Cemip	Cell Migration Inducing Hyaluronidase 1
Chga	Chromogranin A
Chrdl1	Chordin Like 1
Clu	Clusterin
Cr2	Complement Receptor 2
Cpeb2	Cytoplasmic Polyadenylation Element Binding Protein 2
Ctnnb1	Catenin Beta 1 (β-catenin)
DAPI	4’,6-Diamidino-2-Phenylindole, Diacetate
Defa24	Defensin Alpha 24
Des	Desmin
DFM	Double-Fatemapper
Dclk1	Doublecortin Like Kinase 1
Dgkb	Diacylglycerol Kinase Beta
DNA	Deoxyribonucleic Acid
E	Embryonic Day
EDTA	Ethylenediaminetetraacetic Acid
Elavl4	ELAV Like RNA Binding Protein 4
EMP	Erythro-Myeloid Progenitor
Eng	Endoglin
EPHA	Ephrin type-A receptor (Ephrin signaling)
FABS2	Fatty Acid Desaturase 2

Fabp1	Fatty Acid Binding Protein 1
Fabp6	Fatty Acid Binding Protein 6
FACS	Fluorescence-Activated Cell Sorting
FBS	Fetal Bovine Serum
Fcgr1	Fc Gamma Receptor I
Foxp2	Forkhead Box Protein 2
g	Gram
Gda	Guanine Deaminase
GO	Gene Ontology
Grem1	Gremlin 1
GMP	Granulocyte-Monocyte Progenitor
GUCA	Guanylate Cyclase Activator
h	Hour
H&E	Hematoxylin and Eosin
Hnf4g	Hepatocyte Nuclear Factor 4 Gamma
Hmgcs1	3-Hydroxy-3-Methylglutaryl-CoA Synthase 1
Igha	Immunoglobulin Heavy Constant Alpha
Ighd	Immunoglobulin Heavy Constant Delta
Igkc	Immunoglobulin Kappa Constant
IF	Immunofluorescence
IFN	Interferon
IGF	Insulin-like Growth Factor
Ikzf2	Helios, Ikaros Family Zinc Finger 2
IL	Interleukin
Itk	IL2-Inducible T Cell Kinase
Jag1	Jagged Canonical Notch Ligand 1
JAM	Junctional Adhesion Molecule
Jchain	Joining Chain of Multimeric IgA and IgM
KIT	KIT Proto-Oncogene, Receptor Tyrosine Kinase
Kif20b	Kinesin Family Member 20B
Krt19	Keratin 19
Lgr5	Leucine-rich repeat-containing G-protein coupled receptor 5
Lss	Lanosterol Synthase
Lxr	Liver X Receptor
Lyz1	Lysozyme 1
Mal2	Mal, T-Cell Differentiation Protein 2
M-CSF	Macrophage Colony Stimulating Factor
MerTK	Mer Tyrosine Kinase
MHC	Major Histocompatibility Complex
Miki67	Marker of Proliferation Ki-67
min	Minute

MPZ	Myelin Protein Zero
Mme	Membrane Metallo-Endopeptidase
Mrc1	Mannose Receptor C-Type 1
Muc2	Mucin 2
Ncam2	Neural Cell Adhesion Molecule 2
NECTIN	Nectin Cell Adhesion Molecule
NGL	Netrin G Ligand
NGS	Normal Goat Serum
NRG	Neuregulin
OCLN	Occludin
Pax5	Paired Box 5
PBS	Phosphate-Buffered Saline
PDGFRA	Platelet Derived Growth Factor Receptor Alpha
PECAM1	Platelet And Endothelial Cell Adhesion Molecule 1
PCR	Polymerase Chain Reaction
Pdlim3	PDZ and LIM domain 3
Pid1	Phosphotyrosine Interaction Domain Containing 1
Plac8	Placenta Specific 8
Pnrc1	Proline Rich Nuclear Receptor Coactivator 1
pMac	Pre-Macrophage
Ppp1r12b	Protein Phosphatase 1 Regulatory Subunit 12B
RNA	Ribonucleic Acid
RPM	Red Pulp Macrophages
RS	Rat Serum
RT	Room Temperature
Rspo3	R-spondin 3
Ryr3	Ryanodine Receptor 3
Sct	Secretin
SEMA3	Semaphorin 3
Sis	Somatomedin Insulin-like Growth Factor 2
Skap1	Src Kinase Associated Phosphoprotein 1
Sox10	SRY-Box Transcription Factor 10
ST-HSC	Short-Term Hematopoietic Stem Cell
Svep1	Sushi, von Willebrand factor A, EGF and pentraxin domain containing 1
Tagln	Transgelin
tdT	tdTomato (Red Fluorescent Protein)
TENASCIN	Tenascin C
Tff3	Trefoil Factor 3
TGF-β	Transforming Growth Factor Beta
Trpm5	Transient Receptor Potential Cation Channel Subfamily M Member 5
UMAP	Uniform Manifold Approximation and Projection

Viisfatin	Visfatin (NAMPT - Nicotinamide phosphoribosyltransferase)
WT	Wildtype
YFP	Yellow Fluorescent Protein
YS	Yolk Sac

List of Tables

List of Figures

Abstract

The prevalence of unhealthy diets poses a significant global challenge to public health and development. Among dietary risks, excessive salt intake remains a major concern. High-salt diets (HSD) have been linked to numerous health issues, including elevated blood pressure, cardiovascular diseases, and gastric cancer. Importantly, macrophages, the key immune-regulating phagocytes, have emerged as central mediators of HSD-associated adverse effects. The gut-liver axis, being the primary interface for nutritional and microbial content, is particularly vulnerable to HSD-induced stress, promoting tissue damage and persistent inflammatory responses. However, the role of macrophages in mediating these adaptations remains elusive. In this study, we investigated how short- and long-term HSD affects gut and liver macrophages in mice. Long-term HSD induced sex-dependent structural and functional changes across the gut-liver axis, including ileal pathology, gut microbial imbalance, and hepatic lipid accumulation. Functional assays showed increased intestinal permeability, indicating epithelial barrier damage, and impaired recovery in a colitis model, potentially mediated by altered macrophage phagocytic Fcγ receptors (FcγRs). Single-nucleus RNA sequencing of the ileum revealed transcriptional changes in volume regulation pathways, notably the Wnk1-dependent chloride-sensing pathway. Further 3D imaging showed increased macrophage cell volume in both tissues following long-term HSD, potentially affecting their function. High-dimensional flow cytometry enabled detailed characterization of gut and liver macrophage subsets, highlighting an increase in $MHCII^{+}Cx3cr1^{+}CD13^{-}$ macrophages in the ileum of male mice and a reduction in Kupffer cells, the liver-resident macrophages, in females. A novel fate-mapping model to track fetal- and bone marrow-derived macrophages uncovered an enhanced monocyte-driven replacement of fetal-derived macrophages in both tissues with niche-specific dynamics. Functional and transcriptomic analyses further revealed dysregulated macrophage phagocytic activity in both organs, associated with FcγRIIb expression. In conclusion, these findings demonstrate that long-term HSD systemically alters macrophage function and development in the gut and liver, contributing to tissue damage and inflammatory-like responses linked to HSD. This underscores the important role of macrophages and the mechanisms they mediate in HSD-associated diseases.

Preliminary remarks

The work presented in this thesis was conducted at the Rheinische Friedrich- Wilhelms-Universität Bonn in the research groups of Prof. Elvira Mass and Prof. Waldemar Kolanus at Life & Medical Sciences Institute in Bonn, Germany.

I hereby declare that I wrote the present dissertation using only the sources indicated in the text and with no assistance of third parties. All experiments in this study have been designed and performed by myself, with contributions to the shown data from the following people or institutions:

Dr. Lisa Maria Steinheuer (University of Bonn, Institute for Experimental Oncology) performed the analysis of the single-cell RNA-sequencing (Figures 22-34).

Dr. Maria Francesca Viola (University of Bonn, LIMES Institute) supervised the flow cytometry experiments on the gut.

Dr. Waldemar Seel (University of Bonn, Institute of Nutrition and Food Sciences) performed the gut microbiome transcriptional analysis (Figure 10-13).

Dr. Jelena Zurkovic (University of Bonn, LIMES Institute) performed the lipidomics analysis (Figure 21).

Dr. Nelli Blank-stein (University of Bonn, LIMES Institute) performed the single-cell RNA-sequencing procedure 10x Genomics (Figures 22-34).

Nikola Makdissi (University of Bonn, LIMES Institute) performed the antibody injection and blood collection for the in-vivo phagocytosis assay (Figure 67).

Sandra Högler (University of Veterinary Medicine Vienna) performed histological scoring of gut sections (Figure 14, 19).

The Histology Platform, namely Simone Glees and Vanessa Barabasch (Immunosensation Cluster, Bonn University) for preparing the tissues for histological analyses (Figures 16, 17, 19, 20).

Acknowledgments

I would like to express my heartfelt appreciation to my supervisors, **Prof. Dr. Elvira Mass** and **Prof. Dr. Waldemar Kolanus**, for giving me the opportunity to work on this exciting project. Their generous support began even before I arrived in Germany to take up the position.

I am deeply grateful to **Prof. Dr. Elvira Mass** for fostering my scientific independence and encouraging me to pursue my own research ideas. Under her guidance, I acquired some of the most valuable skills of my PhD journey. Her continuous support, constructive feedback, and thoughtful advice were instrumental in shaping and completing this project.

I wish to thank **Prof. Dr. Waldemar Kolanus** for kindly hosting me in his lab throughout my PhD and for always offering the time and support I needed. His feedback consistently had a meaningful and positive impact on my research.

I would further like to acknowledge the members of my doctoral committee — **Prof. Dr. Elvira Mass**, **Prof. Dr. Waldemar Kolanus**, **Prof. Dr. Carmen Ruiz de Almodóvar**, and **Prof. Dr. Ana Ivonne Vazquez-Armendariz** — for their time and for evaluating my work.

I am also grateful to the **ImmunoSensation² Cluster of Excellence** for offering me this PhD opportunity and supporting my participation in the **Bonn International Graduate School of Immunosciences and Infection**, as well as to the **Collaborative Research Center SFB 1454 in Bonn**, funded by the **German Research Foundation**, for supporting this project and promoting innovative research. I also thank the **Bonner Forum Biomedizin** for enabling effective scientific networking.

A special thanks goes to **Dr. Maria Francesca Viola** for her consistent guidance and help throughout all phases of my PhD and for revising my thesis. I am also thankful to **Dr. Lisa Maria Steinheuer**, **Dr. Waldemar Seel**, **Nikola Makdissi**, **Dr. Jelena Zurkovic**, and **Dr. Nelli Blank-Stein** for their significant contributions to this work. In addition, I sincerely thank **Dr. Qendresa Ramani Dervishi** for her thoughtful and detailed feedback on my thesis.

I would like to warmly thank my project teammate, **Linda Müller,** the newest Doctor in the house, who accompanied me throughout my PhD journey. We had a great time working together in the lab — you were always there with support, helpful ideas, and good energy. Your presence truly made a difference.

Thank you so much, **Conny (Cornelia Cygon)**, for your constant support throughout my PhD. I also thank **Maria Embgenbroich** and **Dagmar Odenkirchen** for their support with management and organizational matters.

A big thanks to the entire **GRC team at the LIMES Institute** — **Maria**, **Joachim**, **Stephan**, and the animal caretakers — who were always ready to support me with animal work.

Thank you, **Michael** and **Tom** from the **IT team**, for helping me resolve technical issues whenever they arose.

I acknowledge the **Histology Platform** of the **ImmunoSensation² Cluster** at the **University of Bonn** — namely **Simone Glees** and **Vanessa Barabasch** — for preparing and staining tissue sections.

I also thank the **Core Facilities of the University of Bonn**:

The **Flow Cytometry Core Facility (FCCF)**, where I performed all my flow cytometry measurements;
The **Microscopy Core Facility (MCF)**, where I used the Axiolab scanner for some experiments.

I thank **Prof. Dr. Jonathan Jantsch** for his support and for enabling tissue sodium concentration measurements in his lab, which were carried out by **Dr. Agnes Schröder**.

I also thank **Prof. Dr. Karsten Hiller** and his lab members for the great collaborations.

At the **LIMES Institute**, I was fortunate to be surrounded by warm-hearted people who filled my PhD years with joy and unforgettable memories. I thank all current and former members of the **Kolanus**, **Mass**, **Kiermaier**, and **Netea** groups, who brought so much positivity into my daily life — especially **Carsten**, **Eliana**, **Emily**, **Inaam**, **Linda**, **Maria**, **Marie,** **Nelli**, **Nikola**, **Hao**, **Karo**, **Kati**, **Kerim**, **Maria**, **Marina**, **Seyhmus,** **Alice**, **Bettina**, and **Burçu**.

I want to express my deepest gratitude to my partner, **Zaher**, who supported me unconditionally all over my academic journey — especially during the most difficult days — and always made everything easier for me.

I am also forever thankful to my family, who have always encouraged my passion for research, cared for me from afar, and remained proud of me every step of the way:

Mom — the sweetest and strongest woman I've ever met; **Dad** — the purest form of kindness; **Wissal** — adventure, care, and love in one; **Marwa** — always present, even when far; **Athar** — my warm-hearted little sister; **Taim** — the kindest and most supportive brother. and **Assala** — almost my twin, in both spirit and appearance; Thank you, **Nabiha** for your support and for always checking in on me.
Finally, to my dear old friends — thank you for your presence and friendship over the past 14 years and for all the sweet moments and fun trips. I also want to thank my new friends whom I met in Germany and who became adventure and hangout buddies.

List of Publications

Rafea Nasr, Aya & Komarevtsev, Sergei & Baidamshina, Diana & Ryskulova, Ayan & Makarov, Dmitriy & Stepanenko, Vasiliy & Trizna, Elena & Gorshkova, Anna & Osmolovskiy, Alexander & Miroshnikov, Konstantin & Kayumov, Airat. (2024). Targeting mono- and dual-species biofilms of Staphylococcus aureus and Pseudomonas aeruginosa by the recombinant anticoagulant enzyme PAPC from micromycete Aspergillus ochraceus. Biochimie. 230. 10.1016/j.biochi.2024.11.002.

Rafea Nasr, Aya & Müller, Linda & Jux, Bettina & Makdissi, Nikola & Trowbridge, Justin & Schmidt, Susanne & Schultze, Joachim & Schulte-Schrepping, Jonas & Kolanus, Waldemar & Mass, Elvira. (2024). Differential impact of high-salt levels in vitro and in vivo on macrophage core functions. Molecular Biology Reports. 51. 10.1007/s11033-024-09295-x.

Baidamshina, Diana & **Rafea Nasr, Aya** & Komarevtsev, s & Osmolovskii, A. & Miroshnikov, Konstantin & Kayumov, Airat & Trizna, Elena. (2024). Destruction of Biofilms of Gram-Positive and Gram-Negative Bacteria by Serine Protease PAPC from Aspergillus ochraceus. Microbiology. 93. 227-231. 10.1134/S0026261723604281.

1 Introduction

1.1 High-salt Diets

1.1.1 A Global Health Concern: Overconsumption of Salt

In recent years, salt consumption has become a prominent focus in research and several studies have been conducted worldwide to inform guidelines on healthy salt consumption. According to the U.S. National Academies, consuming a minimum daily amount of 1.25 grams (g) dietary salt (sodium chloride, NaCl) — which contains 0.5 g sodium— is essential for most animals, including humans, where it plays a critical role in fluid balance, nerve transmission, and muscle function[1]. Meanwhile, the World Health Organization (WHO) recommends less than 5 g/day salt — equivalent 2 g of sodium to support cardiovascular health in adults [2].

Extremely low-salt intake of less than 1.25 g /day is rare in healthy individuals, by contrast, almost all populations consume excessive amounts of salt. More specifically, on a global level, adults consume on average 10.78 g/day salt [3] —more than double the limit recommended by the WHO [2]. Sodium and chloride can also be found in forms other than NaCl, such as naturally in a variety of foods. However, in the form of NaCl – as the common salt, it is particularly popular for its characteristics in enhancing food taste and serving as a preservative. The WHO reports that processed foods like breads, meat, snacks, and condiments (e.g., soy and fish sauce) often contain large amounts of NaCl [2]. In addition, a common form of sodium in food is sodium glutamate, which is used as a flavor enhancer in processed foods all over the world [2].

Dietary salt consumption depends on several factors, including the cultural perspective and nutritional habits of a population [3–5]. In line with that, increased salt consumption has been observed in countries with industrial lifestyles, where is accompanied by overconsumption of fats and sugars, like the western diet. Such unhealthy diets consumed over long-term periods of life can affect the overall health of the concerned people and also their offspring [6–8]. However, the specific impact of high-salt diets over long-term periods, and the diverse mechanisms of salt's actions in the human body still require extensive research [2,9].

1.1.2 Excess Sodium Elimination

NaCl is a key osmolar factor that influences osmolarity of body fluids. Excess sodium intake is mainly regulated by the kidneys that filter the blood and excrete excess Na^+ through the urine. Additionally, a small portion of sodium is exerted with the body sweat [10]. However, sodium can be stored in the skin, muscle, and bone without consequent water retention, resulting in osmotically inactive sodium storage [11]. This was discovered in an experiment of long-term space trip simulation where sodium intake and elimination were quantified in human. In this experiment it was found that the amount of excreted sodium was less than the daily constant sodium intake, which indicated that sodium was likely accumulating in the body [10]. Following

this experiment, a sodium reservoir was discovered in the skin of rats and later in the human skin with a non-osmotic immune-dependent mechanism. Specifically, macrophages from the innate myeloid immune compartment sense local sodium concentrations and regulate interstitial electrolyte composition through a tonicity-enhancer–binding protein/vascular endothelial growth factor C (VEGF-C) [11,12].

1.1.3 Sodium Cellular Kinetics and Transport Mechanisms

Sodium has an extracellular concentration of around 140 mM, and Intracellular concentration ranging between 5 and 15 mM. This steep gradient drives sodium influx to the cells when the channels are open. Sodium is transported by several transprters and channels like the Na^+/K^+-ATPase thst is regulated by the cellular energy levels i.e., ATP availability, in addition to osmotic and volume stress, and hormones. Other transporters are the epithelial Na^+ channel ENaC , Na^+/H^+ exchanger, Na^+/Ca^{2+} exchanger (NCX1), Na^+-K^+-$2Cl^-$ transporter (NKCC1, encoded by Slc12a2), and SGLT1/2, the Na^+-glucose cotransporters. The NCX1 encoded by *Slc8a1* gene encodes vital for sodium entry into MΦ under hypertonic conditions [13]. NKCC1 senses and regulates intracellular Cl^- and it is involved in the WNK-SPAK pathway that is also crucial for osmolarity and Cl cellular balance. In brief, Wnk1-encoded protein acts as a chloride sensor that regulates SPAK (encoded by *Stk39 gene*), an intermediate regulator of the cotransporter NKCC1, constituting a chloride-sensing pathway that regulates can regulate cellular homeostasis and functions.

1.1.4 High-salt Diet as a Risk Factor for Non-Communicable Diseases

An estimated 1.89 million mortalities globally per year are associated with consuming excessive amounts of sodium, a well-established cause of elevated blood pressure [14]. High blood pressure increases the risk of cardiovascular diseases, gastric cancer, obesity, osteoporosis, and kidney disease and many other organ-specific complications as shown in Figure 1 [6,15–17].

High blood pressure can be caused by several factors and behaviors, including a high-salt diet (HSD) [18]. There are numerous mechanisms for HSD-driven hypertension. HSD can affect renal excretion of excess sodium leading to increased plasma osmolality, water retention into extracellular matrix, and increased blood volume [19]. Also, HSD can deregulate the Renin-Angiotensin-Aldosterone system (RAAS) contributing to hypertension [20]. Moreover, HSD can stimulate the sympathetic nervous system (SNS) that regulates vasoconstriction and heart rate and even directly damage the vascular endothelium leading to vascular stiffness, which in turns impacts blood pressure [21,22]. Recently, immune system responses to HSD have been proposed as a major contributor to hypertension. More specifically, HSD is proposed to activate inflammatory pathways that affect blood pressure regulation [23].

The kidney sodium overload and hypertension following HSD increases the risk of kidney structural damage, oxidative stress, and fibrosis [15]. Alongside hypertension and CVD, HSD has shown to result in sodium accumulation in the skin and induce inflammatory skin diseases. Synergistically with its effect on *Helicobacter pylori* bacteria (*H pylori*), HSD may also drive the widespread stomach cancer [16]. Moreover, HSD has significant effects on the brain and central nervous system (CNS), particularly inducing neuroinflammation, cognitive impairment, and cerebrovascular dysfunction (Figure 1) [24].

1.1.5 Emerging Links to Immune and Inflammatory Disorders

Excess NaCl consumption has an effect on involve immune-mediated inflammatory diseases. For example, HSD exacerbates several autoimmune diseases like rheumatoid arthritis, multiple sclerosis, and inflammatory bowel diseases [25,26]. Although the genetic basis of autoimmune diseases has been established, environmental and dietary changes like HSD still highly affect their severity [27]. Previous studies showed that HSD can boost murine and human immune TH17 cells – a cell subtype of interleukin-17-producing $CD4^+$ T cells that have a crucial role in autoimmune diseases [28]. TH17 polarization is induced by excess NaCl via the p38/MAPK signaling pathway involving the nuclear factor of activated T cells 5 (NFAT5; called TONEBP) and serum/glucocorticoid-regulated kinase 1 (SGK1). In addition, the anti-inflammatory regulatory T cells (Tregs) were shown to be decreased in high-salt conditions, while the numbers of blood monocytes, and enhanced pro-inflammatory cytokine release like interleukin (IL)-1β were increased [29,30]. These changes, confirmed by multiple studies, suggest a salt-dependent overall shift in immune responses toward a pro-inflammatory profile, implying a state of chronic inflammation that drives exhaustion of the immune system and compromises its defense against infections [31–33].

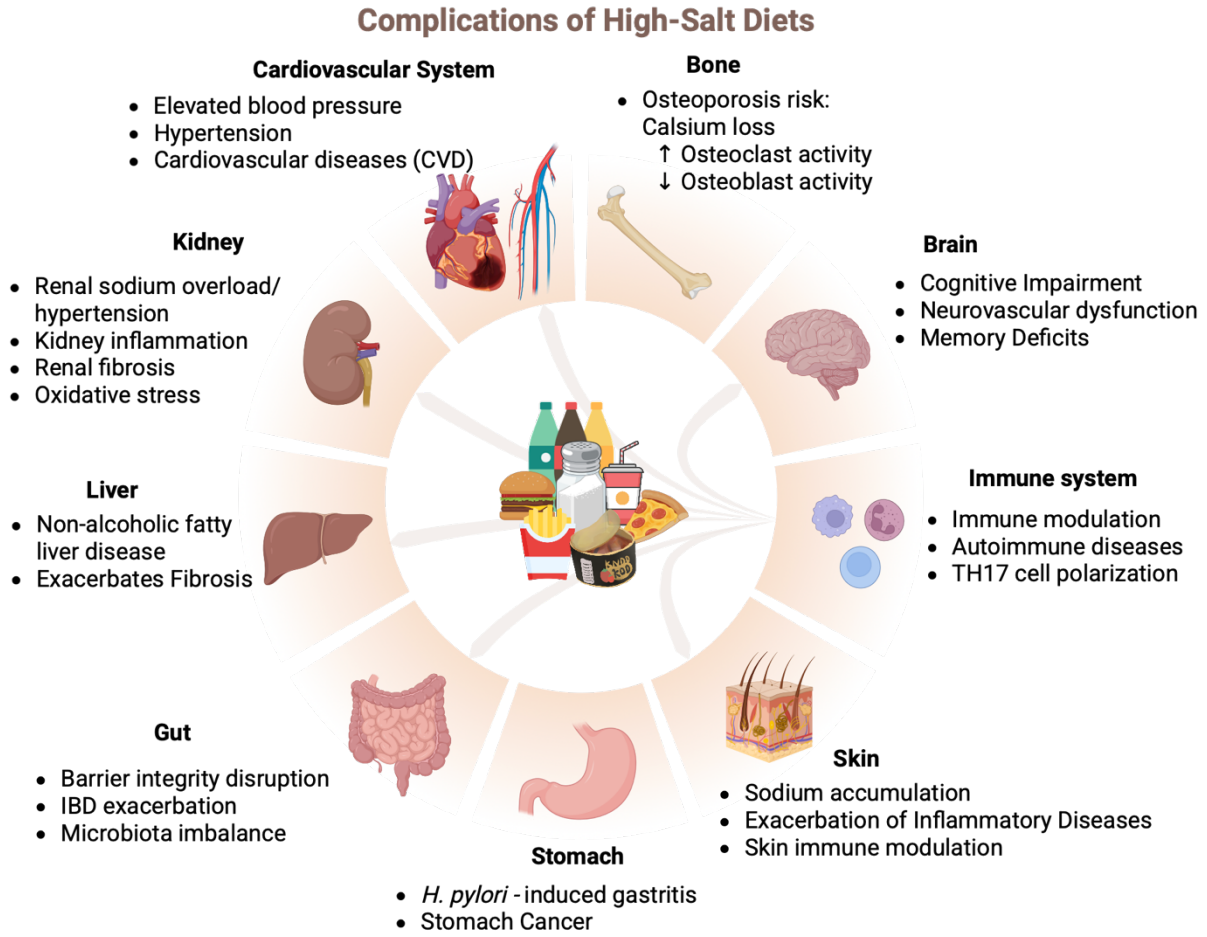

Figure 1 Overview of health Complications associated with high-salt diets (HSD). IBD: intestinal bowl diseases; *H. pylori*: *Helicobacter Pylori*; TH17 cells: T helper 17 cells.

1.2 The Gut-Liver Axis

1.2.1 The Gut

The gut represents the largest interface within the body and comprises the stomach, small intestine, and colon. Food digestion primarily takes place in the stomach, whereas nutrient absorption mainly occurs in the small intestine. The colon, also known as the large intestine, plays a pivotal role in reabsorbing water and electrolytes, in addition to fermenting indigestible components [34]. The small intestine is subdivided based on structural and functional properties into three regions: duodenum, jejunum, and ileum (Figure 2). Duodenum is a short proximal part, that receives the chyme from the stomach, bile, and pancreatic secretions to initiate enzymatic digestion; the jejunum is responsible for sugar, amino, and fatty acid absorption; the ileum is specialized in absorbing remaining nutrients, bile salts, and vitamin B12. The ileum is more involved in immune surveillance because of the abundance of lymphoid follicles called Payer's patches. Payer's patches are clusters of lymphoid follicles that locate in the mucosa and submucosa layers of the small intestine, mainly in the distal ileum, and contribute to regulate the gut immune homeostasis [35]. The gut

has a tubular structure, with a multilayer wall divided into four layers: the mucosa, the submucosa, the muscularis externa, and the serosa [36] (Figure 3).

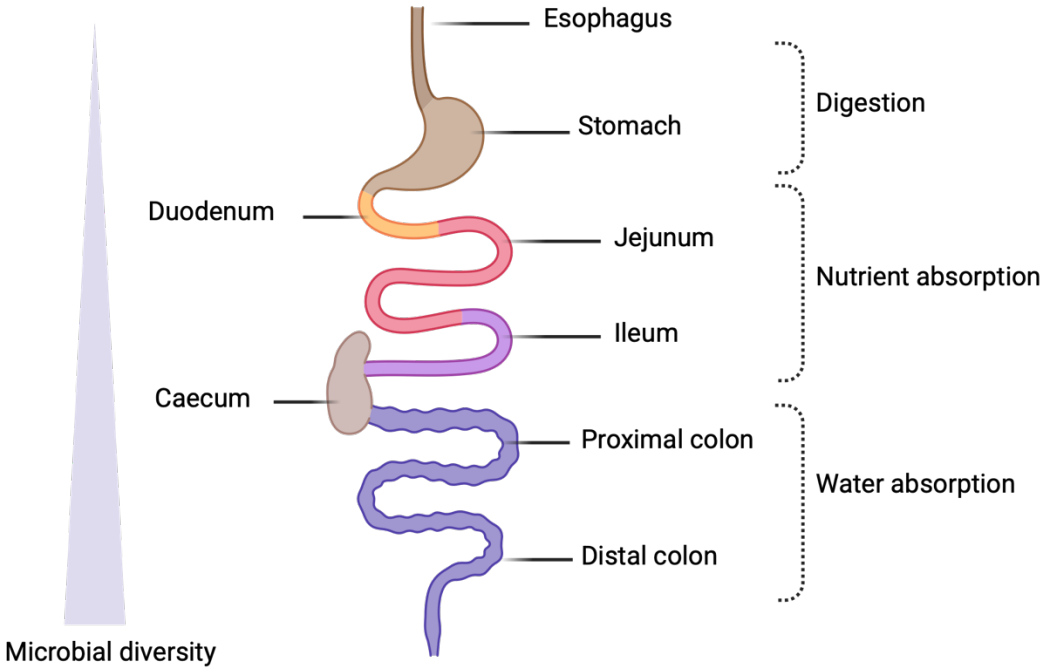

Figure 2 Diagram of gut regions and their main function.

1.2.1.1 Mucosa

The mucosa is the innermost layer, and the most complex structurally and functionally. The mucosa of the small intestine is highly folded, forming villi and microvilli that increase surface area for maximal nutrient absorption. The villi length decreases gradually from about 1.5 mm in the duodenum to 0.5 mm in the distal ileum, and are supported by blood and lymph vessels that are essential for nutrient transportation and immune defense (Figure 3A). Colonic mucosa is rather smooth, as villi are absent, and contains deep, straight crypts (Figure 3B). The mucosa is composed of three layers: muscular mucosae, lamina propria, and epithelium that line the luminal side of the gut wall [37].

In the outer side of the mucosa there is a thin sheet of smooth muscle cells (SMCs) called the muscularis mucosae, and it controls mucosal movements and exposure to nutrients [38]. More proximal to the lumen is the lamina propria layer (LP), that forms the connective tissue of the villi the crypts. The LP consists of non-cellular connective tissue components, like collagen and elastin, blood and lymph vessels, and myofibroblasts. The presence of different immune cell types is distinctive in lamina propria, including mononuclear antigen-presenting cells (APCs), plasma cells, and lymphocytes. Plasma cells reside in the intercrypt region, and lymphocytes are spread above the muscularis externa, while macrophages concentrate in the upper part of lamina propria near the villi tips [39].

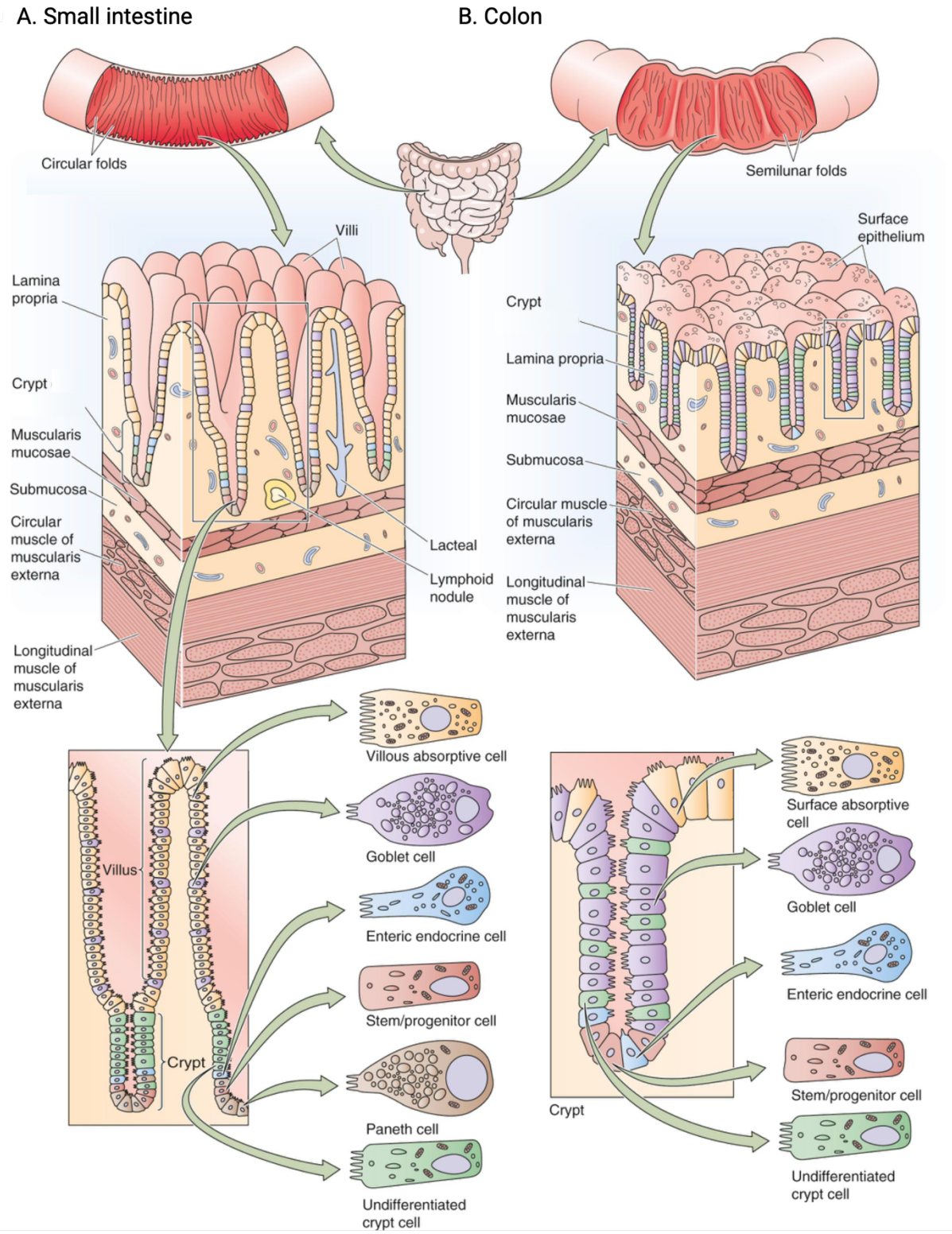

Figure 3 Illustrative diagram of gut histology and endothelial cell distribution. (A) the small intestine; (B) the colon [40].

From the internal lumen side of the mucosa, the gut is lined by a single layer of absorptive and secretory epithelial cells sealed together by tight junctions. Absorptive epithelial cells are the most predominant cell type in the villi epithelium, and their luminal side has a brush-like

cellular wall with numerous microvilli for maximal nutrient absorption. They are also known as enterocytes (ECs) in small intestine and colonocytes in the colon [41] (Figure 3). ECs specialize sequentially from base to the top of the villi in absorbing and processing amino acids, carbohydrates, and lipids. Lipids are deposited in large lipoproteins called chylomicrons, which then to be transferred by lymph vessels, while other nutrients are directly transferred via the bloodstream [41]. Between the adjacent villi bases, crypts extend inside the LP and are enriched with intestinal stem cells (ISCs) and transit proliferating cells (TAs) that replenish the epithelium by cellular turnover [42] (Figure 3).

Secretory epithelial cells are less abundant than ECs and are divided into goblet, Paneth, tuft, and enteroendocrine cells (EECs) [43]. Goblet cells line the epithelium of the small intestine and colon, and they provide a protective coat by secreting mucus to support host defense against pathogens [44]. Paneth cells are located in the crypts of the small intestine but are absent in the colon. They produce antimicrobial peptides and other components that are important in host defense and immunity [45]. Tuft cells are present throughout all gut regions, located between crypts and villi. They are chemosensory epithelial cells that detect and respond to luminal antigens by contributing to appropriate immune responses and regulation of adjacent epithelial cell secretions. Enteroendocrine cells (EECs) are also sensory cells that regulate digestion, absorption, and metabolism by producing a wide variety of gut hormones [46] (Figure 3). Collectively, these specialized epithelial cell subsets work together to maintain intestinal homeostasis by coordinating nutrient absorption, mucus secretion, host defense, fluid balance and many other essential intestinal functions.

1.2.1.2 Submucosa

The submucosa is located between the mucosa and muscularis externa and represents a connective tissue that supports the mucosa and tightly attaches to the underlying muscularis. The submucosa is rich in blood and lymph vessels, and neurons that are grouped in the Meissner's or submucosal plexus – a key component of the enteric nervous system (ENS). Fibroblasts and some immune cell types like mast cells and lymphocytes also reside in the submucosa [47] (Figure 3).

1.2.1.3 Muscularis externa

Muscularis externa (ME) is the outer layer of the gut tubular wall, responsible for gut peristalsis (rhythmic waves of coordinated contractions), and mainly consists of SMCs organized into a tightly coiled inner circular layer and outer longitudinal layer [36]. Between these two muscle layers is the myenteric or Auerbach’s plexus, into which enteric neurons are organized, and together with submucosal plexus, they control peristaltic activity, secretions, and blood flow [48]. The thickness of muscularis externa varies in each part of the tract. In the colon, for example, the muscularis externa is much thicker for applying more force [37]. Additionally, ME contains interstitial cells of Cajal (ICCs), which are intermediaries between enteric nerves and SMCs, as well as resident macrophages that support the ENS by interacting

with neurons and glial cells [49,50]. Together, these components regulate peristalsis and immune responses for tissue homeostasis. Therefore, studying the ME compartments under homeostatic and inflammatory conditions is essential for a comprehensive understanding of gut functional dynamics, as they control gut motility and functions through involvement of neuro-immune interactions.

1.2.1.4 Serosa

The serosa (also called visceral peritoneum) is the outermost layer of the gut wall. It is composed of connective tissue that fixes the gut in place and minimizes friction with other abdominal compartments [51]. External to the serosa lies the mesentery which is a double layer of visceral peritoneum that separates the gut from the posterior abdominal wall. It is rich in blood vessels and lymph nodes, known as mesenteric lymph nodes (mLNs), which support gut immune surveillance and contribute to the mucosal immunity.

1.2.2 The Gut Microbiota

The gut microbiota comprises a wide community of living organisms including bacteria, yeasts, and viruses that coexist and participate in health and disease and has been recently referred to as "the hidden vital organ" [52,53]. Microbiota density gradually increases from the proximal to the distal end of the gut to reach its maximum abundance and diversity in the colon (Figure 2). It is also highly dynamic and varies among individuals, as well as within the same body over time or under different conditions [54].

The microbiota has many digestive roles such as food fermentation, producing vitamins, influencing appetite, controlling utilization of nutrients in the body, as well as metabolic roles like modulation of lipid and bile acid metabolism [55]. In addition, it contributes to epithelial development and has a crucial role in supporting the gut immune homeostasis [56]. The gut microbiota composition also influences other organs in the body, like the liver and the brain either directly by the regulated entry of microbial intermediates into the bloodstream or indirectly via lipid and bile acid metabolism [57,58].

The gut microbiota harbors a wide range of beneficial and potentially pathogenic (opportunistic) bacterial strains. Beneficial bacterial strains can support gut barrier by secreting fatty acids like *Bifidobacterium longum*, or antimicrobial peptides like *Lactobacillus rhamnosus* that is known for restoring microbial balance after antibiotics administration [59,60]. Whereas opportunistic bacterial strains can overgrow due to prolonged antibiotic treatments, immune dysfunction, unhealthy low-fiber diets, and other stress stimuli. For instance, *Clostridioides difficile* and *Escherichia coli* can overgrow under the aforementioned conditions, inducing dysbiosis and damaging the gut barrier by secreting specific toxins [61,62]. The shift in microbiota composition following dietary changes or infections can cause depletion of beneficial bacterial stains and overgrowth of pathogenic strains—a process called dysbiosis. When barrier function is impaired due to dysbiosis or other injuries, it fails to prevent

pathogens and toxins from entering the gut, allowing augmented antigen presentation and activation of immune-inflammatory responses [63]. Also, microbiota composition alterations have been proven to affect stool consistency by causing diarrhea or constipation [64,65].

1.2.3 The Liver

The liver is a large homogenous metabolic organ located on the upper right part of the abdomen and inter-divided into four lobes: the right, left, caudate, and quadrate lobes [66]. The liver tissue is divided by sinusoids of endothelial cells and lined by the liver capsule that is consisted of a single layer of mesothelial cells and a single sheet of capsular fibroblasts [67]. As a key metabolic organ, the liver is responsible for metabolism of carbohydrates, lipids, proteins and amino acids. Carbohydrates metabolism can include glycogenesis and glycogenolysis, and lipid metabolism mainly incorporates fatty acids oxidation and synthesis of triglycerides, cholesterol, and lipoproteins [66]. Meanwhile, amino acids undergo deamination in the liver, resulting in ammonia that needs to be eliminated safely due to its neurotoxicity. Ammonia is then converted into urea via the urea cycle to be transferred to blood and secreted with the urine [68]. The liver has many other roles including detoxification, protein synthesis, and supporting immunological tolerance [66].

The liver is directly connected to the portal vein that brings blood from the digestive system for further processing nutrients, filtering toxins, and breaking down poisonous substances such as drugs and alcohol before entering the general circulation [69]. Hepatocytes are the main functional cells of the liver, constituting about 80 % of its mass and around 60% of total liver cells, and mediating most of its functions [70]. Kupffer cells (KCs), a type of resident macrophages, comprise up to 15 % of liver total cells and help to filtrate incoming blood, by phagocytosing cell debris and pathogens, as well as regulating immune responses [71]. Other cell types also exist in the liver, such as the epithelial cholangiocytes, which line bile ducts and regulate bile flow. Endothelial cells form liver sinusoids, while hepatic stellate cells control blood flow through the sinusoidal system, and can differentiate into myofibroblasts under pathological conditions [72,73].

1.2.4 Interaction Between Gut Microbiota and the Gut–Liver Axis

As concluded by Pabst and colleagues, the enterohepatic tissues are semi-permissive physical, chemical immunological barriers that control exposure to gut content including living microbes [74]. The gut epithelial barrier allows exposure to luminal antigens to some extent as required for the body to develop an immune tolerance and shape the immune system and other processes over the lifespan [35,75] (Figure 4). The liver contributes to controlling gut content dispersion through blood filtering whereas gut-draining lymph prevents extensive lymphatic spread of microorganisms and their antigens and supports homeostatic immune responses [74]. Dietary and microbial metabolites in their turn also interact with immune components and contribute to balanced responses in steady-state conditions. Bile produced by the liver harbors essential regulators for gut and liver homeostasis including bile acids,

immunoglobulins like IgA, and antimicrobial molecules, that directly enter the small intestine, and contribute to modulating microbiota composition and epithelial permeability [57] (Figure 4). This bidirectional communication between gut and liver – through the portal vein, microbiota, and bile – reflects the integration of dietary, genetic, and environmental factors in shaping an adapted and healthy physiological state.

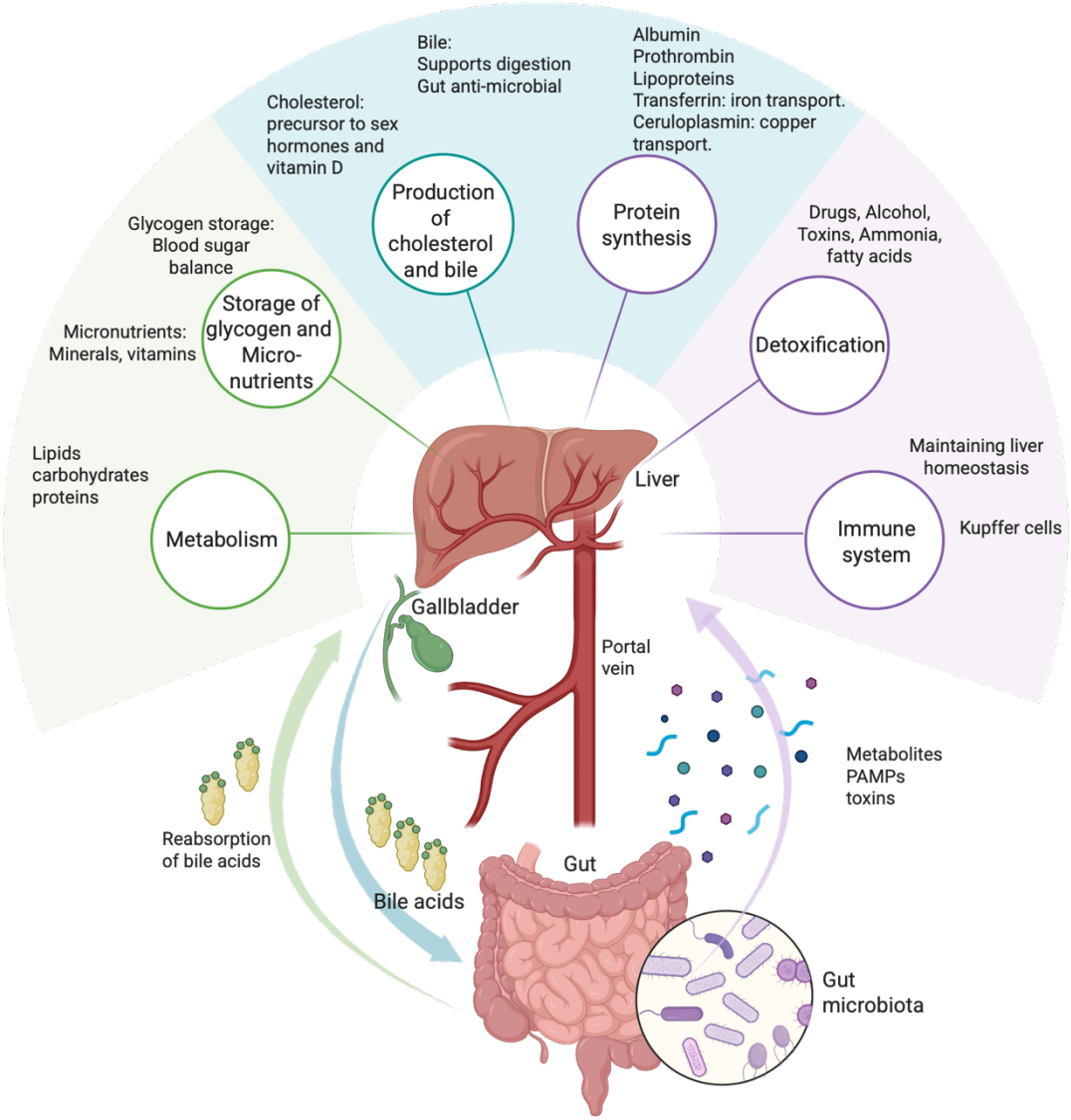

Figure 4 Key functions of the liver and its interactions with the gut. PAMPs: Pathogen-associated molecular patterns.

Unhealthy dietary regimens such as high fat/salt/sugar diets, low fiber diets, or alcohol consumption can influence gut and liver homeostasis and proper functionality [76,77]. For example, high-fat diets can impair gut barrier function and promote chronic gastrointestinal inflammation [78]. Moreover, they can induce hepatic steatosis and oxidative stress, thereby affecting liver metabolic functions and contributing to chronic systemic inflammation [79]. Unhealth diets affects microbiota composition as well, where microbial dysbiosis can disrupt intestinal barrier functionality, enabling the translocation of microbial materials into the gut and liver, leading to inflammatory responses that further contribute to the development of

chronic gut and liver diseases [57]. Dysbiosis is a key driver of several gut diseases, such as inflammatory bowel disease, irritable bowel syndrome, colorectal cancer, and celiac disease [80]. Liver health is highly dependent on gut microbiota composition, since previous studies proved its connection with liver diseases like steatosis and fibrosis [81].

1.2.5 Impact of High-Salt Diet on the Gut-Liver axis

High-salt diets have been implicated in several health issues, especially in cardiovascular diseases. Earlier studies focused on the effect of salt on the vasculature, kidneys, and sympathetic nervous system until recently, when the immune system was discovered to be a main contributor to hypertension [31]. However, the effects of excessive salt intake on the gut-liver axis are still an emerging area of research. Previous studies revealed an association between excess sodium and high risks of constipation [82]. It is well-known that excess salt consumption is linked to the exacerbation of chronic inflammatory diseases. This is correlated to inflammatory bowel diseases that have dysregulated immune responses, therefore**,** do not resolve on their own, leading to persistent or recurring inflammation of the gut [83]. Excess salt has a direct effect on gut integrity, as it impairs the mucus cover of the epithelium, making it exposed to luminal content. This leads to exhaustion of epithelial cells, increased epithelial turnover, tight junction loss, and consequent immune activation [84]. High sodium diets in rodent models have shown an increase in neutrophils and the proinflammatory T_H17 cells in the gut tissues, inducing inflammation and worsening colitis [83]. Microbiota plays a big role in inducing T cell differentiation into T_H17 cells by inducing selective cytokine production, particularly Interleukin (IL)-1β. Colonic inflammation in mice after HSD ingestion was reported to be driven indirectly by a subsequent drop in *Lactobacillus* bacteria abundance and butyrate production [85].

Numerous studies have investigated microbiota alterations in response to HSD, revealing that some bacteria families were more enriched, including Firmicutes such as *Chlostridium* spieces, and Proteobacteria, especially some *Escherichia coli* strains, while other strains like *lactobacillus* species were depleted under excess salt conditions in the gut [85,86]. These discoveries refer to a dysbiosis-like condition after HSD, and highlight the role of microbiota in gut inflammation under HSD conditions.

HSD enables microbial components and harmful substances to reach the liver via the portal vein bloodstream inducing liver damage [85]. Hepatic epithelial cells and macrophages attempt to accommodate the high-salt intake and increased noxious elements influx [33]. The liver then modulates bile acid metabolism and bile composition sent to the small intestine to ameliorate inflammation and control dysbiosis, however, this results in triglyceride accumulation in the liver [87]. The translocated microbial intermediates, mainly short-chain fatty acids (SCFAs) and lipopolysaccharides (LPS) interfere with lipid metabolism, potentially provoking non-alcoholic fatty liver disease (NAFLD) [63]. Kupffer cells respond to the HSD and subsequent dysbiosis by promoting monocyte recruitment, activating NF-k B in hepatic stellate cells that trigger hepatic fibrosis as a compensatory response to the injured liver [33].

1.3 Macrophages and Immune Modulation by High-Salt Diet

1.3.1 Introduction to Macrophages

Macrophages (MΦ) are primary innate immune cells, discovered by Metchnikoff in starfish hatchlings 142 years ago, which were identified to be phagocytes and making part of the mononuclear phagocyte system together with monocytes and dendritic cells [88,89]. While monocytes circulate in the blood and are ready to infiltrate into tissues and further differentiate, MΦ are specialized in tissue maintenance and immune defense functions. MΦ form 3D networks within the tissues they reside, with tissue-specific characteristics dependent on the tissue microenvironment requirements [90]. MΦ reside in body tissues and cavities serving not only as a primary host defense against pathogens and tumors but as key regulators of tissue development and homeostasis [91,92]**.** MΦ functions include phagocytosis – the engulfment of particles such as pathogens, cellular debris and inert particles. Phagocytosis is mainly mediated by receptors like Fcγ receptors, complement receptors, and scavenger receptors. In addition, MΦ perform efferocytosis – a specialized form of phagocytosis for clearing apoptotic and aged cells – a key process for tissue surveillance, immune tolerance, and resolution of inflammation. Efferocytosis involves receptors like MertK (MER Tyrosine Kinase), Tim4 (T cell immunoglobulin and mucin domain-containing protein 4), Axl (AXL Receptor Tyrosine Kinase), Integrins and many others. MΦ are also responsible of antigen presenting to $CD4^+$ T cells via MHC class II (MHCII) and other co-stimulatory molecules like CD80 and CD86. The cytokine secretion profile of MΦ varies with environmental context, type of stimulus, and the phase of infection or tissue injury. Secretion of pro-inflammatory cytokines such as TNF-α, Il-6, and Il-1β occurs in infections and tissue damage. However, in recovery phases or they secrete anti-inflammatory cytokines including Il-10 and TGF-β. These responses are not strictly confined to a binary pro- or anti-inflammatory classification, but instead reflect a dynamic and highly plastic regulatory network. MΦ maintain tissue structure and support regeneration by producing and responding to growth factors and signaling molecules. Meanwhile, they constantly monitor the tissue microenvironment by sensing damage- and pathogen-associated molecular patterns (DAMPs/PAMPs) via pattern recognition receptors like toll-like and nod-like receptors (TLRs/NLRs).

1.3.2 MΦ Ontogeny

MΦ have distinct ontogenies because they can arise from multiple developmental sources at different stages of life depending on developmental timing and tissue context. The distinct origins of MΦ shape their specific tissue distribution, longevity, and functional properties. MΦ arise from two major sources depending on developmental timing and tissue context: fetal progenitors and adult bone marrow-derived monocytes [93].

1.3.2.1 Fetal hematopoiesis and MΦ development

During embryonic development, the fetal hematopoiesis occurs on three temporally and spatially different waves that generate MΦ to serve the embryonic development by their important physiological functions like tissue remodeling via phagocytosing apoptotic cells and cell debris, participating in extracellular matrix production, secreting growth factors and cytokines and other regulatory signaling molecules. The first wave begins around embryonic day 7.5 (E7.5) and called primitive hematopoiesis, where unipotent primitive hematopoietic progenitors in the yolk sac (YS) give rise to embryonic tissue resident MΦ, some of which persist through adulthood like microglia, the resident MΦ in the brain. The second wave starts at E8.5 by emerging diverse multipotent erythro-myeloid progenitors (EMPs) that differentiate into MΦ and other myeloid cells from E10.5 onwards [94]. In contrast to HSCs, EMPs do not hold lymphoid-lineage potential [95]. EMPs first reside the yolk sac on E8.5 and then also migrate to the fetal liver on E10.5 and upregulate the cytokine receptor Tnfrsf11a for further differentiating into pre-macrophages (pMacs) [96]. pMacs then differentiate into embryonic tissue-resident macrophages that colonize different embryonic developing organs like liver, lungs, gut, and peritoneum [97]. These fetal-derived tissue-resident macrophages specialize specifically to their microenvironment and stay until adulthood by local self-maintenance [90,91,98]. The third wave starts at E10.5 with the appearance of HSCs that migrate to the fetal liver as the primary hematopoietic organ, and start maturing from E11.5. Definitive hematopoiesis from mature HSCs give rise to all the different lineage progenitors in the fetal liver along with a consistent replenishing from YS. At E17.5 HSCs migrate to the bone marrow (BM) which becomes the permanent hematopoietic site life [93]. During the third wave, fetal-derived lineage progenitors continue to generate mostly all lineages, which supports the Monocyte-dependent hematopoiesis system. However, most myeloid cells get completely replenished by monocyte-derived cells by adulthood, except tissue-resident MΦ and mast cells [97].

1.3.2.2 Adult Bone Marrow Hematopoiesis

In adulthood, hematopoietic stem cells (HSCs) in the BM continuously replenish all blood circulating cells to maintain immune system and blood functionality [99,100]. Hematopoiesis is hierarchically initially by long-term HSCs (LT-HSCs) giving rise to short-term HSCs (ST-HSCs) in a stringently regulated process [101]. ST-HSCs differentiate into various multipotent progenitors (MPPs), which downstream give more committed multipotent progenitors [102]. The common myeloid progenitors (CMP) initiate erythropoiesis and myelopoiesis by branching into megakaryocyte-erythroid progenitors (MEP) and granulocyte-monocyte progenitors (GMP). GMP specialize into neutrophils and monocytes that can infiltrate tissues and further differentiate to give rise to MΦ [100,103]. HSCs are principally dormant, unless stimulated by severe infections to enter active cell cycle. Secreted inflammatory signals upon infections preferably directs HSCs differentiation towards myelopoiesis in a process called “emergency myelopoiesis” to increase neutrophil and monocyte numbers.

1.3.2.3 Tissue-Specific Developmental Origins of Macrophages

MΦ populations across different organs consist of heterogeneous subpopulations that originate from both embryonic progenitors and hematopoietic stem cells, with their relative contributions varying by tissue [104]. At one end of this ontogenic spectrum lie brain MΦ, which are predominantly derived from fetal precursors giving rise to adult microglia, a strictly self-renewing MΦ population [105]. In contrast, tissues such as the skin, heart, gut, and liver harbor MΦ originating from both embryonic and hematopoietic sources, with the latter contributing increasingly over time. [96,106,107]. For example, the biggest subpopulation of liver MΦ are Kupffer cells which originate from fetal-derived cells, while the other subpopulations originate from BM-derived cells i.e., monocytes.

1.3.3 MΦ Labeling Tools

Since a decade, questions arose about MΦ ontogeny, considering their very early emergence in the YS, and their differentiation from monocytes in the fetal liver and BM. Fate-mapping mouse models enabled labeling of MΦ and their progenitors from either lineage over time, to trace their origins, behaviors, and differentiation pathways in different tissues under steady-state conditions. Some efficient fate-mapping mouse models are *Flt3*^{Cre} for labeling all monocyte-derived cells from fetal liver and BM [98], *Ms4a3*^{Cre} for labeling monocyte-derived monocytes and MΦ [108], *Ccr2*^{CreER} for targeting inflammatory monocytes [105], and *Tnfrsf11a*^{Cre} for tracing fetal-derived tissue resident MΦ [96].

1.3.3.1 Double fate mapper mouse model

The double fate mapper mouse model enables distinguishing fetal-derived tissue-resident MΦ from monocyte-derived MΦ originating from HSCs in BM, by differentially labeling them with different fluorophores. This dual tracking of both MΦ origins allowed the understanding their temporal emergence, longevity, and tissue-specific residency under homeostatic state and was achieved as follows: *Tnfrsf11a*^{Cre}*; Rosa26*$^{LSL\text{-}YFP}$*; Ms4a3*^{FlpO}*; Rosa26*$^{LFL\text{-}tdTomato}$ (Figure 5). The Cre-recombinase and FlpO-recombinase enzymes were used to recognize and cleave two different genetic target sequences. A Cre-promoter for long-lived, tissue-resident MΦ was TNF receptor superfamily member 11a (*Tnfrsf11a*) that is expressed on fetal-derived pMacs and MΦ [96]. In other words, *Tnfrsf11a*^{Cre} transgene enables expression of the Cre-recombinase in *Tnfrsf11a*-expressing cells and deletion of the floxed stop cassette from the Rosa26$^{LSL\text{-}YFP}$ allele. By this, the whole tissue-resident MΦ lineage is permanently labeled by YFP [96] (Figure 5).

The Ms4a3 promoter is used for tracking monocyte-derived monocytes and short-lived MΦ as it's only expressed by the GMP lineage [109]. The *Ms4a3*^{FlpO} transgene enables expression of FlpO-recombinase in *Ms4a3*$^{+}$ cells. FlpO-recombinase recognizes the genetic frt-site inserted in the *Rosa26*$^{LFL\text{-}tdTomato}$*,* leading to enzymatic cleavage of the DNA at the frt-sites, allowing tdTomato fluorescent labeling of the monocyte-derived GMP lineage [109].

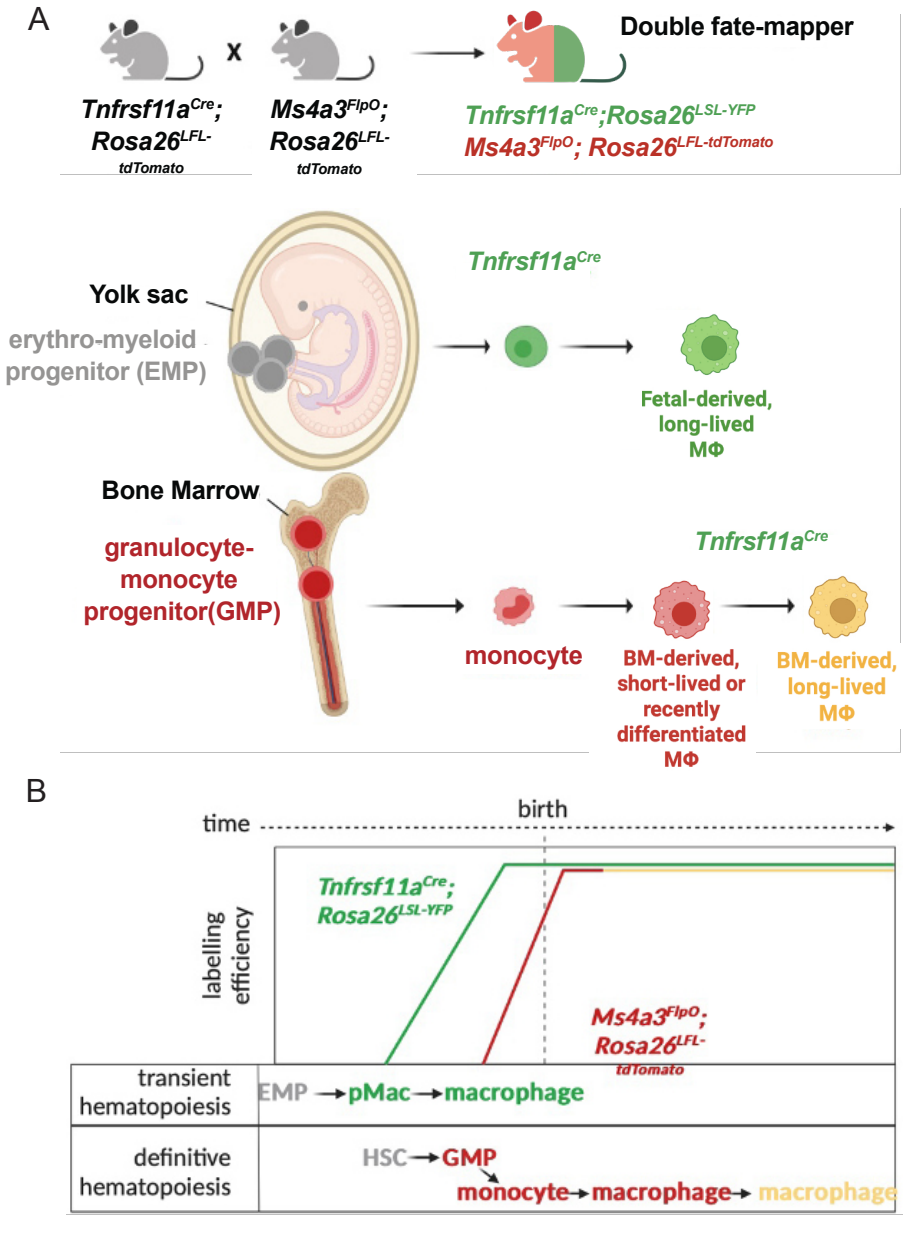

Figure 5 Double fate-mapping mouse model [110]**.** (A) Schematic representation of MΦ ontogeny: *Tnfrsf11a*^{Cre}; *Rosa26*$^{LSL-YFP}$; *Ms4a3*^{FlpO}; *Rosa26*$^{LFL-tdTomato}$ mouse model: fetal-derived MΦ express *Tnfrsf11a* (green) and BM-derived GMPs and monocytes express *Ms4a3* (red). Each lineage-specific gene induces a fluorescent reporter: YFP in fetal-derived cells (green) and tdTomato in monocyte-derived cells (red). monocyte-derived cells upregulate *Tnfrsf11a* (thus YFP) when they differentiate into long-lived MΦ and become positive for both reporters. (B) Temporal resolution of MΦ ontogeny: During embryogenesis, transient hematopoiesis gives rise to EMP, which differentiate into MΦ independently of monocyte-derived cells. At birth, definitive hematopoiesis gives rise to monocyte-derived MΦ, which in some tissues replace the fetal-derived MΦ over time.

This powerful DFM technique facilitates the tracking fetal- and monocyte-derived MΦ within the same mouse over time. Using this tool, MΦ ontogeny and longevity can be assessed in the different adult tissues. The MΦ that are labelled with only YFP originate from YS-derived EMPs, and self-maintain via local proliferation. On the other side, all GMP-derived cells in the

BM are labelled with tdTomato, including monocytes, and short-lived MΦ that that are recently differentiated from monocytes. However, once bone marrow-derived MΦ reside for long time in specific tissues, they also gain the *Tnfrsf11a* expression, making them labelled with YFP, together with tdTomato, and called long-lived monocyte-derived macrophages (Figure 5). The MΦ niche of each organ has specific percentages of these origins, which can also vary by aging or in inflammation.

1.3.4 Gut MΦ

The gut is a large and heterogenous organ, requiring intensive immune defense relevant to each region and each layer. The crucial MΦ roles as gatekeepers of tissue homeostasis makes them one of the key immune cells in the gut, a major defense barrier organ [111]. Therefore, gut MΦ represent a heterogenous mixed niche of cells that participate in the gut host defense and maintaining tissue homeostasis based on their localization in the gut wall layers. However, all gut MΦ express the MΦ canonical markers including F4/80, CD64, CD206 and Iba1 and they are distinctive by their high expression of the chemokine receptor Cx3cr1 [112,113]. Gut MΦ from different layers express overlapping surface markers, they can be however be distinguished by their localization in IF staining, or by mechanical separation in flow cytometry analyses [114–116]. Gut MΦ main functions include sampling and phagocytosing of luminal-derived antigens, pathogens, and apoptotic cells [34]; cytokine release for initiating bactericidal and cytotoxicity activities, regulating epithelial turnover, communicating with adaptive immune system components [114,117,118]; and mediating enteric neuroimmune crosstalk [50,116]. In general, studies showed that LP-MΦ are transcriptionally different and show some slow displacement, while ME-MΦ have a tissue-protective phenotype and are primarily static. Regarding their morphology, ME-MΦ show greater dendrite ramifications than LP-MΦ.

1.3.4.1 Origin of gut MΦ

The gut is seeded by embryonic precursors starting from the second wave of fetal hematopoiesis. Initial studies stated that these cells are not preserved until adulthood. Instead, they get replenished by the infiltrating BM-derived monocytes by weaning [119]. However, recent studies proved that, similar to other organs, the gut contains progenitors that differentiate into a self-maintaining subset of MΦ that can persist into adulthood [107,120]. These long-lived, self-maintaining MΦ colonize specific locations within the gut wall, primarily in the submucosal and myenteric plexuses in submucosa and ME layer respectively, and also in intestinal crypts and around the vasculature. Whereas gut MΦ that are constantly replenished by circulating cells mostly reside the LP layer villi, in closer proximity to the lumen [50,121].

1.3.4.2 Functional heterogeneity of niche-specific gut MΦ

Lamina propria MΦ (LP-MΦ) are the most abundant MΦ population in the gut and predominantly reside within the villi. Most LP-MΦ require a continuous replenishment by monocyte-derived macrophages (short-lived) and known for their highly efficient effector

functions mainly phagocytosis and cytokine release. They communicate with T cells mainly by producing the anti-inflammatory interleukin (IL)-10 in homeostatic conditions that support regulatory T cell maintenance [111]. Moreover, they closely communicate with epithelial cells by secreting cytokines and other molecules to regulate their survival, tight junction integrity, and differentiation from the crypts [118,122]. More MΦ types are also present the mucosa like $CD169^{+}$ MΦ near the crypts and are key regulators of epithelial barrier function and immune homeostasis during inflammation [123] (Figure 6).

The infiltrated circulating monocytes into the gut wall undergo tissue-specific differentiation to acquire gut MΦ phenotype in order to contribute to the LP-MΦ pool. This differentiation process occurs through a series of maturing phases known as monocyte to MΦ waterfall and controlled by the transcription factor Nr4a1 [119,124]. The newly infiltrated monocytes upregulate the major histocompatibility complex type II (MHCII) and downregulate the monocyte marker Ly6C and their extravasation genes. Then, they acquire the Cx3cr1 expression to adopt the mature MΦ phenotype. This monocyte to MΦ waterfall takes 5-6 days until reaching the $Cx3cr1^{high}$ $MHCII^{high}$ $Ly6C^{-}$ accompanied with upregulating MΦ genes essential for their effector functions (phagocytosis, cytokine release, and complement system) [104,119]. However, these newly differentiated MΦ still do not completely resemble resident ones even 12 days after their infiltration, yet, they keep developing over time. It worth to note that this process of monocyte to MΦ differentiation may vary in the colon LP layer due to the different anatomy and microbiome composition [125]. Nevertheless, the LP layer also harbors long-lived self-maintaining MΦ but to a lesser extent, and proved by monocyte-depleted mouse models [112]. Under gut injury or inflammation, monocyte engraftment is favored over resident MΦ self-maintenance [112].

The enteric nervous system is a large division of the peripheral nervous system that regulates gut motility and secretion and is represented by plexuses: the submucosal plexus within the submucosa, and myenteric plexus within the ME layer between circular and the longitudinal muscle layers [126]. Neuron-associated MΦ locate close to the nerve fibers within the enteric plexuses and were identified as self-maintaining by fate-mapping models [127] (Figure 6). Functionally, they mainly showed an ability to maintain neuronal survival. Over 90% submucosal neuron-associated MΦ, and 80% of ME-neuron-associated MΦ were shown to be retained from birth, with little contribution of the monocyte-derived MΦ [107,128].

Blood vessel-associated gut MΦ are located in close proximity to the gut blood vasculature, signifying their role in defending the gut against environmental and inflammatory stimuli and maintaining vasculature integrity [129] (Figure 6). Some subpopulations of blood-associated gut MΦ were identified in the literature, such as mucosal perivascular MΦ and $CD169^{+}$ MΦ [124,130]. Mucosal perivascular MΦ locate in along the villi for supporting the gut-vascular barrier against the intense exposure to microbiota antigens and mostly derive from circulating monocytes [124]. $CD169^{+}$ MΦ were previously mentioned above in the LP-MΦ, and despite their initial link to crypts, they also associated to blood and lymph vessels, as in case of many organs

like the spleen [130]. They are known for triggering monocyte infiltration via upregulating the chemokine CCL8 upon inflammation. Depleting these cells or inhibit CCL8 ameliorates inflammation, suggesting their link to mucosal inflammation progression [131].

Other MΦ niches exist within the gut, such as crypt associated MΦ that closely interact with ISCs and Paneth cells supporting their functionality and homeostasis [132]. This subset still lacks a detailed investigation over their roles in health and disease (Figure 6). Additionally, Peyer's patch-associated MΦ are a distinct MΦ subset that exist within Peyer's patches; however, they lack the expression of main MΦ markers but rather identified as $Tim4^{+}$ $CD4^{+}$ and $Tim4^{+}$ $CD4^{-}$. These cells are transcriptionally characterized as antimicrobial and antiviral are specialized in clearing pathogens and apoptotic cells [133].

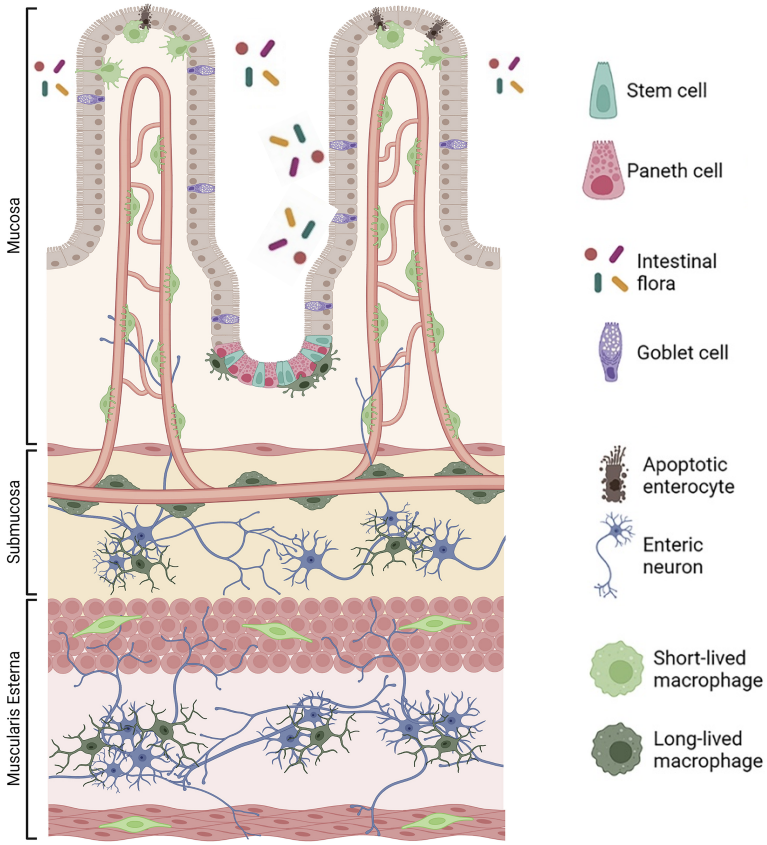

Figure 6 Microanatomical localization of intestinal MΦ adapted from Delfini et al. 2022 [34]. MΦ (green) reside throughout all the different intestinal layers. In the mucosa, MΦ are mainly short lived (light green). Conversely, in the deeper layers of the intestines long-lived, self-maintaining MΦ are present (dark green).

1.3.5 Liver MΦ

Among all organs, the liver has the highest percentage of MΦ, constituting around 15% of its total cells. Thus, the crucial role of liver MΦ in liver homeostasis is well-known and extensively studied. Liver MΦ are efficient scavengers of microbes and their products coming from the gut by the portal vein, sensing by this any instabilities in gut homeostasis, representing immune sentinels capable of regulating immune responses. Hepatic MΦ encompass highly heterogeneous populations differ by their origin, localization, and functions, and also under disease conditions. In the following paragraphs Hepatic MΦ subsets will be described.

Kupffer cells (KCs) are self-maintaining tissue-resident MΦ originating from fetal-liver EMPs, and represent the most abundant MΦ population in the liver. These cells were named after "Karl Wilhelm von Kupffer" who discovered them in 1876 [134,135]. They colonize the sinusoids lining the endothelial cells for optimal filtering of the pathogens and materials derived from the gut. Their phagocytosis function highly depends on the highly expressed Fc receptors for efficiently clearing aged red blood cells and platelets, and complexes of dual-hemoglobin. A key function of KCs under steady state is regulating the metabolism of iron and bilirubin. In addition, the KC expression of the cholesteryl ester transfer protein (CETP) enabled their role in cholesterol metabolism [136].

Despite their very early discovery, distinguishing KCs from other hepatic MΦ was difficult, as they share most MΦ markers including CD64, F4/80, and Mertk. In the past decade, understanding of KCs has expanded thanks to the discovered KC-specific murine marker Clec4F, that enabled generating mouse models for labeling and depleting KCs. Nevertheless, Clec4F is expressed only by mature KCs limited characterizing developing monocytes into KCs [137]. Moreover, the instable expression of this marker in human suggested the need for more efficient approach for studying KCs. The current consensus on KCs markers in mice included Vsig4, Folr2, CD163, CD206, and Clec2 [138]. Notably, Clec2 is expressed on KCs in very early stage before Clec4F and Vsig4 expression [139]. Recent studies also suggested KCs heterogeneity, supported by the differential expression of CD206 and ESAM, dividing them into KC1s which are $CD206^{-}ESAM^{-}$, and KC2s which are $CD206^{+}ESAM^{+}$ [140,141].

Liver capsule MΦ (LCMs) are monocyte-derived MΦ that reside in the liver capsule and express general MΦ markers and specifically Cx3cr1, while lacking all KC-specific markers [142]. They are involved in maintaining capsular integrity and immune surveillance in the liver periphery by defending peritoneal pathogens and microbial products [143,144]. The lipid-associated MΦ (LAMs) are found near the bile ducts in the healthy liver and highly recruited in liver disease like in hepatic steatosis[145]. LAMs are known to have high expression of Trem2 and CD9 surface proteins, and their functions are still not fully studied [142]. However, some studies suggested that LAMs function as pro-fibrotic [146], while in other studies showed immunosuppressive and tissue repair [147].

1.3.6 HSD and MΦ

MΦ are key target cells of elevated extracellular sodium concentrations, contributing to blood pressure regulation and extracellular volume homeostasis via the tonicity-responsive enhancer-binding protein TonEBP (also known as NFAT5). TonEBP activation induces the expression of vascular endothelial growth factor-C (VEGF-C), which in turn promotes lymphangiogenesis. This process enhances interstitial Na^+ clearance and fluid drainage, thereby buffering salt-induced elevation of blood pressure [148,149]. Moreover, the previously mentioned Wnk1-Stk39 chloride-sensing pathway was shown to regulate MΦ effector functions depending on Cl^- influx, where depletion of *Slc12a2* (encoding NKCC1) that is involved in this pathway triggers pro-inflammatory responses and induces MΦ efferocytosis [150,151].

High-salt environment induces a specific MΦ activation state, MΦ (Na), which is different from MΦ (LPS) and MΦ (IFNγ). Molecular mechanisms of the effects of high salt were mediated by the cellular signaling pathways p38/cFos/AP1, Erk1/2/cFos/AP1, and Erk1/2/STAT6 [152,153]. The p38α (also known as MAPK14) is one of the p38 mitogen-activated protein kinases (MAPKs) family that get activated by environmental factors and cytokine induction. Under high-salt conditions, it activates cFos gene transcription known for promoting inflammation, thus shifting MΦ toward a pro-inflammatory state. However, this activation of cFos is via activating Erk1/2 (MAPK3/1) kinases activation, which is not involved in LPS activation of cFos [152–154]. This brought the attention to the HSD-linked suppression of STAT6, a critical mediator of anti-inflammatory responses, as Erk1/2 activation promotes STAT6 protein degradation by help of calpains proteases [152,155]. Besides, other studies showed that high salt boosts MΦ Interferon (IFN)-β production, enabling stronger sensing and increased tolerance to viral stimuli *in-vitro* and viral infections *in*-vivo [156]. In our own previous work, in-vitro studies demonstrated the effects of high salt environment on MΦ functions, revealing that a prolonged exposure to high concentration of salt disrupts phagocytosis and stimulates a migratory behavior towards excess salt concentration [157]

Regarding the systemic impact on MΦ throughout the body, HSD worsened LPS-induced acute lung injury in mice by boosting MΦ pro-inflammatory cytokines and promoting monocyte recruitment [152]. Also, HSD promoted pro-inflammatory polarization of microglia in steady state and also during cerebra ischemia via p38/MAPK signal pathway [32,158]. As mentioned earlier, HSD promotes skin Na^+ storage, mostly via MΦ-Nfat5-dependent manner (TonEBP-VEGF-C signaling) [159]. Moreover, in liver fibrosis mouse models, fibrosis was exacerbated by HSD, accompanied with increase of liver and gut MΦ numbers [33].

Collectively, HSD exerts significant influence on MΦ function across multiple organs. Nevertheless, studies addressing the HSD-induced responses of organ-specific MΦ in the gut and liver remain limited. Given the pivotal role of the gut–liver axis in dietary sensing, metabolic homeostasis, and immune regulation, a deeper understanding of how HSD modulates tissue-resident MΦ within these compartments is essential. Such insights will be

critical for elucidating the mechanisms underlying salt-driven inflammation and its systemic consequences.

1.4 Aims of the thesis

1.4.1 Aim 1– Study the impact of short- and long-term high-salt diet on gut and liver integrity and homeostasis

Besides its well-studied effects on the cardiovascular system and kidneys, a high-salt diet poses many risks to other axes in the body, leading to dysregulation of their homeostatic functions and interactions with other systems, particularly the immune system. The gut-liver-microbiome axis plays a key role in maintaining immune homeostasis in the gut, liver, and other organs. Understanding the effects of the high-salt diet on this axis can provide new insights into salt-driven immunological responses of MΦ within it. Thus far, limited studies have investigated the direct effects of the HSD on the gut-liver-microbiome axis in mice, especially in long-term consumption of 3 months.

The first study presented in this thesis aims to:

- **(i)** Examine the short- and long-term HSD effect on gut integrity, homeostasis, and vulnerability to infections in mice.
- **(ii)** Investigate the effect of long-term HSD on gut microbiome diversity and abundance in mice.
- **(iii)** Examine the liver pathophysiological responses of mice towards the short- and long-term HSD exposure.

1.4.2 Aim 2 – Identify intestinal MΦ subpopulations and investigate whether high-salt diet alters their functions and developmental origin

It has been previously established that MΦ *in-vitro* responds to excess salt concentrations by modulating their behavior and immunological responses mainly showing salt-dependent chemotaxis and shifting towards pro-inflammatory phenotype. In the body, MΦ responses towards HSD are more complex and are influenced by their microenvironment. Despite the rising research studies on intestinal MΦ, the characterization of their subpopulations is still insufficiently explored, nor is the short- and long-term HSD effect on their abundance. Furthermore, Moreover, gut MΦ molecular and developmental responses to the HSD are still understudied.

The second study presented in this thesis aims to:

- **(i)** Identify all gut MΦ subpopulations of mice based on their characteristic surface markers via flow cytometry.
- **(ii)** Investigate the cellular and molecular changes of gut MΦ following HSD exposure in mice, including their interaction with the intestinal epithelial cells.
- **(iii)** Assess the functional properties of gut MΦ in mice subjected to the long-term HSD by performing MΦ-specific functional assays.

(iv) Determine the developmental origin of the different adult gut MΦ subsets with the novel fate-mapping mouse model, and inspect for any developmental alterations when challenged with the long-term HSD.

1.4.3 Aim 3 – Investigate whether high-salt diet affects the development and functions of liver MΦ main subsets

Liver MΦ has been extensively studied in health and disease. They play a critical role in maintaining liver homeostasis and the underlying mechanisms of liver diseases. The effect of either a short- or a long-term HSD on liver MΦ has yet to be thoroughly explored. So far, only one study explored a 4-week-HSD on liver-fibrotic mice showing exacerbated MΦ-dependent fibrosis driven by gut dysbiosis. This brought the need to investigate how liver MΦ remodel their functions and ontogeny in response to the HSD, which is critical for understanding their role in metabolic adaptation, inflammation, and tissue remodeling under dietary changes.

The third study presented in this thesis aims to:

(i) Investigate the cellular and molecular changes of liver MΦ in mice following HSD.
(ii) Explore liver MΦ affected functions by the long-term HSD in mice by performing MΦ-specific functional assays.
(iii) Determine the developmental origin of the different adult gut MΦ subsets with the novel fate-mapping mouse model, and inspect for any developmental alterations when challenged with the long-term HSD.

2 Materials and Methods

2.1 Materials

The following devices (Table 1), consumables (Table 2), reagents (Table 3), buffers (Table 4), and antibodies (Table 5-7) were used to conduct the experiments presented in this thesis.

Table 1 Laboratory Devices

Device	Company
Advia 2120 Hemocytometer	Siemens
Centrifuge 5810 R	Eppendorf SE
Centrifuge 5424	Eppendorf SE
Cryostat CM3050 S	Leica Biosystems
Dissection equipment	Fine Science Tools
Digital Slide Scanner Axioscan 7	ZEISS
Electrophoresis system	VWR
Eppi Shaker (37 °C)	Eppendorf
FACS Aria sorter	BD Biosciences
FACS Symphony	BD Biosciences
Freezer -80 °C	New Brunswick Scientific
Fridge 4 °C	Bosch
LSM 880 Airyscan	Carl Zeiss AG
Mastercycler X50s	Eppendorf
Macroscope	Leica WILD Heerbrugg
Microscope Axio Lab.A1	Carl Zeiss AG
microplate reader spectrophotometer	Tecan SPARK
Neubauer Cell Counting Chamber	Paul Marienfeld GmbH & Co. KG
NextSeq2000 Sequencer	Illumina
37 °C incubator	BINDER
PCR cycler	Applied Biosystems
Precellys Evolution homogenizer	Bertin Instruments
Spectral cell analyzer SONY ID7000	SONY
Spectrophotometer (BioPhotometer)	Eppendorf
Thermo-shaker	Eppendorf
2720 Thermal cycler	Applied Biosystems
Ultracentrifuge	Beckman coulter
Vortex	Scientific industries
Pipetboy Easypet 3	Eppendorf

Table 2 Consumables

Consumables	Company
1.5 mL Eppendorf tubes	Eppendorf
2.0 mL Eppendorf tubes	Eppendorf
15 mL Falcon tubes	Sarstedt, Inc.
50 mL Falcon tubes	Sarstedt, Inc.
5 mL Pipettes	BRAND
10 mL Pipettes	BRAND
1 mL syringes	Braun
96 well plate U-bottom	VWR
12 well plate TC treated CytoOne	Starlab
24 well plate TC treated CytoOne	Starlab
6 well plate TC treated CytoOne	Starlab
70µm easy strainers	VWR
40µm easy strainers	VWR
50 mL Ultracentrifuge open tubes thin wall	Beckman
Pipet-tips (10 µL, 200 µL, 1000 µL)	Sarstedt, Inc.
VWR cell strainer	Avantorä
FACS tubes	Sarstedt, Inc.
Faltenfilter Typ MN 615 ¼	Faltenfilter Typ MN 615 ¼
Glass tissue douncers	KIMBLE
Glass Petri dish coated with SYLGARD	
Magnet EasySep	STEMCELL Technologies
Pasteur pipette	avantor™
10 cm Petri dishes	Labomedic
Tubes 2.0 mL	TubeOne®
Tubes 1.5 mL	TubeOne®
Serological pipettes	Sarstedt, Inc.
Superfrost Plus Adhesion Microscope Slides	Epredia
Fluoromount G	Invitrogen
Disposable scalpel blade with plastic handle	RIBBEL®
Microtome blades	FEATHER
Microvette	Sarstedt, Inc.

Table 3 Reagents and chemicals

Reagent	Company
7-AAD	Sigma-Aldrich
β-mercaptoethanol 50 mM	ITW Reagents
Bovine serum albumin (BSA)	Sigma-Aldrich
Calcium chloride CaCl2 powder	Carl Roth

Collagenase IV	Thermo Fisher Scientific
Collagenase D	Sigma-Aldrich
4’,6-Diamidino-2-phenylindole, diacetate (DAPI)	BioLegend
Dextran 4kDa FITC	Signa-Aldrich
Dextran 70kDa Texas-red	Thermo Fisher Scientific
Dispase II powder	Thermo Fisher Scientific
DMEM	Pan Biotech
DNase I	Thermo Fisher Scientific
D-Sucrose	Thermo Fisher Scientific
Dithiothreitol (DTT)	Thermofischer Scientific
Dulbecco’s phosphate-buffered saline (DPBS, 10x, w/o Ca and Mg)	PAN-Biotech
Ethanol 100 %, molecular biology	Carl Roth
Ethylenediaminetetraacetic acid (EDTA)	Sigma-Aldrich
Fetal bovine serum (FBS),	South America origin
0.2 µm sterile filtered	PAN-Biotech
Fluoromount-G	Thermo Fisher Scientific
Formaldehyde 16 % (w/v)	Fisher Scientific
Giemsa solution	Merck
Hoechst 33258	Life Technologies
HEPES 1M	PAN-Biotech
HBSS 1X	PAN-Biotech
IGEPAL® CA-630	Sigma-Aldrich
Isopropanol (2-Propanol) 99,9%	VWR
Kaisers Glycerin-Gelatine phenolfrei	Carl Roth
Kanamycin	Sigma-Aldrich
Kalium chloride (KCl)	Thermo Fisher Scientific
LB medium	Roth
Magnesium chloride (MgCl2)	Sigma-Aldrich
Magnesiumacetate Tertrahydrat (Mg Acetate)	Sigma-Aldrich
Mayer´s hematoxylin	Carl Roth
MojoSort Streptavidin Nanobeads	Biolegend
Narketan, ketamine hydrochloride	Vetoquinol
Normal goat serum (NGS)	VWR
Oil-red-O powder	Sigma-Aldrich
Optiprep	STEMCELL
PBS tablets (w/o Mg2+ and Ca2+)	Thermo Fisher Scientific
Pen/Strep	Fischer Scientific
Ph-rodo beads	Invitrogen, Thermofisher
Phenylmethylsulfonyl fluoride (PMSF) 100 mM	Sigma-Aldrich
Precision count beads	BioLegend

Protein Block, Serum-Free	Agilent Technologies
Rat serum (RS)	Thermo Fisher Scientific
RNase inhibitor	Sigma-Aldrich
RPMI 1640	PAN-Biotech
Sodium chloride solution for anesthesia 0.9%	Braun
Sodium chloride powder for diet water (NaCl)	Sigma-Aldrich
Sphero Rainbow Calibration Particles (8 peaks)	BD Biosciences
Tissue-tek O.C.T, Sakura Finetek	Thermo Fisher Scientific
Trition-X 100	Thermo Fisher Scientific
Ultracomp eBeads™ Compensation Beads	Thermo Scientific
Xylazine	WDT-Markplatz

Table 4 Buffers and solutions

Buffers and solutions	**Ingredients**		
LB medium+ Kanamycin for Citrobacter rodentium culture	25	g/L	LB medium in Aqua Bidest autoclave, cool down
	+50	µg/mL	Kanamycin
1x Phosphate-buffered saline (PBS)	PBS (10x) without Ca2+, Mg2+ in Aqua Bidest		
Antibody solution (for IF)	5	%	BSA in PBS-T
Blocking solution (for IF)	5	%	BSA
	2	%	NGS in PBS-T
Cushion 29% for nuclei isolation	29	%	Optiprep in ODN
Digestion buffer for liver	1	mg/mL	Collagenase
	100	U/mL	DNase
	2.4	mg/mL	Dispase II
	3	%	FBS in PBS
Digestion buffer for gut Lamina propria	100	U/mL	Collagenase D
	1	Mg/mL	Dispase II
	100	U/mL	Dnase I
	100	µg/mL	Pen/strep
	5	%	FCS
	2	%	HEPES in RPMI
Digestion buffer for gut Muscularis externa	3	%	FBS
	2	%	HEPES
	250	U/mg	Collagenase IV

	100	U/mL	DNase
Gut solution A	1	X	HBSS
	1	%	Pen/Strep
	1	%	FBS
	1	mM	EDTA
Gut solution B (epithelial isolation buffer)	1	mM	DTT in gut solution A
FACS buffer	0.5	% w/v	BSA
	2	mM	EDTA
			in PBS
Fc block	0.5	%	CD16/32 (1:100)
	2	%	RS
			in FACS buffer
Formaldehyde 4 % (w/v)	16	%	Formaldehyde (w/v) in PBS
GM (Gradient Medium) for nuclei isolation	5	mM	CaCl2
	50	%	Optiprep
	3	mM	Mg Acetate
	10	mM	Tris pH 8
	0.1	mM	PMSF
	1	mM	β-mercaptoethanol
			in Aqua Bidest
HB (Homogenization Buffer) for nuclei isolation	320	mM	Sucrose
	5	mM	CaCl2
	3	mM	Mg Acetate
	10	mM	Tris pH8
	0.1	mM	EDTA
	0.1	%	Igepal
	0.1	mM	PMSF
	1	mM	β-mercaptoethanol
			in Aqua Bidest
Isopropanol, 60%	diluted from 99,9% Isopropanol with Aqua Bidest		
Narcotics	20	mg/mL	Xylazine
	100	mg/mL	Ketamine
			in NaCl (0.9 %)
ODM (Optiprep Diluent Medium) for nuclei isolation	150	mM	KCl
	30	mM	MgCl2
	60	mM	Tris pH8
	250	mM	Sucrose
Oil-red-O stock solution	0.5	g	Oil red O powder
	100	mL	99,9% Isopropanol

Oil-red-O working solution	1.5	parts	Oil-red-O stock solution
	1	part	Aqua Bidest
	(e.g., 60mL stock + 40mL water)		
PBS-T	0.3	%	Triton X-100 in PBS
Resuspension buffer for nuclei isolation	1	X	PBS
	1	%	BSA
RNasin Plus	1	mL	Resuspension buffer
	0.2	U/µL	RNase inhibitor
Sodium bicarbonate 100 mM	8.4	g	Sodium bicarbonate
	1	L	Aqua Bidest
Sucrose (30 %)	30	%	sucrose (w/v) in PBS

Table 5 Gut flow cytometry antibodies

Antibody	Conjugate	Clone	Company	Dilution
CD32/CD16	unconjugated	93	BioLegend	1:100
CD11b	BUV661	M1/70	BD Biosciences	1:200
CD11c	BV650	HL3	BD Biosciences	1:800
CD13	PE Cy7	QA19A79	BioLegend	1:400
CD16.2	AF488	9E9	BioLegend	1:400
CD163	APC-Fire810	S15049I	BioLegend	1:800
CD169	BV605	3D6.112	BioLegend	1:800
CD172a	BUV615	P84	BD Biosciences	1:400
CD206	AF700	C068C2	BioLegend	1:400
CD321 (JAM-1)	BV421	H202-106	BD Biosciences	1:200
CD32b	PE	AT130-2	Thermo Fisher	1:400
CD4	BV570	RM4-5	BioLegend	1:400
CD45	BUV805	30-F11	BD Biosciences	1:1000
CD64	PerCP Cy5.5	X54-5/7.1	BioLegend	1:200
Cx3cr1	PE Dazzle 594	SA011F11	BioLegend	1:200
F4/80	APC Cy7	BM8	BioLegend	1:100
Ly-6C	BV510	HK1.4	BioLegend	1:400
Lyve1	eFluor 660	ALY7	Thermo Fisher	1:200
Mertk	BV711	2B10C42	BioLegend	1:800
MHCII	Spark Blue 550	M5/114.15.2	BioLegend	1:800
Tim4	BV785	21H12	BD Biosciences	1:400
XCR1	SparkUV387	ZET	BioLegend	1:400

Table 6 Liver flow cytometry antibodies

Antibody	Conjugate	Clone	Company	Dilution
CD11b	BUV-737	M1/70	BD Biosciences	1:200
CD11c	BV605	N418	BioLegend	1:200
CD16.2	BV785	9E9	BioLegend	1:200
CD19	APC-Cy7	6D5	BioLegend	1:100
CD206	BV711	C068C2	BioLegend	1:200
CD31	BUV-661	390	BD Biosciences	1:200
CD32b	APC	AT130-2	Thermo Fisher	1:200
CD45	BUV-805	30-F11	BD Biosciences	1:800
CD64	PerCP-Cy5.5	X54-5/7.1	BioLegend	1:200
Clec1b (Clec2)	FITC	17D9	Thermo Fisher	1:200
Cx3cr1	PE/Dazzle 594	SA011F11	BioLegend	1:400
F4/80	BV421	BM8	BioLegend	1:200
Mertk	PE-Cy7	2B10C42	BioLegend	1:800
Tim4	BUV-496	RMT4-54	BD Biosciences	1:400
Ly-6C	PE	HK1.4	BioLegend	1:200
MHCII	AF-700	M5/114.15.2	BioLegend	1:400
NKp46	APC-Cy7	29A1.4	BioLegend	1:200
Tcr-ß	APC-Cy7	H57-597	BioLegend	1:50
Vsig4	APC	NLA14	Thermo Fisher	1:200

Table 7 Immunofluorescence staining antibodies

Antibody	Host	Conjugate	Company	Dilution
Iba1	rabbit	-	WAKO	Gut 1:1000 Liver 1:300
F4/80	rat	-	BIO-RAD	Liver 1:300
CD31	Armenian hamster	-	BioLegend	Gut 1:500 Liver 1:300
TubIII	mouse	-	BioLegend	Gut 1:500
α-rabbit IgG	Goat	AF488	Thermo Fisher Scientific	Gut 1:300 Liver 1:1000
α-rat IgG	Goat	AF555	Thermo Fisher Scientific	Liver 1:300
α-armenian hamster IgG	Goat	DyLight 649	BioLegend	Gut 1:300 Liver 1:1000
α -mouse IgG	Goat	AF555	Thermo Fisher Scientific	Gut 1:1000

2.2 Experimental Animals

2.2.1 Breeding

All mice used in the experiments presented in this thesis were from C57BL/6JRcc wildtype strain and housed in specific pathogen-free (SPF) conditions, with 12-h light/dark cycle, with food and water provided ad libitum. All mice were originally of C57BL/6J background and crossed with C57BL/6Jrcc for 2-5 generations. Animal procedures were performed according to the project license 2021.A203 issued by the Landesamt für Natur, Umwelt und Verbraucherschutz (LANUV). To generate the double fate-mapper Tnfrsf11a^{Cre}; Rosa26$^{LSL\text{-}YFP}$ (JAX stock #006148); Ms4a3^{FlpO}; Rosa26$^{FSF\text{-}tdTomato}$ (JAX stock #032864), we bred Tnfrsf11a$^{Cre/+;}$ Rosa26$^{FSF\text{-}tdTomato/FSF\text{-}tdTomato}$ mice with Ms4a3^{FlpO}; Rosa26$^{LSL\text{-}YFP/LSL\text{-}YFP}$ mice.

2.2.2 Genotyping

Upon weaning, the mice were ear-tagged. The acquired tissue was used for genotyping and it was prepared as follows. First, the tissue was dissolved in 200 µL of 50 mM NaOH for 30 min at 95°C. 20 µL of 1M TRISHCl (pH 8) were added for neutralization. Next, it was spun for 5 min at full speed in an Eppendorf centrifuge. The obtained 1 µL of the supernatant was used for genotyping. Per sample 1 µL of the isolated DNA was added to 9 µL of a master mix solution (consisting of 0.5 µL of each primer, 5 µL DreamTaq Green PCR Master Mix and H2O to receive a total volume of 10 µL; Table 8 and 9). The genetic material was amplified in 35 cycles in a PCR cycler (Table 10). Samples were applied on a 1.5 % agarose gel and separated via electrophoresis at 120 V for 30 min. The DNA was stained with the Sybr-safe dye for visualization via UV light.

Table 8 PCR Master-Mix

Reagent	Volume
Primer 1	0.5 µL
Primer 2	0.5 µL
Primer 3	0.5 µL
Primer 4	0.5 µL
DreamTaq Green PCR Master Mix	5 µL
H2O	Top up to 10 µL total volume (Dependent on number of primers needed)
DNA	1 µL

Table 9 PCR Primer for genotyping

Genotype	Primer	sequence Result
Ms4a3-FlpO	P1: AGA GAA ATC ATC AGG GCA GAA AT P2: GAA AGG GGA ACA AGC GAA GAT P3: TTG GCG AGA GGG GAA AGA	517 bp: wt 412 bp: FlpO
R26-FrtStoptdTom	P1: ACG GGC AGT AGG GCT GAG P2: AGC CTG CCC AGA AGA CTC C P3: GGT GTT GGG TCG TTT GTT CA	402 bp: wt 290 bp: FrtStop-tdTom

	P4: TCT AGC TTG GGC TGC AGG T	
R26-LoxStopeYFP	P1: CTG GCT TCT GAG GAC CG P2: CAG GAC AAC GCC CAC ACA P3: AGG GCG AGG AGC TGT TCA P4: TGA AGT CGA TGC CCT TCA	142 bp: wt 384 bp: LoxStop-eYFP
R26-LoxStoptdTom	P1: AAG GGA GCT GCA GTG GAG TA P2: CCG AAA ATC TGT GGG AAG TC P3: GGC ATT AAA GCA GCG TAT CC P4: CTG TTC CTG TAC GGC ATG	297 bp: wt 196 bp: LoxStop-tdTom
*(P = primer, wt = wildtype, bp = base pair)		

Table 10 PCR program

Steps	Temperature	Time	Repeats
1. Initial denaturation	95 °C	3 min	
2. Denaturation	95 °C	30 sec	x 35
3. Primer annealing	60 °C	30 sec	
4. Elongation	72 °C	30 sec	
5. Final extension	72 °C	5 min	

2.3 Experimental Design

In this study, C57BL/6Jrcc wild-type mice were fed either a standard-salt diet (0.3% NaCl in solid food and tap water, referred to herein as control diet CD) or a high-salt diet (4% NaCl in solid food and 0.9% NaCl saline water, referred to herein as HSD). Mice of both groups were subjected to the diet for either three weeks (short-term) or three months (long-term). Male and female mice were consistently studied in separate cohorts (Figure 7).

Only male mice were used for the intestinal permeability assay, colon infection model, ileum transcriptional analysis, MΦ cell volume measurements, and functional assays. Only female mice were used for the in vivo phagocytosis assay. All other analyses were performed on both male and female mice.

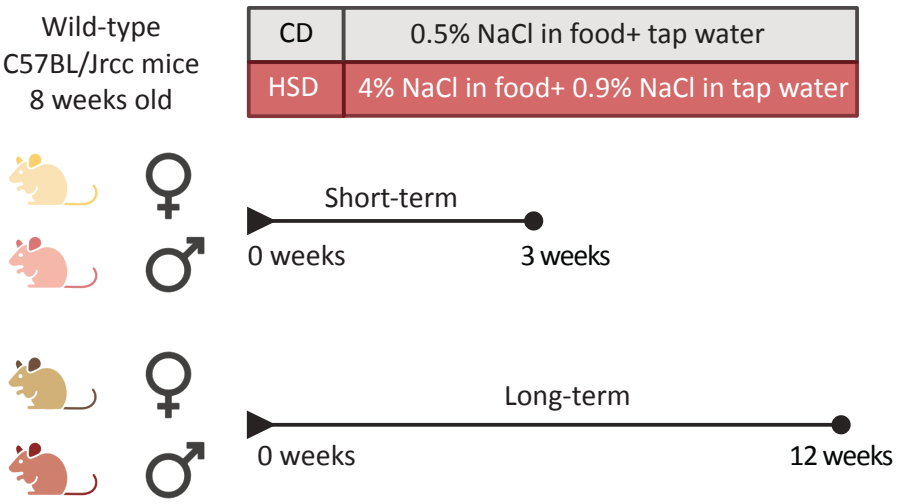

Figure 7 Experimental design diagram for the high-salt diet (HSD) model. CD: control diet; HSD: high-salt diet.

2.4 Organ Isolation

Mice assigned for the HSD experiments were anesthetized with a mixture 120 mg/kg ketamine and 20 mg/kg xylazine according to the project license 2021.A203. Once sedation was confirmed, i.e., mice did not respond with reflexes anymore the abdomen was opened surgically to access the heart. Over 400 µL blood was collected from the heart using a 26 G needle, an EDTA-flushed 1 mL syringe and a heparin-coated collection tube. Afterwards a minor cut was made in the left atrial appendage, allowing the blood to flow out during perfusion. A 26 G needle is inserted into the left ventricle to perfuse the mouse systemically with 20 mL PBS. Next, the gut and liver were collected in a PBS dish on ice.

2.5 Histological Analyses

2.5.1 Preparation of Liver Tissue for Cryo-sectioning

The livers were collected in 6 well plate and fixed in 4 % formaldehyde (in PBS) for 6 h while rotating at 4 °C. The tissue was washed three times with PBS for 10 min while rotating at 4 °C. The liver tissues were then placed in 30 % sucrose (in PBS) overnight at 4°C. After the tissues have sunk to the bottom of the tube, liver tissues were transferred into a tissue mold and covered with OCT. the molds were placed on dry ice to get solid, then stored at -80 °C. The frozen OCT block containing the liver tissue was cut with a Cryostat and 20 µm (for IF staining) or 10 µm section (for ORO staining) were collected on superfrost glass slides. The slides were stored at -20 °C until used.

2.5.2 Immunofluorescence Staining of Gut ME layer Tissue

2 cm of gut ME layer was collected and fixed in 4 % formaldehyde (in PBS) while pinned to a SYLGARD-coated dish, for 30 min with shaking at 4°C. Tissues were then transferred to 48-well plates, and permeabilized samples with permeabilization buffer for 2 hours at room temperature while shaking. Permeabilization buffer was removed and replaced by blocking buffer for 2 hours at room temperature while shaking. Primary antibodies were diluted in blocking buffer according to their dilutions in Table 7. Samples were incubated with primary antibodies over 2 nights, then washed with PBS 3 times, letting slices soak for 10-15 minutes each time. Secondary antibodies were centrifuged at 12000 rpm, 4°C, and diluted in blocking buffer according to recommended dilution. Samples were incubated with secondary antibody for 2h at room temperature, while shaking and keeping them protected from light (Table 7). Samples were washed with PBS 3 times, letting slices soak for 10-15 minutes each time in the dark. Tissues were transferred onto glass slides, and mounted on the slides using Fluoromount G, and sealed the coverslip using nail polish. Finally, samples were Left to harden for 30 minutes while protected from light and store at -20°C.

2.5.3 Immunofluorescence Antibody Staining of Liver Sections

The 20 µm liver tissue sections that were collected on glass slides and stored at -20 °C were thawed at room temperature. Tissue was hydrated through the addition of PBS for 10 min. To permeabilize the liver tissue, PBS-T was added two times for 10 min. Blocking solution was added and incubated at room temperature for 30 min. Slides were rinsed with PBS-T and the primary antibody mix, dissolved in PBS-T containing 1% BSA, was added and incubated over night at 4 °C. Slides were rinsed with PBS-T the next day and washed three times for 5 min with PBST. Then the secondary antibody mix, dissolved in PBS-T containing 1% BSA, was added and incubated for 2 hours at RT. Slides were rinsed with PBS-T and washed for 10 min with PBS-T. Then PBS-T with DAPI (1:10,000 dilution of a 10 mg/mL stock) was added and incubated at RT for 10 min. Slides were subsequently washed with PBS-T for 10 min and air dried before mounting the tissue with Fluoromount G and a cover slide.

2.5.3.1 Microscopy and image analysis of IF-stained gut and liver

Fluorescent antibody labeled gut and liver tissue was imaged with the confocal microscope LSM 880 AiryScan (Carl Zeiss) and the Zen-black software. Gut tissue was cut at 63x magnification, while liver sections were imaged at 40x. Z-stacks were acquired with 1 micron interval at a total thickness of 20 – 30 µm. Tile images were stitched with the Zen-blue software. Images were exported in the czi format and process with the Fiji software.

2.5.3.2 3D rendering analysis

3D rendering analysis was performed by MotiQ plugin in FIJI [160]. Z-stack Images of tissue MΦ were used for this analysis. To analyze the morphology of the MΦ only the Iba-1 labeling channel was used and pre-processed by transforming into grey scale values, enhancing contrast by 0.05 %, subtracting background by 50 pixels, and applying Gaussian blur by 2.00 sigma. Analysis via MotiQ went through three steps: cropping single MΦ cells from the image, then applying a threshold for background subtractions and image segmentation, and lastly, performing the 3D analysis to measure the different MΦ cell morphological parameters. Images of cell skeleton and cell 3D reconstruction were generated, and a data table containing all measured parameter for each cell was created. Afterwards, data underwent filtering by a threshold to exclude unordinary outlier values.

2.5.4 Hematoxylin and Eosin Staining (H&E)

Gut and liver tissues were fixed in 4 % formaldehyde (in PBS) for 6 h while rotating at 4°C. The tissue was washed three times with PBS for 10 min while rotating at 4°C. The tissues were then placed into a 2 mL tube filled with 70 % ethanol for dehydration. The fixed gut and liver tissues were processed by the histology core facility of the university clinic (UKB), embedded in paraffin, cut and stained with hematoxylin and eosin. In short, tissue was mounted in paraffin. Paraffin blocks containing the tissues were cut with a microtome (4 µm) and floating sections were collected on glass slides and dried. In short, staining was performed according to Table 11.

Table 11 Hematoxylin and eosin staining.

Step	Reagent	Incubation time
1	Xylene	5 min
2	Xylene	5 min
3	100 % ethanol	2 min
4	100 % ethanol	2 min
5	96 % ethanol	2 min
6	90 % ethanol	2 min
7	80 % ethanol	2 min
8	70 % ethanol	2 min
9	H2O	1 min
10	Hemalaun	3 min
11	H2O	1 min rinse
12	Eosin	3 min
13	H2O	1 min rinse
14	70 % ethanol	0.5 min
15	80 % ethanol	0.5 min

16	90 % ethanol	0.5 min
17	96 % ethanol	0.5 min
18	100 % ethanol	0.5 min
19	100 % ethanol	0.5 min
20	Xylene	0.5 min
21	Xylene	5 min

2.5.5 Oil-Red-O Staining

The 10 µm liver tissue sections that were collected on glass slides and stored at -20 °C were thawed at room temperature (RT). sections were hydrated through soaking in a chamber containing VE H_2O for 5 min, then dipped gently 5 to7 times in 60% Isopropanol. Then slides were incubated in ORO working solution for 20 min at RT, followed by gently dipping two times in 60% Isopropanol. After that, the sections were observed by using a light microscope to ensure sufficient staining (sections transported in VE H_2O to the microscope). Then, sections counterstained with Mayer´s hematoxylin solution for 3-5 min at RT, followed by washing them in VE H_2O for 1 min at RT, then rinsing with running cold tap water in a 500mL beaker for 4 min. When color of the tissue changed from purple to blue, sections were washed by VE H_2O for 1 min at RT. Slides were mounted with Kaisers Gelatine and gently covered by glass slip, then left for 10 min under the hood to allow the Kaisers Gelatine to set. Sections were imaged directly by Microscope Axio Lab.A1.

2.6 Microbiome Analysis

2.6.1 DNA Extraction

Fecal and cecal specimen were transported on dry ice, and genomic DNA was extracted from approximately 100 mg of each sample using ZR BashingBead lysis tubes (0.1 and 0.5 mm, Zymo Research, Freiburg, Germany) combined with the chemagic DNA Stool 200 Kit H96 (Perkin Elmer, Rodgau, Germany), following the manufacturer's guidelines [161–163]. An additional mechanical disruption was performed by adding lysis buffer and utilizing the Precellys 24 Tissue Homogenizer (Bertin Instruments, Frankfurt am Main, Germany). Post-extraction, the DNA samples were stored at -20°C for subsequent processing.

2.6.2 16S rRNA Library Preparation & Sequencing

All samples underwent amplicon sequencing to profile their metagenomic composition. The V3-V4 region of the 16S rRNA gene was amplified in the first PCR step using the primers Bakt_341F (5’-CCTACGGGNGGCWGCAG-3’) and Bakt_805R (5’-GACTACHVGGGTATCT AATCC-3’). The PCR products were barcoded and combined in equal concentrations (4 nm), and pool as described in [164] The final pooled sample was quantified using the Qubit dsDNA HS Assay Kit (Thermo Fisher Scientific, Waltham, MA, USA), and the fragment sizes were verified with a

D1000 ScreenTape. Sequencing was carried out on an Illumina MiSeq platform with the MiSeq Reagent Kit v3 using a 2 × 300 cycle configuration. The pool was clustered at a final loading concentration of 8 pM with a 30% Phi-X spike-in.

2.6.3 Bioinformatics

The 16S rRNA sequencing data were processed using QIIME 2 version 2022.8 [165], where quality control and denoising were performed using DADA2 [166]. The resulting denoised sequences were classified using SILVA SSU 138 database to annotate amplicon sequencing variants (ASVs) with over 99% sequence similarity. All microbiome analysis steps up to this point were performed by Dr. Waldemar Seel. A rarefied feature table with a minimum depth of 18,421 reads was exported to be further analyzed by MicrobiomeAnalyst platform. Samples with fewer than 10,000 reads were excluded. MicrobiomeAnalyst was used to study diversity metrics, including alpha diversity measures (Observed features, Shannon entropy, Pielou's evenness, and Faith's PD) and beta diversity (Bray-Curtis, Jaccard, weighted and unweighted UniFrac). PERMANOVA was applied to assess the significance of differences [167,168]. Furthermore, the Linear discriminant analysis Effect Size analysis (LefSe) was performed to investigate differential abundance between CD and HSD in females and males.

2.7 Lipidomic Analyses

Liver tissues were collected, weighed (approximately 50 mg), frozen at –80 °C, and subsequently provided to Jelena Zurkovic for lipidomic analysis. Lipidome raw measurements were quantified in relation to internal standards measured simultaneously by the same instrument. The resulting values were normalized by the amount of tissue to obtain measurements in pmol/mg. All lipid species that exhibited consistent levels across all samples were excluded from the dataset, as they are considered uninformative for the diet-effect. Additionally, species classified as triacylglycerols (TG) with an odd number of double bonds were omitted, as they were unlikely to have originated from mice. This resulted in a set of 19 lipid classes, namely Cholesteryl ester (CE), Ceramide (Cer), Diacylglycerol (DG), Dihexosylceramide (DiHexCer), Hexosylceramide (HexCer), Lysophosphatidylcholine (LPC), Ether-linked lysophosphatidylcholine (LPC-O), Lysophosphatidylethanolamine (LPE), Monoacylglycerol (MG), Phosphatidic acid (PA), Phosphatidylcholine (PC), Ether-linked phosphatidylcholine (PC-O), Phosphatidylethanolamine (PE), Ether-linked phosphatidylethanolamine (PE-O), Phosphatidylglycerol (PG), Phosphatidylserine (PS), Sphingomyelin (SM), Unsaturated fatty acyl tails of triacylglycerol (TG unsat), and Saturated fatty acyl tails of triacylglycerol (TG sat). After the selection process, the dataset contained 402 metabolites. For each sample, the species within the same class were combined by calculating their mean values. The results were then summarized by computing the mean per condition. Log2 fold changes were calculated by comparing HSD to CD condition. For each lipid class, an independent sample t-test was used to detect changes between HSD and CD means.

2.8 Intestinal Paracellular Permeability Assay

2.8.1 Dextran Administration and Sample Harvesting

After 3 months of CD or HSD feeding, male mice were fasted for 6 h, then 100 µL of 4-kDa FITC dextran (Sigma-Aldrich, 40 mg/mL in PBS) and 100 µL 70-kDa Texas-red dextran (Thermo Fisher Scientific, 5 mg/mL in PBS) was applied orally at a single dose to each mouse of CD and HSD groups. The mice were anaesthetized after 30 min, 2 and 4 h, and blood from the retrobulbar capillary plexus was sampled into heparinized tubes for 4 and 70 kDa dextran analyses. Plasma was obtained after centrifugation at 2000x g for 5 min. Another group of three mice were not treated with dextran and their plasma served as blank. Fluoresce intensity of FITC and Texas-red dextran sugars in plasma at the 30 min, 2 and 4 h time points by Tecan Spark Microplate reader.

2.8.2 Measuring Dextran Fluorescence

To measure the concentration of dextran that reached the bloodstream, collected plasma was diluted in PBS to reach 100 µL. Fluorescence was measured spectrophotometrically (Tecan Spark Microplate reader, Germany) in 96-well black plates. For FITC, excitation: 488 nm, emission: 528 nm, 70% gain. And for Texas red, excitation: 600 nm and emission: 625 nm, 100% gain. FITC and Texas-red dextran concentrations were calculated with the help of standard concentrations prepared in PBS ranging from 0 to 25 µg/mL of both 4-kDa FITC dextran or 70-kDa Texas-red dextran. Emission signals in plasma of mice receiving PBS were subtracted from those of mice treated with the 4-kDa or the 70-kDa FITC dextran.

2.9 Bacterial Infection of Mouse Colon

To investigate the impact of HSD on colitis resolution and infection clearance, the *Citrobacter rodentium* (*C. rodentium*) bacterial strain was used, a murine model pathogen for enteropathogenic *E. coli.*

2.9.1 Preparing Bacteria

All procedures involving *C. rodentium* were carried out under biosafety level 2 (S2) conditions. *C. rodentium* strain DBS100 ICC180 (116) was kindly provided by Dr. Heike Weighardt and originally obtained from Dr. Matthias Lochner (Hannover). To determine a growth curve for *C. rodentium*, one colony of *C. rodentium* was grown in 100 mL of LB medium supplemented with kanamycin (50 mg/mL). The OD_{600} of the culture was measured using a Bio-photometer (Eppendorf) at 3; 4.5; 6; 7; 7.5 and 8 hours. At each time-point dilutions of *C. rodentium* were plated onto LB agar supplemented with kanamycin (30 mg/mL) to determine the exact CFU of *C. rodentium* (Figure 8). All further infection experiments with *C. rodentium* were based on this growth curve. 10^9-10^{10} CFU/mL of *C. rodentium*, equated to an OD_{600} absorption of about 0.6 (Figure 1).

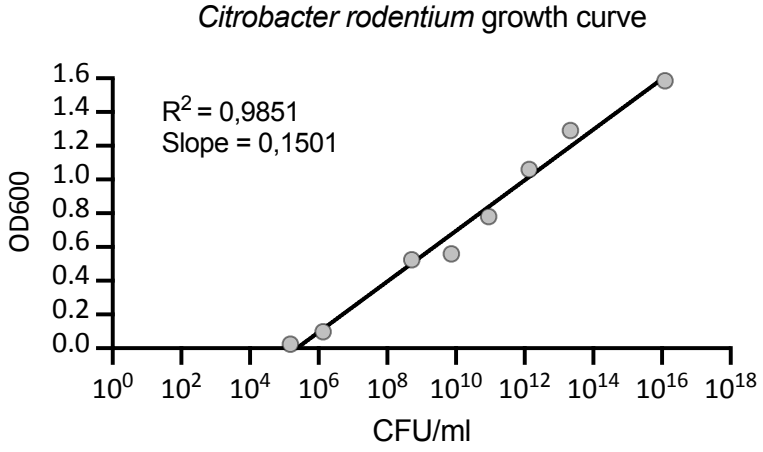

Figure 8 Growth curve of *C. rodentium*. The OD_{600} of the culture of *C. rodentium* was measured at several time-points. The CFU of *C. rodentium* was determined at these time-points and displayed according to the measured OD_{600} values.

2.9.2 Citrobacter rodentium Infection in Mice

For the *in-vivo* colon infection model, 2 mL of the *C. rodentium* culture at OD_{600}= 6 were taken, and centrifuged down at room temperature, 3200g for 20 min. Pellet was resuspended with 2 mL sterile PBS and kept cold until administrated. After 3 months of CD or HSD, male mice were transferred to S2 area of the animal facility, starved overnight, and orally infected by use of a gavage needle with 200 µl PBS containing around 10^9 CFUs each. Mice were scored every 2 days for their weight, behavior, feces consistency, and blood existence in the feces. Feces consistency was scored in an unbiased and blinded approach. Fecal occult blood (FOB) rapid tests were used to check blood existence in the feces. The following scoring system was used to determine the severity of the infection (Table 12). By summing the mouse weight change, Feces consistency score, and blood existence score in the feces, disease activity index (DAI) was determined.

Table 12 Clinical scoring system for *C. rodentium* bacterial infection

Score*	Stool	Blood existence in stool	Body weight
0	Hard stool	No blood (visible or occult)	None
1	Loose stool		Up to 5% weight loss
2	Soft stool	Occult blood (positive test)	5-10% weight loss
3	Shapeless stool		10-15% weight loss
4	Diarrhea	Visible blood and positive test	Over 15% weight loss

* Each parameter was scored individually, and the values were then summed and averaged to calculate the disease activity index (DAI).

2.9.3 Processing and Analyzing Organs and Feces After Infection

After 22 days of the infection, mice were anaesthetized according to the project license, and transcardially perfused with 20 mL PBS each. Feces, liver, gut, and mesentery lymph nodes (mLN) were collected, weighted around 100mg portion, and homogenized in 1 mL sterile PBS by Precellys Evolution homogenizer (Bertin Instruments). 100 µL of the Homogenate was diluted in 900 µL PBS, and from this diluted solution, a serial of 1:10 dilutions were performed. 25 µL of the undiluted sample and its diluted solutions were spread cultured on LB Agar + Kanamycin 30 mg/mL 10 cm dishes (each on quarter of the dish) and incubated overnight at 37°C. CFUs were counted in the appropriate dilutions (where CFUs are countable, ranging between 8 -75 in each quarter) and actual further concentrations of *C. rodentium* in the prementioned samples was identified. Proximal colon 1 cm tubes were also collected and fixed with 4 % formaldehyde for 6h, then 70% ethanol. Colon then was embedded, sectioned, and processed further for H&E staining by the histology core facility of the university clinic (UKB).

2.10 Single-Nuclei RNA Sequencing Analysis

2.10.1 Nuclei Isolation

Frozen ileum LP and ME tissues were cut tissue on dry ice (max 0.4mg tissue), then transferred immediately in homogenizer containing 1 mL of ice-cold HB buffer with 5 µL RNase inhibitor. Tissue was homogenized 5 times with douncer A and 10 times with douncer B, then filtered through 70 µm cell strainer into 50ml Falcon tube. Strainer was washed with 1,65 mL HB to a final volume of 2,6 5mL. Then, 2,65 mL of GM medium was added to the sample to a final volume 5,3 mL. Afterwards, in an ultracentrifuge tube, 4mL of 29% Cushion was first layered, and then the sample was layered on top of the cushion using a P1000 pipette, without disturbing the cushion. tubes weight was adjusted with HB to be equal among samples. Samples then were centrifuged by an ultracentrifuge (Beckman) in an SW41Ti rotor, at 7.700rmp and 4°C for 30min. Supernatant was removed with a plastic Pasteur pipette, and the lower supernatant was removed with P200 pipette. Pellet containing the isolated nuclei was resuspend in 200 µL of resuspension buffer (+Rnase inhibitor and DAPI), transfer to a FACS tube through a 0.4 µm filter. Tube was washed out with further 100-200 µL of resuspension buffer (+Rnase inhibitor and DAPI), and pooled with the previous nuclei. 10 µL of the nuclei were stained with trypan blue and counted by Neubauer counting chamber to check their quality and count. Then, $DAPI^+$ nuclei were sorted into pre-coated 1.5ml tubes (Tubes were filled with resuspension buffer and left at 4°C for 24 hours before sorting) using Aria sorter (BD Bioscience). Number of sorted nuclei were 10x the required amount for further sequencing steps as ~70% of the nuclei does not get pelleted. Sorted nuclei were centrifuged for 3 min at 400g, then without stopping speed was increased to 600g for another 5 min. Pellet was resuspended in the required volume of 10x Genomics buffer plus 3 µL extra, and loaded on 10x Genomics lanes. With the remaining 3 µL, 2 µL was taken to resuspend in 100µl resuspension buffer and perform a quality check in the flow core (Symphony, BD Bioscience).

Sample was run completely to check number of nuclei to determine how many loaded with ~60% captured.

2.10.2 Single-Nuclei Library Preparation and Single-Cell RNA-Sequencing

This single-nuclei experiment was performed using 10x Genomics technology by Dr. Nelli Blank-Stein. Therefore, sorted nuclei were counted and the viability was examined by trypan blue staining using a Neubauer counting chamber. Next, the nuclei suspension was adjusted to a concentration of 1000 nuclei/µL and processed by using the 10x Genomics Chromium Controller and the Chromium Next GEM Single cell 3'Reagent Kit v3.1 (Dual Index) (PN-1000268, 0x Genomics, Pleasanton, CA, USA) according to the standard manufacturer's protocol. The loaded cells were adjusted to 16,000 cells/sample to target a recovered cell number or 10,000 cells/sample for library preparation and sequencing. The cDNA integrity and concentration measurements as well as the library concentration and size distribution were assessed using an Agilent high-sensitivity D5000 assay on a Tapestation 2200 system (Agilent Technologies). The cDNA libraries were quantified using a high-sensitivity dsDNA assay (Qubit, Thermo Fisher Scientific). In the final library preparation, amplified cDNA was fragmented, and size selected using SPRIselect magnetic beads (Beckman-Coulter) to purify for a library with a size distribution of 200 - 600 bp. After adaptor ligation and sample indexing, the final fragment size and concentration were measured and samples were pooled in an equimolar range. Samples were sequenced with a sequencing depth of > 30,000 reads/cell with 50 bp paired-end reads on an Illumina NextSeq2000 system.

2.10.3 Single-Cell Data Alignment, Read Processing, Data Analysis and Annotation

Raw Single-nucleus RNA sequencing data was demultiplexed and aligned to Mus musculus reference genome (mm10), and processed using CellRanger (v7.1.0) for read alignment and gene quantification. Alignment and subsequent analysis were performed by Dr. Lisa Maria Steinheuer. Downstream analysis was conducted in Seurat (v4.1.1) with default preprocessing parameters. Nuclei expressing at least 200 genes across a minimum of three nuclei were retained. Further filtering removed nuclei with fewer than 500 or more than 5,500 detected genes, as well as those with mitochondrial RNA content exceeding 10%. Data normalization and scaling followed Seurat's standard pipeline. Sample integration was performed using FindIntegrationAnchors with default settings. UMAP visualization was based on the first 20 principal components (PCs), and clustering was performed at a resolution of 0.5. Doublets were identified and removed using scDblFinder (v1.4.0) with default parameters. Cell clusters were annotated using a reference marker gene panel. For MΦ subclustering, the first 20 PCs were used with a clustering resolution of 0.5. Differential expression analysis within MΦ subclusters compared the high-salt diet (HSD) group to the normal diet (NSD) group using the Wilcoxon rank-sum test. DEGs were ranked by adjusted p-value, and the top and bottom 100 genes were selected for functional enrichment analysis separately. Overrepresentation analysis (ORA) was performed using the clusterProfiler (v2.18.1) package, querying the Hallmark, Reactome, and Gene Ontology (GO)-Biological Process (BP) databases

from the msigdbr package (v7.5.1). Cell-cell communication between MΦ and enterocytes between HSD and NSD was assessed individually for each MΦ subset using CellChat (v1.6.0) with default parameters. Genes were considered overexpressed if detected in at least 10% of cells, with a minimum of 10 cells per group required for interaction inference.

2.11 Flow Cytometry Analysis

2.11.1 Preparation of Gut Tissues

Entire length of intestine was collected, from stomach to anal sphincter. Total length of the different gut regions was measured, and for stomach, weight was taken. Single intestinal regions were dissected and their length for flow cytometry was measured, and flushed with PBS. Muscularis Externa was separated form underlying lamina propria.

2.11.1.1 Gut muscularis externa

Gut tissue of the different regions was minced in 500ul ME digestion buffer without enzymes, then 1mL of digestion medium with enzymes was added, and incubated 30 minutes with agitation at 37°C. Sample solution was resuspended and filtered through 70um filter, then filter was washed with 10mL FACS buffer. Samples Spun down at 4°C, 350g for 8min, and cells pellet was resuspended in 200ul FACS buffer and plated in 96-well plate for staining. Plate was centrifuged at 500g for 5min and pellets were stained with 20µl extracellular antibodies indicated in Table 5 for 30 minutes at 4°C. After centrifugation at 4°C, 350g for 5min, pellets resuspended with 100µl FACS buffer.

2.11.1.2 The gut lamina propria

LP tissue was cut into two segments and incubate with 10mL per sample preheated gut solution B for 20 minutes with agitation at 37°C. Afterwards, tissue was collected and incubated with 10mL per sample for 20 minutes with agitation at 37°C. The remaining tissue was placed in 500ul LP digestion buffer without enzymes and minced. Then, 1mL of digestion medium with enzymes was added, and incubated 30 minutes with agitation at 37°C. Sample solution was resuspended and filtered through 70um filter, then filter was washed with 10mL FACS buffer. Samples Spun down at 4°C, 350g for 8min, and cells pellet was resuspended in 200ul FACS buffer and plated in 96-well plate for staining. Plate was centrifuged at 500g for 5min and pellets were stained with 20µl extracellular antibodies indicated in Table 5.

2.11.1.3 Gut sample acquisition and analysis

Gut samples were acquired on the Sony ID7000 7L spectral analyzer (Flow cytometry core facility, Bonn) and saved with unmixing. Samples were further analyzed by FlowJo software.

2.11.2 Processing of Liver Tissue for Flow Cytometry Analysis

The whole organ weight was determined and subsequently 400-500 mg of the liver tissue were used for flow cytometry (exact weight determined). This liver tissue was transferred into a 6 well plate with FACS buffer.

2.11.2.1 Liver digestion

FACS buffer was replaced by 0.5 mL digestion mix (Dispase, DNase, collagenase (D). The tissue was cut into small pieces with blunt scissors and placed in a 37 °C shaker (90 rpm) for 30 min. The suspension was transferred through a 70 µm strainer into a 15 mL tube and flushed with 3 mL FACS buffer. To discard hepatocytes, samples were centrifuged with 50 g for 3 min at 4 °C. Then, the supernatant was transferred to a new tube and recentrifuged with 400g for 5 min at 4 °C, pellet was resuspended in 1 mL FACS buffer and transferred to FACS tubes, and recentrifuged again with 400g for 5 min at 4 °C.

2.11.2.2 Liver cell staining

The pellet was resuspended in 50 µL Fc-blocking solution and incubated for 5 - 10 min on ice. Afterwards, 1 mL fresh FACS buffer was added and centrifuged (400g for 5 min at 4 °C). Pellet was resuspended with 20 µL of the antibody mix (Table 6) and incubated for 30 min at 4 °C. After topping up with 1 mL FACS buffer the cells were pelleted (400 g, 5 min, 4 °C) and resuspended in 400 µL FACS buffer.

2.11.2.3 Liver sample acquisition and analysis

For measuring the labeled cells with a flow cytometer, 100 µL of the suspension was filtered through a 70 µm strainer and an equal volume of Hoechst+ counting beads was added (DAPI was diluted by 1:5000 from a 10 mg/mL stock, counting beads were diluted by 1:10). Labeled cells were acquired with the BD Symphony flow cytometer and the Diva software. Exported data were analyzed with the FlowJo software.

2.12 Ex-vivo Phagocytosis Assay

2.12.1 Preparing gut cell suspension for MΦ enrichment

5 cm of ileum was taken for digestion without layer separation. Epithelial isolation and further digestion were performed as mentioned earlier for gut LP layer (2.2.6.1). After getting the cell pellet, it was resuspended in 500 µL FACS buffer and transferred to FACS tubes, and centrifuged again at 4°C, 400 g, 5 min.

For liver, around 400 mg piece of liver was taken for MΦ isolation. Liver digestion was performed as mentioned before according to 2.2.6.2 until reaching the cell suspension. The cell suspension was centrifuged at 4°C, 400 g, 5 min.

2.12.2 Magnetic Enrichment of Liver and Gut MΦ

The supernatant was discarded and the pellet resuspended in 200 µL of FACS buffer containing 5% Rat serum and 0.5% Fc block, and incubated 10 min on ice. 1 µL biotinylated CD11b antibody was added (by ratio 1:200) and further incubated 15 min on ice. 5 mL of FACS buffer were added, and spun down at 400 g, 5 min, at 4°C. Supernatant was discard and pellet was resuspended with 360 µL FACS buffer. 40ul of MojoSort streptavidin magnetic beads were added and incubated for 15 minutes. Samples were washed with 5 mL FACS buffer, spun down at 400 g, 5 min, 4°C. Cell pellets were resuspended in 2 mL FACS buffer and transferred cell suspension into a FACS tube.

FACS tubes were placed into the cold EasyCell magnet for 5 min on ice in a FACS tube. While keeping the FACS tube in the magnet, supernatant was poured into a fresh FACS tube. The tube was taken out of the magnet and resuspended the pellet in 1 mL FACS buffer and transferred the cells to a collection falcon. The FACS tube containing the flow-through was place in the magnet and once again incubated for 5 minutes on ice. This step of magnetic enrichment was repeated 3 times. After the final incubation on the magnet, the supernatant was discarded and 5mL of FACS buffer were added to the enriched cells, centrifuged at 400 g, 4°C, 8 min. Cell pellets were resuspended in 500 µL MΦ medium DMEM and counted. Plate 105 cells per well in 96-well plate (for further flow-cytometry based readouts). Isolated cells from the gut were cultured with M-CSF, while liver cells were cultured with DMEM only.

2.12.3 *C.rodentium* Staining

C.rodentium were cultured in LB medium+ Kanamycin 50 µg/mL with shaking 200 rpm. The optical density OD600 was measured regularly every 30 min and correlated to the *C.rodentium* growth curve to identify *C.rodentium* concentration CFUs/mL to reach the OD600 that correlates to 1. 10^{10} per mL (Depending on *C.rodentium* growth curve, OD600 for 1. 10^{10} CFUs/mL is 0.696). 1 mL bacteria were centrifuge at 4000 g for 20 min. Supernatant of LB medium was discarded and bacterial pellet was resuspended with 1 mL sterile PBS and centrifuged again at 4°C, 4000 g for 20 min. The bacteria were resuspended with 1 mL 100 mM Sodium bicarbonate pH= 8.5. The required amount of *C.rodentium* CFUs for the assays was calculated. Volume containing the required CFUs number was transferred to a new 1 mL Eppendorf tube. The pHrodo red dye was added to the required volume of bacteria in a final concentration of 0.5 mM (Stock concentration is 10mM), and incubated at room temperature for 1 hour with shaking. Afterwards, stained bacteria were centrifuged for 20 min, 4000 g at 4°C, and pellet was resuspended in PBS and repeated washing with PBS 3 times. On the last

centrifugation, pellet was resuspended with DMEM medium containing 10% FCS and stored in the fridge until used, for no more than 30 min.

2.12.4 *Ex-Vivo* Phagocytosis Assessment of Gut and Liver MΦ

For assessing macs phagocytosis capacity, isolated and cultured MΦ were plated 10^5 per well, and stained *C. rodentium* live bacteria was added in a ratio of 1 MΦ: 160 CFUs *C. rodentium,* and further incubated for 1 hour at 37°C. A control well containing cultured MΦ with *C. rodentium* was incubated at 4°C to serve as a negative control. Suspension of MΦ and *C. rodentium* was then centrifuged, and stained with MΦ canonical surface markers and FcγRs mentioned in Table 5, and incubated for 30 min at 4°C. MΦ were then centrifuged and pellet was resuspended in 100 µL FACS buffer and acquired by the flow cytometer Symphony (BD Biosciences). Percentage of MΦ that engulphed *C. rodentium* was determined, in addition to the mean fluorescence intensity (MFI) of *C. rodentium* labeling, CD16.2 (FcγRI), CD32b (FcγRIIb), and CD64 (FcγRIV) in MΦ.

2.13 *In-Vivo* Phagocytosis Assay

Phagocytic capacity was assessed by an *in-vivo* platelet depletion assay by using a well-studied immune thrombocytopenia mouse model (ITP). To assess KC function after long-term HSD in female mice, platelet baseline levels were measured in the retro-orbitally harvested blood with heparinized micro-hematocrit capillary tubes (Cat# MODU163613, VWR) using an Advia 2120 Hemocytometer (Siemens). Next, 0.375 µg/g BW (i.p.) of 6A6-IgG2c anti-platelet antibody was injected intra-peritoneally, and blood was sampled after 4, 24, and 72 hours, to assess for platelet counts as described above. Residual platelets count was compared between CD and HSD conditions.

3 Results

Before investigating gut and liver MΦ responses following a high-salt diet (HSD), it was first necessary to assess the direct effects of HSD on these organs, given the currently limited data available. Accordingly, and in line with the first aim of this thesis, pathological changes in the gut, liver, and gut microbiota were characterized. Building on these findings and aligning with the second aim, gut MΦ were examined in terms of their phenotype, morphology, developmental origin, and functional responses to HSD, as well as their potential role in mediating diet-induced adverse effects. Finally, in accordance with the third aim, liver MΦ were analyzed to elucidate their specific adaptations to HSD exposure.

3.1 Characterization of Gut Pathology in Response to Short- and Long-Term High-Salt Diet

3.1.1 Changes in Body Weight Gain

As a first step, body weight of mice was monitored throughout the HSD periods to detect any changes. Over 3 weeks and 12 weeks of diet exposure, female HSD-fed mice showed no changes in body weight gain compared to CD-fed mice (Figure 9A). Male HSD-fed mice also showed no weight gain changes compared to CD-fed mice over the first 3 weeks. However, starting from weeks 5 to 12 of HSD feeding, male HSD-fed mice exhibited a significant reduction in mean body weight gain in comparison to CD (Figure 9B). In summary, this result showed a male-specific effect of long-term HSD on mouse weight gain.

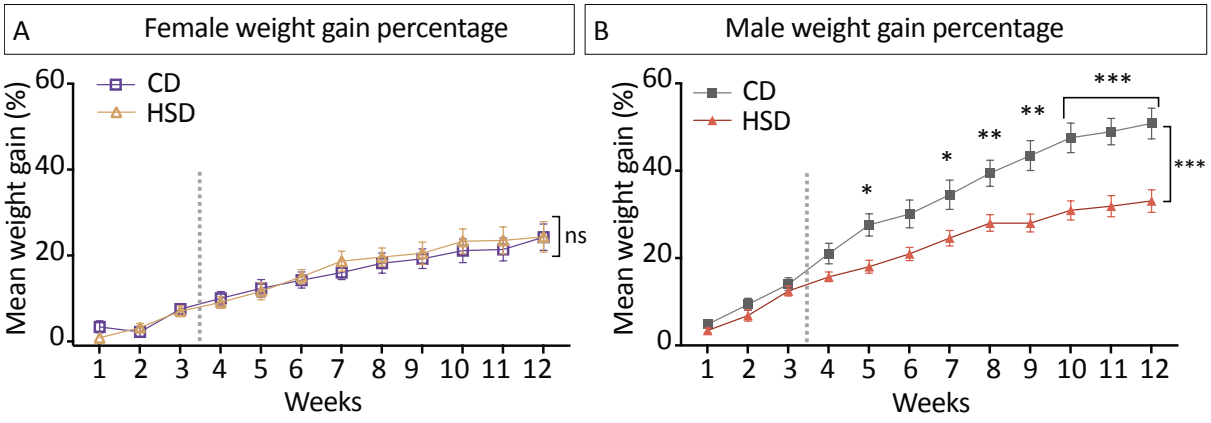

Figure 9 HSD effects on body weight gain. Mean body weight gain percentage through 12 weeks of CD and HSD in (A) female mice (n = 10/diet from 3 different experiments), and (B) male mice (n = 12/diet from 2 different experiments); Each data point represents the mean body weight gain of mice; error bars indicate the Standard Error of the Mean (SEM). Differences at individual time points were assessed using two-way ANOVA (mixed-effects model), * *p*-value (*p*) < 0.05, ***p* < 0.01, ****p* < 0.001, ns: not significant (p > 0.05); Overall line change across the entire period were analyzed using a linear regression, ****p* < 0.001, ns: not significant (p > 0.05).

3.1.2 Effects of Long-Term High-Salt Diet on Stool Hydration and Microbiome Composition

3.1.2.1 Water content in feces

To investigate whether long-term HSD impacts stool fluidity, we assessed the stool water content of HSD-fed and CD-fed mice after long-term HSD. HSD-fed male mice showed a significantly decreased fecal water content compared to CD-fed mice (with a mean of 57.9 for CD, and 53.5 for HSD, p = 0.036, unpaired t-test), implying a potential relationship between salt intake, constipation, and microbiome composition (Figure 10A).

3.1.2.2 Microbiome composition changes

While the microbiota responds rapidly i.e., within days to dietary changes, the long-term effects involve deeper, more systemic adaptations, including immune modulation, metabolic changes, and gut barrier integrity [76]. The caecal microbiota is generally richer and more responsive to dietary perturbations than the fecal microbiota. For this, we investigated both caecal and fecal microbiomes in response to long-term HSD.

The caecal microbiome of females demonstrated that alpha diversity was unchanged after the long-term HSD (p = 0.273), meaning the microbial richness and evenness were maintained between the long-term HSD and CD groups (Figure 10B). However, the male caecal microbiome showed an increase of its alpha diversity in the long-term HSD compared to CD males by a mean rank difference of 11.46 without reaching a statistical significance (p = 0.065). This indicates that overall microbial richness and evenness were slightly increased in the long-term HSD (Figure 10B). In the fecal microbiome, no changes were observed upon long-term HSD in either females or males (p > 0.999 for males, and p =0.170 for females) (Figure 3C).

Regarding the microbiome structure, the female caecal microbiome showed no changes in beta diversity following long-term HSD (p= 0.52). By contrast, the male caecal microbiome structure was altered significantly (p=0.001), as indicated by distinct clustering in the beta diversity analysis (Figure 10D). This distinct clustering was more evident in the 3D PCoA plot (Supplementary Figure 3). The same result was obtained for the fecal microbiome where male HSD mice samples clustered separately with a significant difference in beta diversity (Figure 10E). These findings indicate that the microbial community composition in male mice is altered upon HSD.

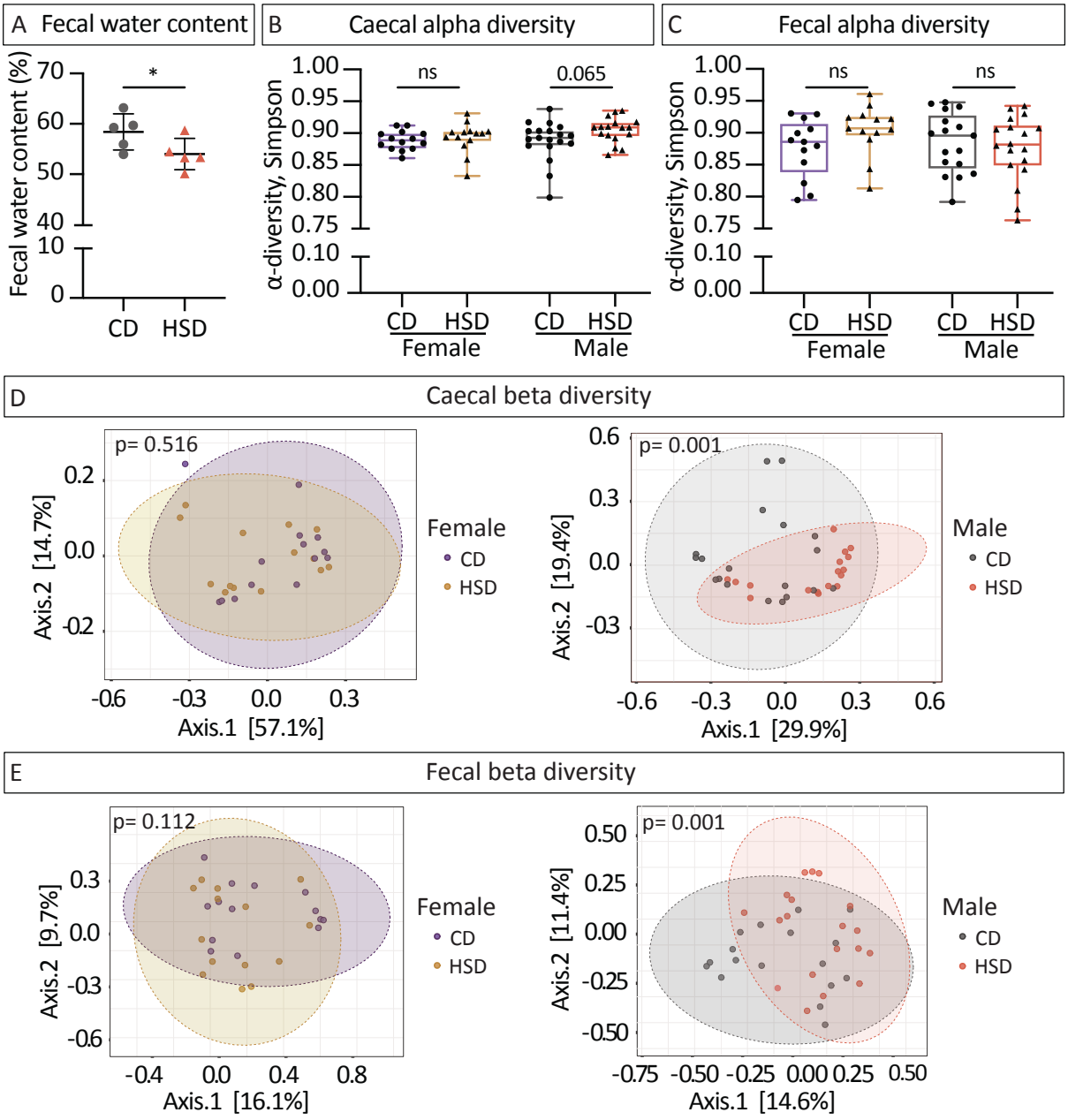

Figure 10 Caecal and fecal microbiome diversity changes in mice upon long-term HSD. Mice were fed either CD or HSD for 3 months to achieve long-term HSD treatment. For microbiome analysis, genomic DNA was extracted from caecal and fecal samples, and then underwent amplicon sequencing to profile their metagenomic composition, and analyzed by QIIME2 to annotate amplicon sequencing variants for further diversity and abundance analysis. (A) Fecal water content change between CD and HSD (n = 4-5, p-vaalue was obtained using independent sample t-test, *$p < 0.05$); (B, C) alpha diversity changes of (B) caecal and (C) fecal microbiome (Simpson index, female mice n = 13-14, male mice n = 17-19, p-values were obtained using Kruskal-Wallis test); (D, E) beta diversity changes of (D) caecal and (E) fecal microbiome (distance metric Jaccard, female mice n = 13-14, male mice n = 17-19, p-values were obtained using PERMANOVA test).

Taxa abundance profiling of the caecal and fecal microbiomes on the phylum level showed that long-term HSD significantly increased Bacteroidotas' abundance in the caecal microbiome compared to CD in the male group with a *p*-value of 0.002. However, this shift

was not observed in fecal microbiome (p = 0.225). In females, the abundance of Bacteroidota was unchanged between CD and HSD (p = 0.760 in caecal and 0.999 in fecal microbiome) (Figure 11A, B). On the contrary, Actinobacteriota abundance significantly decreased in the male microbiome (p= 0.009 in caecal and 0.032 in fecal microbiome) but remained unchanged in the female microbiome upon long-term HSD (p = 0.972 in caecal and 0.220, Figure 11B). Other featured bacterial phyla like Firmicutes, Desulfobacterota, Pastescibacteria, and Proteobacteria in gut microbiome showed unchanged abundancies following long-term HSD in both sexes (p > 0.05) (Figure 11A, B).

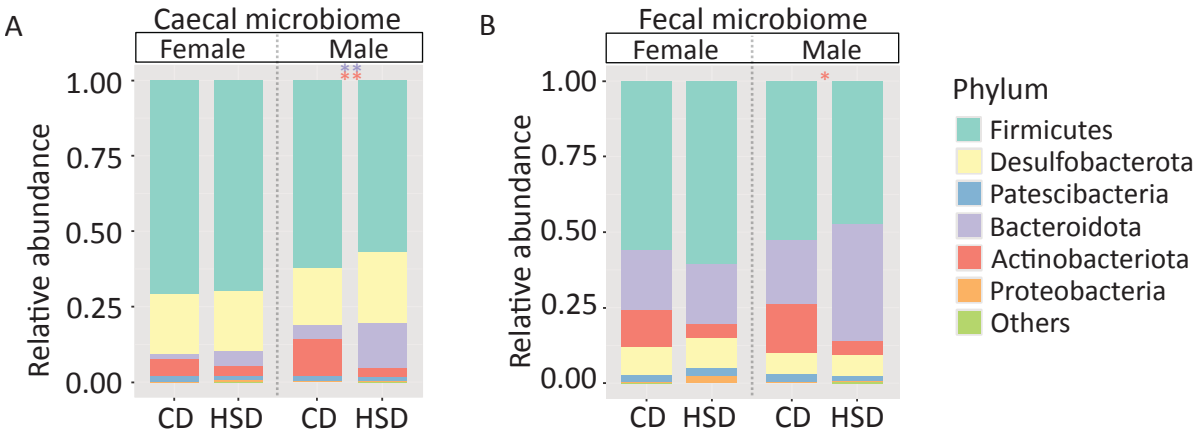

Figure 11 Gut microbiome phyla abundance changes upon the long-term HSD. Genomic DNA was extracted from caecal and fecal samples of CD and HSD mice, and then underwent amplicon sequencing to profile their metagenomic composition, and analyzed by QIIME2 to annotate amplicon sequencing variants for further diversity and abundance analysis. (A) Gut phyla changes in (A) caecal and (B) fecal microbiome. Female mice n = 13-14, male mice n = 17-19, Mann-Whitney test.

On the genus level, the Linear Discriminant Analysis Effect Size (LEfSe) revealed genera with differential abundance (p < 0.05, LDA > 2) between HSD and CD microbiomes (Figure 12B). In the caecal microbiome, some genera were significantly enriched after long-term HSD in the microbiome of both sexes, including the *Muribaculaceae*, *Alistipes, Odoribacter* (Bacteroidota)*, Eubacterium-Coprostanoligenes* (Firmicutes), and *Escherichia shigella* (Proteobacteria) (Figure 12A). Whereas *Lachnospiraceae_UCG_006, Oscilibacter* (Bacteroidota), and *Rickenellaceae* (Firmicutes) were only increased in male HSD-fed mice (Figure 12A). On the other hand, *Bifidobacterium* (Actinobacteriota) decreased their abundance in male mice microbiomes upon HSD while remaining unchanged in females (Figure 12A). Detailed violin plots with individual sample distribution are shown for *Muribaculaceae, Bifidobacterium,* and *Lactobacillus.* Given the well-established role of Lactobacillus species in promoting gut health and maintaining microbiome balance, their abundance was specifically examined [85,169]. Although no statistically significant change was observed, a minor reduction was noted in the male microbiome (p = 0.120).

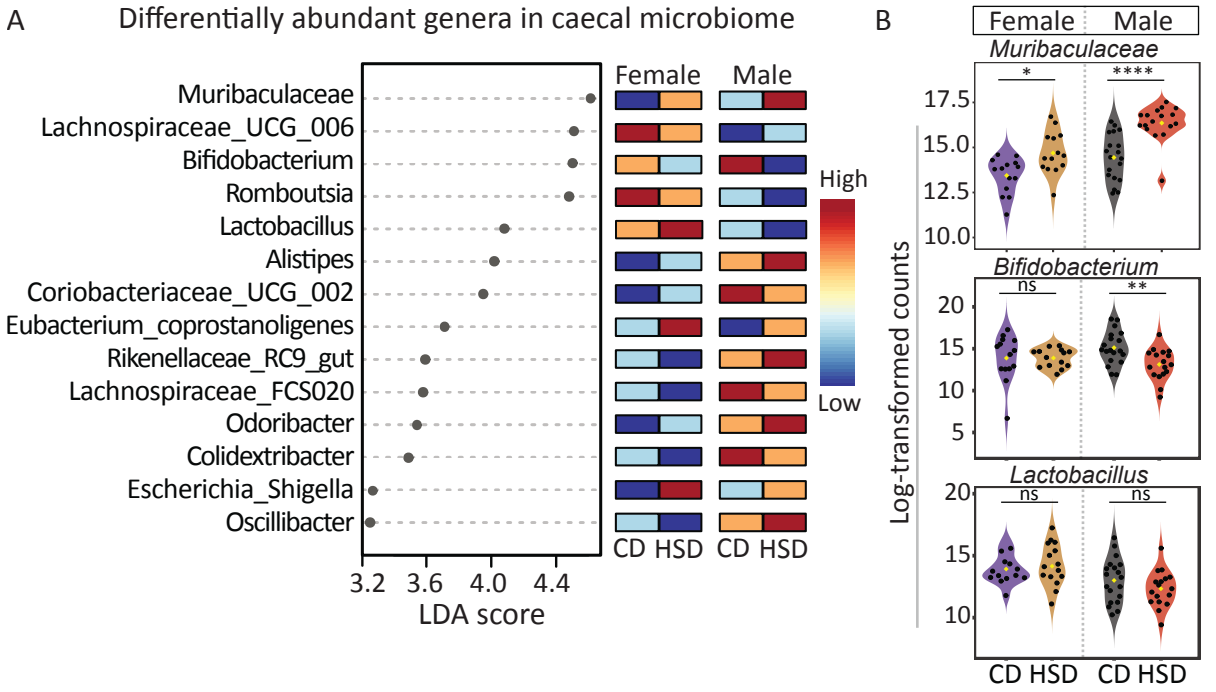

Figure 12 Caecal microbiome genera changes upon long-term HSD. Genomic DNA was extracted from caecal and fecal samples of CD and HSD mice, and then underwent amplicon sequencing to profile their metagenomic composition, and analyzed by QIIME2 to annotate amplicon sequencing variants for further diversity and abundance analysis. (A) Differential abundance and effect size (LDA score) of microbiome genera; (B) Count changes of selected genera upon HSD. Female mice n = 13-14, male mice n = 17-19, Linear Discriminant Analysis (LDA) for effect size; *p*-values in panel B were estimated using Kruskal-Wallis rank sum test for differential abundance, *$p < 0.05$, **$p < 0.01$, ***$p < 0.001$, ****$p < 0.0001$.

The relative abundances of the majority of fecal bacterial genera upon long-term HSD were comparable to their counterparts in the caecum (Figure 13A), such as *Escherichia_shigella* and *Eubacterium_coprostanoligenes* being significantly increased upon HSD in both sexes (Figure 5B). Nonetheless, some genera were more featured in the fecal microbiome, such as *Lachnoclostridium, Marvinbryantia* (Firmicutes), and *Parabacteroides* (Bacteroidota), which were significantly more abundant in the HSD-fed mice of both sexes (Figure 6A, B). Moreover, the relative abundance of fecal *Parvibacter* (Actinobacteriota) decreased under long-term HSD feeding in a sex-independent manner (Figure 13A). In summary, long-term HSD feeding significantly affected gut microbial diversity in males but not in females by significantly increasing Bacteroidota phylum and decreasing Actinbacteriota phylum abundance compared to CD. These results suggest a potential gut dysbiosis in response to the long-term HSD.

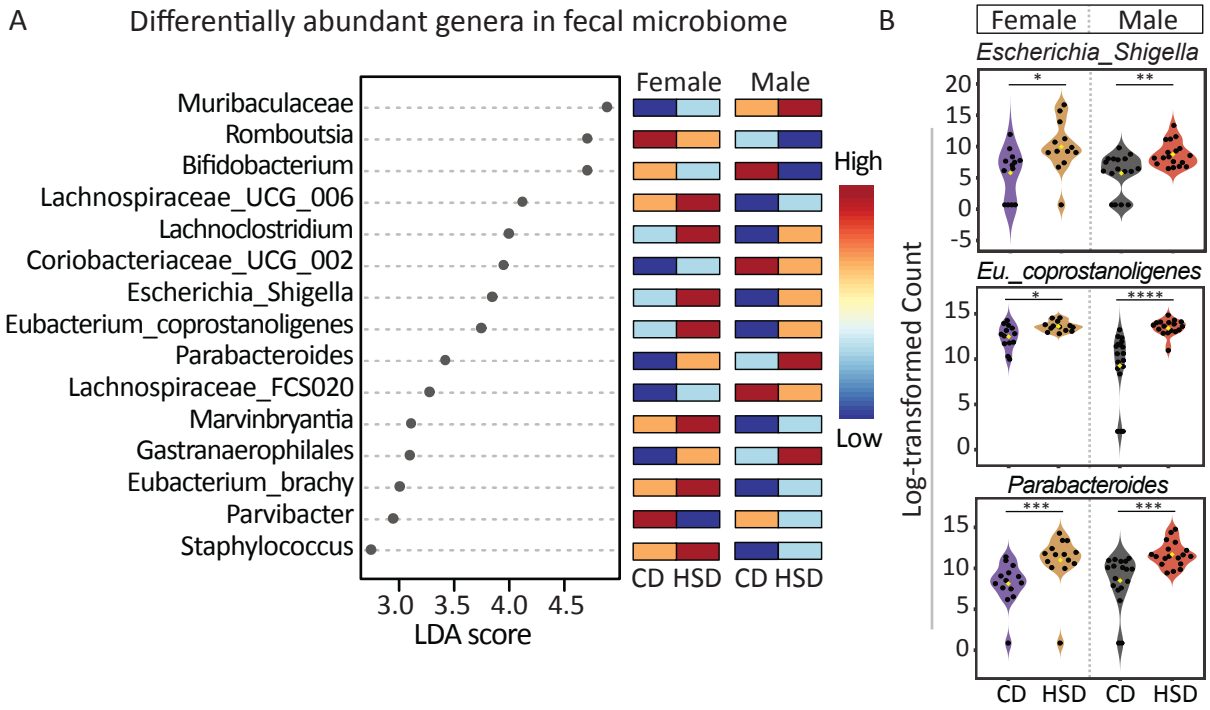

Figure 13 Fecal microbiome genera changes upon long-term HSD. Genomic DNA was extracted from caecal and fecal samples of CD and HSD mice, and then underwent amplicon sequencing to profile their metagenomic composition, and analyzed by QIIME2 to annotate amplicon sequencing variants for further diversity and abundance analysis. (A) Differential abundance and effect size (LDA score) of microbiome genera; (B) Count changes of selected genera upon HSD. Female mice n = 13-14, male mice n = 17-19, Linear Discriminant Analysis (LDA) for effect size; *p*-values in panel B were estimated using Kruskal-Wallis rank sum test for differential abundance, *$p < 0.05$, **$p < 0.01$, ***$p < 0.001$, ****$p < 0.0001$.

3.1.3 Assessment of Gut Pathology

3.1.3.1 Evaluation of Gut Length and Histopathology

Despite extensive research on the gastrointestinal system and its microbiome, the effects of a high-salt diet on the gut are still understudied. Gut health is determined through diverse factors, including its permeability to nutrients and pathogens, immune cell infiltration, and morphological changes [170]. To have an initial glimpse on the gut after HSD, a pathological scoring was performed based on a standard classification of mouse gut pathology that mainly accounts for inflammatory cell infiltrate and gut tissue architecture [170]. The unbiased pathological assessment of the small intestine, caecum, and colon showed a significantly higher pathological score only in the small intestine of HSD-fed mice compared to controls regardless of their sex with a *p*-value of 0.046 (Figure 14).

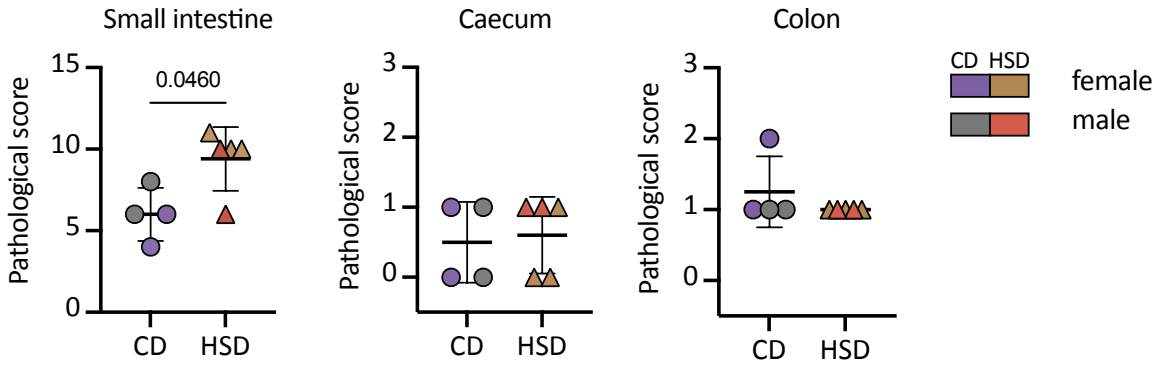

Figure 14 Unbiased pathological assessment of main gut regions upon long-term HSD. 8-week-old mice were fed either CD or HSD for 3 months to achieve long-term HSD treatment, respectively. The small intestine, caecum, and colon were cut open longitudinally and rolled from the proximal to the distal side. Transverse sections showing all role layers were taken for H&E staining and further assessed by a specialist pathologist; N = 4-5, 2 sex-separated experiments, statistical comparisons were done using independent sample t-tests.

Gut length and architecture were further assessed after short- and long- HSD in both male and female mice. After short-term HSD, small intestine length remained unchanged in males but was significantly increased in females compared to their respective CD groups ($p = 0.023$). Likewise, the small intestines of both sexes after long-term HSD showed the same result ($p = 0.002$ for females, $p > 0.05$ for males) (Figure 15A). However, colon length significantly decreased in male mice after short- and long-term HSD ($p = 0.008$ and 0.005, respectively), but it remained unchanged in female mice ($p > 0.05$) (Figure 15B, C). These distinctive results in male and female gut length suggest sex-specific effects of HSD. While small intestine length changes are considered non-pathological, colon shortening in males is typically associated with colon inflammation [171,172].

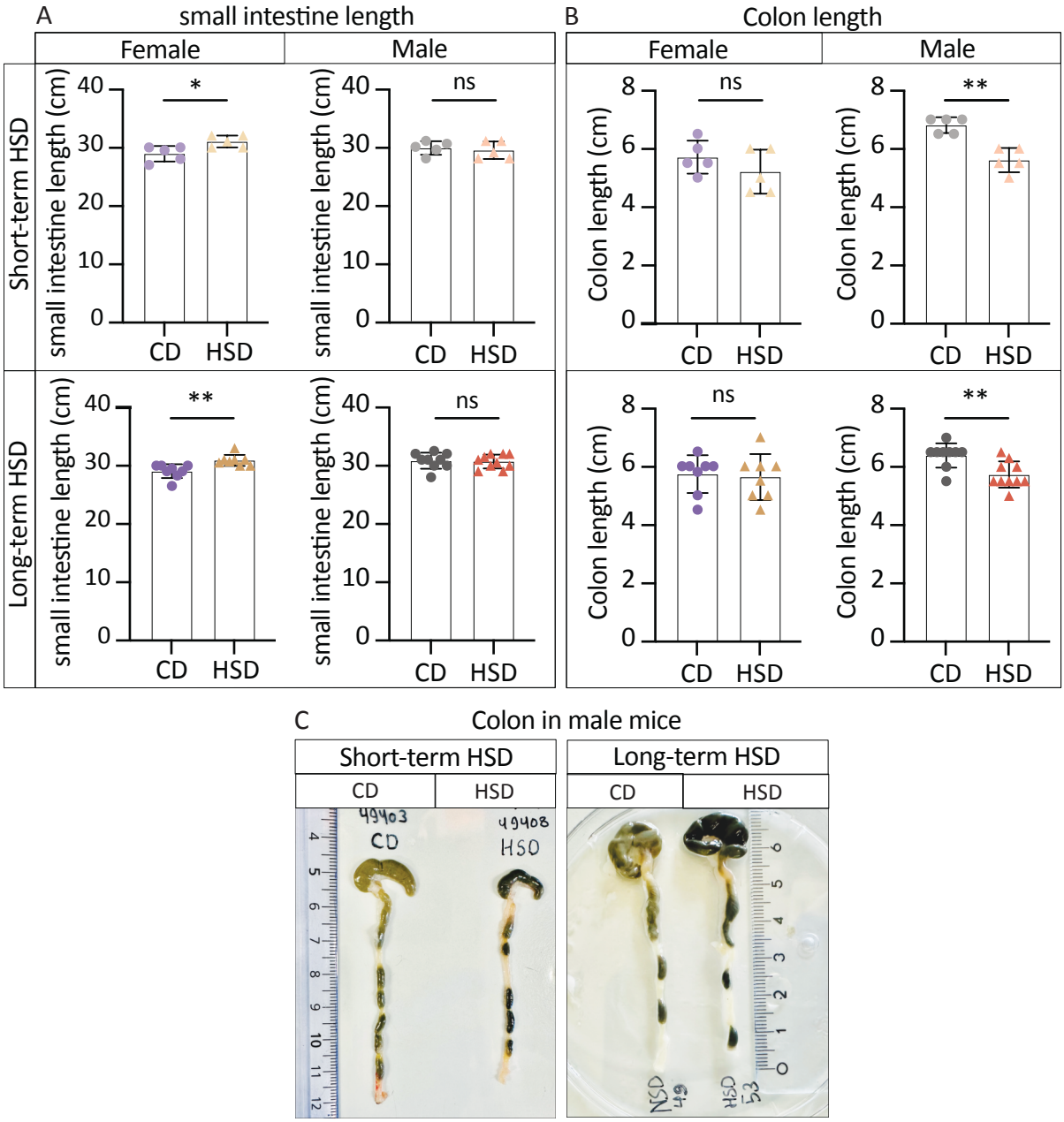

Figure 15 Gut length changes upon short and long-term HSD feeding in female and male mice. 8-week-old mice were fed either CD or HSD for 3 weeks or 3 months to achieve short- or long-term HSD treatment, respectively. (A) Small intestine length changes; (B) Colon length changes in short-and long-term periods; (C) Representative images comparing CD and HSD colons; n = 5, long-term HSD mice n = 8-10, independent sample *t*-test or Mann-Whitney test was applied based on the distribution of the data, *$p < 0.05$, **$p < 0.01$.

Based on the initial pathological scoring results, which indicated a high score in the small intestine, histological assessment was subsequently focused on the ileum. This region was selected due to its well-established high microbial abundance and diversity, as well as the presence of Peyer's patches, which underscore its close association with intestinal immune networks. After short-term HSD, ME and LP of the ileum of females showed a relatively normal structure compared to that in CD-fed mice ($p > 0.05$) (Figure 16A). Similarly, upon short-term

HSD, male mice showed no Crypt and villi structural changes and a minimal ME thickening, which however failed to reach statistical significance (p = 0.077) (Figure 16 (B).

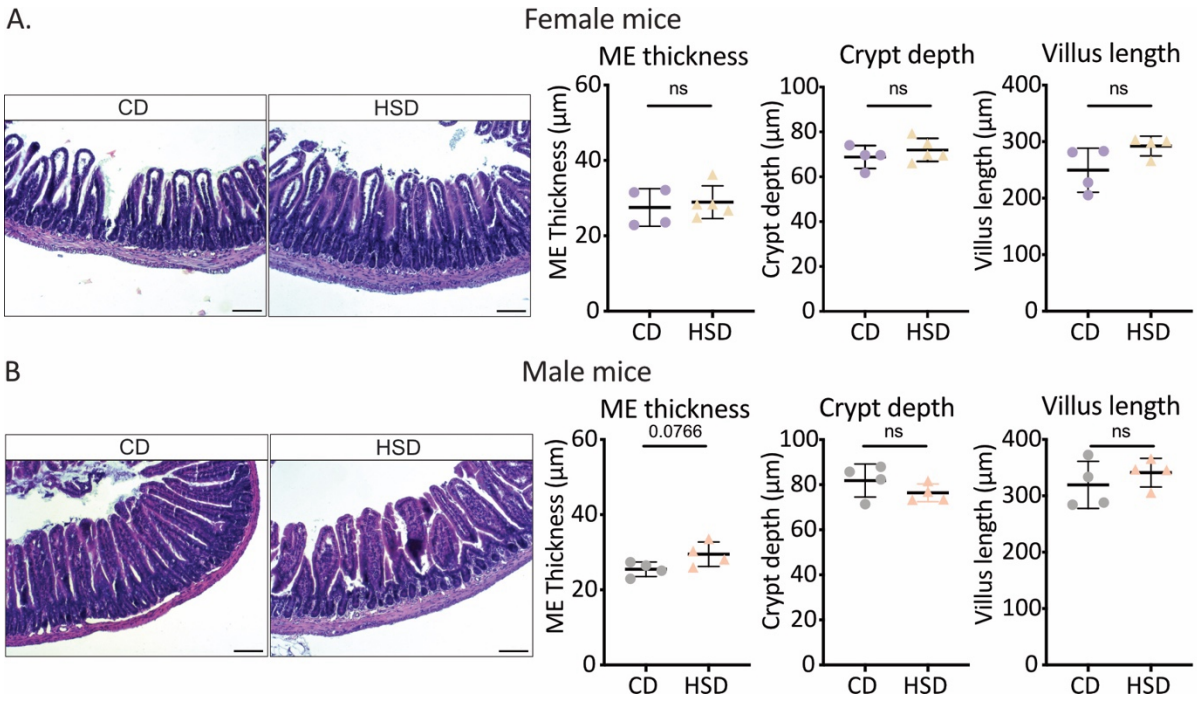

Figure 16 Ileum morphological changes upon short-term HSD feeding in (A) female and (B) male mice; Mice were fed either CD or HSD for 3 weeks to achieve short-term HSD treatment. Ileum tubes of 1 cm were embedded in paraffin and then cut, stained with H&E staining, imaged, and analyzed by FIJI. N = 4-6, independent sample *t*-test or Mann-Whitney test was applied based on the distribution of the data.

Long-term HSD significantly increased ME thickness in male mice only (p = 0.002) and decreased crypt depth (p = 0.0256in both mouse sexes (Figure 17 A, B). Ileal villi of long-term HSD-fed male mice appeared more blunted than elongated, with apparent increased cell infiltration or proliferation compared to CD-fed mice (Figure 17B). In summary, gut morphology in long-term HSD-fed mice differed significantly from that in CD-fed mice, with shorter colon length, higher pathological scores, ileal muscularis externa thickening, and crypt shallowing. These findings indicate that long-term HSD potentially linked to gut injury or inflammation.

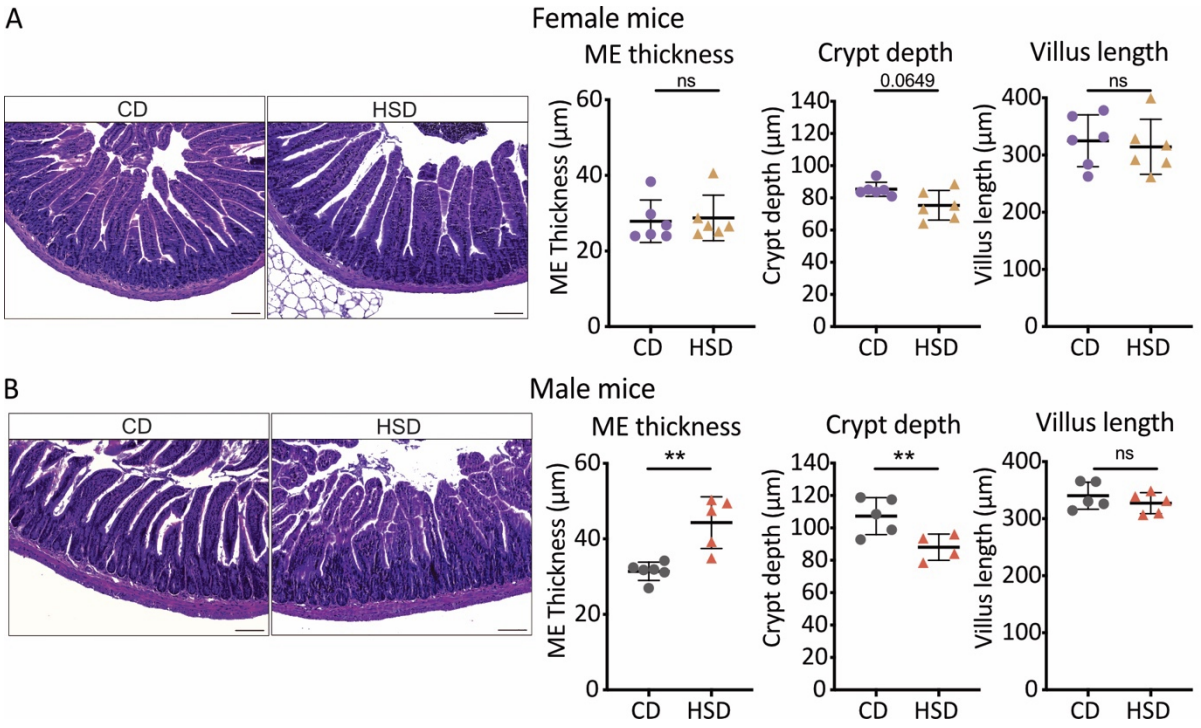

Figure 17 Ileum morphological changes upon long-term HSD feeding in (A) female and (B) male mice. Mice were fed either CD or HSD for 3 months to achieve long-term HSD treatment. Ileum tubes of 1 cm were embedded in paraffin and then cut, stained with H&E staining, imaged, and analyzed by FIJI; n = 4-6, independent sample *t*-test or Mann-Whitney test was applied based on the distribution of the data, , $*p < 0.05$, $**p < 0.01$.

3.1.4 Long-Term High-Salt Diet Affects Gut Barrier Integrity

Gut epithelial barrier integrity is essential for a healthy gut because it maintains a balance between allowing nutrient absorption and preventing harmful substances from entering the body. Increased intestinal permeability has been observed in high-fat diets and IBD as a result of epithelial dysregulation [173,174]. To assess the gut permeability upon long-term HSD in male mice, fluorescent heavy sugar dextran was used for an *in vivo* gut permeability assay. Two distinct dextran molecular weights were employed: 4 kDa (46944, Sigma-Aldrich) and 70 kDa (D1830, Invitrogen). Since the 4 kDa dextran can penetrate the lining and reach the blood, it is commonly used to measure gut permeability. 70 kDa dextran is less likely to pass through the epithelium in healthy conditions; thus, it is usually used to measure gut transit time (Figure 18A).

The FITC 4kDa dextran was detected in the plasma already at 0.5h time point after dextran oral administration in both conditions. At this time point, HSD-fed mice exhibited a significant increase in plasma 4kDa dextran concentration reaching a mean of 225 µg/ml compared to CD-fed mice with 140 µg/ml, indicating higher gut permeability under long-term HSD (p = 0.003). Throughout 4h after dextran administration, dextran was cleared from the bloodstream more rapidly in control animals than in HSD animals with a *p-value of* 0.040 (Figure 18B). Low concentrations of 70 kDa dextran were also detected in plasma, with the

mean concentrations following a similar trend as for 4kDa dextran without reaching a significant level ($p > 0.05$) (Figure 18C). This indicates that the gut epithelial barrier in HSD-fed mice is more permeable compared to CD-fed mice. In summary, long-term excess salt intake disrupted gut barrier integrity in male mice by increasing intestinal permeability, which facilitates microbial antigen translocation from the lumen to the blood and then to other organs like the liver, causing further homeostasis disruption [174].

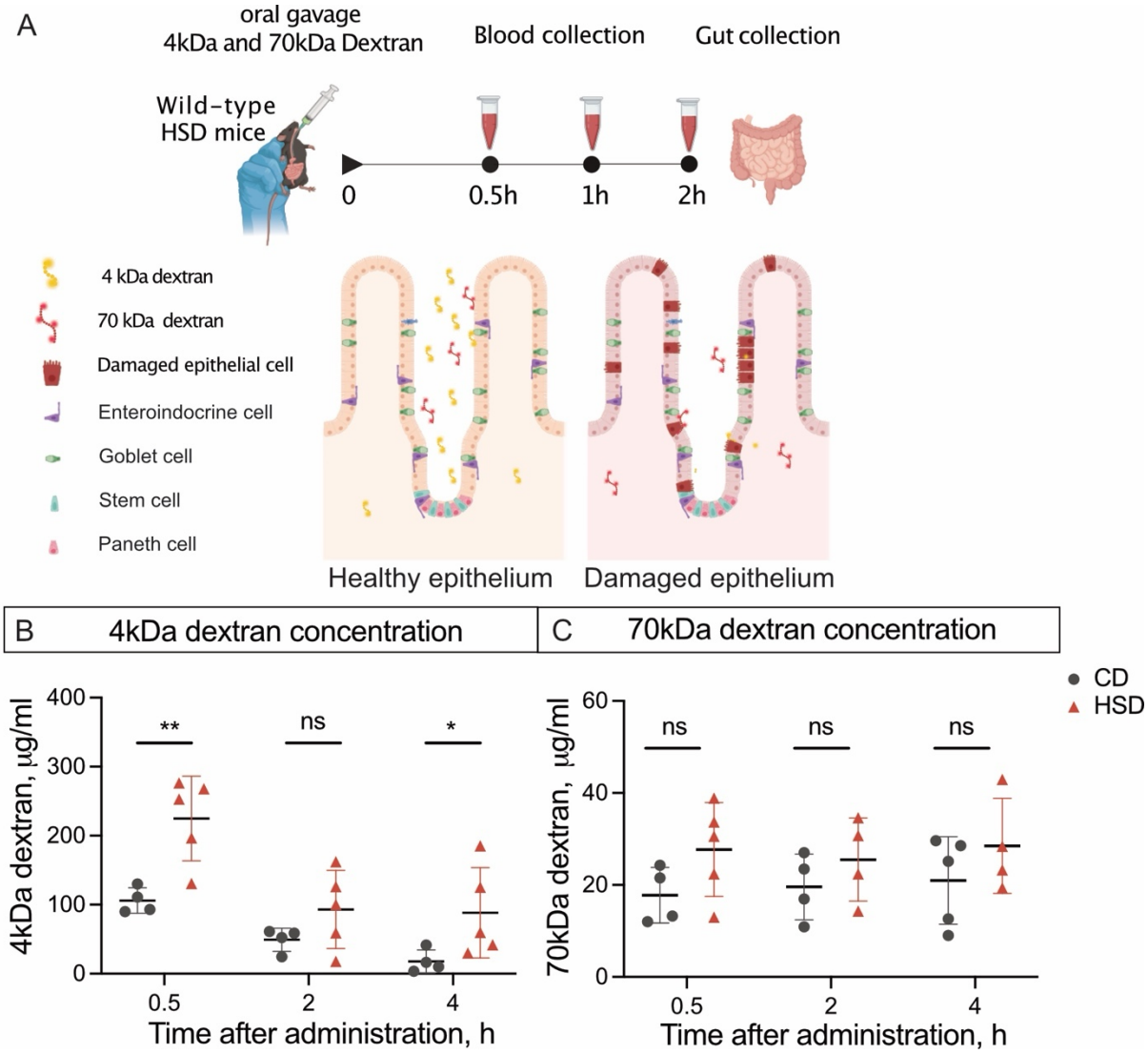

Figure 18 Epithelium permeability assessment using fluorescent dextran in male mice upon long-term HSD. Overview of gut epithelium permeability assay where 4kDa and 70kDa fluorescent dextran was administrated to long-term CD and HSD-fed mice. The concentration of both dextran sizes in plasma was measured at 0.5, 2,4 hours after dextran oral administration; n = 5, p-values were obtained using Two-way ANOVA, *$p < 0.05$, **$p < 0.01$.

3.1.5 Long-term HSD modulates the host response to gut infections

Previous studies have shown that short-term high salt intake can exacerbate colitis and affect the colon immune response in mice, specifically of MΦ and DCs [26,175]. To investigate the impact of long-term HSD on gut infection resolution and infection clearance, *C. rodentium* infection model was used, a murine model pathogen for enteropathogenic *E. coli.* This model provides a well-characterized timeline of infection and resolution, and a capacity to elicit well-defined mucosal immune responses, making it highly suitable for evaluating infection resolution and barrier integrity under high-salt intake. Therefore, male mice were orally infected with *C. rodentium* and scored for 3 weeks after the infection (Figure 19A). Disease activity index (DAI) was scored every 3 days by 3 parameters: mouse body weight, stool consistency, and fecal occult blood.

The overall trajectory of the DAI curve was significantly elevated in HSD-treated mice; however, only day 22 showed a statistically significant difference between groups at the individual time point level, reflecting a cumulative effect of disease activity over time (p = 0.012). The colony-forming unit count (CFUs) of *C. rodentium* was assessed in the liver, mesenteric lymph nodes (mLNs), and stool. Liver samples of both HSD and CD groups harbored no CFUs 3 weeks after the infection. In mLNs, some HSD mice still had *C. rodentium* CFUs even after 3 weeks of the infection, the stool of HSD mice showed no significant change in CFU count compared to controls (Figure 19C). As *C. rodentium* infection mainly targets the proximal colon of the mice, a blinded unbiased histomorphological examination of the proximal and distal colon was performed 3 weeks after the infection. Colon inflammation signs used for scoring were immune cell infiltration, goblet cell loss, hyperplasia, epithelial loss, and crypt lengthening. The proximal colon of HSD mice scored an insignificant pathological score compared to that of CD mice (p = 0.379) (Figure 19D). In summary, the findings suggested that clearance of *C. rodentium* colon infection was impaired in the long-term HSD-fed animals compared to CD-fed ones.

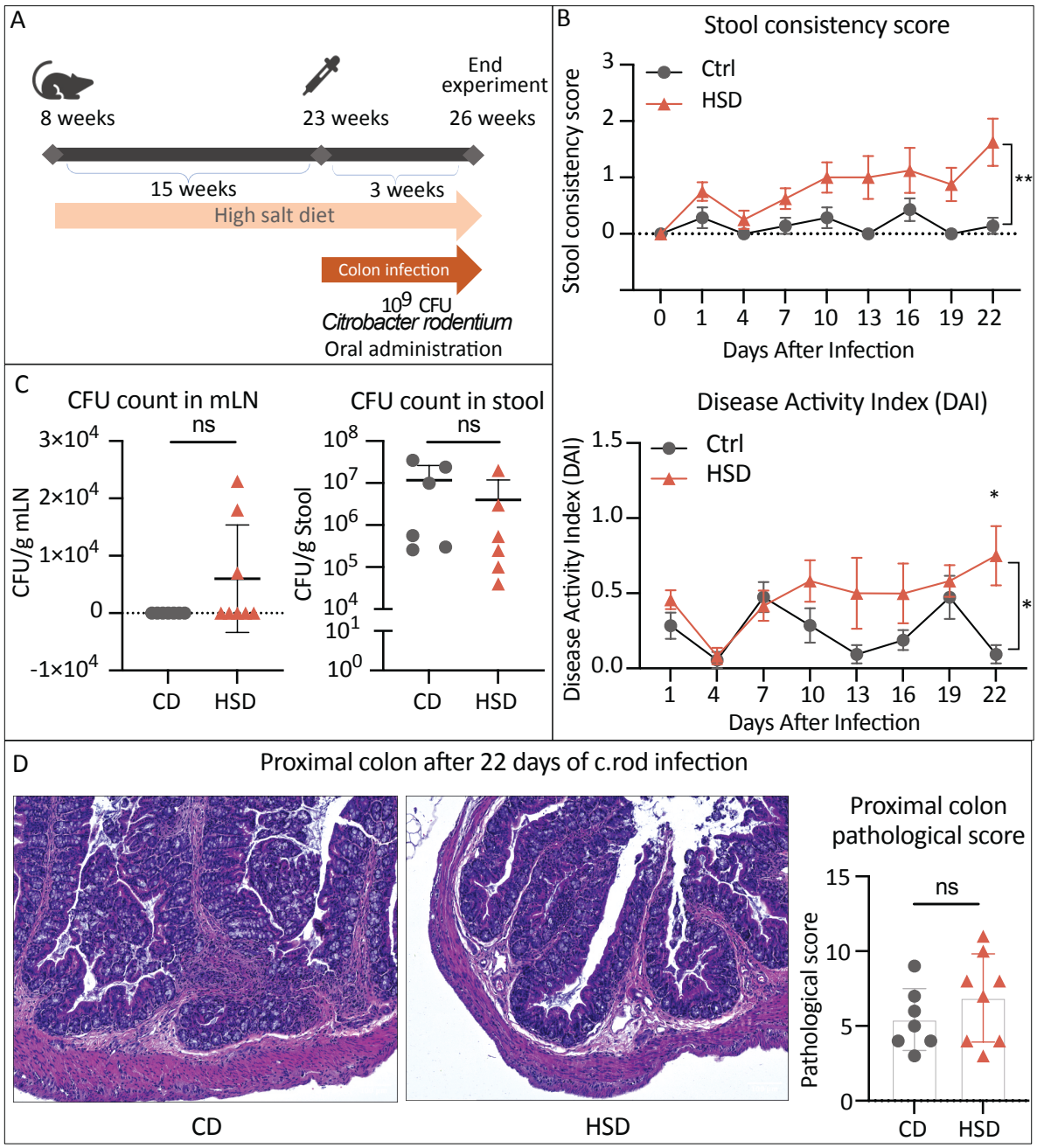

Figure 19 Assessment of long-term HSD male mice recovery response 3 weeks after *C. rodentium* colon infection. Long-term CD- and HSD-fed mice were orally administrated 10^9 CFUs of *C. rodentium* in PBS and scored for 3 weeks. (A) Diagram of the colon infection model; (B) Stool consistency score (above), and Disease activity index (below) of CD and HSD mice, involving body weight change, stool consistency score, and fecal occult blood score, (n = 8, *p*-value was obtained using Two-Way ANOVA test, **p*-value < 0.05, ***p*-value < 0.01); (C) CFU count in mLN (left) and CFUs count in stool (right); (D) Representative images of proximal colon and its pathological score (n = 8, *p*-value was obtained using Mann-Whitney test, **p*-value < 0.05, ***p*-value < 0.01).

3.2 Characterization of Liver Pathology in Response to Short- and Long-Term High-Salt Diet

Current research on the impact of high-salt diets (HSD) on liver health, particularly in long-term exposures, is limited, emphasizing the need for further study. Actual liver weights from CD and HSD-fed groups showed no significant changes after short- and long-term HSD in both sexes (Supplementary Figure 4A, C). However, a slight increase in liver-to-body weight ratio (LW/BW) was observed in short-term HSD-fed female mice, but this effect was not sustained after long-term HSD and was absent in males (Supplementary Figure 4B, D). Histological analysis via Hematoxylin and Eosin (H&E) staining showed that the livers of short-term HSD-fed male mice had minor ballooning degeneration or lipid accumulation and occasional immune cell infiltration compared to CD-fed mice, while females remained unaffected (Figure 20A). Long-term HSD mice exhibited increased liver ballooning degeneration or lipid accumulation without notable immune cell infiltration or fibrosis in both sexes but were more prominent in male animals (Figure 20B). Lipid accumulation in the liver was further assessed by Oil-Red-O staining in the male long-term HSD-fed mice, indicating elevated lipid droplet area compared to CD-fed mice with a *p*-value of 0.037, as shown in the representative images and the quantification of lipid droplet area (Figure 20C, D).

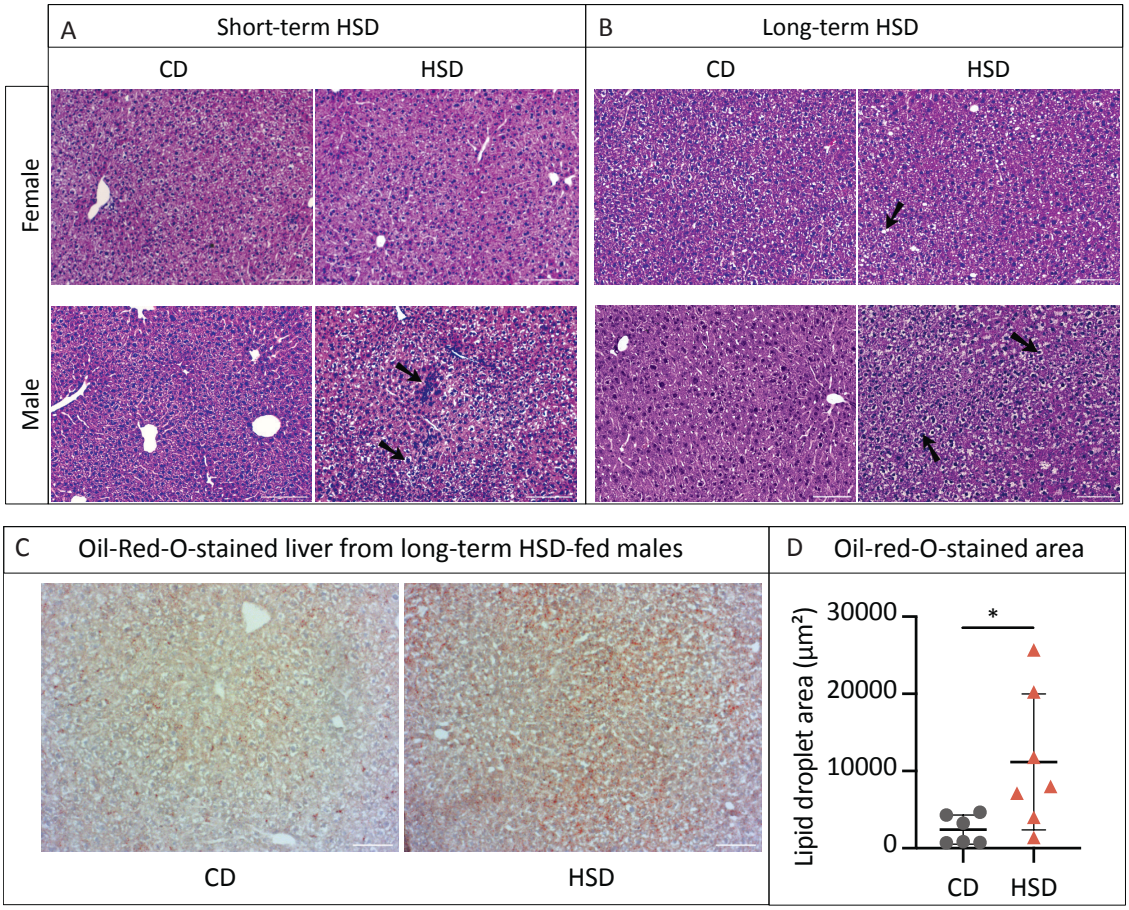

Figure 20 Liver histological changes in female and male mice upon short- and long-term HSD. Mice were fed either CD or HSD for 3 weeks and 3 months to achieve short- and long-term HSD treatment. The liver medial lobe was fixed, dehydrated, embedded in paraffin for H&E staining, or in O.C.T

compound for Oil-Red-O staining, and analyzed by FIJI. A, B) H&E-stained liver sections upon (A) short-term HSD, (B) long-term HSD. (C) Oil-Red-O-stained liver sections following long-term HSD; (D) Quantification of the Oil-Red-O-stained lipid droplet area (n = 5-7, p-values were obtained using independent sample t-tests, *p-value < 0.05).

Since accumulated lipid droplets usually comprise cholesteryl esters and glycerolipids like diacylglycerols (DGs) and triacylglycerols (TGs), an unbiased lipidomics analysis was performed to validate lipid droplet accumulation and identify which type of lipids are increased in HSD mice livers. As short-term HSD-fed females showed LW/BW percentage increase, they were also included in the lipidomic analysis, and they showed unaltered levels of total lipids and glycerolipids in the liver compared to CD ($p > 0.05$) (Figure 21A). Likewise, long-term HSD-fed female mice showed no substantial changes in liver total lipids and acylglycerols (Figure 21B). In the male group, long-term HSD revealed a significant increase in DGs levels compared to CD-fed mice ($p = 0.023$), however, overall lipid levels remained unchanged (Figure 21C). Altogether, short-term HSD increased the LW/BW percentage exclusively in female mice without affecting lipid levels. In contrast, long-term HSD-fed mice showed an unaltered LW/BW ratio but led to lipid droplet accumulation and significantly elevated DG levels in comparison to CD-fed mice. These findings indicated long-term HSD promoted liver lipid modulation independent of liver mass.

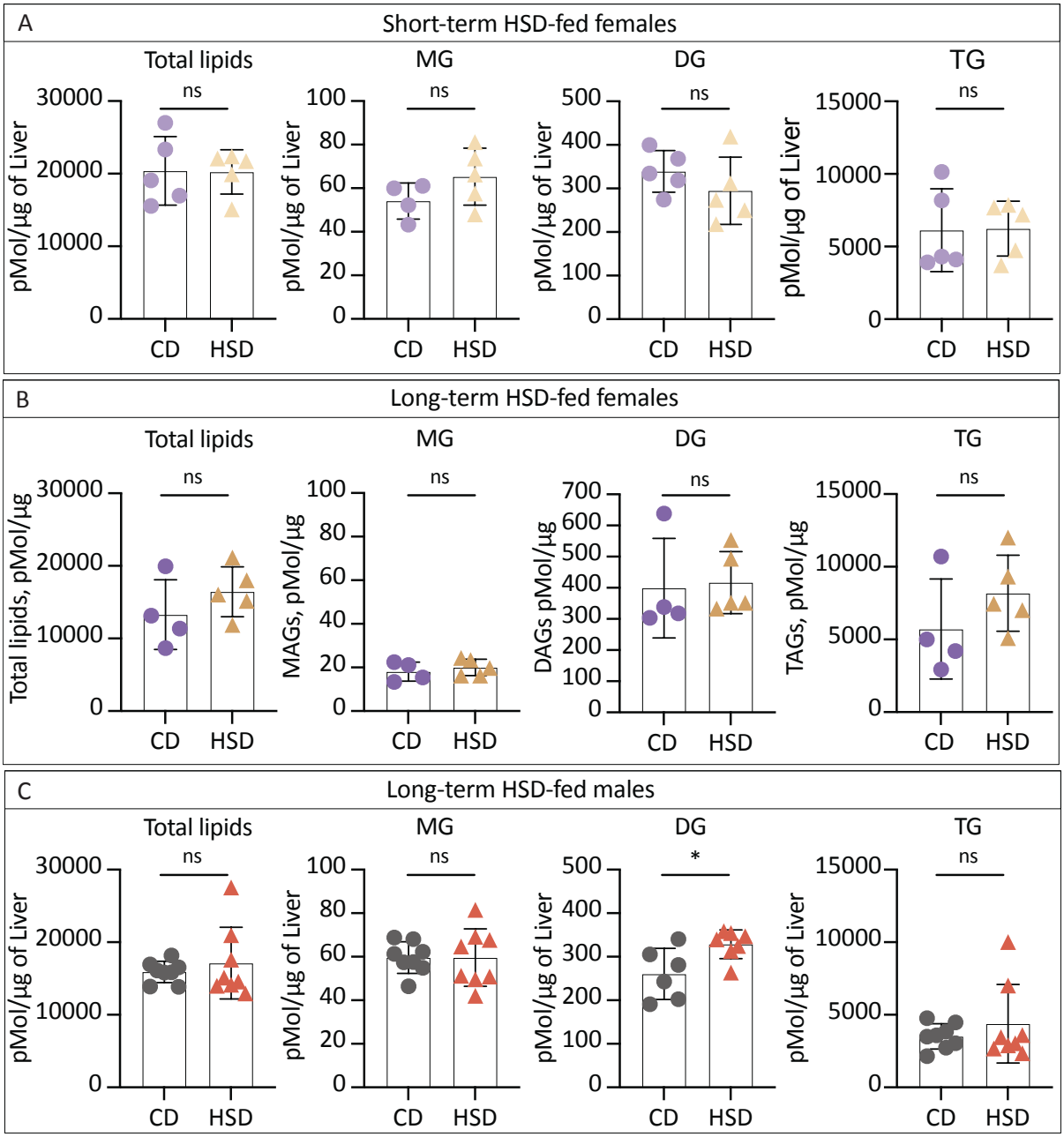

Figure 21 Liver total lipids and glycerolipids concentration upon short – and long-term HSD. Mice were fed either CD or HSD for 3 weeks and 3 months to achieve short- and long-term HSD treatment. Liver right lobe was frozen at -80 C and then homogenized and processed for Mass-Spectrometry lipidomics analysis. (A) Female mice liver lipid concentrations upon short-term HSD; (B) Female mice liver lipid concentrations upon long-term HSD; (B) Male mice liver lipid concentrations upon long-term HSD; females n = 4-5, males: n = 6-8, t-test or Mann-Whitney test were applied based on the distribution of the data, $*p < 0.05$.

3.3 Deciphering Ileum MΦ Diversity and Functions under Long-Term HSD – a Single-Nucleus RNA Sequencing Perspective.

3.3.1 Identification and Profiling of cell populations in the Gut ileum

Based on the resulted ileal histopathology and increased intestinal permeability upon long-term HSD, the ileum was further investigated to characterize its various cell types and assess the response of MΦ in the ileum upon long-term HSD. The ileum is known to have a higher sensitivity to salt intake than other small intestine parts due to the abundance of microbial communities and the dense immune network in the ileum [176]. For this, a single-nuclei RNA sequencing analysis (snRNA-seq) was performed on the mouse ileum upon long-term HSD. Ileum LP and ME layers were collected from long-term CD- and HSD-fed male mice for nuclei isolation and subsequent snRNA-seq analysis. For each diet, ileum samples of two mice were pooled together into one sample. 32,808 single-nuclei transcriptomes passed the quality threshold: 16,214 from the CD and 16,594 from the HSD ileum. Seurat's Standard UMAP Pipeline was utilized to define cell clusters and perform UMAP [177,178]. A total of 24 cell clusters were identified, encompassing most known mouse adult ileum populations (Figure 22).

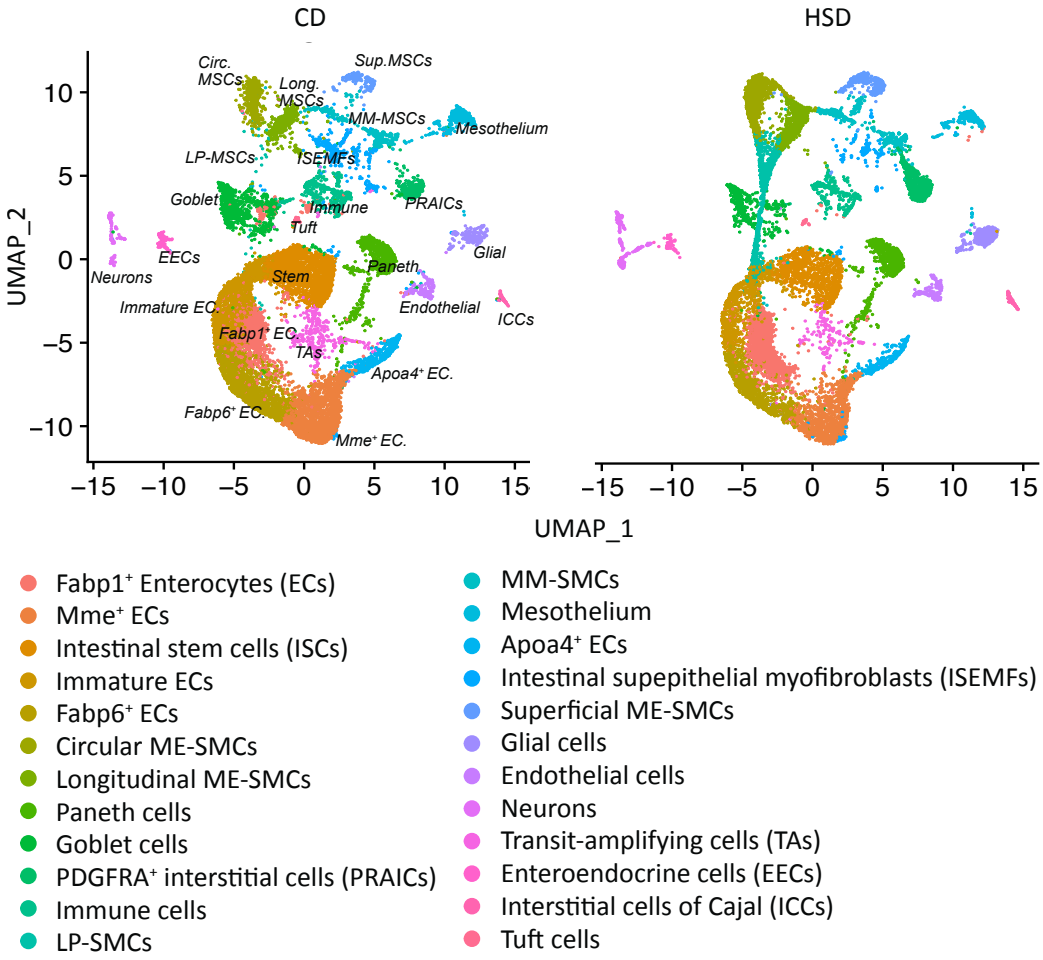

Figure 22 UMAP of ileum LP and ME cell types following the long-term HSD feeding. Ileum LP and ME layers of long-term CD and HSD conditions were collected for nuclei isolation and subsequent

Single nuclei RNA sequencing analysis. CD: Control diet; HSD: High salt diet, ME: Muscularis externa, LP: Lamina propria, EC: enterocytes, MM: Muscularis Mucosae, SMCs: Smooth muscle cells; ileum LP and ME layers of 2 mice per diet were pooled into one sample.

Epithelial cells constituted the largest group within the ileum, including both absorptive and secretory cells. Absorptive cells, referred to as enterocytes (ECs), express high levels of the *Gda* and *Sis* genes and were subclustered based on their differential expression of enterocyte feature genes into five subpopulations: Fabp1$^+$ ECs, Fabp6$^+$ ECs, Apoa4$^+$ ECs, Mme$^+$ ECs, and immature ECs, which have low expression of EC genes and high expression of *Krt19*, *Hnf4g*, and other stem cell markers. Transit-amplifying cells (TAs) moderately expressed enterocyte-specific genes and predominantly express proliferating genes such as *Mki67* and *Kif20b*. Intestinal stem cells (ISCs), which replenish the gut epithelium, were identified by the expression of *Cd44* and *Lgr5* (Figure 23).

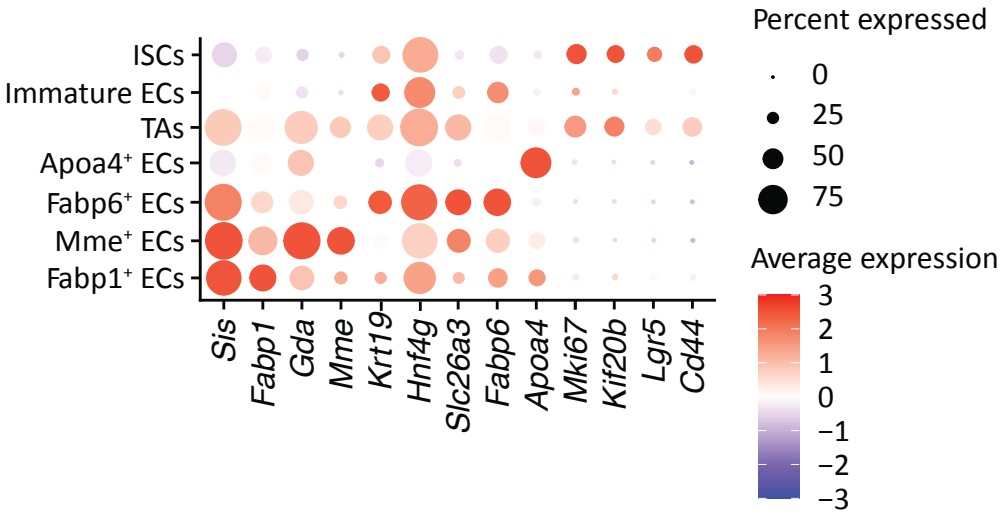

Figure 23 Expression dot plot of signature genes that identify ECs, proliferating epithelial cells, and stem cells upon long-term HSD feeding. Ileum LP and ME layers of long-term CD and HSD conditions were collected for nuclei isolation and subsequent Single nuclei RNA sequencing analysis. Ileum LP and ME layer samples of 2 mice were pooled into one sample for each diet.

Secretory cells, including Paneth, Goblet, Tuft, and enteroendocrine cells (EECs), were defined according to their feature gene expression. Paneth cells expressed *Lyz1* and *Defa24*; Goblet cells expressed *Muc2* and *Tff3*; Tuft cells expressed *Dclk1* and *Trpm5*; and EECs expressed *Chga* and *Sct* (Figure 24). PDGFRA$^+$ interstitial cells (PRAICs) are identified by their high expression of *Pdgfra* and *Cacna1d*, typically located in the muscularis externa layer. Intestinal subepithelial myofibroblasts (ISEMFs) are found in the lamina propria layer beneath the epithelia, characterized by expressing *Pid1* and *Svep1*. Ileal endothelial cells express the typical *Pecam1*, *CDh5*, and *Eng* endothelial genes. Enteric neurons and glial cells cluster separately from one another due to their distinct gene transcriptomic profiles. Enteric neurons were identified primarily by expressing *Elavl4* and *Ncam2*, along with other neurotransmitter-related genes, ion channels, and synaptic markers. Glial cells are

characterized by their strong expression of *Sox10* and *Cdh19*, as well as other genes associated with glial function, neuroprotection, and immune interactions (Figure 24).

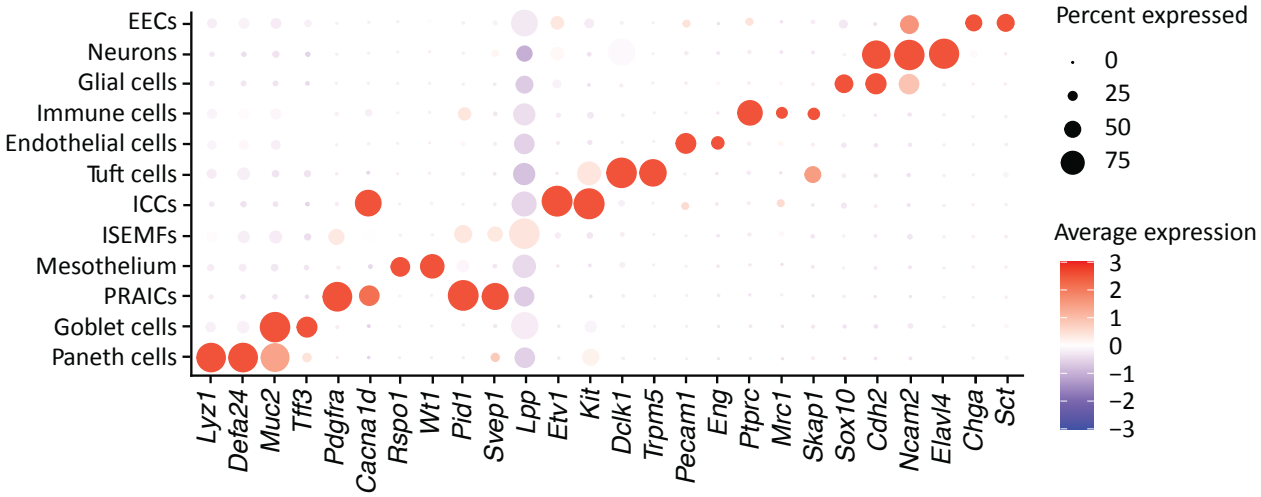

Figure 24 Expression dot plot of signature genes identifying ileum cell types. Ileum cell types are Secretory epithelial cells (Goblet, Paneth, EECs, and Tuft cells), interstitial cells (PRAICs, ICCs), mesothelium, ISEMFs, Neurons, glial cells, and immune cells. Ileum LP and ME layers of long-term CD and HSD conditions were collected for nuclei isolation and subsequent Single nuclei RNA sequencing analysis. Ileum LP and ME layer samples of 2 mice were pooled into one sample for each diet.

Smooth muscle cells (SMCs) were characterized by five key genes: *Myh11*, *Acta2*, *Des*, *Rspo3*, and *Tagln*, and were further divided into five clusters: longitudinal, circular, and superficial SMCs, which are from ME layer, LP layer SMCs (LP-SMCs), and Muscularis Mucosae SMCs (MM-MSCs) (Figure 25). Circular and longitudinal SMCs differed in the expression levels of their feature genes: longitudinal SMCs exhibited lower expression of *Myh11*, *Acta2*, *Actg2*, *Des*, and *Tagln*. Whereas superficial SMCs showed a high expression of *Bmpr1b*, *Grem1*, and *Chrdl1*. MM-MSCs moderately expressed smooth muscle cell markers and highly expressed *Adamdec1.* LP-SMCs were identified by the high expression of *Acta2, Actg2, Des,* and *Tagln*, with lower expression of *Myh11, Rspo3, and Grem1* than other cell types (Figure 25).

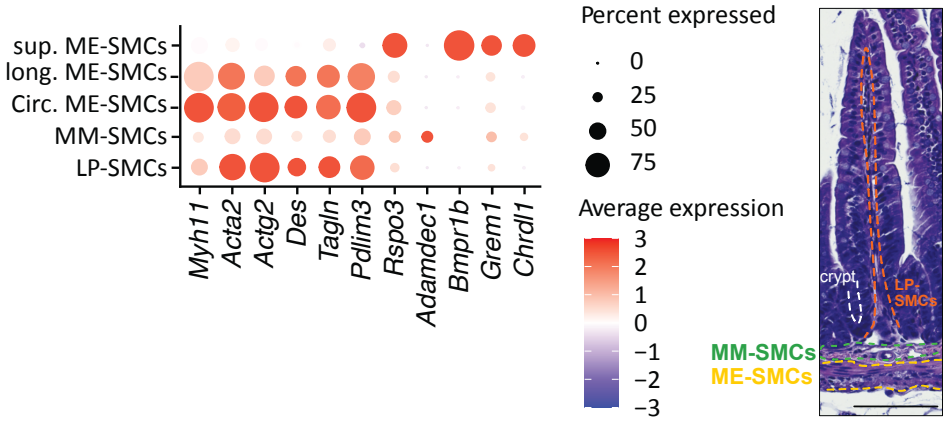

Figure 25 Expression dot plot of signature genes identifying ileum smooth muscle cells. ME-SMCs (circular, longitudinal, and superficial SMCs) LP MSCs (LP- SMCs), Muscularis Mucosae MSCs (MM- SMCs). Right: H&E-stained ileum wall showing ileum SMCs location, scale bar= 100 µm. Ileum LP and ME layers of long-term CD and HSD conditions were collected for nuclei isolation and subsequent Single nuclei RNA sequencing analysis. Ileum LP and ME layer samples of 2 mice were pooled into one sample for each diet.

Immune cells formed 3.23% of the total filtered cell count and were subclustered into major immune cell types: T cells, B cells, plasma cells, and MΦ (Figure 26A). Although key T cell markers were not detected, T cells could still be identified by their high expression of *Skap1, Itk,* and *Ikzf2* (Figure 26B). B cells clustered with high expression of key B cell markers including *Bank1, Cr2, Pax5*, and *Ighd*, while plasma cells exhibited high expression of *Jchain, Igha,* and *Igkc* (Figure 26B).

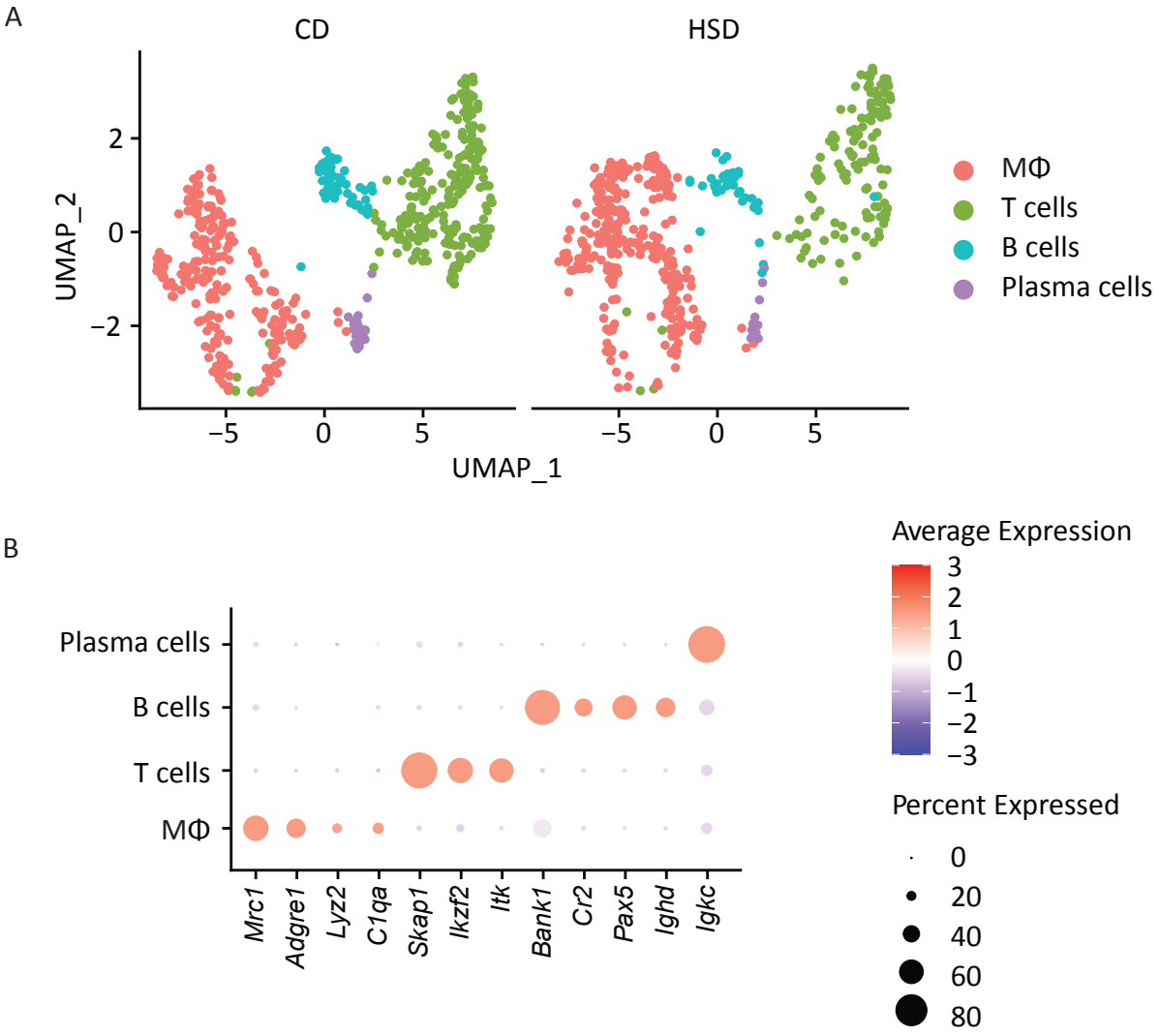

Figure 26 Umap of the detectable immune cell clusters in the mouse ileum and their featured genes. Ileum LP and ME layers of long-term CD and HSD conditions were collected for nuclei isolation and subsequent Single nuclei RNA sequencing analysis. Ileum LP and ME layer samples of 2 mice were pooled into one sample for each diet. (A) UMAP of ileum MΦ, T cells, B cells, and plasma cells in long-term CD and HSD conditions. (B) Gene expression dot plot of immune cell signature genes.

MΦ were characterized by their expression of the MΦ canonical genes *Adgre1, Lyz2*, *C1q*, and Mrc1 (Figure 26B), and were further divided into 3 subclusters that were annotated based on their feature MΦ gene expression as CD163$^+$, MHCII$^+$, and Plac8$^+$ MΦ that were visualized as UMAP were HSD condition seemed too have altered MHCII$^+$ MΦ cluster (Figure 27A, B).

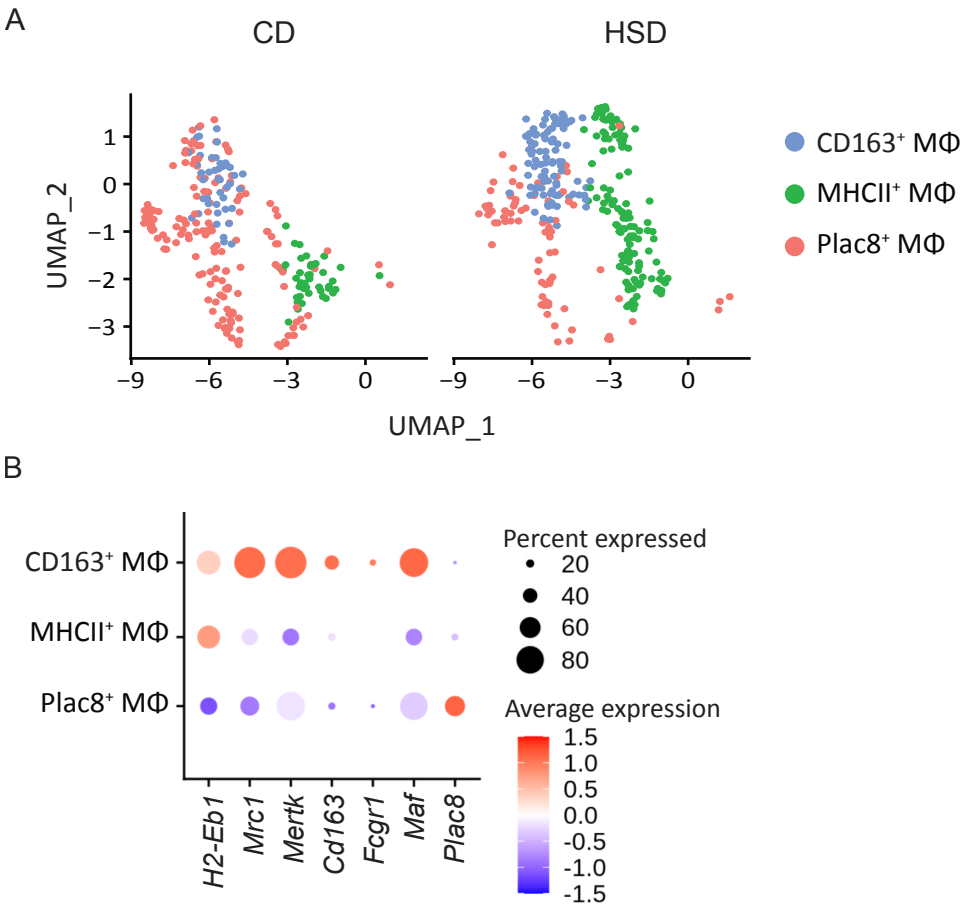

Figure 27 MΦ subpopulations in the ileum. Ileum LP and ME layers of long-term CD and HSD conditions were collected for nuclei isolation and subsequent Single nuclei RNA sequencing analysis. Ileum LP and ME layer samples of 2 mice were pooled into one sample for each diet. (A) UMAP of MΦ subsets following the long-term CD and HSD. (B) Expression dot plot of the signature genes of MΦ subsets.

3.3.2 Functional Enrichment Analysis of MΦ Gene Expression Following HSD

To reveal ileum MΦ responses to long-term HSD, functional gene enrichment analyses of differentially expressed MΦ genes between HSD and CD were performed. Gene ontology analysis (GO) revealed that MΦ from HSD upregulate terms connected to pro-inflammatory responses such as *activation of immune response, Leukocyte proliferation, monocyte differentiation, antigen presentation,* and *regulation of cytokine production*. Nonetheless, HSD appeared to enhance MΦ phagocytosis, as indicated by the upregulation of the GO term *regulation of endocytosis* (Figure 28). Alongside these HSD-driven changes, excess NaCl intake drove the downregulation of GO terms such as *Na$^+$ transport* and the Na$^+$-dependent *organic*

anion transport. Likewise*, lipid processes*, *bile acid metabolism*, *and cholesterol homeostasis* were downregulated, suggesting that HSD appears to disrupt cellular metabolism. Moreover, *MΦ tight junction* assembly was impaired upon HSD, which can affect their migratory behavior and interaction with epithelial cells (Figure 28) [179].

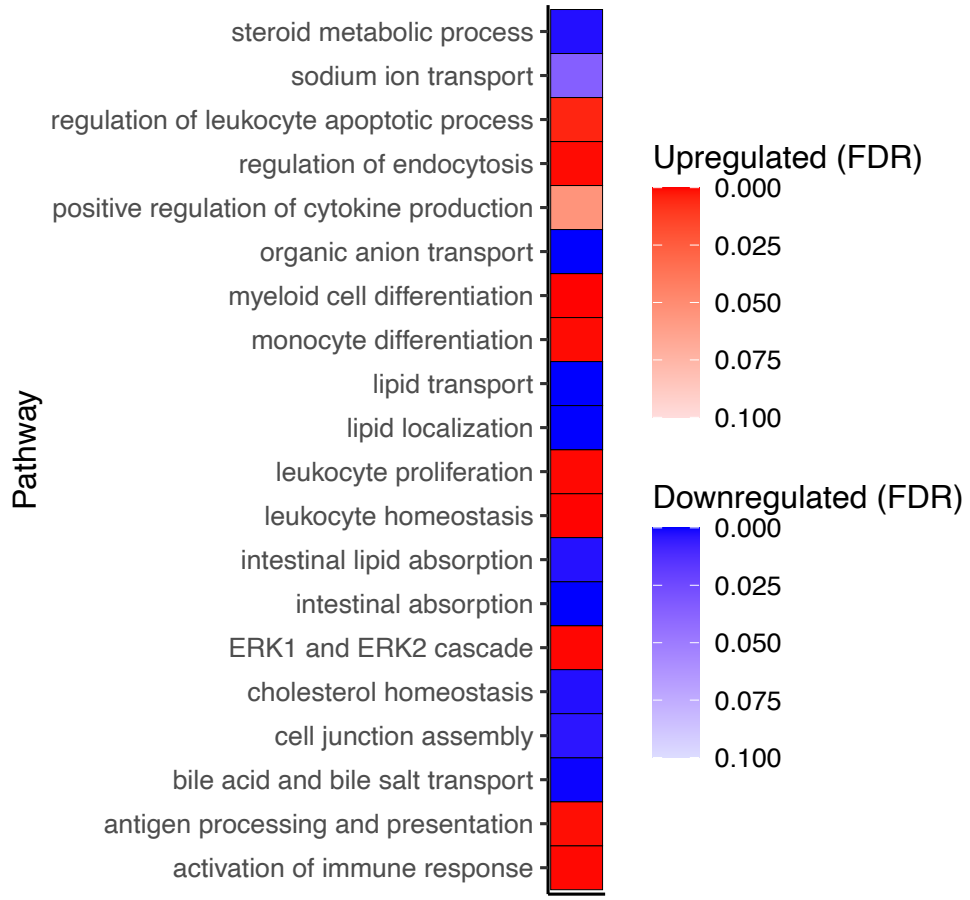

Figure 28 Heatmap showing functional enrichment of differentially expressed GO biological processes in ileal MΦ after long-term HSD, based on the single nuclei RNA-seq data. Ileum LP and ME layers of long-term CD and HSD conditions were collected for nuclei isolation and subsequent Single nuclei RNA sequencing analysis. Ileum LP and ME layer samples of 2 mice were pooled into one sample for each diet. FDR: False Discovery Rate.

Afterwards, the hallmark analysis of the three ileal MΦ subsets upon long-term HSD was performed, highlighting an upregulated *inflammatory response* predominantly in MHCII$^+$ MΦ upon the HSD, characterized by the overexpression of inflammation-related genes including *Msr1, Il1b, Il10ra, C3ar1, C5ar1, Ccl7, Hif1a, Nlrp3* (Figure 29A, B). Additionally, *interferon alpha and gamma responses* were increased in MHCII$^+$ and CD163$^+$ subsets (Figure 29A, C). *Myogenesis* and *epithelial-mesenchymal transition* were also upregulated in both CD163$^+$ and Plac8$^+$ MΦ, indicating MΦ contribution to the smooth muscle development process and also the regulation of epithelial cells in the gut upon HSD. On the other hand, *cholesterol homeostasis* was downregulated in both CD163$^+$ and Plac8$^+$ MΦ (Figure 29C, E). The downregulated cholesterol homeostasis was manifested by the decreased expression of

cholesterol-linked genes like *Ctnnb1, Pnrc1, Mal2, Cpeb2, Clu, Fads2, Hmgcs1,* and overexpression of *Atxn2, Jag1, and Lss* which reflected a feedback activation and metabolic stress (Figure 29D). In summary, long-term HSD appeared to transcriptionally increase ileal MΦ inflammatory activity, especially of CD163⁺ MΦ, while decreasing ion transport and lipid homeostasis processes, which are essential for MΦ functionality.

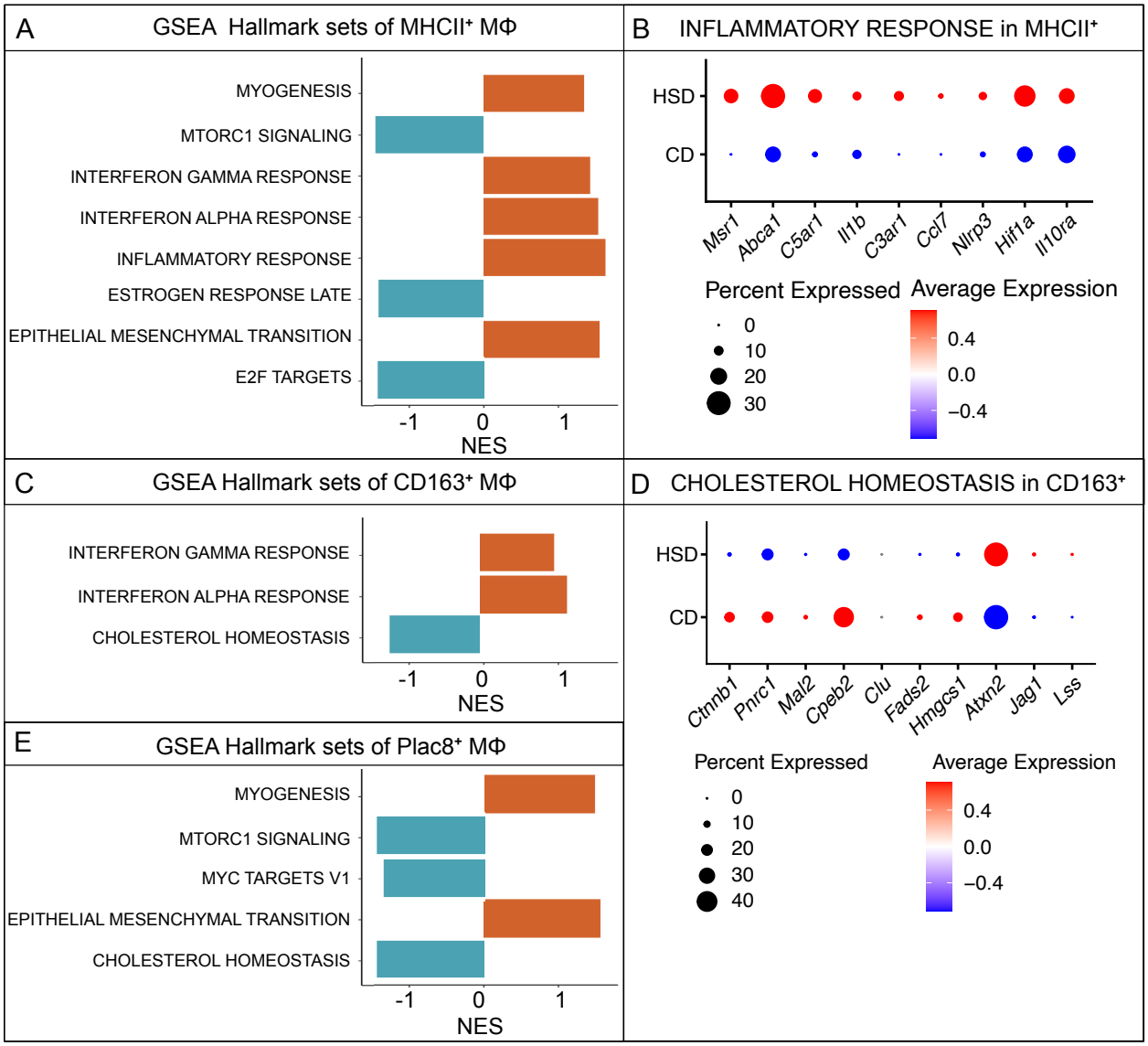

Figure 29 Hallmark analysis of ileum MΦ subsets upon long-term HSD. Ileum LP and ME layers of long-term CD and HSD conditions were collected for nuclei isolation and subsequent Single nuclei RNA sequencing analysis. Ileum LP and ME layer samples of 2 mice were pooled into one sample for each diet. (A) Hallmark sets of MHCII⁺ MΦ. (B) Expression of genes included in the Inflammatory response Hallmark term in MHCII⁺ MΦ. (C) Hallmark sets of CD163⁺ MΦ. (D) Expression of genes included in the Cholesterol homeostasis term in MHCII+ MΦ. (E) Hallmark sets of Plac8⁺ MΦ.

3.3.3 Specific Genes Linked to MΦ Functions and Cell Volume upon High-Salt Diet

The expression of selected ileum MΦ genes was further investigated to assess MΦ functional responses to long-term HSD. Gene expression of ion transporters and their regulators were evaluated, as they play a crucial role in governing MΦ immune functions. Following long-term HSD, *Slc8a1* gene that encodes Na^+/Ca^{2+} exchanger 1 (NCX1), was significantly downregulated in $CD163^+$ MΦ and, to a lesser degree, in $Plac8^+$ MΦ, indicating a negative feedback mechanism to decrease sodium influx into MΦ (Figure 30). Long-term HSD feeding downregulated *Slc12a2* gene that encodes an Na^+-K^+-$2Cl^-$ cotransporter (NKCC1) and its regulator gene *Stk39* in $MHCII^+$ and $CD163^+$ MΦ, accompanied by an increased expression of *Wnk1*, a chloride sensing regulator, and *Mertk, an efferocytosis receptor* (Figure 30). In line with the loss of *Slc12a2* expression upon HSD in $MHCII^+$ MΦ, an increase of *Mertk* expression was observed, one of the key receptors to recognize and engulf apoptotic cells. *NKCC1 (Slc12a2)*, along with its regulators, *Wnk1* and SPAK, control MΦ cell volume by modulating cytosolic chloride levels, and inhibition of any of these proteins can increase MΦ cell volume and induce efferocytosis and pro-inflammatory responses [151]. Based on that, the HSD-driven transcriptional dysregulation of these proteins in both $MHCII^+$ and $CD163^+$ MΦ suggests a potential cell volume change (Figure 30).

Furthermore, Fc gamma receptors (FcγRs) are essential for MΦ immune functions, including phagocytosis, antigen presentation, cytokine release, and antibody-dependent cellular cytotoxicity (ADCC) [180]. In mice, FcγRI, FcγRIII, and FcγRIV activate downstream signaling pathways, while FcγRIIB directs an inhibitory program. The co-expression of these activating and inhibitory receptors on MΦ sets a threshold for immune cell activation influencing MΦ core functions. However, the effect of long-term HSD on FcγR expression and function is yet to be studied. In response to long-term HSD, the expression of *Fcgr2b*, encoding the inhibitory FcγRIIb, was elevated in $MHCII^+$ and $CD163^+$ MΦ subsets. In contrast, *Fcgr4* encoding the activating FcγRIV was primarily decreased in $CD163^+$ MΦ (Figure 30). However, changes in both genes upon HSD failed to reach statistical significance. Altogether, chronic excess NaCl intake seems to transcriptionally impair MΦ chloride-sensing pathway components and increase Mertk-dependent MΦ efferocytosis, along with MΦ FcγRs dysregulation, potentially suggesting a switch into pro-inflammatory MΦ responses.

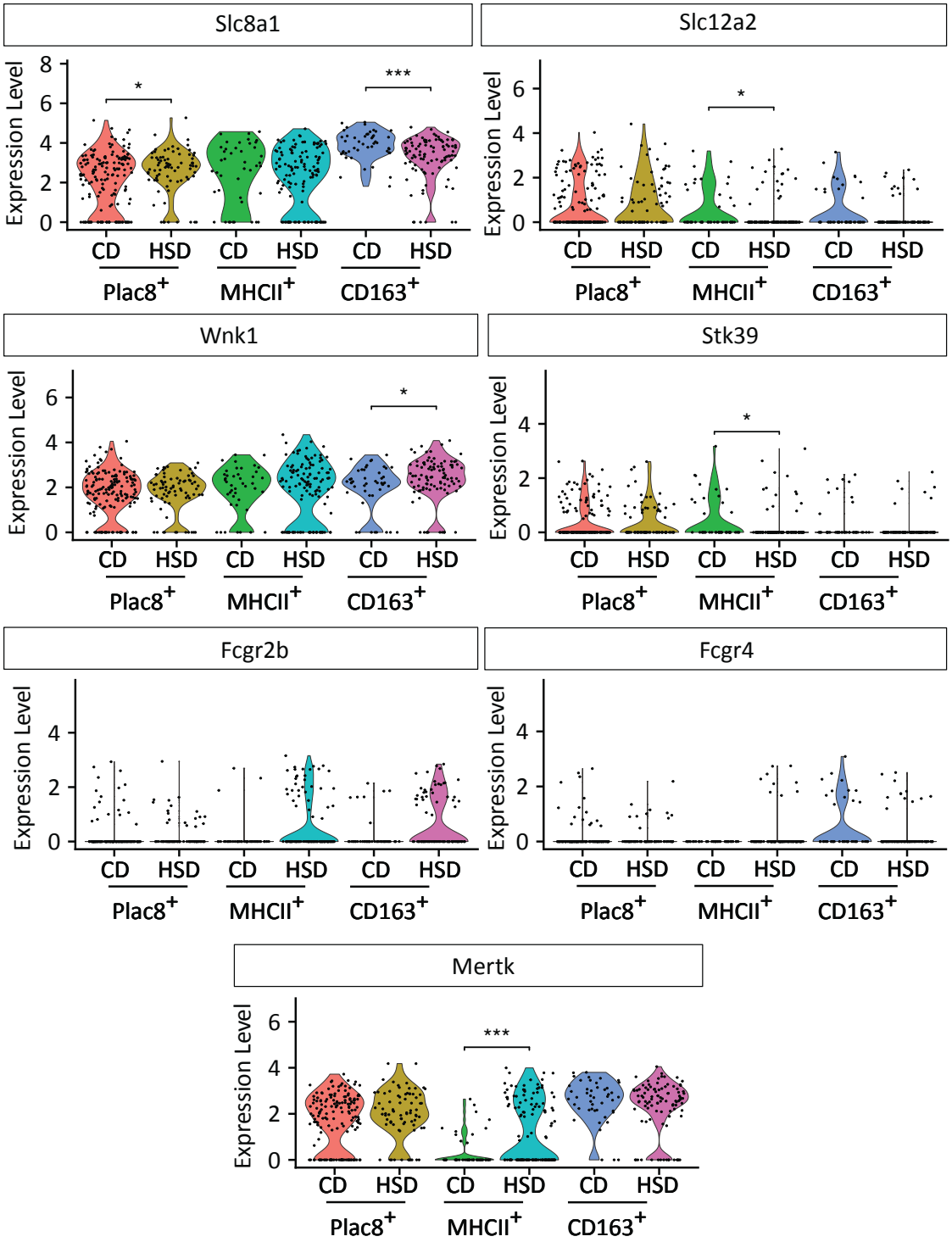

Figure 30 Expression of selected genes in ileal MΦ subsets after long-term HSD. Ileum LP and ME layers of long-term CD and HSD conditions were collected for nuclei isolation and subsequent Single nuclei RNA sequencing analysis. Ileum LP and ME layer samples of 2 mice were pooled into one sample for each diet, Wilcoxon Rank Sum test.

3.3.4 Investigation of Transcriptional MΦ–Enterocyte Interactions

In addition to their antigen-presenting and immune defense functions, MΦ interact with ECs in various ways, including regulating nutrient absorption and transport, tight junctions and barrier function, as well as metabolite and lipid signaling [181–184]. MΦ-enterocyte communication (MΦ–EC) in the ileum following long-term HSD was analyzed using the CellChat pipeline [185]. While the number of ligand-receptor interactions was relatively comparable between CD- and HSD-fed mice (382 vs. 372, respectively; Figure 31A), the interaction strength increased in the HSD condition, indicating MΦ-EC total signaling enhancement (11,446 vs. 14,777; Figure 31B).

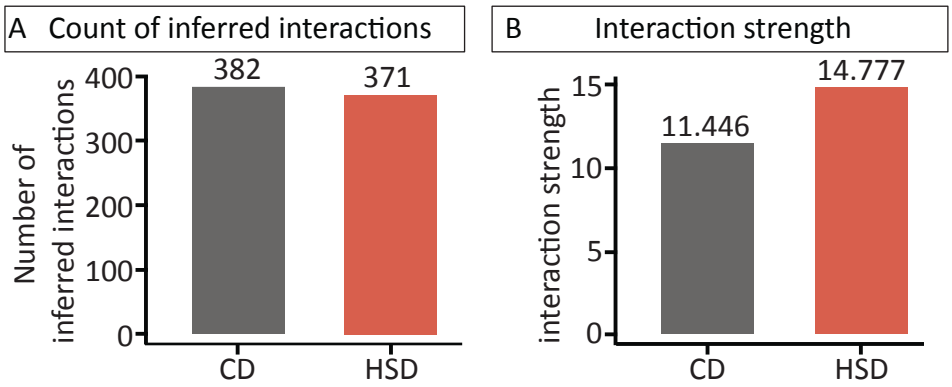

Figure 31 Inferred interactions of ileum MΦ-EC subpopulations in comparison between CD and HSD. Ileum LP and ME layers of long-term CD and HSD conditions were collected for nuclei isolation and subsequent Single nuclei RNA sequencing analysis. Ileum LP and ME layer samples of 2 mice were pooled into one sample for each diet. (A) Number of inferred interactions. (B) Interaction strength of the inferred interactions.

To identify the cell subpopulations with significant signaling changes between CD and HSD, signaling role analysis on the aggregated cell-cell communication network was generated. All three MΦ subsets had increased incoming interaction strength in the HSD condition by a magnitude of around 0.5 (Figure 32). While the outgoing interaction strength of MHCII$^+$ MΦ remained similar to that of CD, CD163$^+$ and Plac8$^+$ MΦ showed a notable increase in their outgoing interaction strength. All EC subsets showed a moderate increase in incoming and outgoing signaling under HSD conditions (Figure 32).

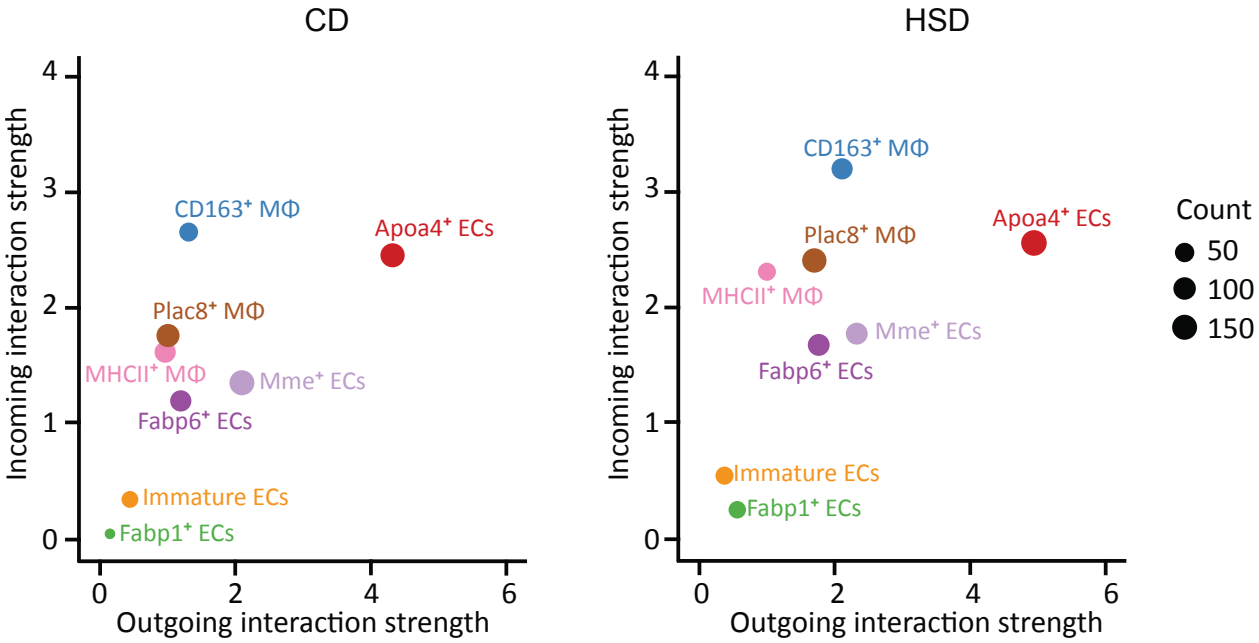

Figure 32 Signaling role scatter plot of ileum MΦ and EC subsets in long-term CD and HSD conditions. Ileum LP and ME layers of long-term CD and HSD conditions were collected for nuclei isolation and subsequent Single nuclei RNA sequencing analysis. Ileum LP and ME layer samples of 2 mice were pooled into one sample for each diet. Dot size is proportional to the number of inferred links (both outgoing and incoming) associated with each cell group. Interaction strength is the computed communication probability, generated based on the two centrality measures (outdegree and indegree with weights).

To study the signaling changes of each subpopulation, the differential strength of outgoing and incoming signals was compared in MΦ-ECs subsets. Following the long-term HSD, CD163$^+$ MΦ sent stronger signals to EC subsets than in CD, predominantly to Mme$^+$, Apoa4$^+$, and Fabp6$^+$ ECs. In return, CD163$^+$ MΦ received stronger signals from Fabp6$^+$, Mme$^+$, and immature ECs (Figure 33). Plac8$^+$ MΦ also conveyed slightly stronger interactions to ECs upon the long-term HSD, especially Fabp6$^+$ and Apoa4$^+$ ECs. In return, Plac8$^+$ MΦ received markedly stronger communication from Apoa4$^+$ and Fabp6$^+$ ECs and slightly from Immature EC (Figure 33). Whereas signals from Mme$^+$ ECs to Plac8$^+$ MΦ were downregulated upon the long-term HSD. In contrast to other MΦ subsets, MHCII$^+$ MΦ reduced interaction strength with EC subsets in response to the HSD (Figure 33). In summary, CD163$^+$ and Plac8$^+$ MΦ subsets enhanced their communication with ECs, mainly Apoa4$^+$ and Fabp6$^+$ ECs, while MHCII$^+$ lost their interaction with ECs.

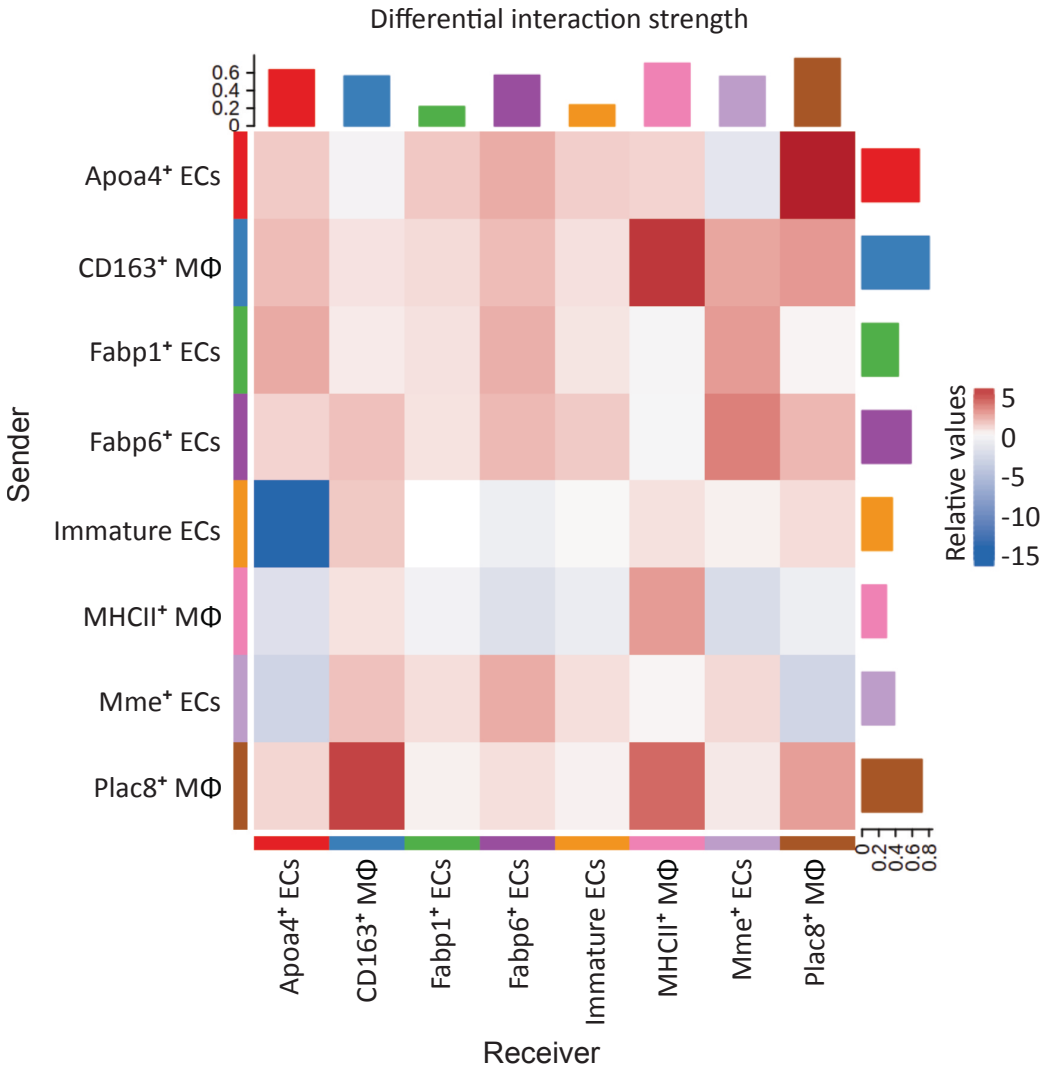

Figure 33 Differential interaction strength heatmap of MΦ-ECs subsets upon the long-term HSD. Ileum LP and ME layers of long-term CD and HSD conditions were collected for nuclei isolation and subsequent Single nuclei RNA sequencing analysis. Ileum LP and ME layer samples of 2 mice were pooled into one sample for each diet. The Y-axis represents the signaling sender subpopulations, while the X-axis represents the signaling receiver ones. Heatmap gradient coloring represents the relative value of the differential interaction strength of each cell group as blue-white-red, ranging from the lowest (blue) to the highest (red). The scale axis at the end of each axis represents the cumulative interaction strength of each cell group. Black signs represent the notable changes in MΦ-ECs communications.

Furthermore, key intercellular signaling pathways between MΦ subsets and ECs were analyzed by assessing changes in their relative information flow (Figure 34). For example, HSD enhanced immune activation pathways like CD45 in the 3 MΦ subsets, though more prominent in MHCII⁺ MΦ. CCL pathway was also enhanced in CD163⁺ and Plac8⁺ MΦ, suggesting chemokine-mediated recruitment of immune cells. Moreover, HSD enhanced MΦ-EC pathways such as BMP, EPHA, and JAM in ileum MΦ subsets suggest gut epithelial remodeling, while boosted GUCA indicates calcium ion signaling. Additionally, EGF was upregulated upon HSD in the 3 MΦ subsets and IGF only in CD163⁺ MΦ possibly implying MΦ

contribution to gut epithelial proliferation. In contrast, CD highlighted homeostatic pathways in the different MΦ subsets primarily associated with immune surveillance as in KIT, SEMA4, antigen presentation as in CD80 in CD163⁺ MΦ, cell adhesion like CADM and NECTIN, and metabolic-immune balance like VISFATIN (Figure 34). In summary, HSD feeding enhanced CD163⁺ and Plac8⁺ MΦ communication with enterocytes by increasing interaction strength, specifically featuring immune activation and epithelial remodeling pathways compared to the homeostatic signaling observed under CD feeding. Despite the upregulated CD45 signaling, MHCII⁺ MΦ had less interaction with epithelial cells following long-term HSD. These findings indicate a shift in gut immuno-epithelial crosstalk driven by long-term HSD.

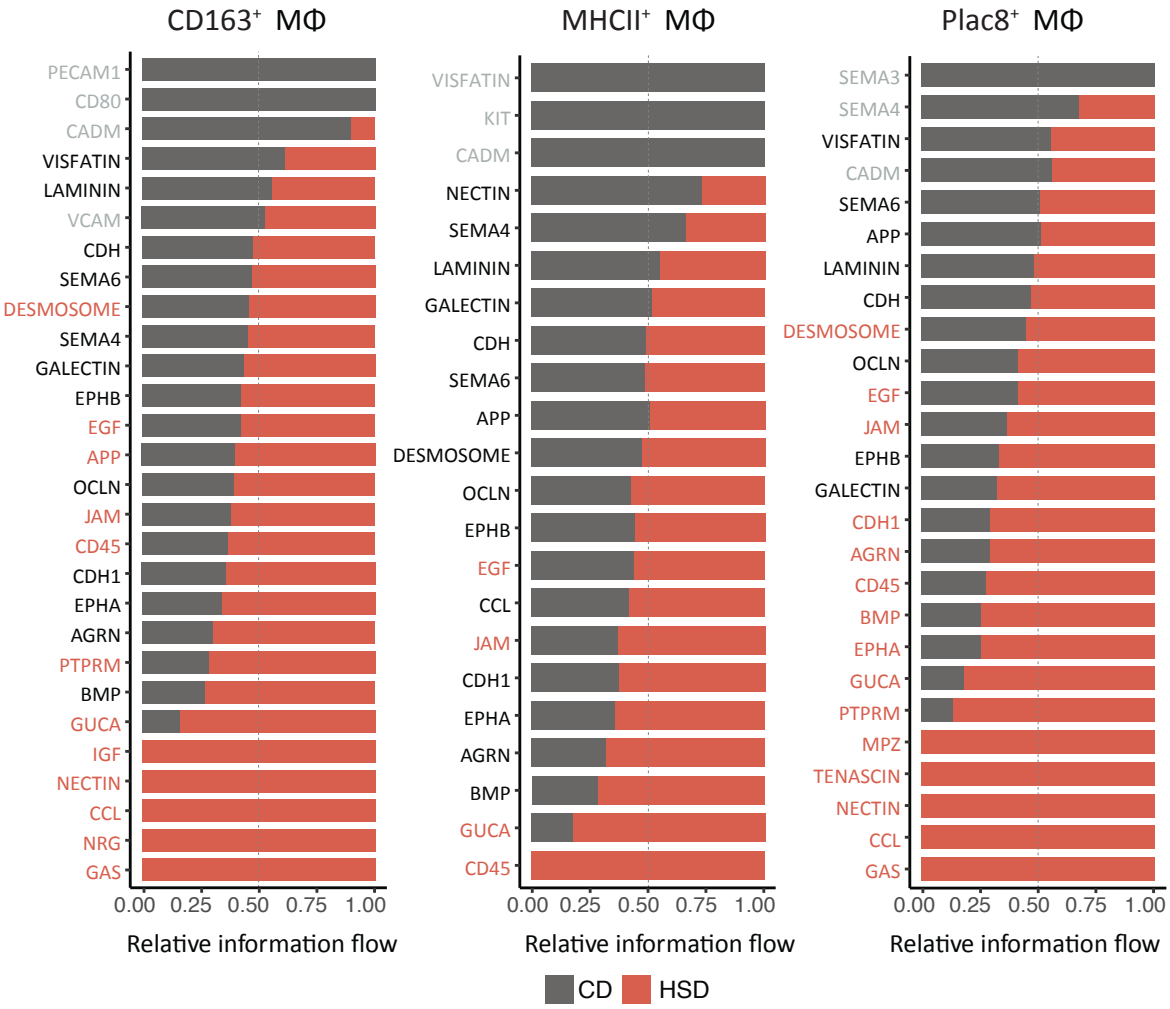

Figure 34 Ranked signaling networks of MΦ subsets with ECs upon long-term HSD based on the relative information flow. Ileum LP and ME layers of long-term CD and HSD conditions were collected for nuclei isolation and subsequent Single nuclei RNA sequencing analysis. Ileum LP and ME layer samples of 2 mice were pooled into one sample for each diet. Signaling pathways that are significantly enhanced in CD or HSD are highlighted by the diet's color code.

3.4 Ileum-MΦ Cell Volume Changes Following Long-Term HSD

Sodium and chloride channels and their regulating ion pathways play a crucial role in MΦ cell volume control by modulating osmotic balance and ion homeostasis. [13,186–188] Based on the

SnRNA sequencing analysis, the chloride transporter Slc12a2, and its regulators Wnk1 and Stk39 showed a coordinated shift in their gene expression in ileal MΦ, potentially influencing their cell volume.

To investigate the direct effect of long-term HSD on ileum MΦ cell volume, immunofluorescence staining of MΦ (Iba-1), blood vessels (CD31), and nerve fibers (Tub-III) was performed. The ileum ME layer was selected for MΦ cell volume analysis due to its uniform, single-layered MΦ distribution, which facilitates unbiased analysis. Ileum ME MΦ were classified based on their localization to blood-vessel-associated MΦ (VAMs), nerve-associated MΦ (NAMs), and interstitial macrophages (IMs) (Figure 35). 3D-rendering analysis of ileal MΦ by the MotiQ plugin in FIJI provided cell volume and cell surface of MΦ upon long-term HSD feeding.

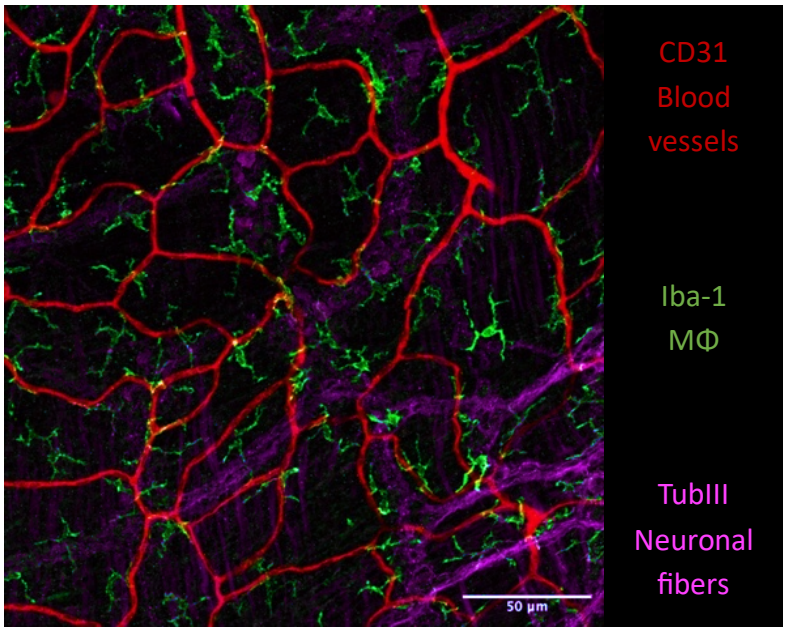

Figure 35 representative image of the ileum ME layer of a mouse stained with Iba1 for staining MΦ, CD31 for staining blood vessels, and Tub-III for staining nerves.

The ME layer VAMs of HSD-fed mice showed a significant increase in their cell volume (p = 0.029) and cell surface (p = 0.030) compared to those in CD-fed mice, as visualized in the representative images of CD and HSD ME layer showing stained MΦ and blood vessels (Figure 36A, B). This trend was less prominent in NAMs that showed a significant increase in cell volume (p = 0.030) but no statistically meaningful change in cell surface (Figure 36B). However, interstitial MΦ maintained their cell volume and surface after the HSD feeding (p > 0.05) (Figure 36B). In summary, long-term HSD feeding specifically increased cell volume and surface area of VAMs in the ileal ME layer, potentially mediated by the Wnk1-dependent Cl-sensing pathway, suggesting a possible impact on MΦ core functions like efferocytosis and phagocytosis.

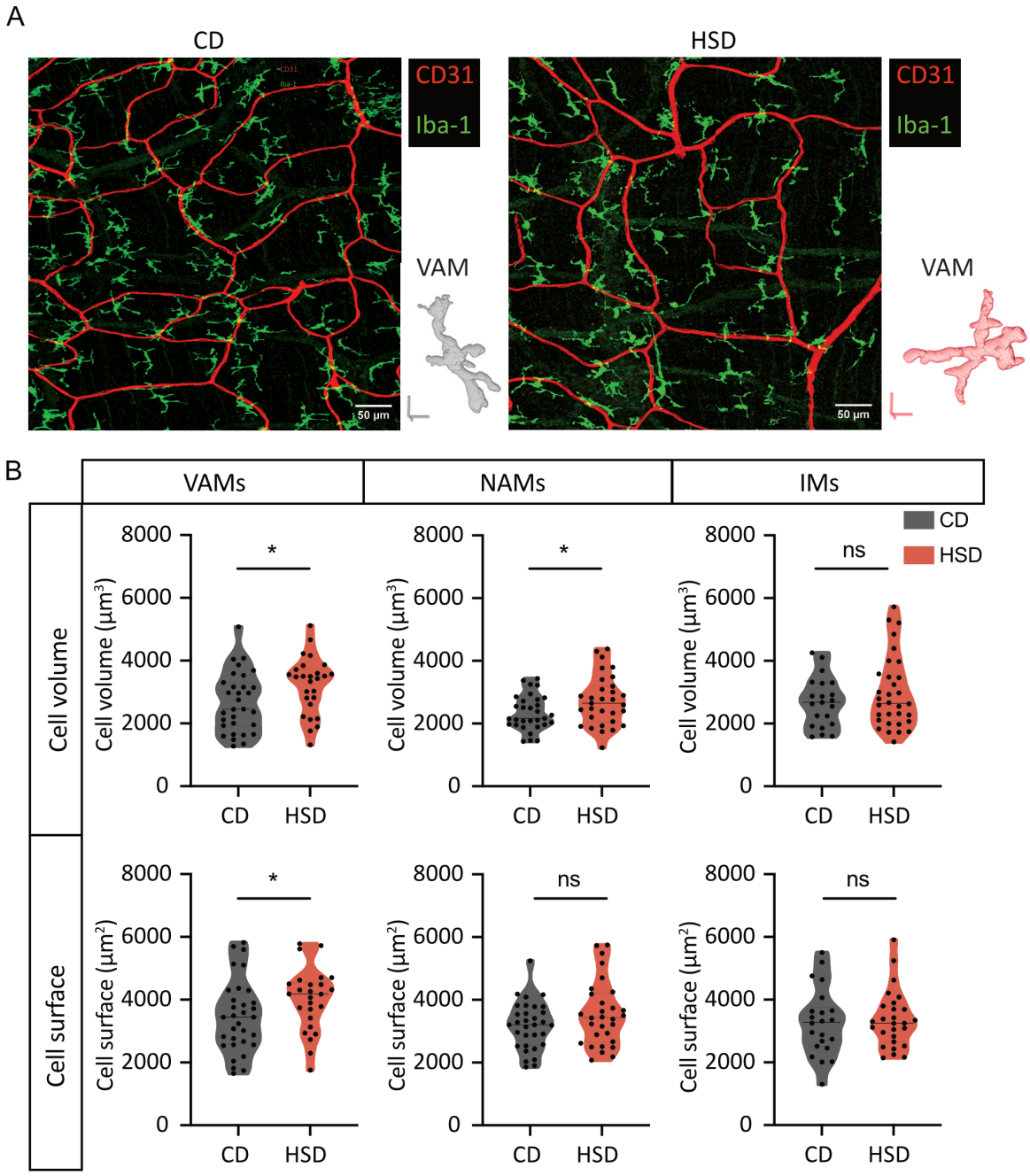

Figure 36 3D-rendering of ileum ME MΦ showing cell volume and cell surface parameters upon long-term HSD. Male mice underwent either CD or HSD for 3 months to achieve long-term treatment. (A) representative images of ME layer after long-term HSD; (B) quantitative analysis results of cell volume and cell surface in VAMs, NAMs, and IMs. The ileum ME layer was isolated and fixed, then stained with fluorescent antibodies. Labeling with Iba1 for MΦ (green), CD31 for blood vessels (red), DAPI for nuclei labeling (not shown), and Tub-III for nerve fibers (not shown) and mounted on a microscope slide for imaging. n = 22-32 cell/diet from 3 different CD and HSD mice, *p*-values were obtained using t-tests, *$p < 0.05$. CD: Control diet; HSD: high-salt diet; VAMs: blood-vessel associated MΦ; NAMs: nerve-associated MΦ; IMs: interstitial MΦ.

3.5 MΦ Heterogeneity and Ontogeny in the Gut Under High Salt Diet

3.5.1 Characterization of Gut MΦ Subsets

The gut MΦ niche is highly heterogeneous, comprising a wide range of subpopulations identified by cell surface proteins and categorized by their cell lineage, localization, and inflammatory response to infections. Despite their distinct localization, MΦ from LP and ME layers share expression of canonical MΦ markers, making mechanical isolation of the two layers the optimal option to study the MΦ heterogeneity in each layer separately. Spectral flow cytometry allowed the characterization of gut MΦ subsets using numerous MΦ-specific surface markers. After gating on the $CD11b^+$ myeloid cells, gut MΦ were gated by F4/80 expression in both layers (Supplementary Figure 5A, B). Subpopulations were initially distinguished by the CD163 expression; $CD163^+$ MΦ are abundant in ME and minimal in the LP layer. $CD163^-$ MΦ were divided into $MHCII^+$ and $MHCII^-$ MΦ. $MHCII^+$ are quite abundant in both layers, and in the LP, they include $CD169^+CD11c^+$, $Tim4^+$, $Lyve1^+$, $CD13^+$, $CD13^-$, and $MHCII^+Cx3cr1^+$ (Supplementary Figure 5A). $MHCII^-$ MΦ are further split into $Cx3cr1^+$ and $Cx3cr1^-$. In the ME layer, a similar strategy was followed, with adjustments to $MHCII^+$ subsets like $CD169^+CD206^+$ and $CD321^+Cx3cr1^+$ MΦ (Supplementary Figure 5B). $CD321^+Cx3cr1^+$ MΦ are abundant in the ME, they are referred to as nerve-associated MΦ [50].

These MΦ subsets showed distinct developmental origins in a steady state as shown in the ileum LP layer, supporting their specific phenotypes and responses (Figure 37A). In general, all subsets exhibit mixed origins from both fetal and bone marrow (BM)-derived cells; however, the relative contributions of these origins differ between subsets, shaping their specific roles within the tissue. Notably, the two $MHCII^-$ subsets, $MHCII^-Cx3cr1^+$ and $MHCII^-Cx3cr1^-$, are predominantly composed of short-lived, monocyte-derived cells differentiating from circulating monocytes. Moreover, the phagocytic capacity differs among gut MΦ subsets, as demonstrated in ileal LP MΦ, highlighting their distinct functional roles within the tissue—potentially influenced by their spatial localization. Notably, $Lyve1^+$ MΦ, which also express high levels of Tim4, exhibit the highest phagocytic capacity, followed by $CD163^+$ MΦ (Figure 37B).

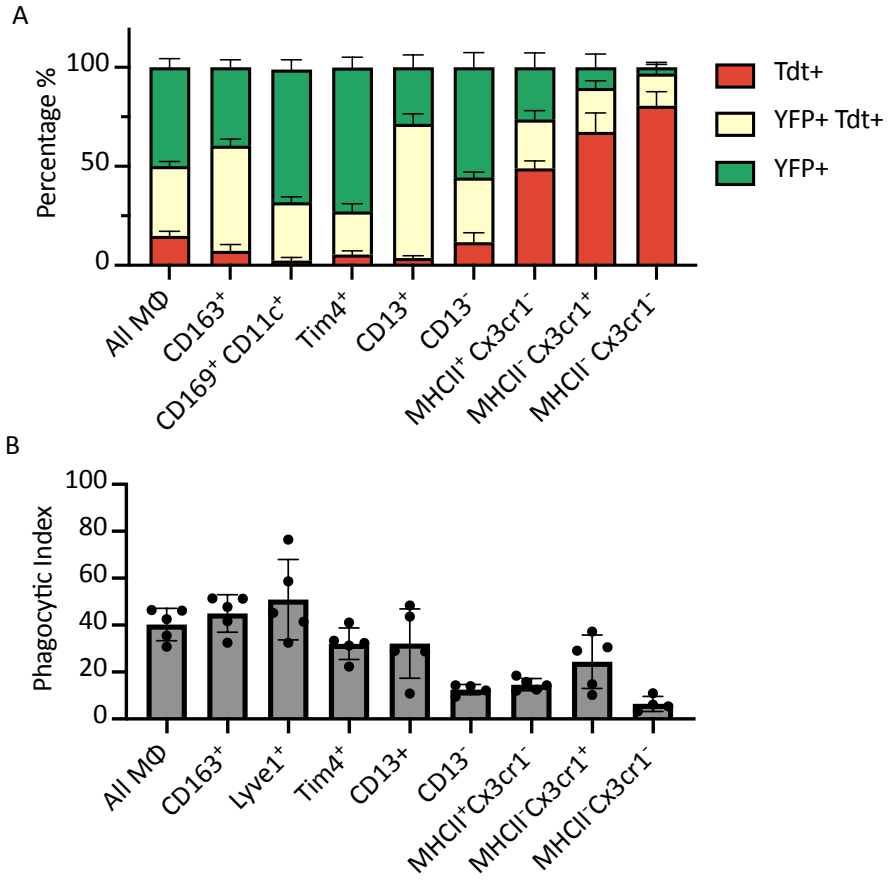

Figure 37 Characterization of ileum MΦ developmental origin and phagocytic activity in steady state. (A) Developmental origin of ileum MΦ subpopulations in males mice; The Tnfrsf11a^{Cre}; Rosa26$^{LSL\text{-}YFP}$; Ms4a3^{FlpO}; Rosa26$^{LFL\text{-}tdTomato}$ fate mapping model labels monocyte-derived cells with lived monocyte-derived cells with tdTomato (red) and fetal-derived cells with YFP (green); The tdTomato^{+} monocyte-derived cells acquire YFP labeling, when differentiating into long-lived tissue MΦ (yellow); (B) Phagocytic capacity of gut MΦ subpopulations; Male mice were fed CD or HSD for 3 months, and then liver MΦ were isolated, cultured with stained *C. rodentium* for 1h in a ratio 1 MΦ:160 CFUs, then stained with MΦ markers for Flow cytometry analysis.

3.5.2 Cell Count Changes of MΦ Subsets Upon Short-Term HSD Feeding

The cell counts of MΦ and their subsets were analyzed in each gut region following both short- and long-term HSD. In the short-term HSD, the various gut regions were examined in female mice, including the stomach, duodenum, jejunum, ileum, proximal, and distal colon, whereas in males, only the ileum was studied. For long-term HSD mice of both sexes, MΦ counts were assessed across all the aforementioned gut regions. Monocyte counts were assessed in only the stomach of female mice due to their low resulted numbers in other regions, and in all gut regions of male mice.

(i) Stomach – In female mice, short- and long-term HSD did not alter the total count of stomach LP monocytes, MΦ, and MΦ subpopulations compared to CD-fed mice (Figure 38A, B). Similarly, stomach ME monocytes and MΦ counts remained unchanged in both short- and long-term HSD (Figure 38C, D). In male mice, long-term

HSD showed no significant effects on cell counts of stomach monocytes, MΦ, and MΦ subpopulations of both layers (Figure 39A, B).

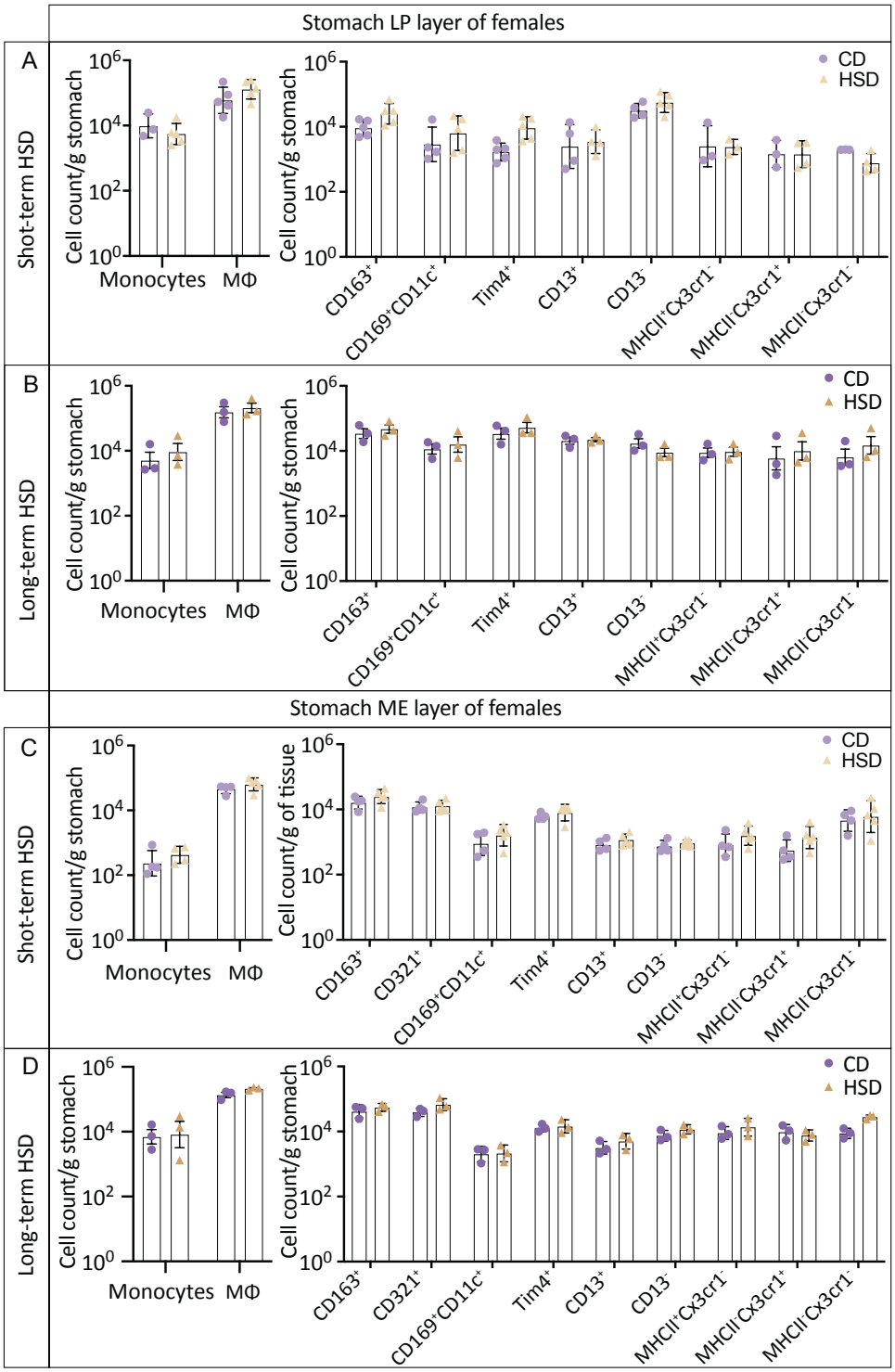

Figure 38 Cell counts of stomach LP and ME monocytes, total MΦ, and MΦ subpopulations in female mice upon short- and long-term HSD. (A) Stomach LP cell counts upon short-term HSD; and (B) long-term HSD; (C) Stomach ME cell counts upon short-term HSD; and (D) long-term HSD; n = 3-5, data points are log (10)-transformed, error bars represent standard deviation (SD), data was analyzed using two-way ANOVAs, *p-value < 0.05.

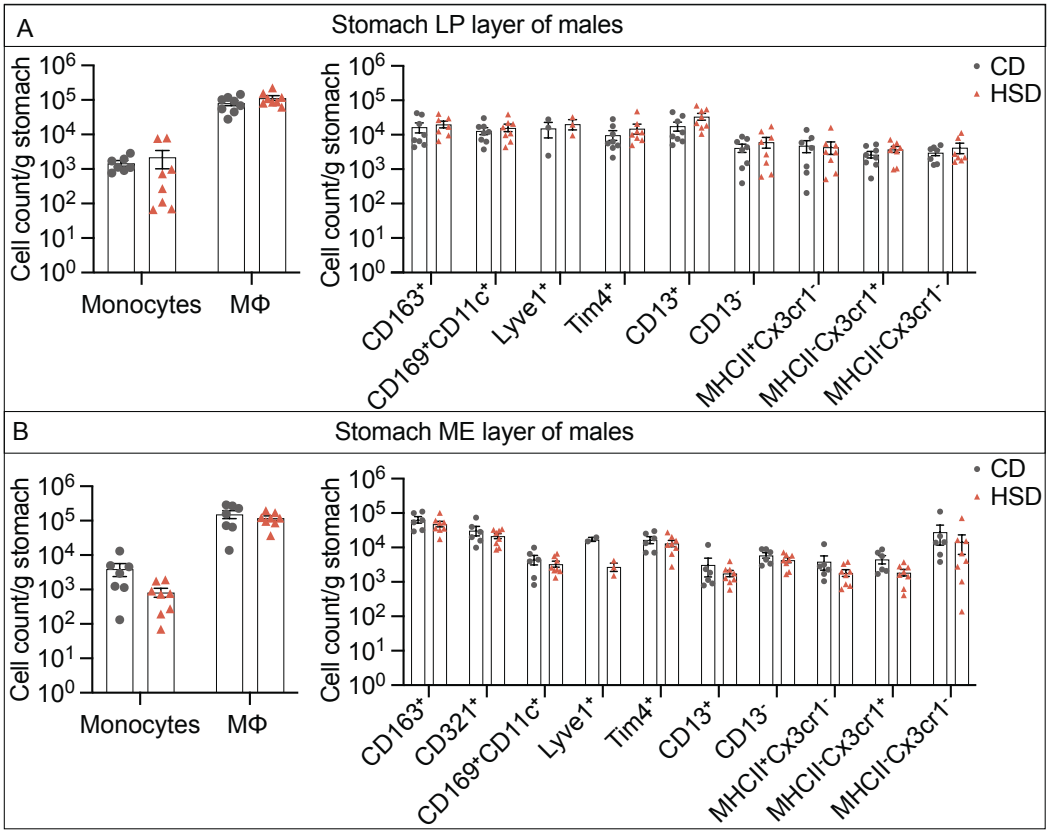

Figure 39 Cell counts of stomach LP and ME Monocytes, total MΦ, and MΦ subpopulations in male mice upon long-term HSD. (A) Stomach LP cell counts upon long-term HSD; (B) Stomach ME cell counts upon long-term HSD; n = 8 from 2 experiments, data points are log (10)-transformed, error bars represent SD, data was analyzed using two-way ANOVAs, *p-value < 0.05.

(ii) Duodenum – In female mice, duodenum LP and ME MΦ cell counts remained comparable between HSD and CD either on short- (Figure 40A, C) or long-term feeding (Figure 34B, D). Male duodenum MΦ counts showed a similar result upon long-term HSD feeding in both LP (Figure 41A) and ME layers (Figure 41B).

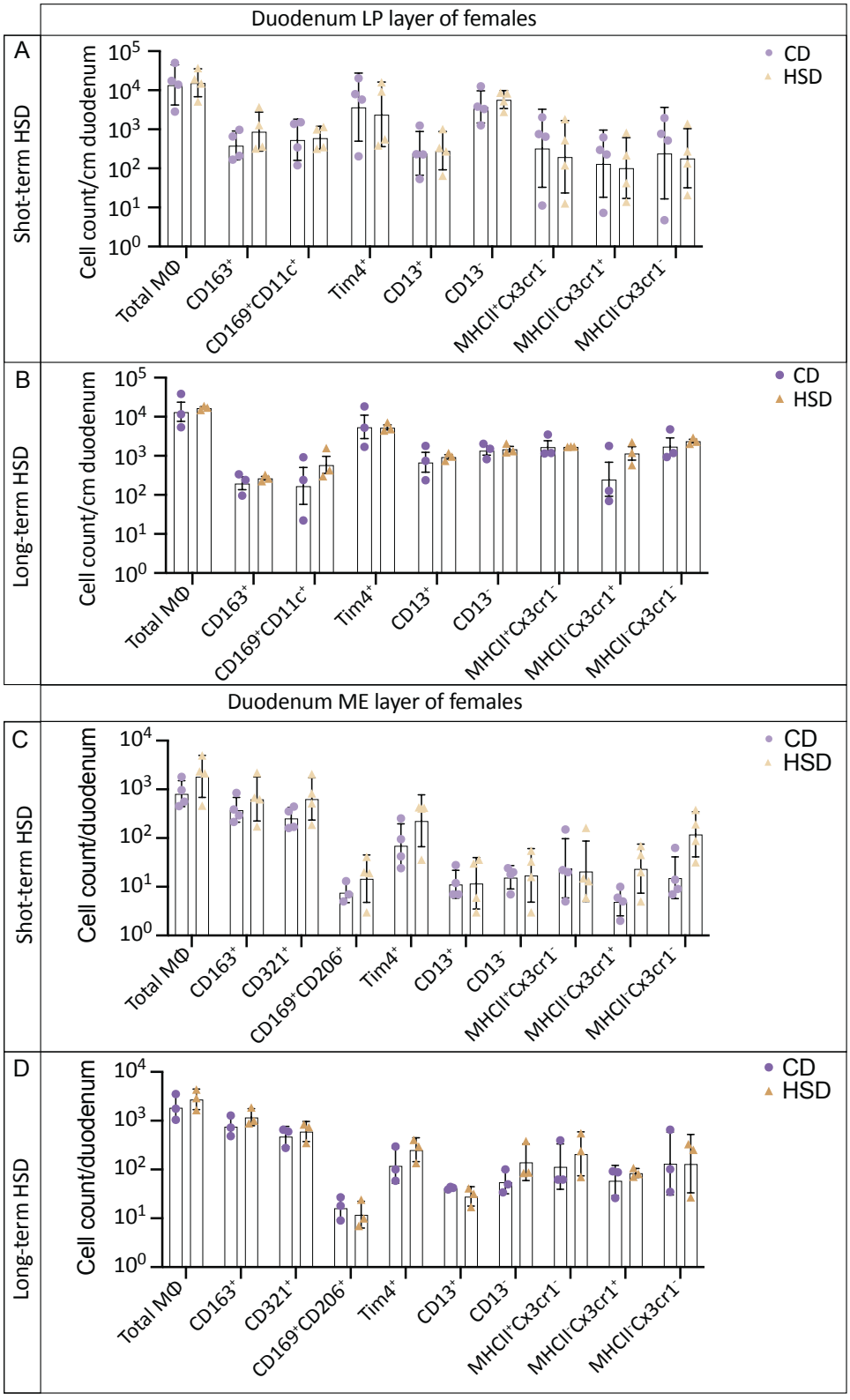

Figure 40 Cell counts of duodenum LP and ME Monocytes, total MΦ, and MΦ subpopulations in female mice upon short- and long-term HSD. (A) Duodenum LP MΦ counts upon short-term HSD, and (B) long-term HSD; (C) duodenum ME cell counts upon short-term HSD, and (D) long-term HSD; n = 3-5, data points are log (10)-transformed, error bars represent SD, data was analyzed using two-way ANOVAs, *p-value < 0.05.

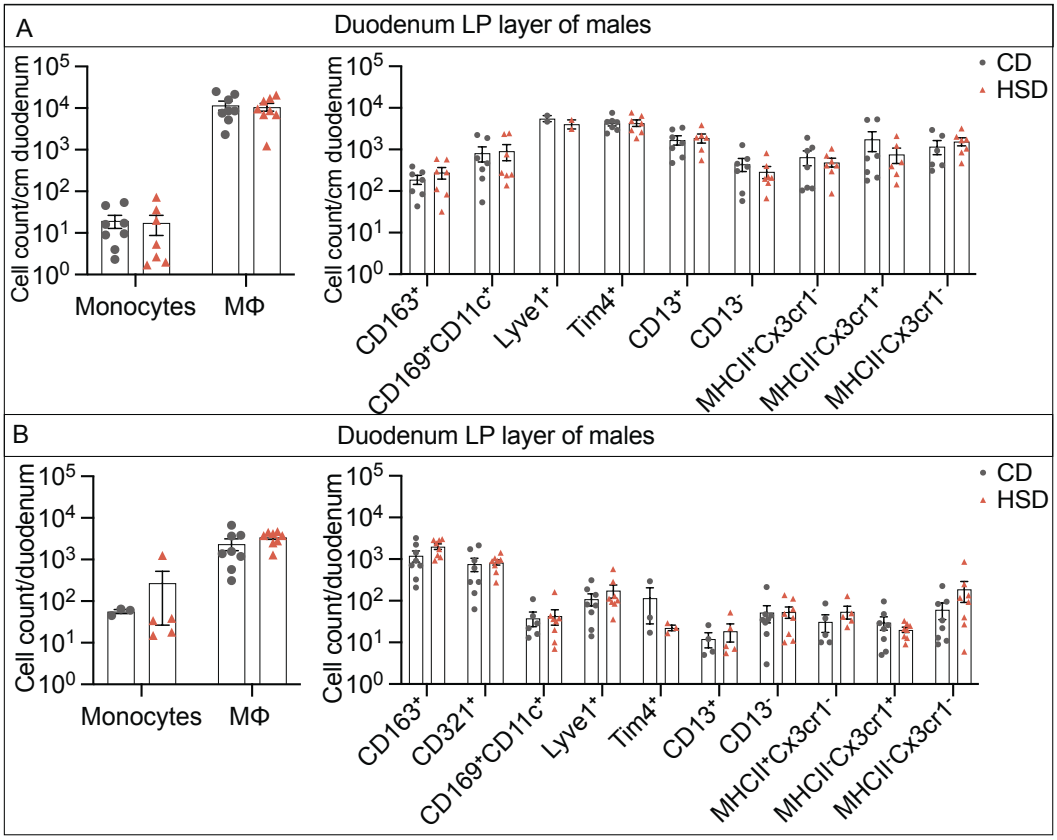

Figure 41 Cell count of duodenum LP and ME Monocytes, total MΦ, and MΦ subpopulations in male mice upon long-term HSD. (A) Duodenum LP cell counts upon long-term HSD; (B) duodenum ME cell counts upon long-term HSD; n = 8, from 2 experiments, data points are log (10)-transformed, error bars represent SD, data was analyzed using two-way ANOVAs, *p-value < 0.05.

(iii) Jejunum – Similar to the duodenum, female jejunum LP and ME MΦ cell counts remained comparable between HSD and CD either on short- (Figure 42A, C) or long-term HSD feeding (Figure 42B, D). Also, for the male group, jejunum monocytes and MΦ counts did not show statistically significant changes upon long-term HSD feeding in both the LP and ME layers (Figure 43A, B).

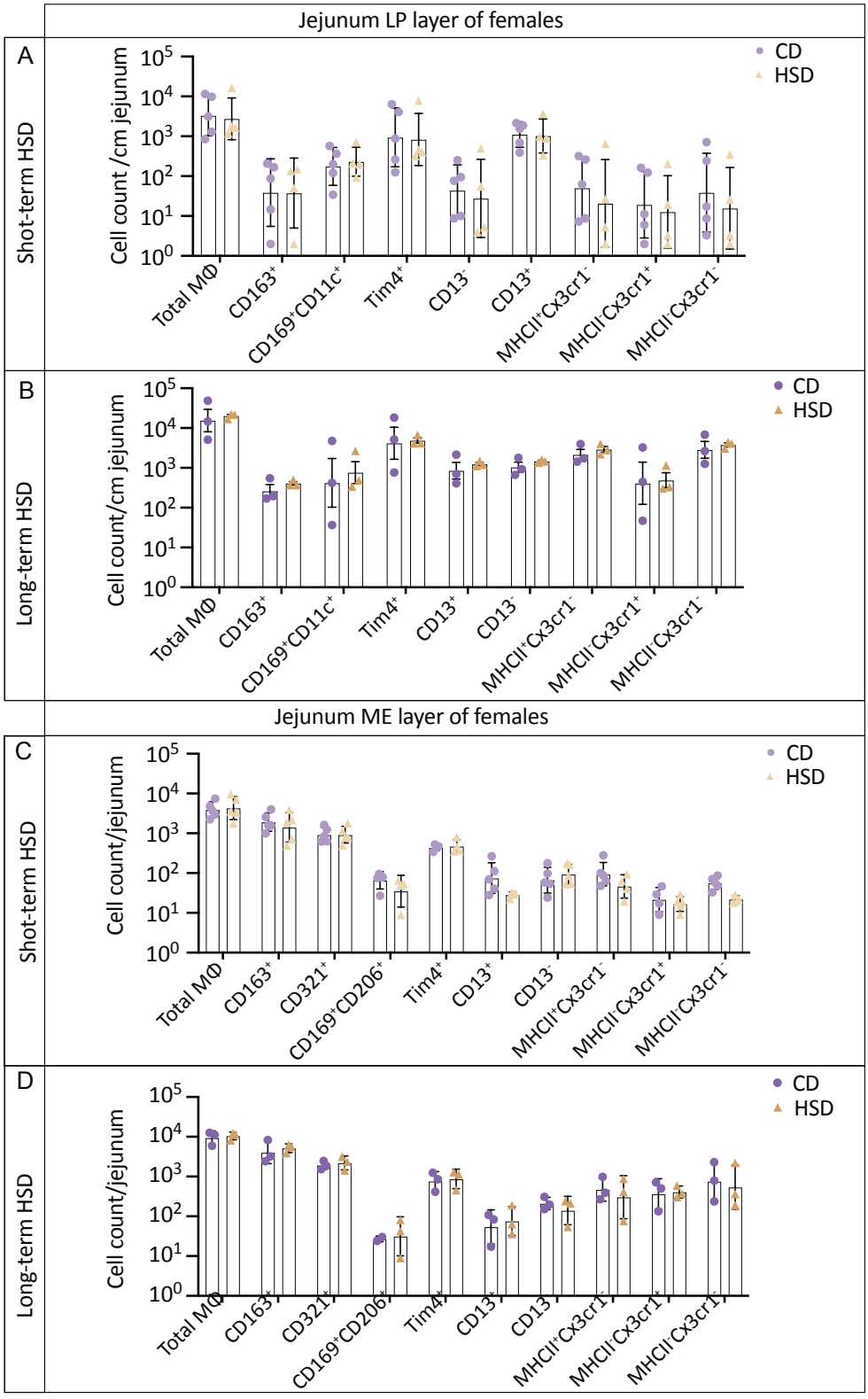

Figure 42 Cell count of jejunum LP and ME Monocytes, total MΦ, and MΦ subpopulations in female mice upon short- and long-term HSD. (A) Jejunum LP cell counts upon short-term HSD; (B) jejunum LP cell counts upon long-term HSD; (C) jejunum ME cell counts upon short-term HSD; (D) jejunum ME cell counts upon long-term HSD; n = 3-5, data points are log (10)-transformed, error bars represent SD, data was analyzed using two-way ANOVAs, *p-value < 0.05.

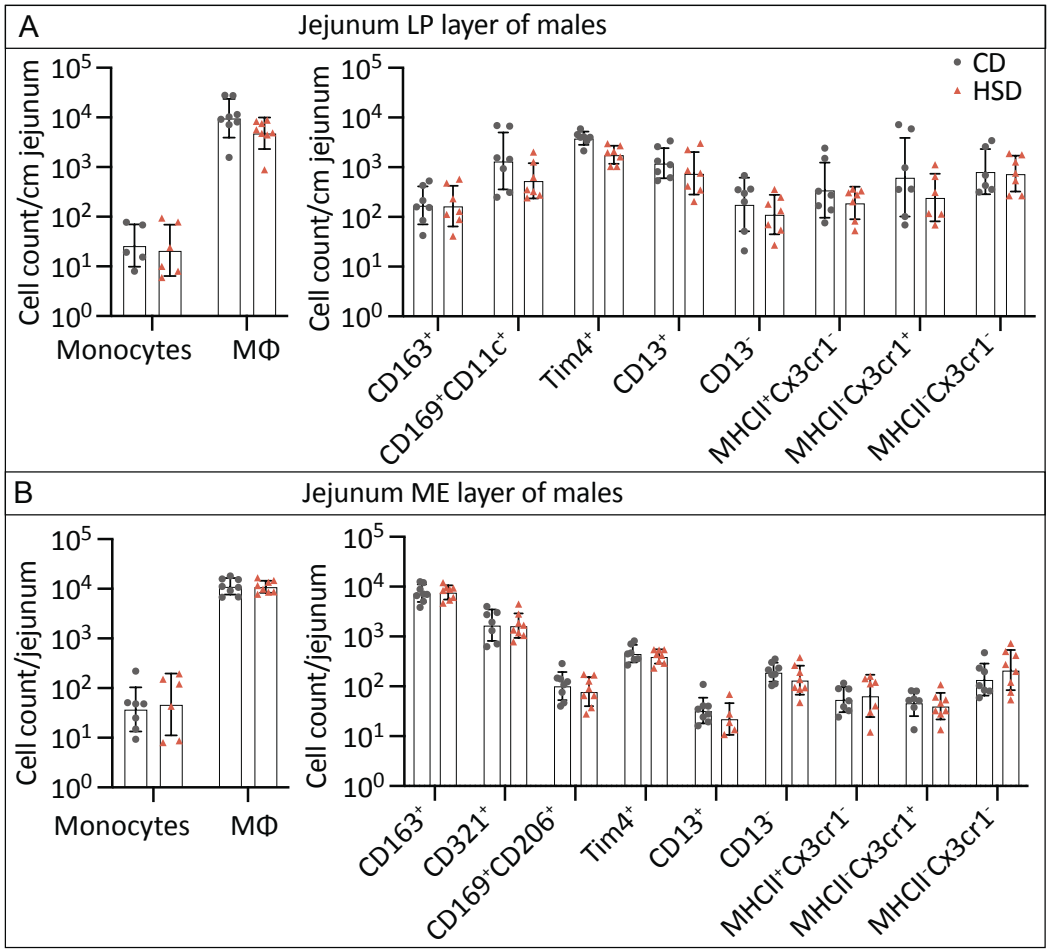

Figure 43 Cell count of jejunum LP and ME Monocytes, total MΦ, and MΦ subpopulations in male mice upon long-term HSD. (A) Jejunum LP cell counts upon long-term HSD; (B) jejunum ME cell counts upon long-term HSD; n = 8, from 2 experiments, data points are log (10)-transformed, error bars represent SD, data was analyzed using two-way ANOVAs, *p-value < 0.05.

(iv) Ileum – Female mice showed no notable changes in ileum MΦ count under short- and long-term HSD either in LP (Figure 44A, B) or ME layers (Figure 44C, D). In male mice, the ileum LP layer showed a minor increase in total monocyte count that failed to reach statistical significance (p = 0.050), but MΦ counts remained unchanged upon short-term HSD (Figure 45A). However, monocytes in the ileum ME layer were significantly increased in short-term HSD (p = 0.008), while counts of total MΦ and their subsets did not show significant changes compared to their controls (CD) (Figure 45C). On long-term HSD feeding, ileal monocytes and total MΦ in LP and ME layers were unchanged between HSD and CD (Figure 39 B, D). However, the $CD13^-$ MΦ subpopulation from the LP layer significantly increased upon long-term HSD with a p-value of 0.014 (Figure 45B). The MΦ cell count increase following long-term HSD was less prominent in the ME layer (Figure 45D).

(v) Proximal colon – In the female group, short-term HSD did not affect cell counts of proximal colon MΦ in the LP layer compared to CD feeding (Figure 46A). Whereas in the ME layer, the MΦ count was increased in response to the short-term HSD without being statistically meaningful (Figure 46C). Upon long-term HSD, proximal colon MΦ of both layers showed no remarkable cell count changes compared to CD feeding (Figure 46B, D). In the male group, the LP and ME layers of the proximal colon maintained the monocytes and total MΦ counts upon long-term HSD feeding (Figure 47A, B).

(vi) Distal colon – The cell counts of distal colon MΦ showed no significant changes upon short- and long-HSD periods in both female and male groups (Figure 48, Figure 49).

In summary, short-term HSD increased monocyte cell counts in ileum LP and ME layers without affecting MΦ cell counts, while long-term HSD increased specific MΦ subsets in the ileum namely $CD13^-$ especially in the LP layer. Other gut regions showed no MΦ cell count changes in response to either short- or long-term HSD.

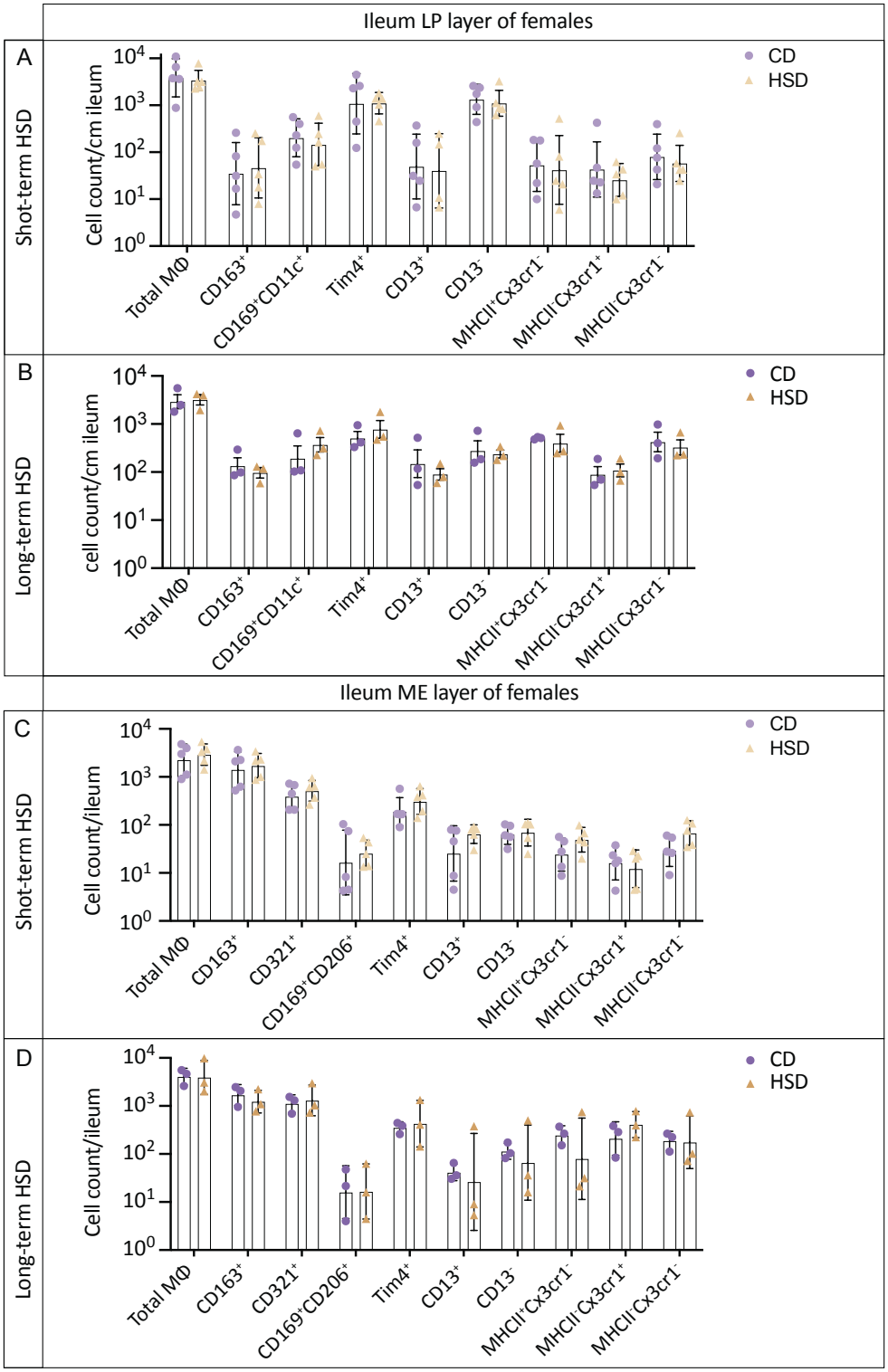

Figure 44 Cell count of ileum LP and ME Monocytes, total MΦ, and MΦ subpopulations in female mice upon short- and long-term HSD. (A) Ileum LP cell counts upon short-term HSD; (B) ileum LP cell counts upon long-term HSD; (C) ileum ME cell counts upon short-term HSD; (D) jejunum ME cell counts upon long-term HSD; n = 3-5, data points are log (10)-transformed, error bars represent SD, data was analyzed using two-way ANOVAs, *p-value < 0.05.

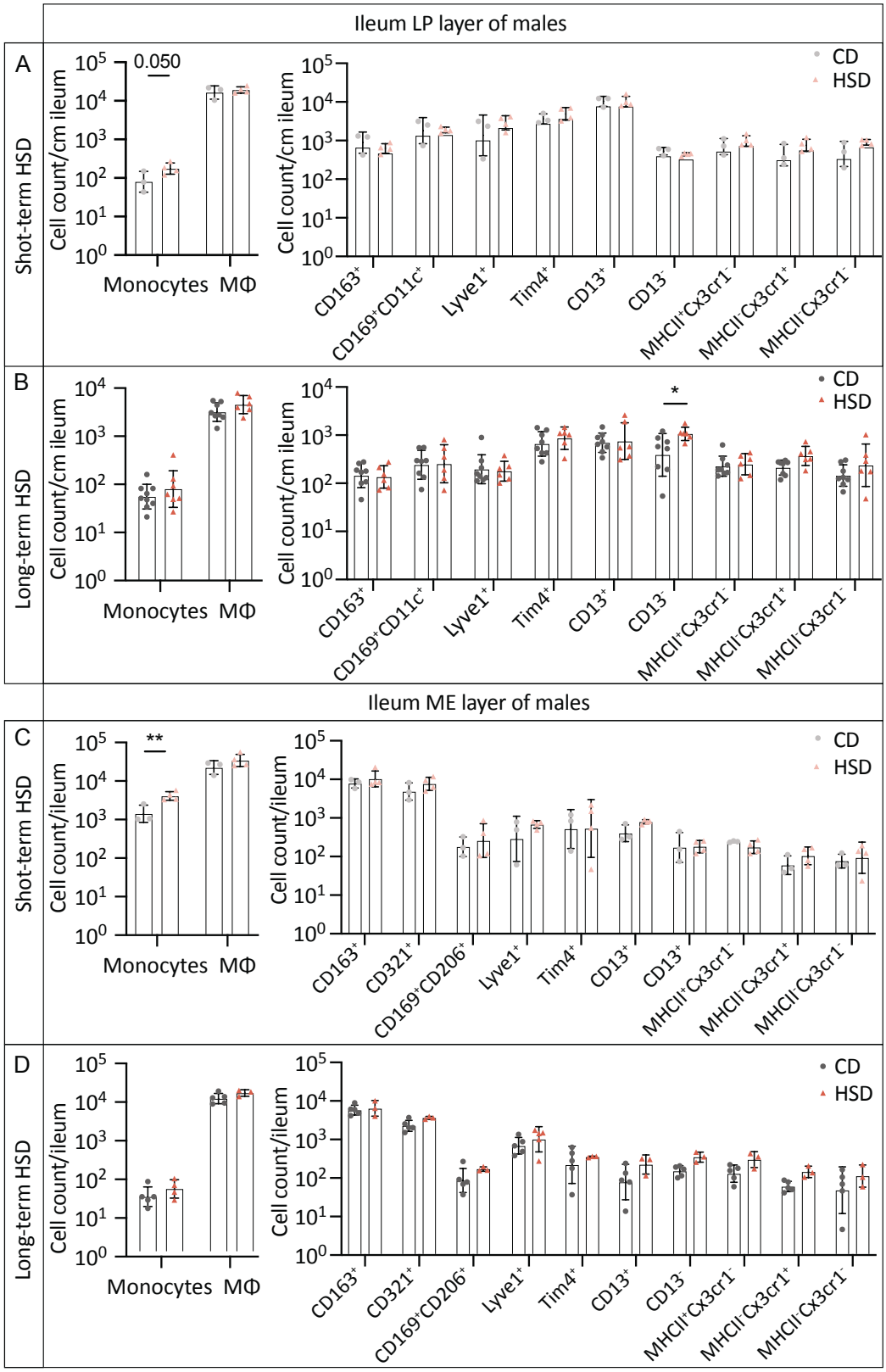

Figure 45 Cell count of ileum LP and ME Monocytes, total MΦ, and MΦ subpopulations in male mice upon long-term HSD. (A) Ileum LP cell counts upon long-term HSD, (B) n = 3-4; (B) ileum ME cell counts upon long-term HSD, n = 8 for B from 2 experiments, and n = 3-4 for A, C, and D, data points are log (10)-transformed, error bars represent SD, data was analyzed using two-way ANOVAs, *p-value < 0.05.

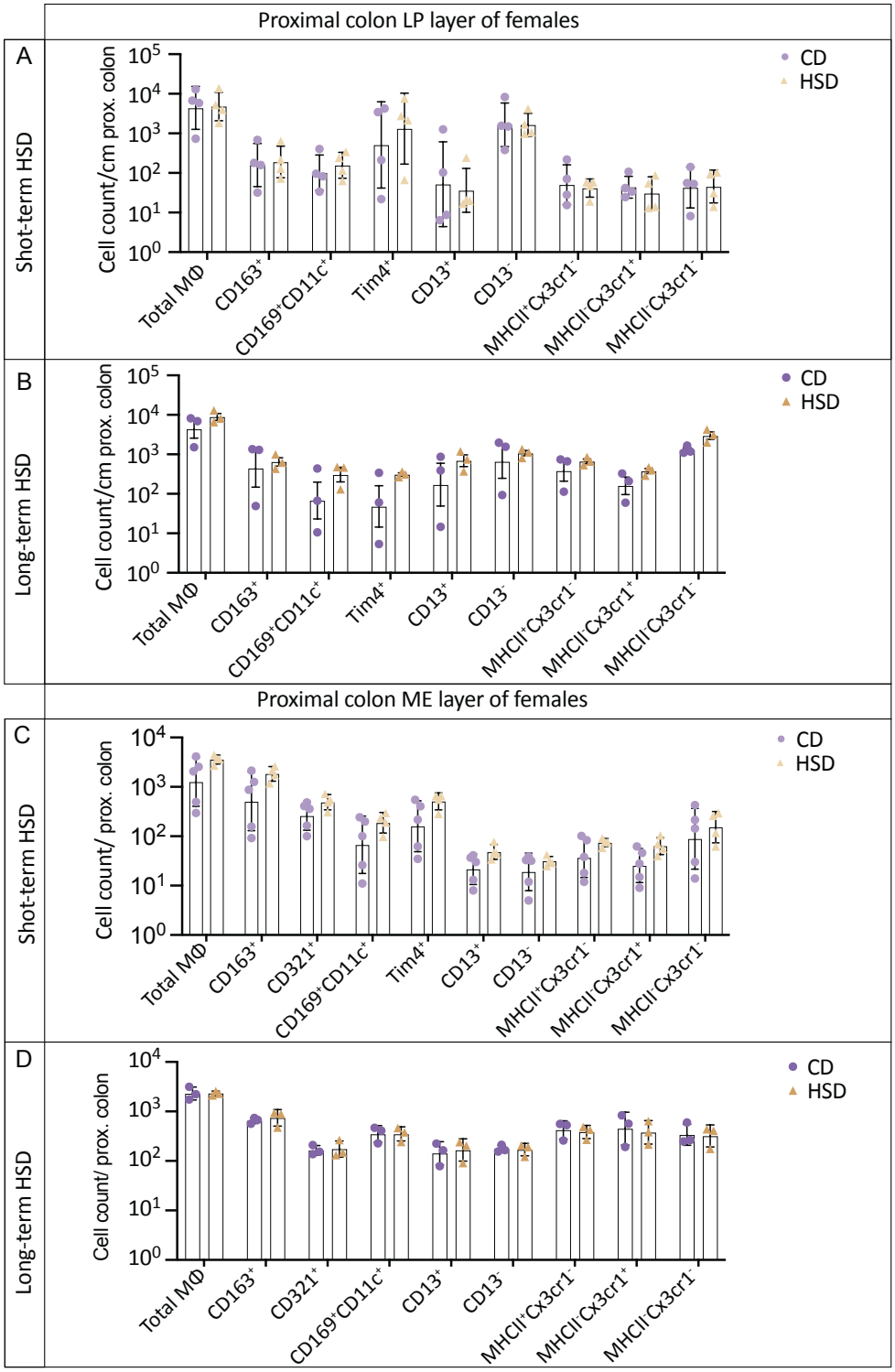

Figure 46 Cell count of proximal colon LP and ME Monocytes, total MΦ, and MΦ subpopulations in female mice upon short- and long-term HSD. (A) Proximal colon LP cell counts upon short-term HSD; (B) proximal colon LP cell counts upon long-term HSD; (C) proximal colon ME cell counts upon short-term HSD; (D) proximal colon ME cell counts upon long-term HSD; n = 3-5, data points are log (10)-transformed, error bars represent SD, data was analyzed using two-way ANOVAs, *p-value < 0.05.

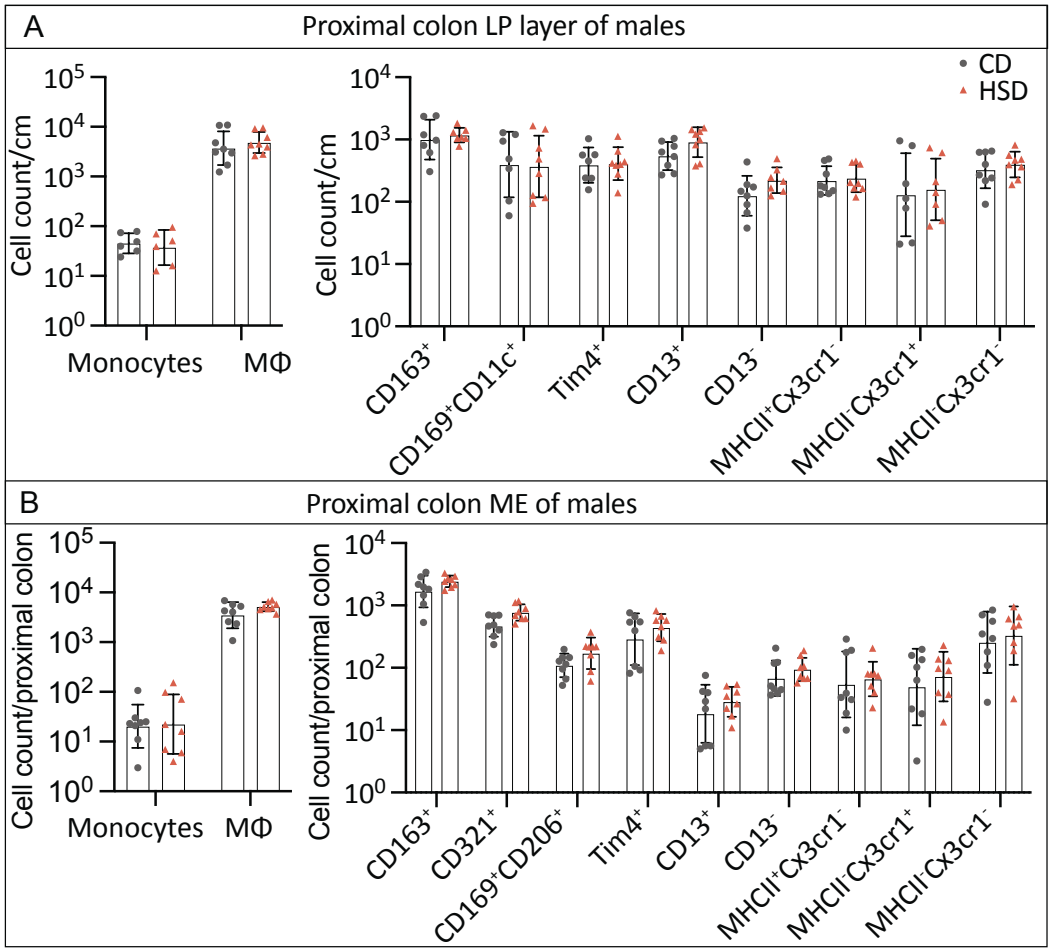

Figure 47 Cell count of proximal colon LP and ME Monocytes, total MΦ, and MΦ subpopulations in male mice upon long-term HSD. (A) Proximal colon LP cell counts upon long-term HSD; (B) proximal colon ME cell counts upon long-term HSD; n = 8 from 2 experiments; data points are log (10)-transformed, error bars represent SD, data was analyzed using two-way ANOVAs, *p-value < 0.05.

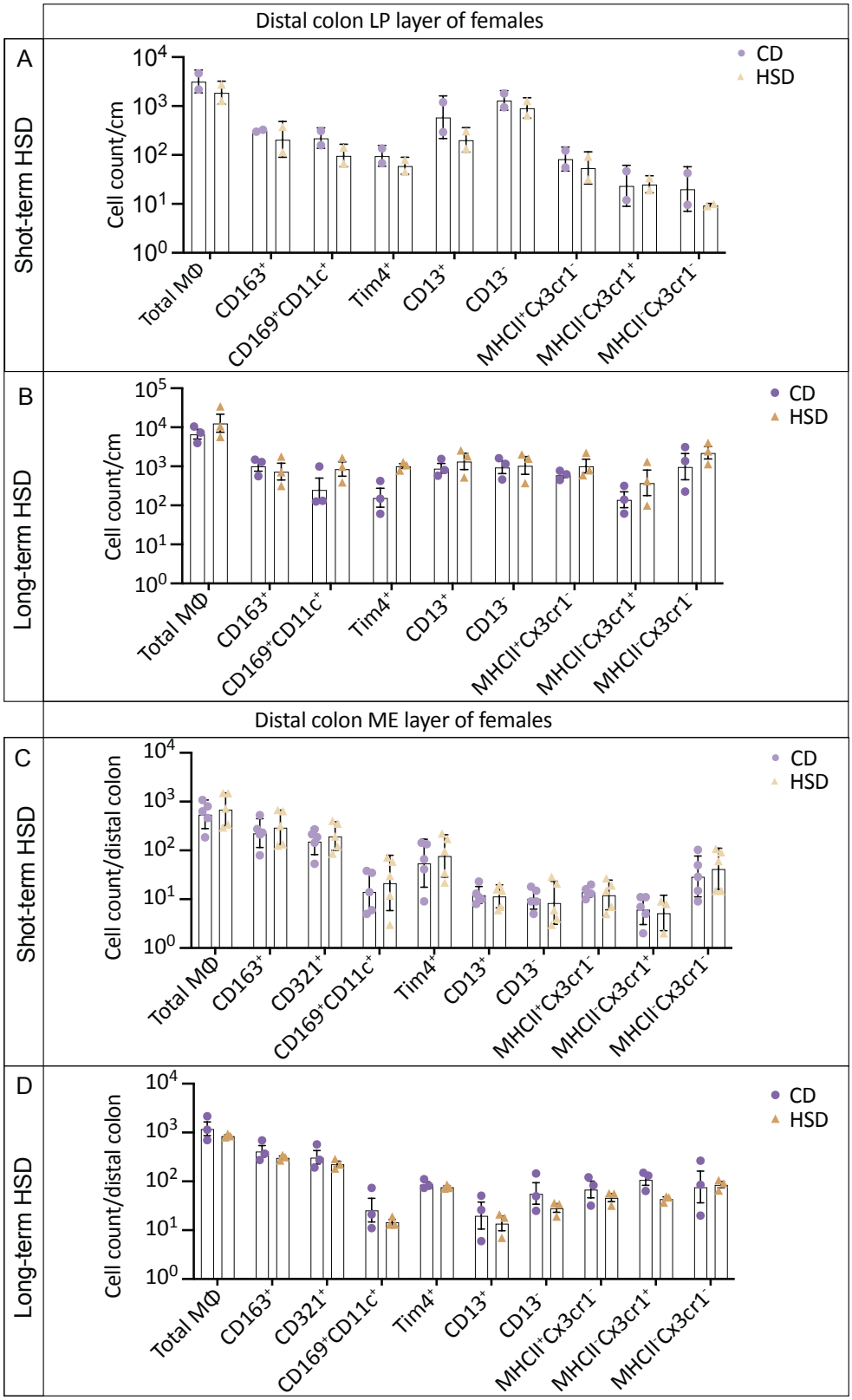

Figure 48 Cell count of distal colon LP and ME Monocytes, total MΦ, and MΦ subpopulations in female mice upon short- and long-term HSD. (A) Distal colon LP cell counts upon short-term HSD; (B) distal colon LP cell counts upon long-term HSD; (C) distal colon ME cell counts upon short-term HSD; (D) distal colon ME cell counts upon long-term HSD; n = 3-5, data points are log (10)-transformed, error bars represent SD, data was analyzed using two-way ANOVAs, *p-value < 0.05.

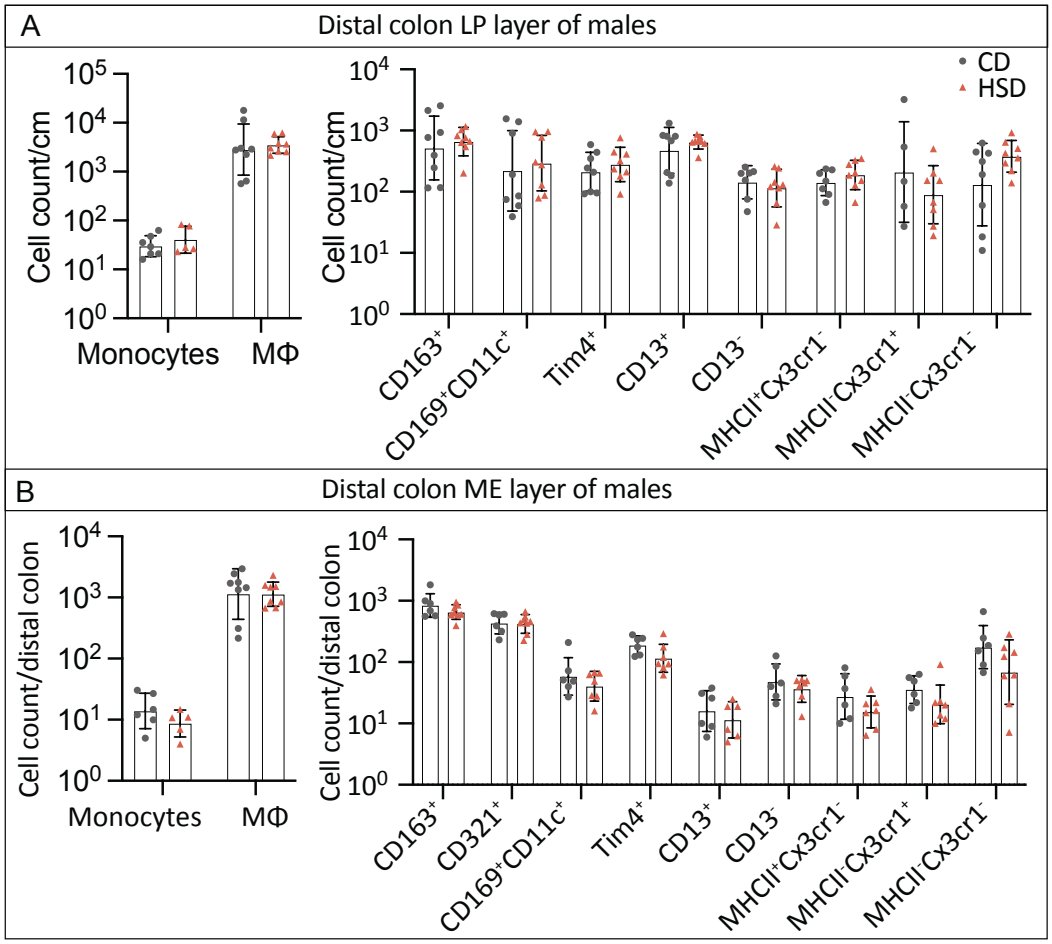

Figure 49 Cell count of distal colon LP and ME Monocytes, total MΦ, and MΦ subpopulations in male mice upon long-term HSD. (A) Distal colon LP cell counts upon long-term HSD; (B) distal colon ME cell counts upon long-term HSD; n = 5 from 2 experiments, data points are log (10)-transformed, error bars represent SD, data was analyzed using two-way ANOVAs, *p-value < 0.05.

3.5.3 Ontogeny Alterations of Gut MΦ and Their Subpopulations

The effect of HSD on gut and liver MΦ origin is still poorly studied. An innovative genetically modified mouse model provided the opportunity to investigate MΦ ontogeny upon HSD by using fluorescent reporters driven by lineage-specific promoters. This model is *Tnfrsf11a*$^{Cre/+}$; *Rosa26LSL*$^{-YFP/+}$; *Ms4a3*$^{FlpO/+}$; *Rosa26LFL*$^{-tdTomato/+}$ and is referred to as the double-fate mapping model (Introduction 1.3.3). In this model, *Tnfrsf11a*-expressing fetal-derived cells are labeled with a yellow fluorescent protein (YFP), and *Ms4a3*-expressing monocyte-derived cells with tdTomato. Monocyte-derived monocytes infiltrate tissues and differentiate into MΦ that become resident, gaining *Tnfrsf11a* expression. By this, they express tdTomato from the early stages and acquire YFP after transitioning into long-lived MΦ. This study investigated double fate mapper mice for their MΦ origin changes upon long-term HSD in the gut regions: stomach, duodenum, ileum, proximal and distal colon (Figure 50). Gut MΦ subsets were identified based on the shown gating strategy (Supplementary Figure 6).

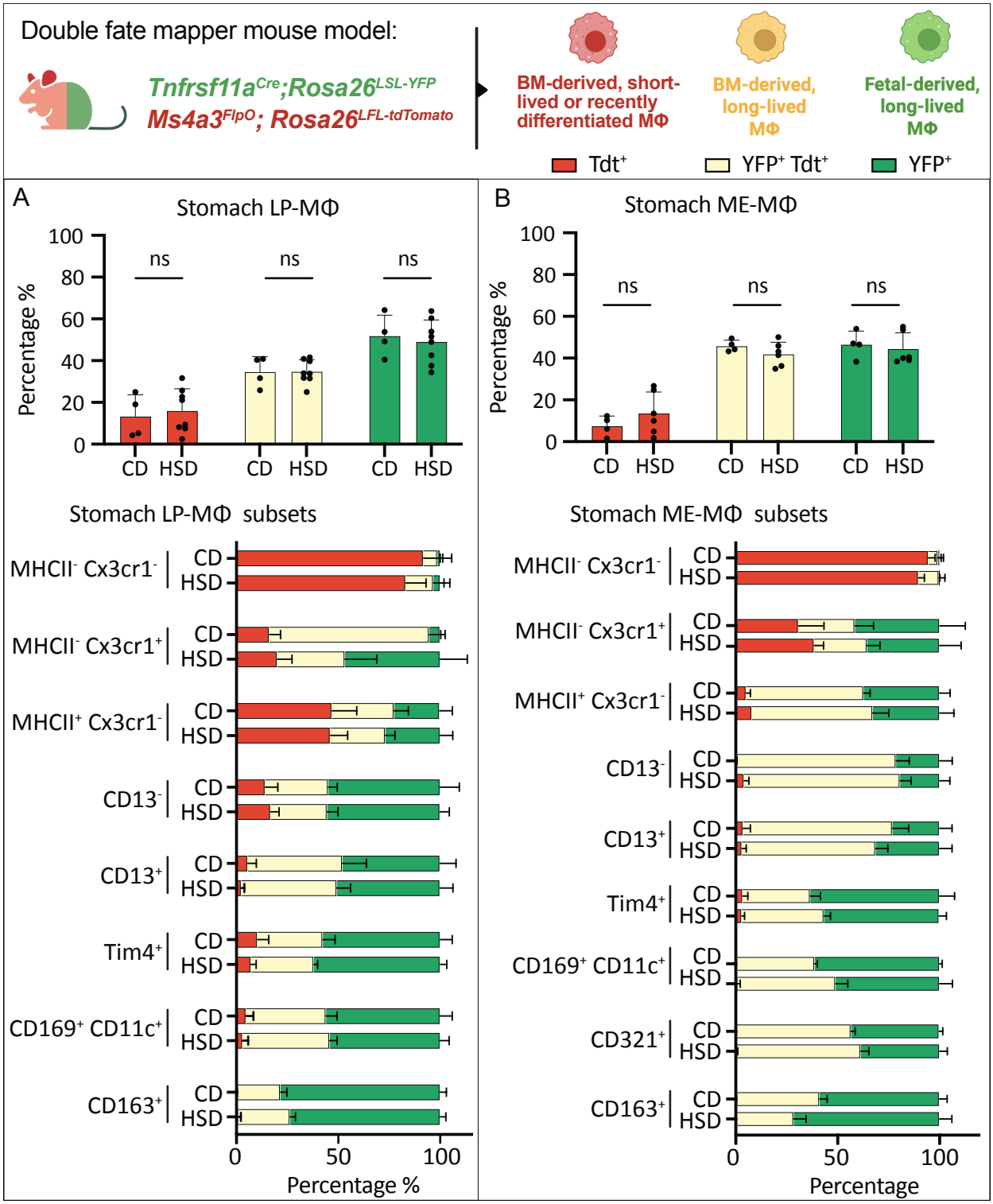

Figure 50 Quantification of monocyte-derived and fetal-derived stomach MΦ upon long-term HSD. The Tnfrsf11a^{Cre}; Rosa26$^{LSL-YFP}$; Ms4a3^{FlpO}; Rosa26$^{LFL-tdTomato}$ fate mapping model labels monocyte-derived cells with tdTomato (red) and fetal-derived cells with YFP (green). The tdTomato^{+} monocyte-derived cells acquire YFP labeling, when differentiating into long-lived tissue MΦ (yellow). Mice were fed CD or HSD for 3 months to achieve a long-term HSD. (A) Stomach LP layer MΦ Ontogeny changes; (B) stomach ME layer MΦ Ontogeny changes; n = 4-8, data was analyzed using two-way ANOVAs, *p-value < 0.05.

In male mice, stomach MΦ and their subsets in the LP and ME layers showed no changes in their origin upon long-term HSD (Figure 50A, B). Duodenum MΦ of LP showed an increase in the percentages of long-lived monocyte-derived MΦ specifically in $CD163^+$ MΦ while a decrease in fetal-derived MΦ like in $CD13^-$ (Figure 51A). Although total MΦ maintained their origin percentages in the duodenum ME layer, the MHCII-$Cx3cr1^-$ MΦ subset significantly increased their percentage of short-lived monocyte-derived cells compared to CD (Figure 51B).

In the ileum LP layer, long-term HSD showed a significant increase of long-lived monocyte-derived MΦ percentage at the expense of fetal-derived resident MΦ ($p = 0.033$) (Figure 52A). This ontogeny switch was significantly evident in the specific LP-MΦ subsets $CD169^+CD11c^+$, $Tim4^+$, $CD13^+$, $CD13^-$ and MHCII$^-$$Cx3cr1^+$ MΦ (Figure 52A). Long-term HSD weakly affected the ME-MΦ ontogeny of the ileum, showing no significant change in total MΦ (Figure 52B). However, $CD13^-$ ME-MΦ subset showed a significant increase of long-lived monocyte-derived MΦ percentage at the expense of fetal-derived resident MΦ (Figure 52B).

LP long-lived monocyte-derived MΦ in the proximal colon showed a slight increase in their percentage with HSD feeding, while in proximal colon ME layer, the rise in long-lived monocyte-derived (Figure 53B). Meanwhile, the percentages of fetal- and monocyte-derived MΦ in the distal colon ME layer did not change after HSD feeding (Figure 54A, B).

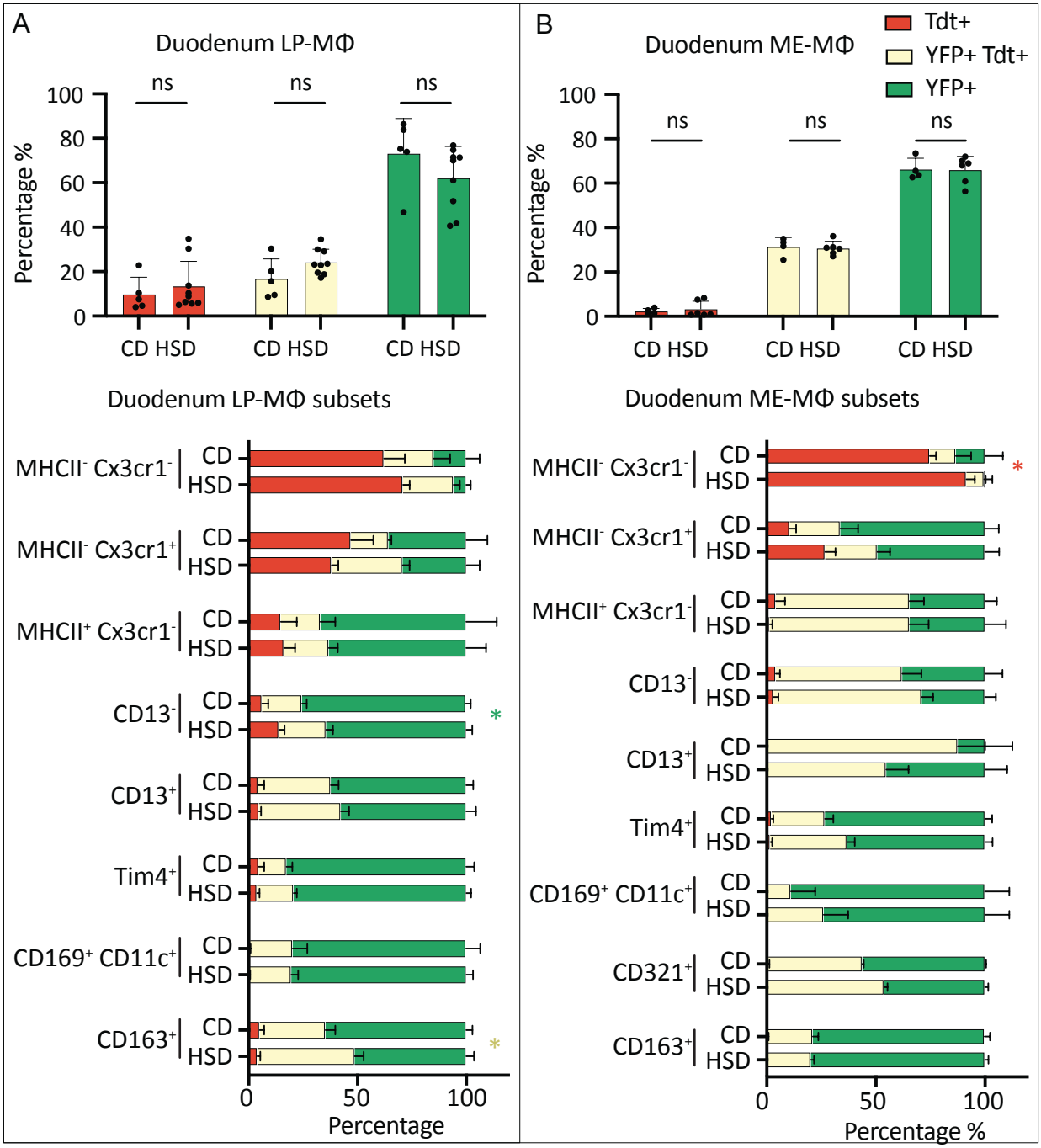

Figure 51 Quantification of monocyte-derived and fetal-derived duodenum MΦ upon long-term HSD in male mice. The *Tnfrsf11a*^{Cre}*; Rosa26*$^{LSL\text{-}YFP}$*; Ms4a3*^{FlpO}*; Rosa26*$^{LFL\text{-}tdTomato}$ fate mapping model labels monocyte-derived cells with tdTomato (red) and fetal-derived cells with YFP (green). The tdTomato^{+} monocyte-derived cells acquire YFP labeling when differentiating into long-lived tissue MΦ (yellow). Mice were fed CD or HSD for 3 months to achieve a long-term HSD. (A) Duodenum LP layer MΦ Ontogeny changes; (B) duodenum ME layer MΦ Ontogeny changes; n = 6-9, data was analyzed using two-way ANOVAs, **p*-value < 0.05.

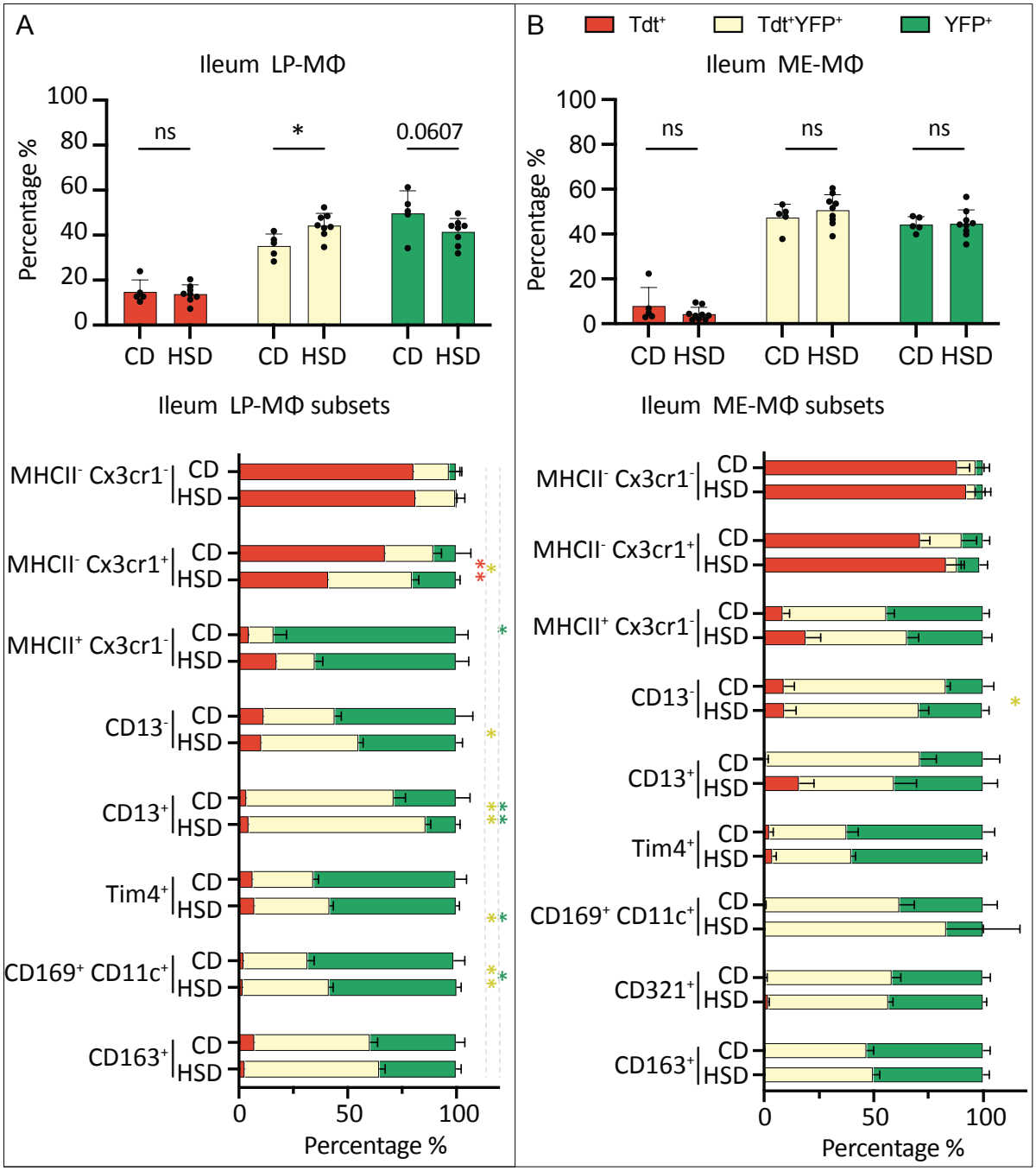

Figure 52 Quantification of monocyte-derived and fetal-derived ileal MΦ upon long-term HSD in male mice. The *Tnfrsf11a*^{Cre}*; Rosa26*$^{LSL\text{-}YFP}$*; Ms4a3*^{FlpO}*; Rosa26*$^{LFL\text{-}tdTomato}$ fate-mapping model labels monocyte-derived cells with lived monocyte-derived cells with tdTomato (red) and fetal-derived cells with YFP (green). The tdTomato^{+} monocyte-derived cells acquire YFP labeling, when differentiating into long-lived tissue MΦ (yellow). Mice were fed CD or HSD for 3 months to achieve a long-term HSD. (A) Ileal LP-MΦ ontogeny changes; (B) ileal ME-MΦ ontogeny changes; n = 5-8, data was analyzed using two-way ANOVAs, *p-value < 0.05, ** p-value < 0.01.

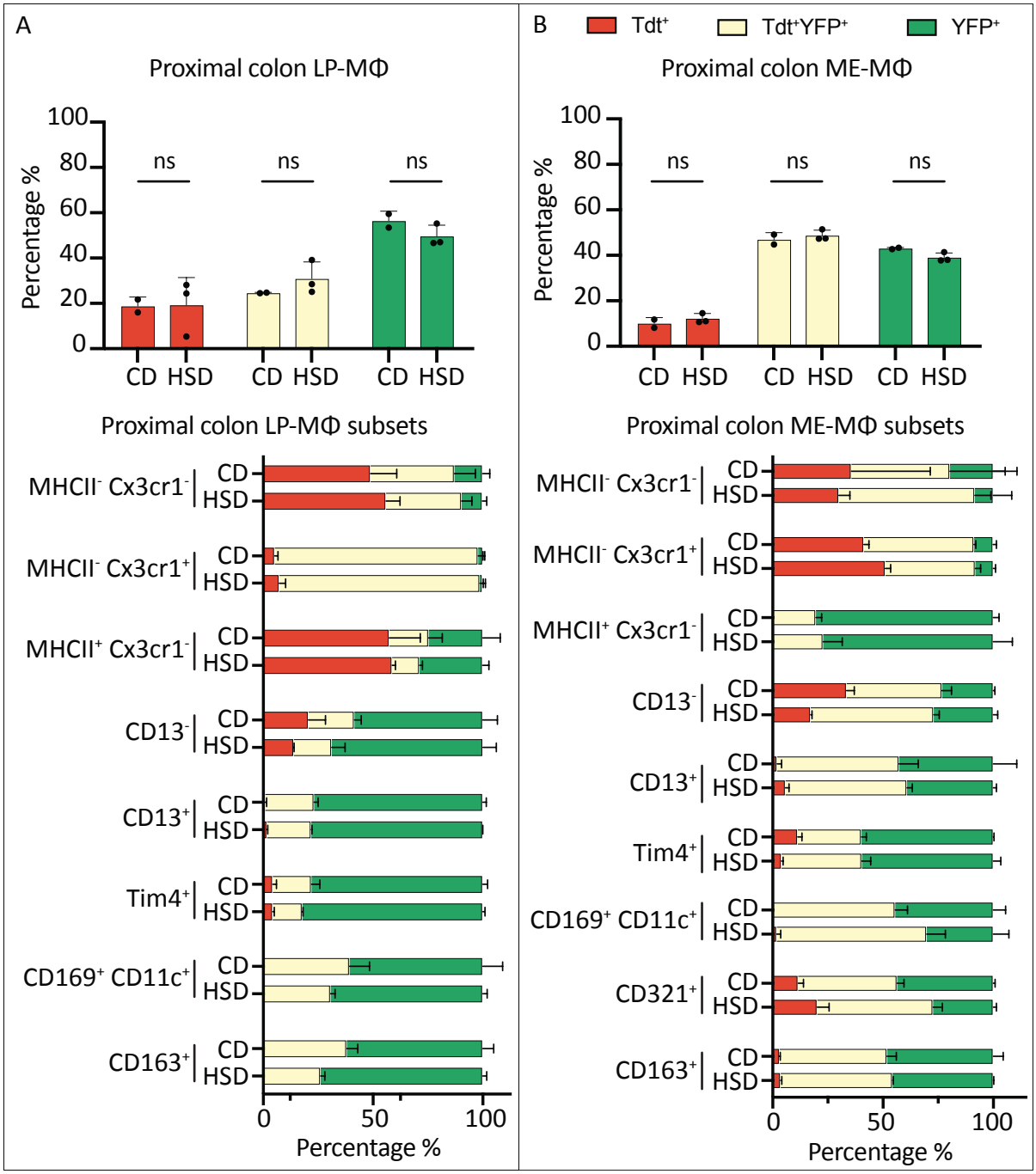

Figure 53 Quantification of monocyte-derived and fetal-derived LP-MΦ of proximal colon upon long-term HSD. The *Tnfrsf11a*^{Cre}*; Rosa26*$^{LSL\text{-}YFP}$*; Ms4a3*^{FlpO}*; Rosa26*$^{LFL\text{-}tdTomato}$ fate mapping model labels monocyte-derived cells with tdTomato (red) and fetal-derived cells with YFP (green). The tdTomato^{+} monocyte-derived cells acquire YFP labeling, when differentiating into long-lived tissue MΦ (yellow). Mice were fed CD or HSD for 3 months to achieve a long-term HSD. (A) Proximal colon LP-MΦ ontogeny changes; (B) proximal colon ME layer MΦ ontogeny changes; n =2-3, data was analyzed using two-way ANOVAs, **p*-value < 0.05.

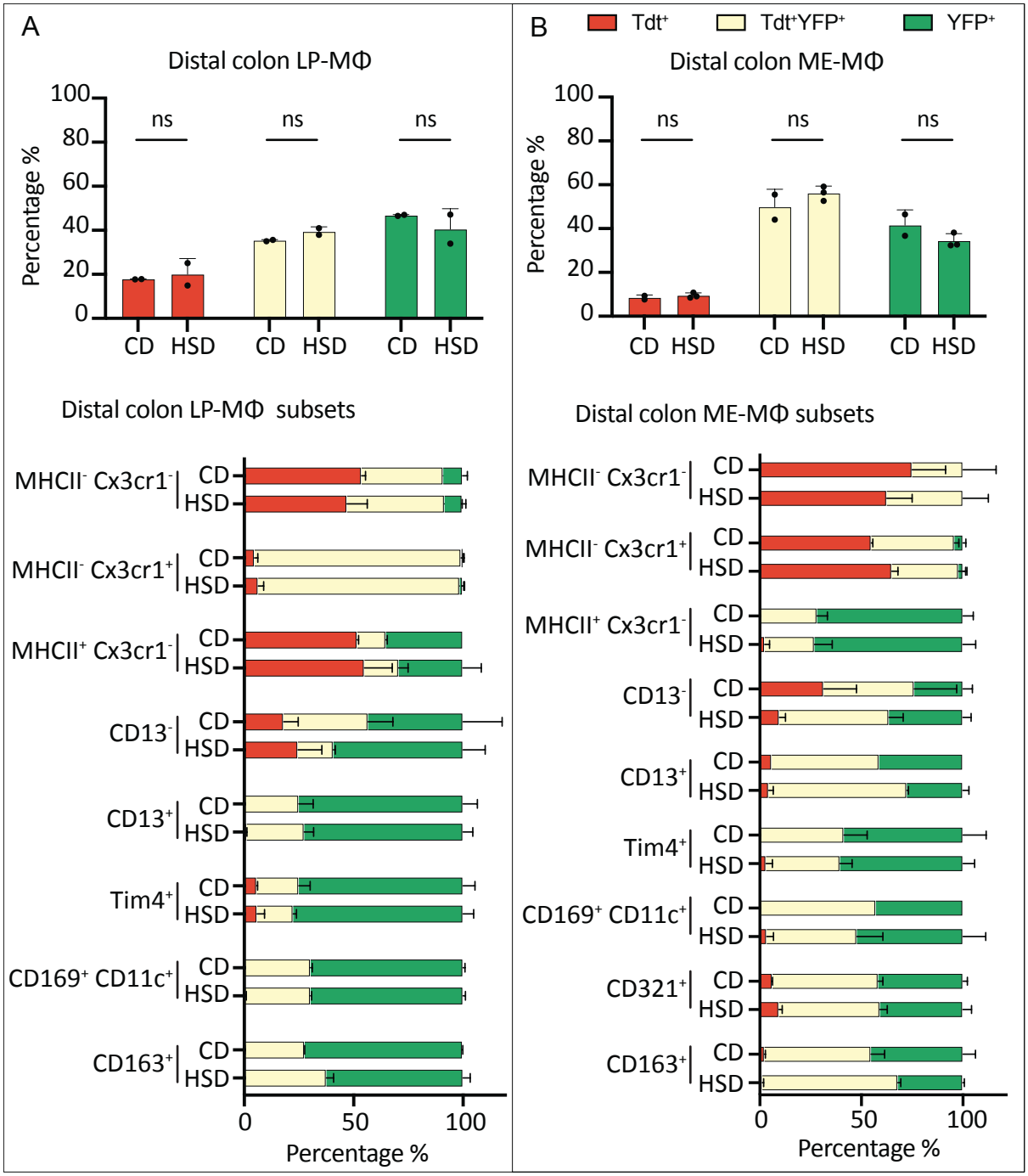

Figure 54 Quantification of monocyte-derived and fetal-derived LP-MΦ in distal colon upon long-term HSD. The *Tnfrsf11a*^{Cre}*; Rosa26*$^{LSL\text{-}YFP}$*; Ms4a3*^{FlpO}*; Rosa26*$^{LFL\text{-}tdTomato}$ fate mapping model labels monocyte-derived cells with tdTomato (red) and fetal-derived cells with YFP (green). The tdTomato^{+} monocyte-derived cells acquire YFP labeling, when differentiating into long-lived tissue MΦ (yellow). Mice were fed CD or HSD for 3 months to achieve a long-term HSD. (A) Distal colon LP-MΦ ontogeny changes; (B) distal colon ME-MΦ ontogeny changes; n =2, data was analyzed using two-way ANOVAs, **p*-value < 0.05.

Female mice were also analyzed for changes in gut MΦ ontogeny due to long-term HSD, focusing on the stomach, duodenum, and ileum. In these three gut regions, the percentages

of MΦ origins under HSD didn't show significant changes under HSD feeding (Figure 55). Despite missing a statistical significance, ileum long-lived monocyte-derived MΦ were slightly increased (Figure 55). In summary, long-term HSD significantly increased long-lived monocyte-derived MΦ percentage in the male ileum layers specifically in CD163^{+}, Tim4^{+}, and CD13^{+} MΦ subsets and, to a lesser extent, in other gut parts such as the duodenum and colon. This monocyte-derived cells expansion would reflect infiltration and differentiation of monocytes as introduced by the monocyte expansion upon HSD.

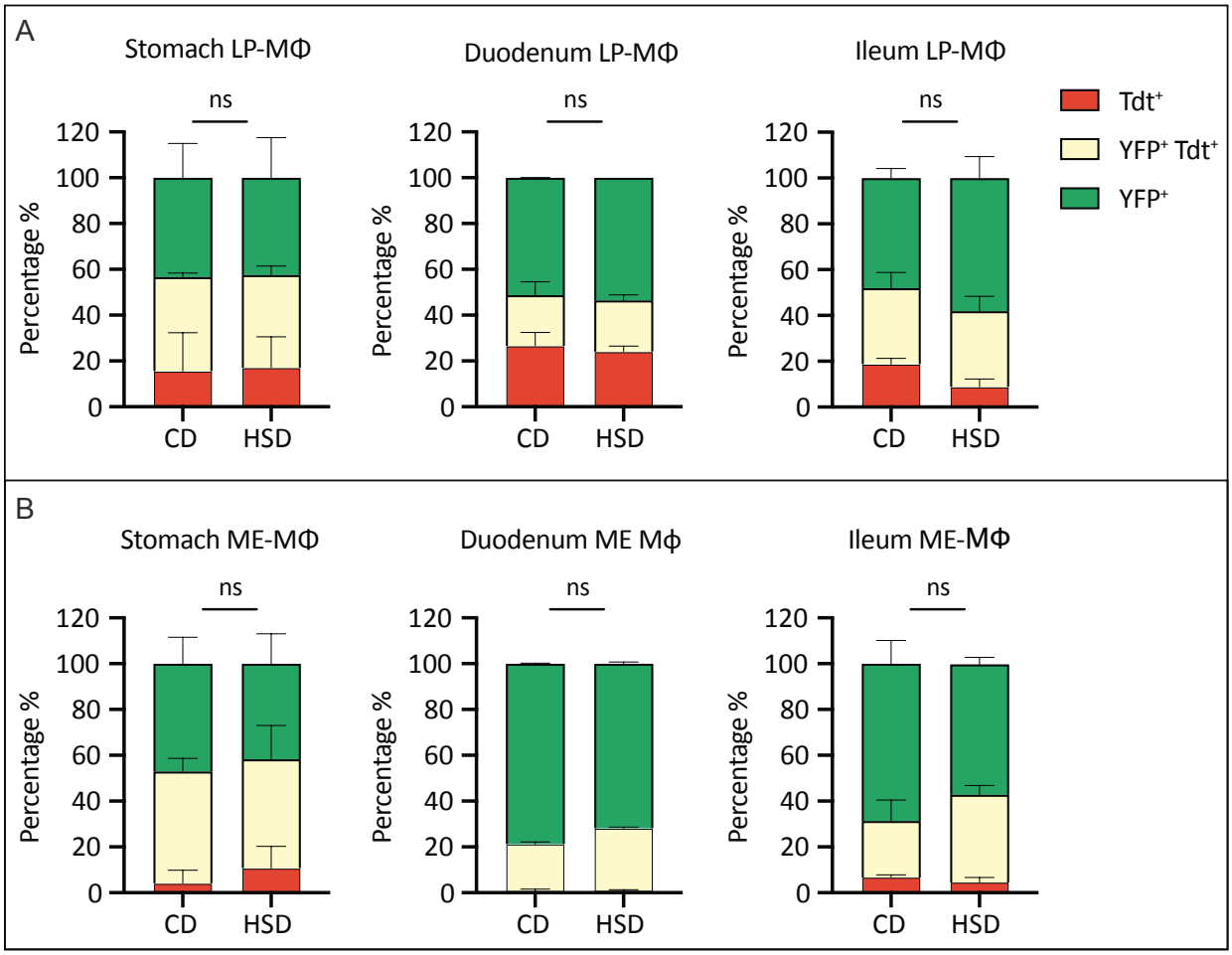

Figure 55 Quantification of monocyte-derived and fetal-derived gut MΦ upon long-term HSD in female mice. The *Tnfrsf11a^{Cre}; Rosa26$^{LSL-YFP}$; Ms4a3^{FlpO}; Rosa26$^{LFL-tdTomato}$* fate-mapping model labels monocyte-derived cells with tdTomato (red) and fetal-derived cells with YFP (green). The tdTomato^{+} monocyte-derived cells acquire YFP labeling when differentiating into long-lived tissue MΦ (yellow). Mice were fed CD or HSD for 3 months to achieve a long-term HSD. (A) Gut LP-MΦ ontogeny changes in stomach, duodenum, and ileum; (B) gut ME layer MΦ ontogeny changes in stomach, duodenum, and ileum; n = 2-5, data was analyzed using two-way ANOVAs, *p-value < 0.05.

3.6 Modulation of Ileum MΦ Phagocytosis and Efferocytosis Under High-Salt Diet

Based on the ileum SnRNA-seq results, MΦ FcγR and Mertk gene expression was altered in response to long-term HSD feeding, with FcγRIIb being overexpressed and FcγRIV downregulated compared to CD feeding. To validate the transcriptional findings, MΦ FcγRs and Mertk marker expression was analyzed upon short- and long-term HSD in the ileum of male mice. Flow cytometry enabled inspecting this phenotype by calculating the proteins' mean fluorescence intensity (MFI). Three subtypes of FcγRs were analyzed: the activating CD16.2 (FcγRI) and CD64 (FcγRIV), and the inhibitory CD32b (FcγRIIb).

3.6.1 FcγRs and Mertk Expression Under Long-Term High-Salt Diet

In the ileum LP layer, short-term HSD increased CD16.2 expression of the $MHCII^{-}Cx3cr1^{+}$ MΦ subset (p = 0.0013), and CD32b expression in the $CD13^{-}$ MΦ subset (p =0.0002) (Figure 56A, B). CD64 expression remained unchanged in all other MΦ subsets upon short-term HSD (Figure 56C). Following the 3-month long-term HSD, unaltered CD16.2 expression levels (Figure 57A). In contrast, CD32b increased in all the different MΦ subsets, significantly in $CD169^{+}CD11c^{+}$ (p = 0.0316) and $MHCII^{+}Cx3cr1^{-}$ MΦ (p = 0.0066) (Figure 57B). All MΦ subsets maintained their CD64 expression upon long-term HSD (Figure 57C). ME ileum layer showed the same trends of FcγRs expression upon HSD as in the LP layer (Supplementary Figure 7).

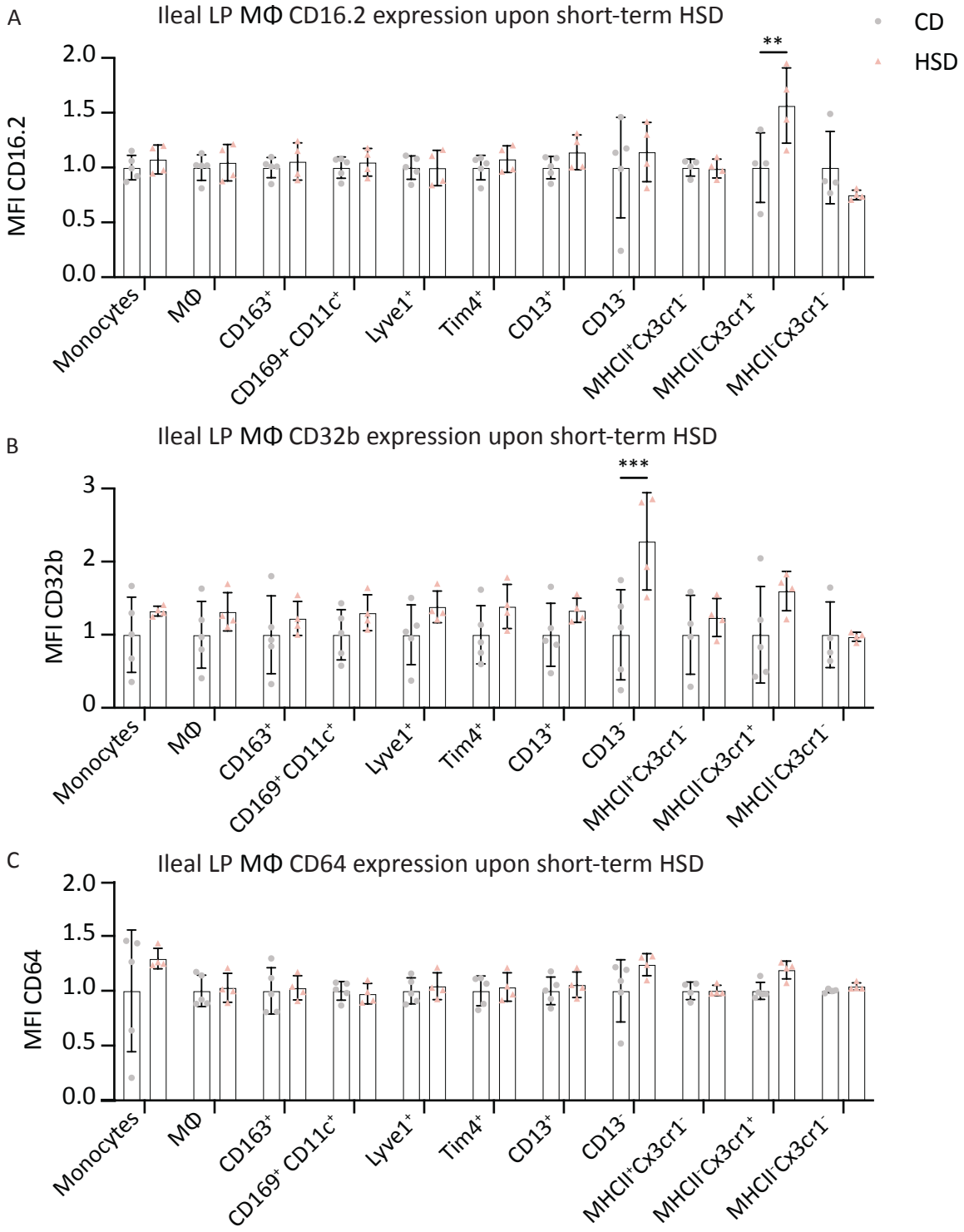

Figure 56 FcγRs expression changes in Ileum LP layer after short-term HSD. FcγRs expression is represented by normalized mean fluorescence intensity (MFI) of FcγRs (CD16.2, CD32b, CD64) in ileum MΦ subsets upon short-term HSD. Mice were fed CD or HSD for 3 months to achieve a long-term HSD. (A) CD16 MFI; (B) CD32b MFI; (C) CD64 MFI; n = 4; data was analyzed using two-way ANOVAs, *p-value < 0.05, ** p-value < 0.01, *** p-value < 0.001.

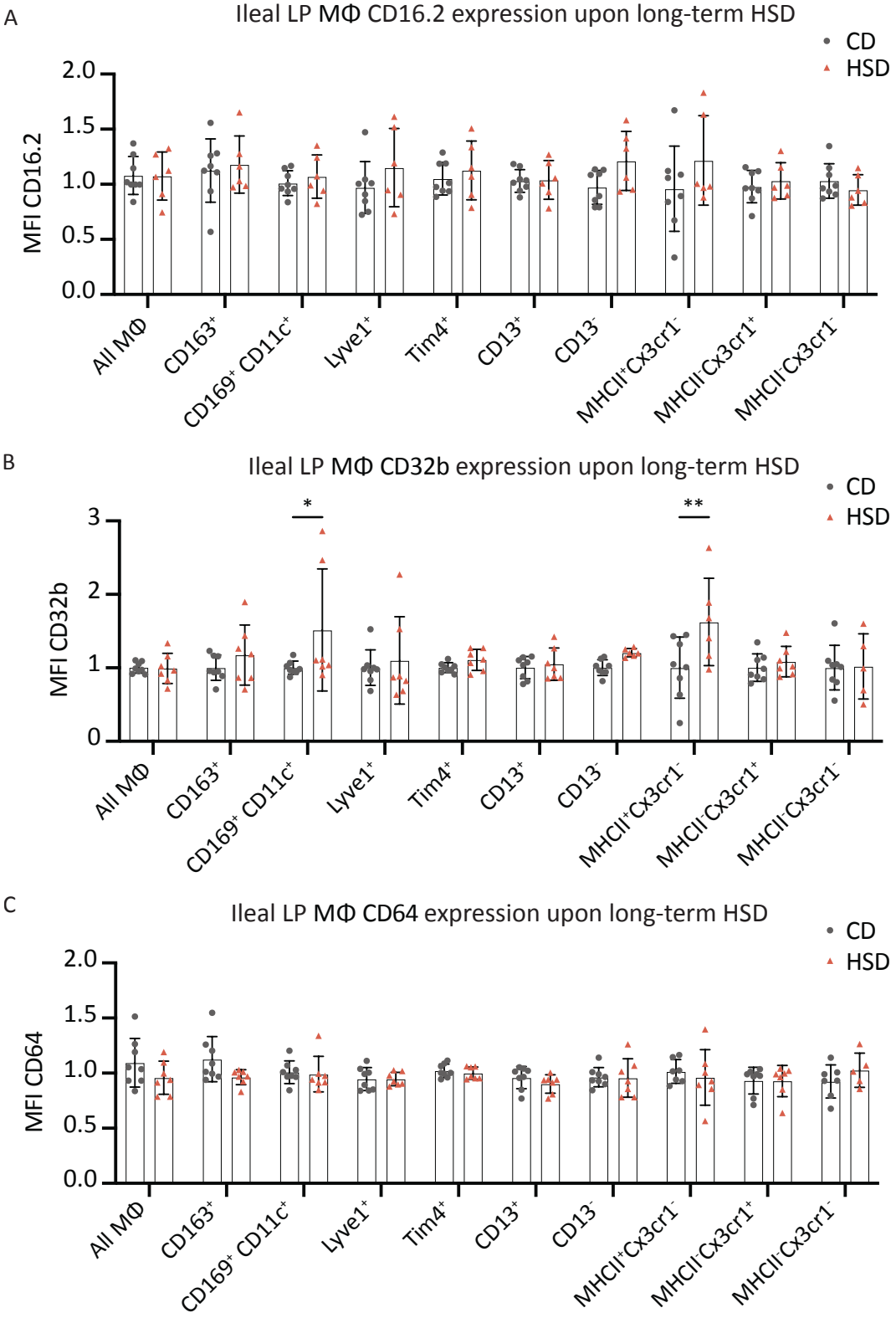

Figure 57 Mean Fluorescence intensity (MFI) of FcγRs in the gut MΦ subsets upon long-term HSD. (A) CD16 MFI; (B) CD32b MFI; (C) CD64 MFI; n = 5; data was analyzed using two-way ANOVAs, *p-value < 0.05, ** p-value < 0.01.

MertK expression in total LP MΦ and their subsets in the ileum remained unchanged after short-term high-salt diet (HSD), except in the MHCII^{+}Cx3cr1^{-} subset, where MertK expression

was significantly increased compared to CD (p = 0.024) (Figure 58A). Following long-term HSD, total LP MΦ Mertk expression remained unchanged but some MΦ subsets like MHCII$^-$Cx3cr1$^+$ increased Mertk expression (Figure 58B). In summary, short-term HSD feeding mildly increased Mertk, CD16.2, and CD32b protein expression in certain ileum MΦ subsets, and over long-term HSD feeding the CD32b and Mertk overexpression was still observed, although in different MΦ subsets.

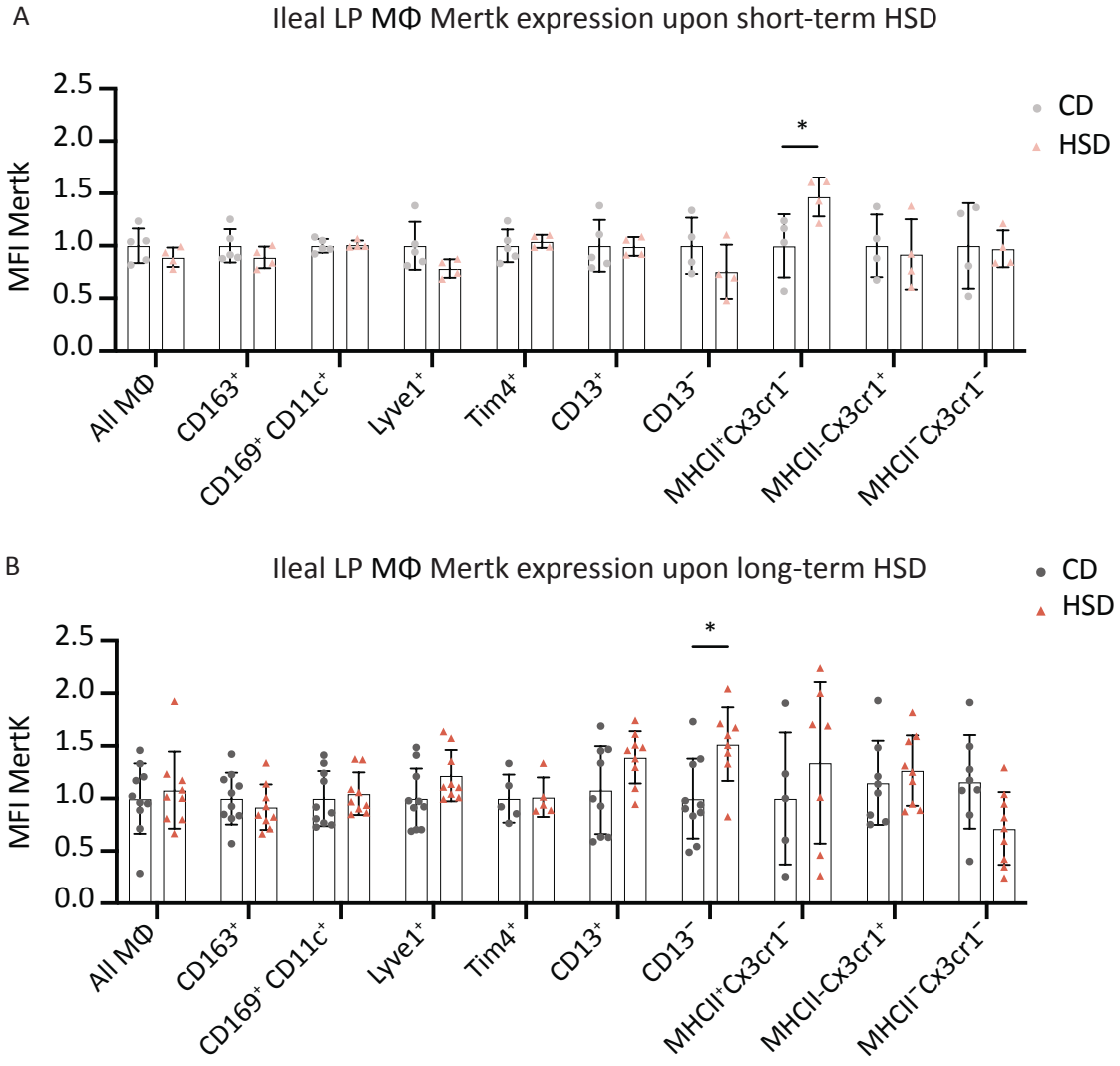

Figure 58 Mean Fluorescence intensity (MFI) of Mertk in the gut MΦ subsets upon (A) long-term HSD; (B) long-term HSD; n = 3-5; data was analyzed using two-way ANOVAs, *p-value < 0.05.

3.6.2 Evaluating Ileum MΦ FcγR-Dependent Phagocytosis *Ex-vivo*

The altered FcγRs are key regulators of MΦ phagocytosis– one of the main MΦ functions. The significant increase in CD32b gene and protein expression in specific ileal MΦ subpopulations brought the need to investigate MΦ FcγR-dependent phagocytosis function upon long-term HSD. To follow the phagocytosis functionality upon long-term HSD feeding, ileum MΦ were isolated after 3 months of the HSD intake and cultured with stained live *Citrobacter rodentium*

bacteria (*C. rodentium)* for 1 hour, and phagocytosis was assessed by measuring *C. rodentium*$^{+}$ MΦ and the MFI of *C. rodentium* signal (Figure 59A), in MΦ and their subsets that were identified as shown in the gating strategy (Supplementary Figure 8).

Results showed that HSD feeding increased total ileum MΦ phagocytosis of *C. rodentium* prominently in Lyve1^{+} and CD13^{+} subsets (p = 0.0422 and 0.0305, respectively). Phagocytic index (calculated by multiplying *C. rodentium*$^{+}$ MΦ percentage with *C. rodentium* MFI) supported this result where Lyve1^{+} and CD13^{+} MΦ subsets showed increased phagocytosis index upon long-term HSD intake (p = 0.0026 and 0.0065, respectively; Figure 59B). Altogether, long-term HSD induced ileal MΦ phagocytosis in selective subpopulations namely in Lyve1^{+} and CD13^{+} MΦ mostly by impacting FcγRIIb expression.

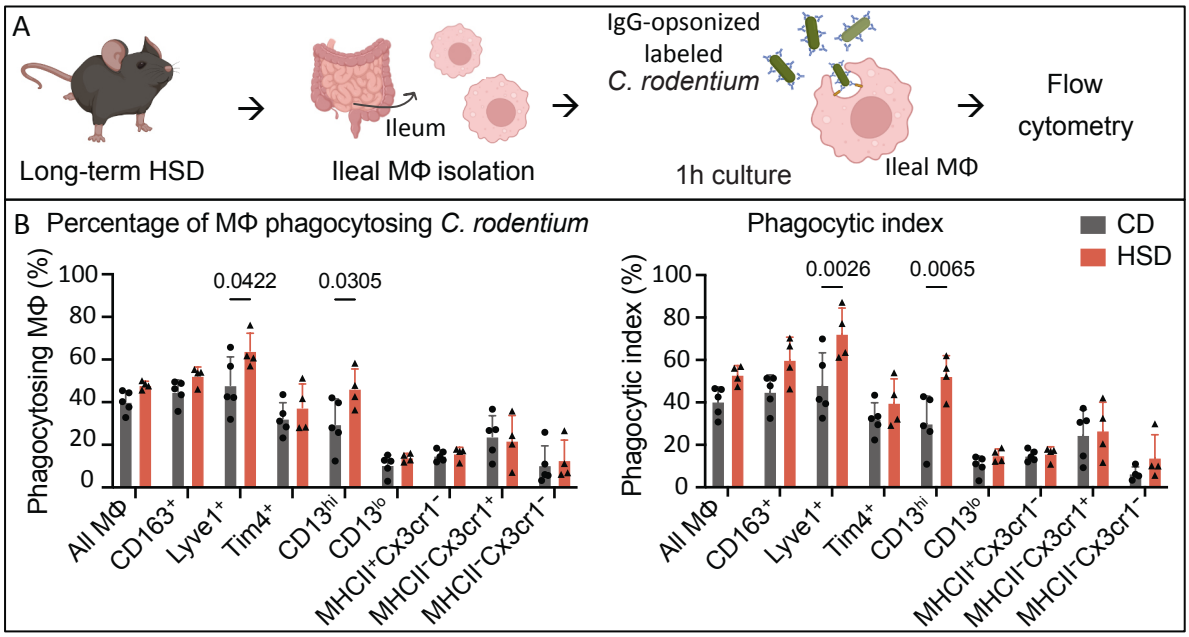

Figure 59 Assessment of ileum MΦ phagocytosis capacity *ex-vivo* upon long-term HSD. Male mice were fed CD or HSD for 3 months, and then liver MΦ were isolated, cultured with stained *C. rodentium* for 1h in a ratio 1 MΦ to 160 CFUs, then stained with MΦ markers for Flow cytometry analysis; n = 5, p-values were obtained using 2-way ANOVA; CFUs: colony forming units.

3.7 Influence of High-Salt Diet on Liver MΦ Volume, Dynamics, and Ontogeny

3.7.1 Liver MΦ Cell Volume Changes

As explained in the introduction and section 2.3, ion homeostasis plays a crucial role in MΦ cell volume regulation, which is essential for MΦ function. To investigate the effects of long-term HSD on liver MΦ cell volume, liver sections from long-term HSD-fed mice were stained with Iba-1 to fluorescently label MΦ. A 3D rendering analysis of liver MΦ was performed using the MotiQ plugin in FIJI. Cell volume and cell surface were unchanged upon short-term HSD compared to CD. However, the number of branches was significantly increased upon short-term HSD (p = 0.0041) (Figure 60A). MΦ from long-term HSD-fed mice exhibited a significant

increase in cell volume and surface area compared to those from CD-fed mice, as shown in the images (p = 0.0003 and 0.0001, respectively; Figure 60B). Additionally, cell branches also still increased after long-term HSD (p = 0.0012) (Figure 60B). These findings revealed that long-term HSD significantly increases MΦ cell volume, surface, and branching, potentially linked to the HSD-responsive chloride-sensing pathways and suggesting subsequent impacts on MΦ functionality.

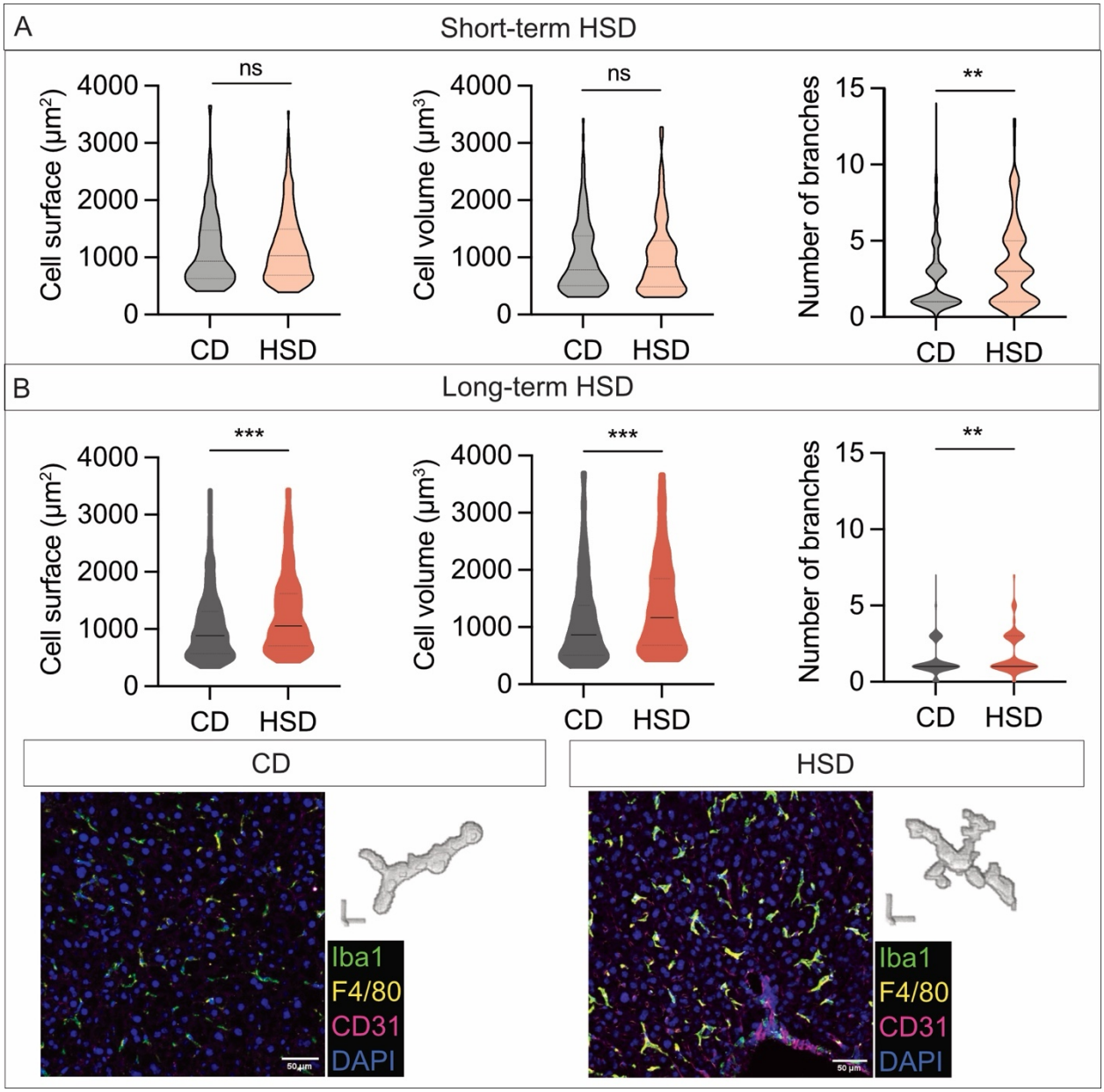

Figure 60 3D-rendering of liver MΦ showing cell surface, cell volume, and number of branches in HSD-fed male mice. Liver sections were stained with DAPI and Iba-1, imaged, and analyzed by MotiQ plugin in FIJI. (A) MΦ morphological changes upon Short-term HSD; (B) MΦ morphological changes upon long-term HSD, below: representative images of long-term CD and HSD liver MΦ. 3D measurements were obtained from approximately 150 MΦ from 2 mice/ diet. *P*-values were obtained using t-tests, *p-value < 0.05, **p-value < 0.01, ***p-value < 0.001.

3.7.2 Liver MΦ Heterogeneity and Cell Count Changes Following High-Salt Diet

Liver MΦ are divided into Kupffer cells (KCs) and monocyte-derived MΦ (MoMΦ) which differ by their origin and can be distinguished by their differential marker expression. KCs are CD11b^{lo} and F4/80^{hi}, Tim4^{+}and Vsig4^{+} and are, while MoMΦ are CD11b^{+} F4/80$^{int\ (intermediate)}$ Cx3cr1^{+} and Ly6C^{+}. KCs are the predominant MΦ in healthy liver and mostly originate from yolk sac-derived erythromyeloid progenitors (EMPs). MoMΦ can be split into two main populations Ly6C^{hi} and Ly6C^{lo} MoMΦs. A remarkable subset of MoMΦ that reside liver capsule in a steady state is Liver capsule MΦ (LCMs) which are CD11b^{+} F4/80^{+} MHCII^{+} but Tim4^{-} Ly6C^{-}. Using flow cytometry, KCs and MoMΦ, including Cx3cr1^{+}MHCII^{-} and Cx3cr1^{+}MHCII^{+} MoMΦ were identified (Supplementary Figure 9). Cell counts of MΦ and other myeloid cell populations were assessed following either short- or long-term HSD feeding in both sexes of mice. The investigated myeloid populations, aside from MΦ, included monocytes, neutrophils, and conventional dendritic cells 1 and 2.

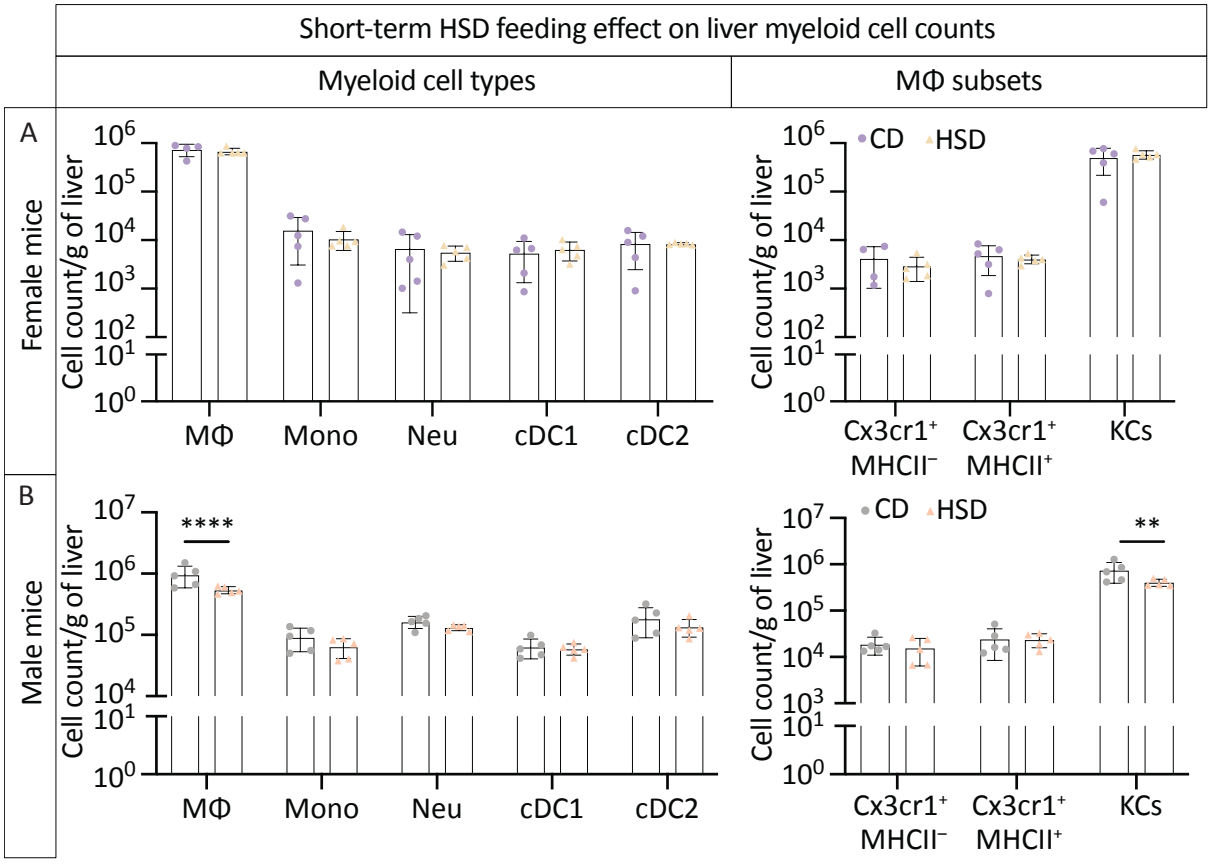

Figure 61 Liver myeloid cell counts upon short-term HSD in (A) female mice and (B) male mice; Mice were fed either CD or HSD for 3 weeks to achieve short-term HSD model; N = 5, *p*-values were obtained using two-way ANOVA, *p-value < 0.05, **p-value < 0.01, ***p-value < 0.001, ****p-value < 0.0001. KCs: Kupffer cells, MΦ: macrophages; Mono: Monocytes; Neu: Neutrophils; cDC: classical dendritic cells.

Short-term HSD feeding in female mice did not affect liver myeloid cell counts, including MΦ subsets, compared to CD (Figure 61A). In contrast, male liver total MΦ counts significantly decreased compared to CD-fed mice ($p < 0.0001$), which was evident in the significantly decreased KCs counts ($p = 0.0042$) (Figure 61B). Long-term HSD feeding in female mice significantly decreased liver MΦ counts ($p < 0.0001$), specifically in Kupffer cells (KCs, $p < 0.0001$), while CX3CR1^{+}MHC-II^{-} and CX3CR1^{+}MHCII^{+} MΦ, as well as other myeloid cells, remained unchanged compared to CD-fed controls (Figure 62A). In contrast, male mice exhibited an increased MΦ count ($p = 0.0357$), possibly driven by a minor expansion of the KCs numbers that failed to reach a statistical significance ($p = 0.083$), whereas KCs numbers were unaffected. Other myeloid cell populations remained unchanged following long-term HSD feeding (Figure 62B). Altogether, short-term HSD led to an increase in total liver macrophage numbers in males but not in females. This effect was less pronounced after long-term HSD; however, long-term HSD significantly reduced macrophage numbers in females.

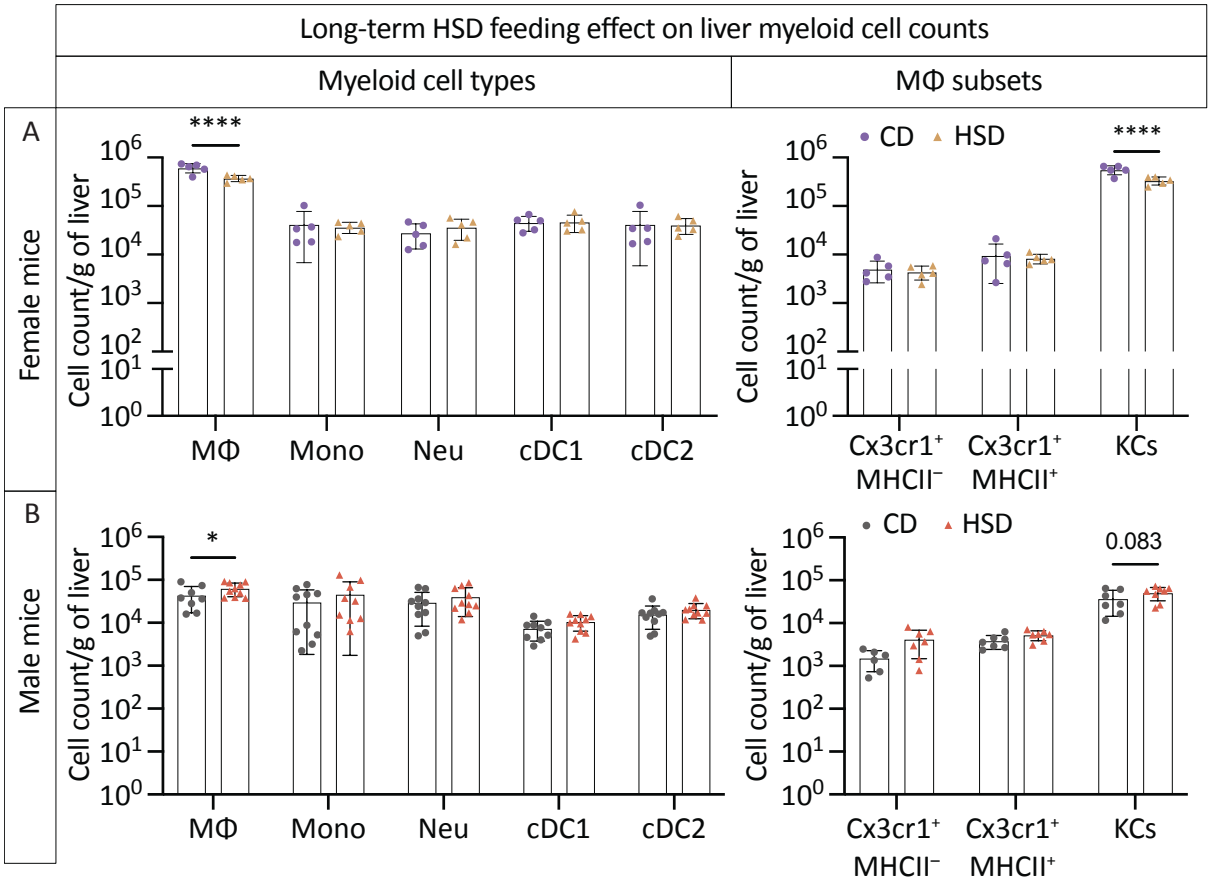

Figure 62 Liver myeloid cell counts upon long-term HSD. Mice were fed either CD or HSD for 3 months to achieve a long-term HSD model; (A) female mice (n = 5) and (B) male mice (n = 10); , *p*-values were obtained using two-way ANOVA, *p-value < 0.05, **p-value < 0.01, ***p-value < 0.001, ****p-value < 0.0001. The Y-axis is log^{10}-transformed. KCs: Kupffer cells, MΦ: macrophages; Mono: Monocytes; Neu: Neutrophils; cDC: classical dendritic cells.

3.7.3 Ontogenic Alterations of Liver MΦ Following High-Salt Diet

Kupffer cells originate from the yolk sac while the LCMs and NAMs originate from the bone marrow. Using the aforementioned mouse double fate mapper mouse model, the origin of liver MΦ and their subsets in both sexes was explored upon long-term HSD feeding. Liver MΦ subsets were identified as shown in the gating strategy (Supplementary Figure 10). Monocytes were also analyzed to prove the model's reliability, where they harbored around 90% of Tdt^+ monocyte-derived cells in male mice and 80% in females, and the rest 10% were Tdt^+ YFP^+ monocyte-derived cells that could be early differentiating monocytes to MΦ (Figure 63A, B, Monocytes CD).

Kupffer cells of female mice constituted around 95% of the fetal-derived MΦ and less than 5% of long-lived monocyte-derived MΦ (Figure 63A). In males, fetal-derived MΦ percentage made up 85%, and the long-lived monocyte-derived MΦ reached around 15% of Kupffer cells, indicating higher long-lived monocyte-derived MΦ in the males than in females (Figure 63B). Liver $Cx3cr1^+MHCII^-$ MΦ of females constituted around 20% of each fetal-derived and long-lived monocyte-derived MΦ and 60% of short-lived monocyte-derived MΦ (Figure 63A). In males, they comprised 40% of fetal-derived MΦ, 20% long-lived, and 40% short-lived MΦ (Figure 63B). Meanwhile, $Cx3cr1^+MHCII^+$ MΦ of females constituted around 65% of fetal-derived MΦ, 10% of long-lived monocyte-derived MΦ, and 25% of short-lived monocyte-derived MΦ (Figure 63A). In males, they comprised 45% of fetal-derived MΦ, 35% long-lived, and 20% short-lived MΦ (Figure 63B). Following long-term HSD, Kupffer cells in both male and female mice retained their origin, similar to long-term CD-fed mice (Figure 63A, B). In contrast, within the $CX3CR1^+MHCII^-$ subset, the proportion of short-lived monocyte-derived MΦ significantly increased at the expense of fetal-derived cells in both sexes (Figure 63A, B). Moreover, long-term HSD did not significantly alter the origin of the $CX3CR1^+MHCII^+$ subset in either sex, although an insignificant increase in short-lived monocyte-derived MΦ was observed in females compared to long-term CD (Figure 63A). In summary, among liver MΦ, the $CX3CR1^+MHCII^-$ subset primarily responded to long-term HSD by showing an increased proportion of short-lived monocyte-derived cells at the expense of fetal-derived MΦ.

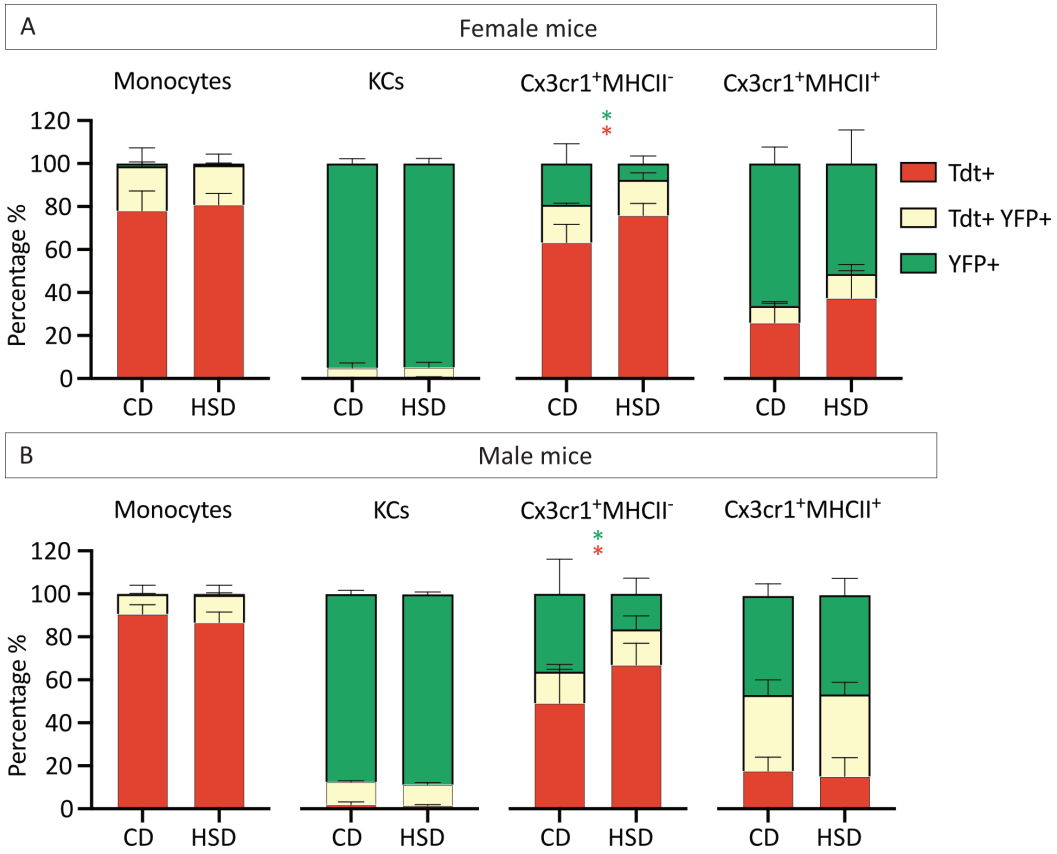

Figure 63 Ontogeny of liver MΦ subsets upon long-term HSD. The *Tnfrsf11a*^{Cre}; *Rosa26*$^{LSL\text{-}YFP}$; *Ms4a3*^{FlpO}; *Rosa26*$^{LFL\text{-}tdTomato}$ fate-mapping model labels monocyte-derived cells with tdTomato (red) and fetal-derived cells with YFP (green). The tdTomato^{+} monocyte-derived cells acquire YFP labeling when differentiating into long-lived tissue MΦ (yellow). Mice of both sexes were fed CD or HSD for 3 months to achieve a long-term HSD. (A) male mice, and (B) female mice; n = 4-6, data was analyzed using two-way ANOVAs, *p-value < 0.05.

3.8 Modulation of Liver MΦ Phagocytosis and Efferocytosis Under High-Salt Diet

3.8.1 FcγRs and Mertk Expression under Long-Term High-Salt Diet

As FcγRs and Mertk expression were altered in certain ileum MΦ subsets following HSD, their expression was also examined in liver MΦ by measuring mean fluorescence intensity (MFI) to assess whether they exhibited a similar response. Following short-term HSD, female mice showed a reduced CD16.2 marker expression in liver CX3CR1^{+}MHC-II^{+} MΦ (p =0.022), while CD32b and Mertk expression was unchanged (Figure 64A, C, E). On the other hand, male mice showed unchanged expression of CD16.2 and CD32b upon short-term HSD (Figure 64B, D). However, liver MΦ —particularly KCs—exhibited elevated Mertk expression compared to CD-fed controls (p = 0.042 for total MΦ and 0.0204 for KCs), whereas other MΦ subsets maintained baseline expression levels (Figure 64F).

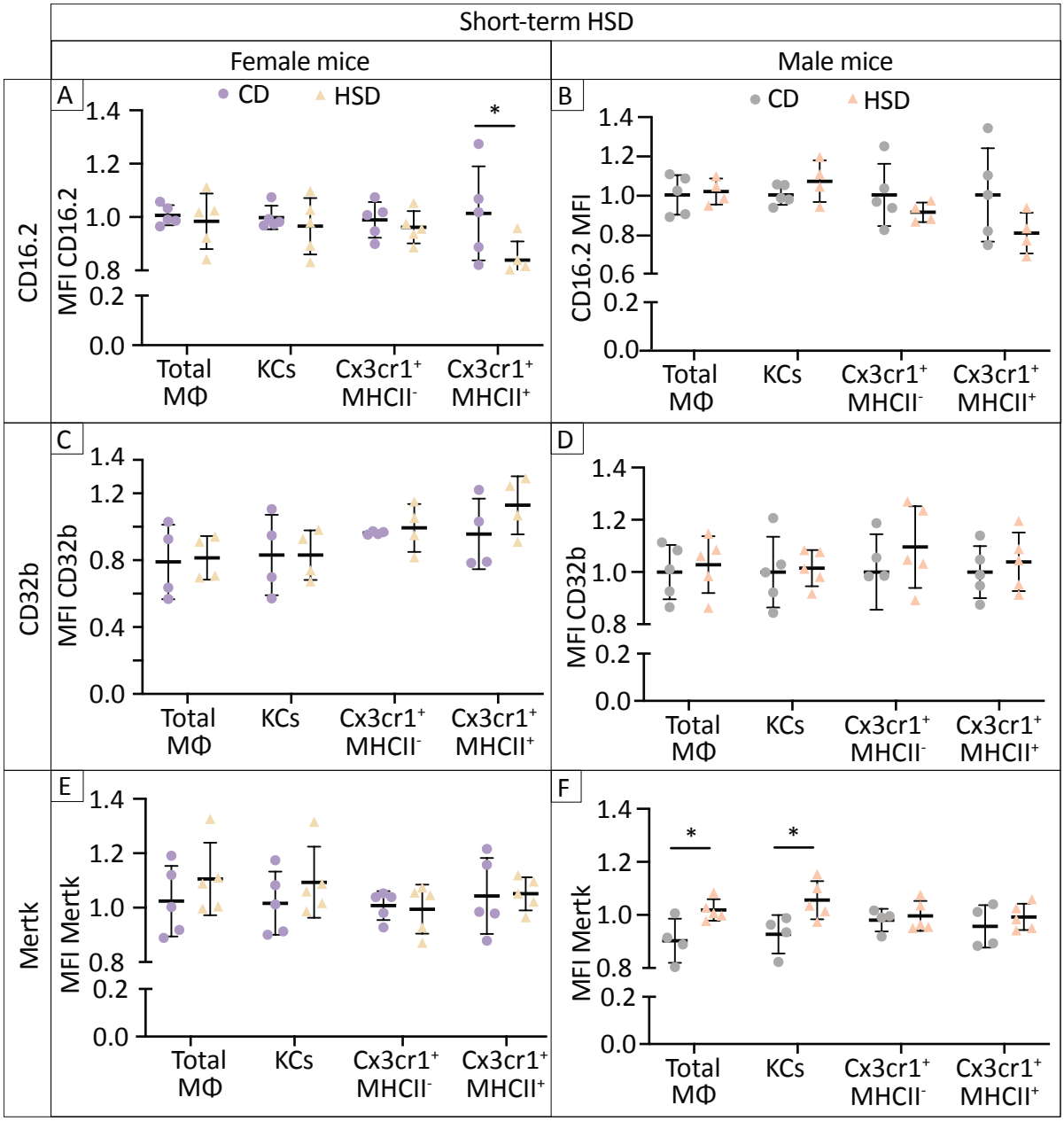

Figure 64 FcγRs and Mertk expression in Liver MΦ subsets upon short-term HSD. Mice of both sexes were fed either CD or HSD for 3 weeks to achieve short-term HSD model A, B) CD16.2 MFI changes in (A) female, and (B) male mice. (C, D) CD32b.2 MFI changes in (A) female, and (B) male mice. (E, F) Mertk MFI changes in (A) female, and (B) male; n = 5, data was analyzed using two-way ANOVAs, *p-value < 0.05.

Following long-term HSD, liver MΦ maintained their CD16.2 expression levels similar to those of CD-fed mice, while CD32b expression was significantly elevated in liver MΦ (p = 0.013), especially in KCs (p = 0.034) (Figure 65). Notably, the efferocytosis receptor Mertk was still significantly overexpressed in liver MΦ even after long-term HSD (p = 0.028), a trend confined to only KCs (p = 0.044), while other MΦ subsets maintained comparable Mertk MFI levels to CD-fed mice (Figure 65). Marker expression changes of liver MΦ in females upon long-term HSD were not investigated in this study. In summary, short-term HSD reduced CD16.2

expression in female animals, while it increased MertK expression in males—a change that persisted under long-term HSD alongside elevated CD32b expression. These findings suggest that HSD may modulate FcγR–dependent MΦ functions such as phagocytosis, as well as MertK-mediated efferocytosis.

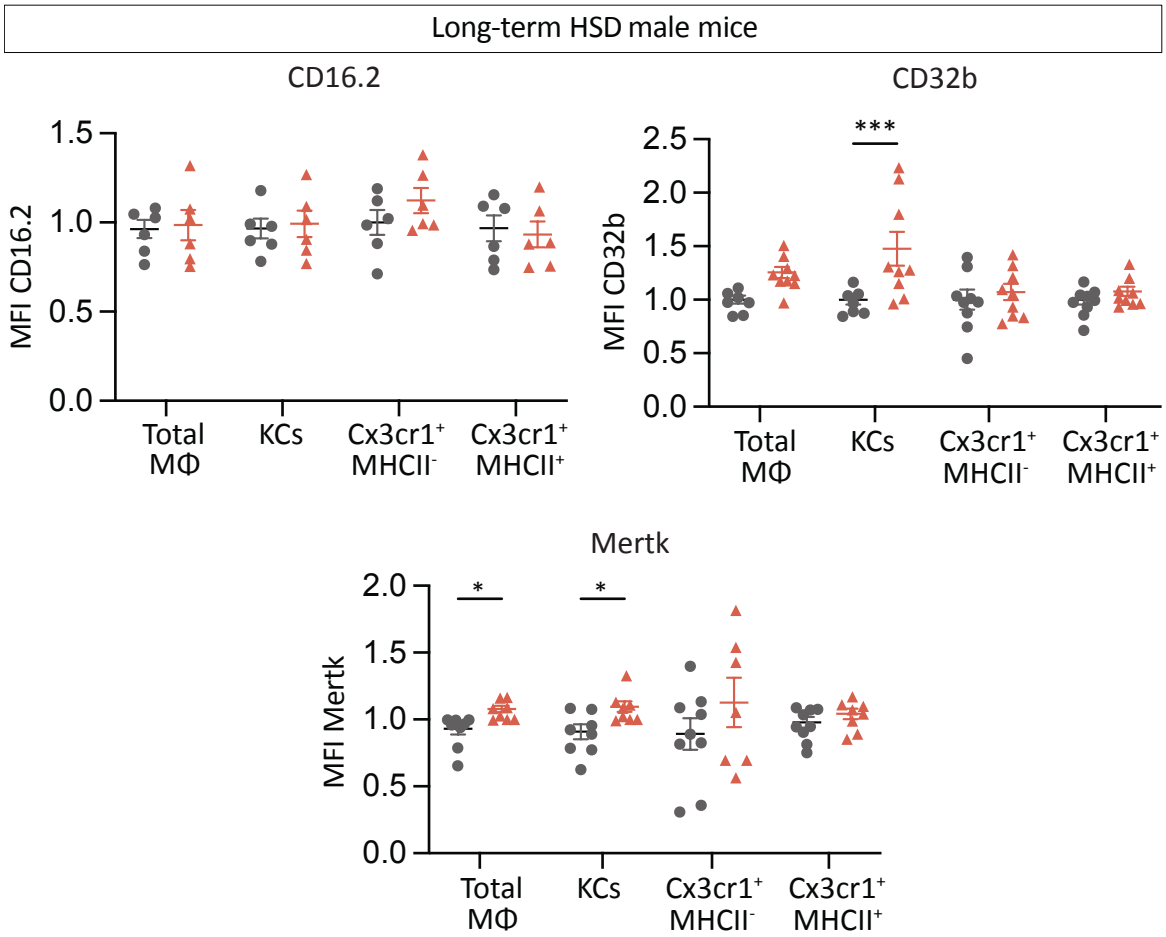

Figure 65 FcγRs and Mertk expression in Liver MΦ subsets following long-term HSD. Mice were fed either CD or HSD for 3 months to achieve a long-term HSD model; N = 6-10 from 2 experiments, data was analyzed using two-way ANOVA analysis, *$p < 0.05$, **$p < 0.01$, ***$p < 0.001$.

3.8.2 Evaluating Liver MΦ FcγR-Dependent Phagocytosis Following Long-Term High-Salt Diet

3.8.2.1 *Ex-vivo* Evaluation of Liver MΦ FcγR-Dependent Phagocytosis Activity

The altered FcγRs gene and protein expression of FcγRs brought the need to assess MΦ FcγR-dependent phagocytosis ex-vivo. For this, liver MΦ of male mice were isolated at the end of long-term HSD and incubated for an hour with *Citrobacter Rodentium* bacteria (*C. rodentium*), and then the phagocytosing MΦ were quantified (Figure 66A). Liver MΦ subsets were identified as shown in the gating strategy (Supplementary Figure 11). Liver MΦ isolated from HSD-fed mice exhibited a slightly reduced percentage of phagocyting cells compared to those from CD-fed mice without reaching a statistical significance ($p = 0.059$) (Figure 66B). This

reduction of phagocytosis was supported by a significant decrease in the phagocytic index that multiplies phagocytic cells with the MFI of the engulfed *C. rodentium* (p = 0.048) (Figure 66B). FcγRs expression after the phagocytosis assay followed the same trend as before, where CD32b expression MFI significantly increased (p = 0.016) and CD16.2 and CD64 remained unchanged in HSD compared to CD condition (Figure 66C).

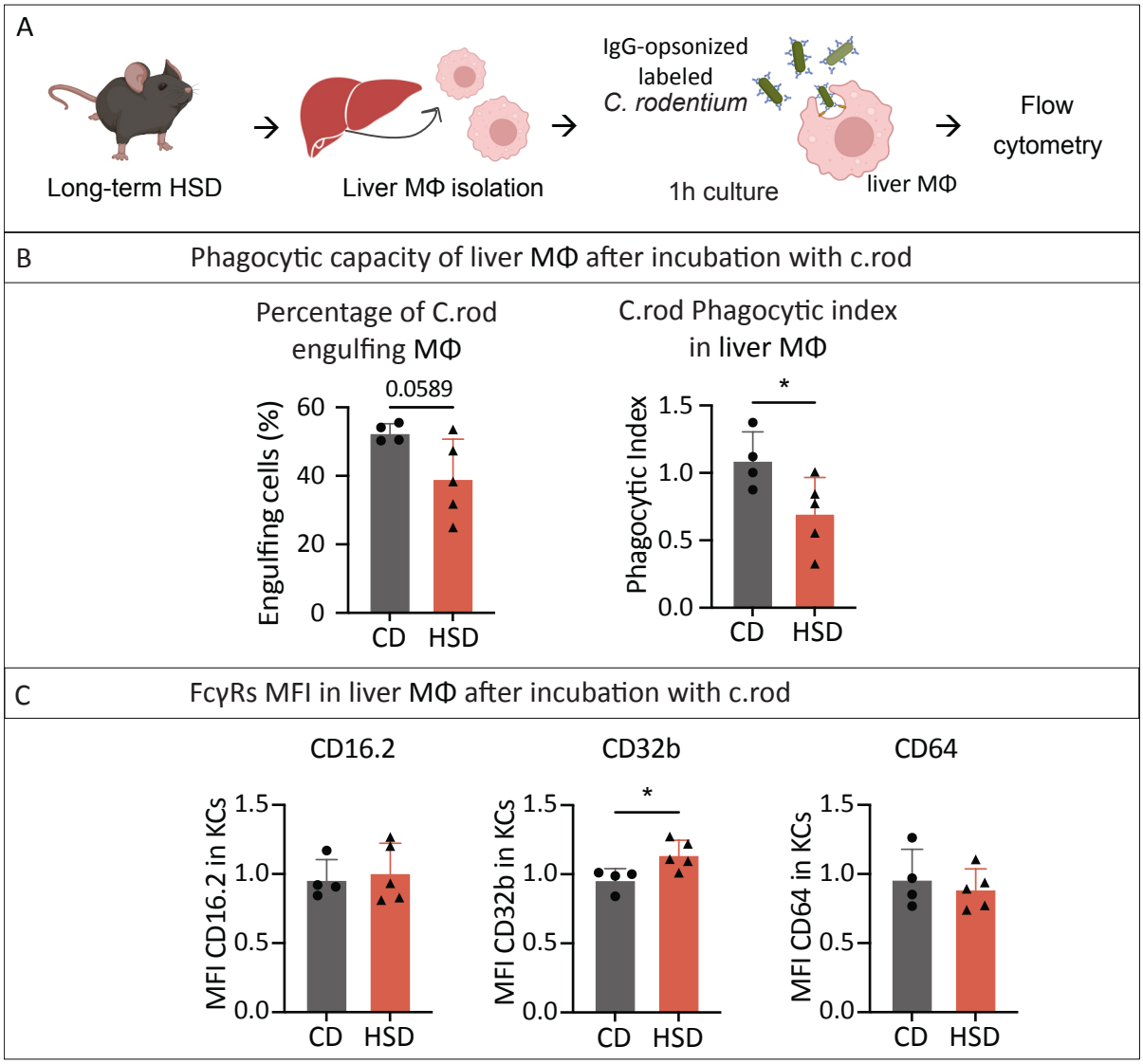

Figure 66 Assessment of liver MΦ FcR-dependent phagocytic capacity in long-term HSD male mice. Male mice were fed CD or HSD for 3 months, and then liver MΦ were isolated, cultured with stained *C. rodentium* for 1h in a ratio of 1 MΦ:160 CFUs, then stained with MΦ markers for Flow cytometry analysis. (A) Percentage of Phagocyting MΦ and their phagocytic index; (B) FcRs expression in liver MΦ after 1 hour of incubation with *C. rodentium*, p-values were obtained using t-tests, *p-value < 0.05.

3.8.2.2 *In-vivo* Evaluation of Liver MΦ FcγR-Dependent Phagocytosis Activity

Liver MΦ, especially KCs phagocytose platelets under specific conditions mainly to maintain blood homeostasis, prevent thrombosis and inflammation, and contribute to immune defense

by clearing senescent, damaged, or pathogen-bound platelets. To this end, an *in-vivo* platelet depletion assay was conducted to assess the phagocytic capacity in female mice by using a well-studied immune thrombocytopenia mouse model (ITP). Anti-platelet IgG antibodies were injected intraperitoneally into wild-type female mice that had undergone a long-term high-salt diet (HSD). Residual platelets were then quantified in the blood at 4, 8, 24, and 72 hours after the antibody injection (Figure 67). After 72 hours, platelets are expected to recover their counts in the blood. Starting from 8 hours after the IgG antibody injection, residual platelets of HSD-fed mice were significantly higher than in CD-fed mice (p = 0.013), indicating impaired phagocytosis of IgG-bound platelets. The shift persisted even until 72 hours after the injection and implied a reduced phagocytic capacity of liver MΦ in response to long-term HSD (Figure 67). In summary, long-term HSD feeding reduced MΦ phagocytosis capacity of bacteria ex-vivo, and platelets in-vivo, accompanied by increased MΦ CD32b expression levels. These findings suggested a functional dysregulation of liver MΦ after a long-term HSD with the involvement of the overexpressed FcγR CD32b as a hint to understand the mechanism behind MΦ phagocytosis impairment upon HSD.

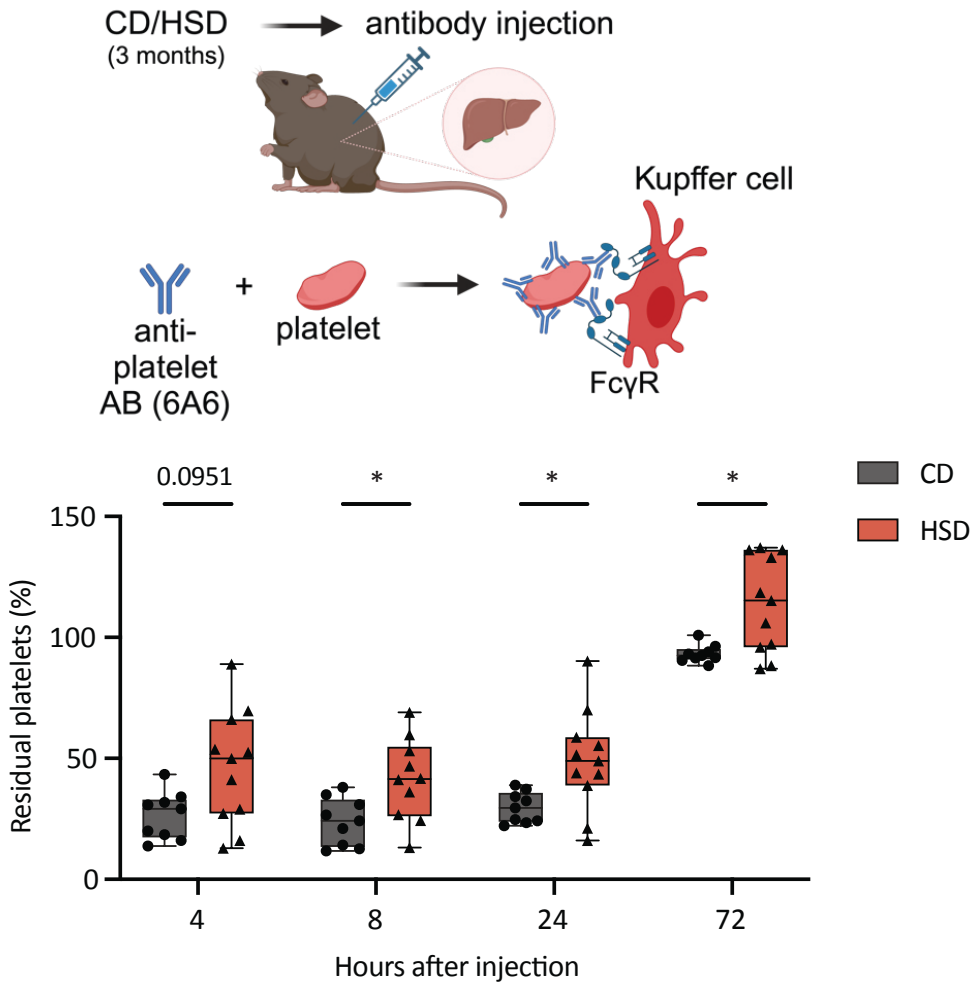

Figure 67 In-vivo assessment of liver MΦ phagocytosis of labeled platelets upon long-term HSD. Residual platelets were measured in the blood at 4, 8, 24, and 72 hours after the IgG anti-platelets antibody injection; n = 11, data was analyzed using two-way ANOVAs, *p-value < 0.05.

4 Discussion

High-salt diet has recently become one of public health's most significant dietary concerns. In addition to being a source of high levels of fat and sugar, processed foods are also a primary source of excess daily salt intake. Studies on high-salt diets focus more on the cardiovascular and renal consequences of acute exposure to excess salt. However, studies regarding the effects of high-salt diets on the immune system are limited, particularly concerning long-term exposure.

The immune system is both a target and a mediator of HSD-induced pathology, due to its regulation of homeostatic and inflammatory responses throughout the whole body. Studying HSD in this context is essential to uncover mechanisms linking diet, inflammation, and disease, and therefore developing preventive and therapeutic strategies.

Macrophages (MΦ) are innate immune cells essential in maintaining homeostasis and defending against diseases. They act as the first responders to infections and play a vital role in engulfing and digesting pathogens, clearing debris, and initiating immune responses. Previous studies have shown that bone marrow-derived MΦ (BMDMs) induce proinflammatory responses and can upregulate chemotaxis towards excess salt concentrations. In earlier research conducted as part of this study, prolonged exposure to high salt concentrations disrupted the BMDM phagocytosis capacity of polystyrene beads, tumor cells, and thymic cells by up to 50% [157]. Moreover, it stimulated a migratory behavior in BMDMs towards excess salt concentration [157]. However, MΦ sensing and responding to salt is dependent on their tissue microenvironment and hardly resembles *in-vitro* settings. Hence, further investigations on the physiological implications of salt overload on MΦ in their specific niches in the body are essential to comprehend the complexities of salt-mediated immune modulation and its implications in disease pathogenesis.

4.1 Impact of Short- and Long-Term High-Salt Diet on Gut and Liver Integrity

4.1.1 High-Salt Diet Effects on Body Weight and Microbiome Composition

The current study explored the pathological effects of feeding mice with the 3-week (short) and 3-month (long) high-salt diet. The mouse body weight was assessed weekly through the periods of the diets in both female and male mice. In the females, mice fed with HSD showed normal weight gain through short and long-term HSD, comparable to CD-fed mice. In contrast, HSD-fed male mice significantly gained less body weight than CD-fed mice starting from the fifth week. This result suggested a male-specific influence of the long-term HSD on mouse body weight. A previous study on male mice with a 3-month HSD of 8% NaCl and unlimited access to tap water also showed that HSD mice weighed less than controls [189]. Although both studies yielded similar outcomes of body weight change, it is important to note that Mutchler’s group used normal tap water with the 8% NaCl high salt diet while we provided

0.9% NaCl in drinking water, which likely plays a key role in sustaining elevated sodium levels and ensuring consistent salt exposure with only 4% NaCl in the food. In another study, a 3-month long-term HSD reduced the body weight of male rats starting from the sixth week [17]. This male-specific reduction of body weight gain may be because of multiple reasons, of an altered appetite and food intake, salt-induced fluid regulation and energy consumption, and altered gut microbiota and metabolism due to sex-dependent adaptations to HSD [10,17,31].

Furthermore, an interesting question was whether organs other than the skin accumulate excess sodium. For this, sodium concentrations were measured in the dry weight of the different gut regions and the liver and the wet weight of the mesentery lymph nodes by mass spectrometry. As potassium levels in the tissues highly depend on sodium balance, potassium concentrations were also measured. The unchanged concentrations of Na^+ and K^+ after long-term HSD indicate that excess sodium does not accumulate in the gut regions and the liver. Since the gut efficiently absorbs the excess Na^+ and does not store significant amounts, it transfers sodium to the blood circulation. The liver receives the excess sodium from the blood without storing it, and it is known to help in regulating Na^+ levels through the renin-angiotensin-aldosterone system [190]. Studies showed that part of the high Na^+ concentrations in blood is later stored in Na^+ reservoirs in the skin, while the rest was shown to be excreted through the urine [11,191,192].

Gut and liver homeostasis are strongly dependent on the stability of the gut microbiota composition. The gut microbiota is the ecosystem of all microorganisms that reside in the gut lumen, which increase in abundance and diversity from the proximal to the distal end of the gut and contribute to digestion, metabolism, and immune functions. Previous studies demonstrated that a 2-week HSD negatively affects microbiome composition in male mice by decreasing lactobacillus, a beneficial gram-positive anaerobic bacterial genus [31]. The current study investigated long-term HSD effects on gut microbiome in female and male mice.

The fecal water content was assessed after long-term HSD and a reduction in water content percentage was noted compared to CD. Reduced fecal water content can affect gut microbiome composition by increasing pathogenic and opportunistic bacteria [193]. The caecal microbiome showed more significant changes in response to HSD than the fecal microbiome, as it is more sensitive to dietary changes [194]. The increased alpha diversity of the male HSD microbiome indicated that long-term HSD caused higher bacterial richness and evenness than CD, meaning more versatile and equally distributed bacterial strains within samples. The increased beta diversity in HSD-fed males implied a substantial shift in HSD microbiome composition compared to CD. This result indicates that bacterial species adapted to the new high-salt environment by changing their abundance as some bacterial species thrive in high-salt environments, and others get depleted [195,196].

The enriched phylum Bacteroidetes, and the decreased Actinobacteriota, and Firmicutes only in males point to specific alterations in their microbiome composition. These three phyla work

collectively to regulate gut health in a balanced microbiome. Bacteroidetes regulate metabolic and immune responses, and their increase under long-term HSD might refer to compensatory gut dysbiosis [86]. Furthermore, the genera *Muribaculaceae*, *Alistipes*, and *Odoribacter* from Bacteroidetes were significantly increased upon the HSD. Interestingly, an increased abundance of the *Muribaculaceae* family was linked to ameliorating inflammatory responses in IBD, type 2 diabetes, and obesity and was negatively correlated to body weight [197–200]. Similarly, studies on *Alistipes* suggested their induction of anti-inflammatory responses in the gut and liver [201]. However, other studies indicated that Alistipes promote colorectal cancer [202]. *Odoribacter* was increased in HSD-sugar-fed rats in a previous study and is recognized for pyruvate production that induces anti-inflammatory responses [203]. *Escherichia Shigella* are known to have very low abundance in a healthy gut, and the significant increase of their abundance in long-term HSD may have adverse outcomes, including compromised gut barrier integrity and leaky gut, causing further systemic inflammation and exacerbating colitis and infections [204].

Moreover, *Eubacterium-Coprostanoligenes* are anaerobic gram-positive bacteria from Firmicutes and were significantly enriched under the HSD compared to CD. Studies showed that *Eubacterium-Coprostanoligenes* can convert cholesterol to unabsorbable coprostanol, as shown in studies of high-fat diets with decreased sphingosine levels [205,206]. This implies their possible role in lipid metabolism and cholesterol homeostasis when enriched in the long-term HSD, although no direct evidence is available. The genera *Bifidobacterium*, *Romboutsia*, *and Colidextribacter* were significantly decreased in response to long-term HSD in both sexes and are mostly considered beneficial for gut homeostasis. Depletion of these bacterial genera was also seen in a 14-day HSD study and was linked to IBD due to inducing gut barrier dysfunction and a subsequent reduction in pathogen defense, leading to gut dysbiosis [207–209]. *Lactobacillus* is the most well-studied beneficial bacteria in the gut microbiome. Interestingly, HSD caused a depletion of *Lactobacillus* in the male group but a significant increase in the female group. Depletion of Lactobacillus decreases lactic acid production allowing pathogens to thrive, and also affects the highly efficient Lactobacillus-dependent cholesterol-lowering activity [210,211]. The enrichment of *Lactobacillus* in females could serve as a compensatory mechanism to protect the gut against pathogen overgrowth [58,169]. Besides, female hormones like progesterone contribute to increasing lactobacillus abundance in IBD [212]. Other genera were additionally featured in the fecal microbiome, with *Lachnoclostridium* and *Marvinbryantia* significantly increasing in the HSD samples. A study has indicated a causal relationship between an increased abundance of *Lachnoclostridium*, *Marvinbryantia*, and the above-mentioned *Eubacterium-Coprostanoligenes* and intervertebral disc degeneration (IVDD), which is linked to pro-inflammatory diets [213,214]. Altogether, the microbiome responses to the HSD are directed towards gut dysbiosis by overrepresenting pro-inflammatory bacterial species and reducing beneficial ones, as well as dysregulation of lipid metabolism. Dysbiosis impairs MΦ response to pathogens, where they may become overactive, resulting in tissue damage, an inability to resolve inflammation, and metabolic disorders [215]

In summary, the difficulty of male mice to gain weight could suggest alterations in appetite and metabolic processes, pointing towards new microbiota adaptation. However, the excess Na^+ was shown to not accumulate in the gut and liver organs thanks to their physiological type of transferring Na^+ to blood to be partially excreted through urine or stored in the skin. This suggests that excess Na^+ might indirectly affect MΦ responses in the gut-liver axis, possibly through microbiome changes and constant handling of Na^+. and Cl^-. The microbiome analysis revealed the dysregulations in microbiome composition, denoting gut microbial dysbiosis upon the long-term HSD, suggesting a high risk on overall health initiated in the gut-liver axis.

4.1.2 Characterization of Gut Pathology in Response to Short- and Long-Term High-Salt Diet

To assess whether HSD affects gut homeostasis over short- or long-term feeding, different parameters were measured beside the microbiome composition, including gut length and structural morphology, epithelial barrier permeability, and response to bacterial infections. The SI elongation in female animals upon short- and long-term HSD, has never been reported before and could reflect female-specific gut adaptations to the dietary change. In the literature, SI length has been correlated to food intake quantity where high-energetic diets such as high-fat diet and high-sugar diets shortened the small intestine length due to eating less than chow diets, and the energetically depleted food caused hyperphagia leading to gut extension [216]. Although HSD food intake was not directly measured, the used high-salt diet had 17,6 MJ/kg while CD had 18,3 MJ/kg gross energy, implying a possible reason for the increased gut length in the HSD females. However, this relationship effect was not observed in males.

By contrast, males had a normal SI length, but significant colon shortening following short- and long-term HSD. Colon shortening was also observed in other unhealthy diets such as high-fat diets, and is linked to many colon diseases like colitis [85,217], reflecting the cumulative effects of inflammation-driven tissue damage, fibrosis, and muscular remodeling, that compromise colonic structure and reduce its length. Therefore, further investigations must follow the HSD's role in inducing gut damage.

Further histological assessments were performed on the mouse ileum, the last part of the SI, for its importance in having a more condensed and diverse microbiome and more immune networks than other SI regions [35]. Short-term HSD caused mild changes to ileum tissue structure, while long-term HSD showed more pathological signs, such as a significant decrease in crypt depth and an increase in ME thickness. These changes were notable in male mice but not in females, possibly referring to the higher sensitivity of males to HSD. Muscularis thickening could be induced due to many factors, including inflammations and infections, hypertrophy, hyperplasia, fibrosis, and aging [218,219]. In the HSD condition, chronic constipation caused by increased sodium and water absorption could be the theory behind muscularis thickening by cell hypertrophy, as it can increase the workload of the smooth muscle layers

[220]. The combined morphological alterations of the ileum wall upon the long-term HSD suggest a damaged intestinal barrier.

Furthermore, the in vivo epithelial permeability assay in male mice revealed a significant increase in gut permeability to the fluorescent dextran, as evidenced by its elevated concentration in plasma following long-term HSD, implying a 'leaky gut' condition. A previous study showed that just 3 weeks of a 4% NaCl HSD also increased mouse gut permeability, indicating that epithelial damage begins early during short-term HSD exposure [85]. Multiple factors could underlie the HSD-induced increase in epithelial permeability. One potential contributor is gut microbiome dysbiosis, which may impair epithelial integrity. Another is persistent salt-mediated lysis of the protective mucus layer—although this was not directly assessed in the present study—which may expose the epithelium to luminal contents [221]. These findings of reduced body weight gain, colon shortening, histological changes, and increased gut permeability combined suggested impaired gut barrier functions, possibly promoting chronic low-grade inflammation.

The influence of long-term HSD on gut infection resolution was further investigated. A *C. rodentium* colon infection, *a murine model pathogen for enteropathogenic E. coli,* was used as a well-studied model for the assessment of infection clearance and mucosal immunity, based on the defined infection course [222,223]. Only day 22 post-infection showed a significant increase in disease activity index in HSD mice; However, the overall curve trajectory was significantly elevated, indicating a cumulative effect of prolonged disease activity. This suggests that HSD likely impaired full recovery even 22 days after infection. Further, when performing colony-forming unit (CFU) assays as a proxy of successful bacterial clearing, *C. rodentium* CFUs were occasionally detected in mesenteric lymph nodes of some HSD-fed mice 22 days post-infection, which might suggest persistent epithelial damage and impaired clearance of the infection, likely facilitated by prior dysbiosis and barrier disruption. However, only a few mice of the HSD group exhibited this outcome, demanding further investigation into infection clearance impairment following long-term HSD. In summary, long-term HSD strongly disrupted gut and microbiome homeostasis in male mice, mediated by gut dysbiosis, increased gut permeability, colon shortening, morphological changes, and delayed colon infection recovery. In contrast, females appeared more protected from these HSD-driven pathological consequences.

4.1.3 Characterization of Liver Pathology in Response to Short- and Long-Term High-Salt Diet

The liver is linked with the gut by a bidirectional combination via the portal vein, bile acids, and lipids regulation, immune crosstalk, and microbiota-derived metabolites. Therefore, it's highly influenced by gut homeostasis. The liver is highly enriched in innate immune cells that regularly sample the circulating nutrients and endotoxins derived from the gut and build responses to them. HSD can profoundly impact liver health through the liver-gut-microbiota

axis. Studies on human and animal models reported that high-salt diets contribute to the development of non-alcoholic fatty liver disease (NAFLD), progression of liver fibrosis, oxidative stress, and mitochondrial dysfunction [77,224], highlighting the role of sodium levels balance in liver homeostasis.

This study concisely explored liver responses to short- and long-term HSD. The percentage of liver weight to body weight was unchanged in males of both diet periods and in females of long-term HSD. However, this ratio was increased in females after short-term HSD and may be due to metabolic stress upon starting the HSD. However, the reason behind this change specifically in females is not yet understood. Accordingly, long-term HSD seemed to not cause changes to liver mass, but still cause some modulation in liver structure particularly in males, including clear, vacuolated hepatocytes in H&E, and points of minor degeneration. The wide empty-looking hepatocytes are described in steatosis conditions, and here could refer to lipid droplet accumulation [225].

To check whether the HSD-linked cell ballooning in the liver is due to lipid accumulation, liver sections of the male long-term HSD group were stained with Oil-Red-O staining, showing significant lipid droplet accumulation. The liver lipid accumulation suggests a link to the gut microbial dysbiosis, where many lipid-regulating bacterial genera were decreased. Further lipidomic analysis was done to check for the changes in specific lipid classes. The male-specific increase in the liver levels of the intermediate lipids diacylglycerides (DGs) upon long-term HSD explained the resulting lipid accumulation. In another study, the DGs elevation was linked to compromised insulin signaling via protein kinase C activation (PKC), which disrupts the metabolism of fats and sugars [226]. And because they operate as bioactive lipid intermediates, DGs are also linked to metabolic dysfunction. Therefore, the raised buildup of liver DGs following HSD without an associated increase in triacylglycerides (TGs), potentially drives metabolic imbalance that may lead to hepatic insulin resistance. Altogether, long-term HSD influenced male liver homeostasis by causing minor structural changes, accompanied by lipid accumulation, particularly the DGs lipid intermediates, which could point to metabolic dysregulation and consequent insulin resistance.

4.1.4 Conclusion

In conclusion, this study highlighted the significant impact of long-term HSD on gut-liver axis homeostasis, particularly emphasizing the pronounced detrimental effect observed in male mice. In contrast, females appeared relatively protected from long-term HSD-induced alterations, showing no evident structural damage in gut and liver tissues, and less pronounced gut microbial dysbiosis compared to males.

4.2 Ileum MΦ Transcriptional Diversity and Responses Following Long-Term High-Salt Diet

This study demonstrated that long-term HSD feeding caused significant gut damage in male mice, marked by ileal structural pathology and elevated intestinal permeability. The gut immune network is one of the key factors contributing to gut homeostasis. Gut MΦ are the first responders to gut microbiome changes, and interact with other immune cells of the adaptive immune system, hereby shaping local immune responses and maintaining mucosal homeostasis. Transcriptional profiling of the ileal LP and ME layers provided a comprehensive overview of ileum MΦ potential functional changes and communications with gut epithelium under long-term HSD. Ileum cell types, including epithelial, smooth muscle, interstitial, neuronal, and immune cells, were identified. Gut MΦ were identified by their canonical genes *Adgre1, Lyz2*, *C1q*, and *Mrc1*.

Functional gene enrichment analysis uncovered MΦ responses to long-term HSD, encompassing upregulation of GO terms linked to activation of immune responses, cytokine production, proliferation and differentiation of myeloid cells, and apoptotic cell clearance. On the other side, ileum MΦ downregulated GO terms linked to lipid metabolism processes and cholesterol homeostasis upon the HSD. These transcriptional MΦ responses may contribute to metabolic reprogramming and switching to a pro-inflammatory response [227]. As reported in previous studies, MΦ efferocytosis is linked to lipid metabolism through glycolysis and lipid oxidization [228]. Also, lipid metabolism downregulation is linked to an increased expression of MΦ scavenger receptors to maintain efferocytosis activity [225,229]. Consistent with this, transcriptional data revealed that the downregulation of lipid homeostasis pathways was accompanied by the upregulation of *Mertk*, a key efferocytosis receptor. These findings highlight the need for further functional assays of efferocytosis and lipid metabolism to elucidate the mechanisms by which a high-salt diet influences ileal MΦ function. According to the literature, bile acids are synthesized from cholesterol and contribute to inducing MΦ anti-inflammatory responses [230,231]. Hence, the findings suggest that the transcriptional suppression of bile acid metabolism in MΦ under HSD conditions may play a role in promoting pro-inflammatory responses. Moreover, downregulating the GO term of MΦ cell junction assembly upon HSD may hint at MΦ migratory behavior and affect their interaction with epithelial cells, possibly correlating with the previously shown HSD-induced gut hyperpermeability [232].

The MΦ cell cluster was subdivided into three main clusters depending on their key featured genes including $CD163^+$, $MHCII^+$, and $Plac8^+$ MΦ. The highlighted upregulation of inflammatory response in $MHCII^+$ MΦ supported by increased expression of complement- and inflammasome-associated genes indicates their key role in initiating inflammatory responses. In addition, IFN-α and IFN-γ responses were also upregulated in $MHCII^+$ and also $CD163^+$ MΦ, supporting potential enhanced inflammatory responses. As known from previous studies, IFN-γ induces the differentiation of inflammatory monocytes that respond to uncontrolled

microbial entry to the gut, creating a vicious circle of inflammation [233]. Therefore, investigating monocyte and MΦ cellular changes upon HSD would provide a further understanding of the HSD-induced inflammatory process. Meanwhile, the downregulated cholesterol homeostasis in Plac8$^+$ MΦ would potentially influence MΦ functions and membrane integrity [228].

In addition, HSD stimulated myogenesis controlled by MHCII$^+$ and Plac8$^+$ MΦ. Studies showed that under inflammatory conditions, MΦ produce growth factors and other mediators that support myogenesis and remodeling of smooth muscles [234]. This MΦ-myogenesis link could explain the HSD-induced ME thickening result observed histologically, and the involvement of MΦ in this process. However, further validation of the relevance of this association under HSD conditions is essential. The subsets MHCII$^+$ and Plac8$^+$ MΦ also upregulated the epithelial-to-mesenchymal transition (EMT) – a process where epithelial cells lose their cell polarity and cell-cell adhesion and gain migratory and invasive behavior to become mesenchymal cells [235]. Upon inflammatory stimuli or tissue damage, MΦ secrete TGF-β, IL-6, and TNF-α, which are known from other studies to induce epithelial-to-mesenchymal transition. Therefore, the HSD-induced myogenesis and EMT processes by MΦ may hint towards MΦ pro-inflammatory responses and their role in gut tissue remodeling under long-term HSD; however, this remains to be confirmed through functional assays.

Furthermore, specific genes were explored for their expression in MΦ after long-term HSD. Sodium and chloride channels, along with their regulating pathways, are crucial for regulating MΦ cell volume and efferocytosis by modulating osmotic balance and ion homeostasis [13,186–188]. In CD163$^+$ and Plac8$^+$ MΦ of HSD, the downregulation of *Slc8a1* (Ncx1) – essential for Na^+ entry into MΦ [13], suggests a potential feedback mechanism to limit Na^+ influx. The Slc12a2 and its regulators Wnk1 and SPAK (Stk39) represent a chloride-sensing pathway that plays a major role in regulating efferocytosis and controlling MΦ cell volume by modulating cytosolic chloride levels. This chloride-sensing pathway was disrupted in MHCII$^+$ and CD163$^+$ MΦ upon HSD, characterized by upregulating *Wnk1* and downregulating the downstream genes encoding *Slc12a2* and *Stk39*, indicating dysregulation of MΦ ion transport and cell volume control [151]. Activated Wnk1 is also known to be linked to increased efferocytosis, as manifested by the overexpression of *Mertk* in MHCII$^+$ MΦ, which interferes with the HSD-induced pro-inflammatory responses of MΦ. Anti-inflammatory responses such as *Il-10ra* and *Mertk* increased expression in MHCII$^+$ MΦ may serve as a compensatory mechanism for clearing cell debris or dying cells.

4.2.1 Transcriptional Profiling Reveals High-Salt Diet-Driven Alterations in Ileal MΦ–Enterocyte Interactions

Gut MΦ regulate epithelial cells by secreting cytokines and growth factors, and interact with them through integrins and adhesion molecules [236]. Previous findings including epithelial hyperpermeability and altered MΦ responses like the enhanced epithelial-to-mesenchymal transition, lipid, and bile acid metabolism dysregulation prompted the investigation into

whether long-term HSD affects the ileum MΦ-EC interaction. The transcriptional analysis of the ileum revealed an enhanced MΦ-EC signaling upon HSD, which could be attributed to the enhanced immune surveillance and the damaged leaky epithelium. Thereafter, HSD increased incoming signaling to all three MΦ subsets, but increased outgoing signaling of only CD163$^+$ and Plac8$^+$ MΦ towards ECs, indicating more involvement in EC regulation than MHCII$^+$ MΦ which lost the communication with ECs.

The HSD-enhanced outgoing signaling between CD163$^+$ MΦ and EC subsets, primarily Fabp6$^+$ and Mme$^+$ ECs can play a crucial role in epithelial remodeling due to the known role of CD163$^+$ MΦ in tissue remodeling [237,238]. Besides, the ileal Fabp6$^+$ ECs are a key regulator of bile acid metabolism, and their stronger communication with CD163$^+$ MΦ upon HSD together with the significantly downregulated bile acid transport GO term in MΦ hints towards altered bile acid homeostasis [239]. The enhanced outgoing signaling from CD163$^+$ and plac8$^+$ MΦ to Apoa4$^+$ ECs is possibly linked to lipid handling since Apoa4$^+$ ECs are known to be involved in lipid metabolism regulation [240]. The lost EC interaction with MHCII$^+$ MΦ that are known for their maintaining tolerance to commensal microbiota, could potentially affect the role of the immune system in distinguishing harmless from harmful signals, possibly leading to impaired gut barrier integrity [111].

Knowing which MΦ-EC signaling pathways are featured by CD and HSD is necessary to understand the consequent immuno-epithelial responses. CD-featured signaling pathways were focused on homeostatic processes, like the KIT pathway that is involved in cell survival, proliferation, and differentiation [241]. Also, SEMA3 contributes to maintaining anti-inflammatory responses indicating its role in resolving inflammation, and CD80 maintains immune defense by proper antigen-presenting [242,243]. On the contrary, HSD feeding enhanced pathways related to immune activation like CD45, and chemokine-mediated immune cell recruitment like CCL, emphasizing the pro-inflammatory immune activation shown in the functional enrichment analyses [244,245]. Many pathways involved in epithelium remodeling were also featured in HSD suggesting the MΦ role in regulating epithelial structure and function following HSD.

In summary, transcriptional profiling of ileal MΦ suggested a potential pro-inflammatory response to long-term HSD, specifically in the MHCII$^+$ subset, which, together with CD163$^+$ MΦ, disrupt their Cl^--sensing pathway components, implying an altered cell volume regulation. Moreover, long-term HSD reduced cholesterol homeostasis of ileal CD163$^+$ and Plac8$^+$ MΦ subsets and altered their interactions with enterocyte populations, contributing to epithelial tissue remodeling, which could also be linked to changes in lipid and bile acid metabolism. These observations imply that HSD might potentially influence ileal MΦ functions, NaCl-dependent cell volume control, and epithelial communication, potentially contributing to a chronically inflamed gut environment. However, these hypotheses require validation through cell volume and functional assays such as cytokine release, phagocytosis, and efferocytosis analyses.

4.2.2 MΦ Cell Volume changes following a Long-Term High-Salt Diet

Cell volume control through the Cl^--sensing pathways, disrupted by the chronic excess of NaCl consumption, presents a novel approach to further study mechanisms underlying MΦ effector functional changes. As a first step, MΦ cell volume was assessed upon long-term HSD based on their localization within the ileum ME layer by 3D rendering. Remarkably, increased cell volume and surface were prominent in Blood-vessel-associated MΦ (VAMs) more than nerve-associated MΦ (NAMs) and interstitial MΦ (IMs), potentially due to their proximity to blood vessels serving as gatekeepers for blood nutrients and pathogens. Whether augmented MΦ volume affects their functions like phagocytosis, efferocytosis, and chemotaxis still needs to be investigated by further functional assays.

Based on the previous input on transcriptionally altered Cl^--sensing pathways components and ileal VAMs cell volume increase following HSD, liver MΦ were also investigated for their cell volume upon long-term HSD. Similarly, they showed consistent results with the ileum following long-term HSD, as KCs cell volume, surface, and branching were increased compared to controls. These changes in MΦ volume may be associated with a disrupted chloride-sensing pathway in response to excess NaCl intake, suggesting a chronic adaptation to altered osmolarity potentially mediated by sodium-linked transporters. Additionally, the upregulation of *Mertk* under high-salt conditions could indirectly influence MΦ volume by modulating cytoskeletal organization, membrane remodeling during efferocytosis, and signaling cascades that affect ion transporter activity.

4.2.3 Ileum MΦ Heterogeneity in the Gut Under Long-Term High-Salt Diet

In this study, gut MΦ *heterogeneity* was characterized in the different gut regions. Most gut MΦ are defined by the expression of F4/80 in both LP and ME layers. Although gut MΦ are known for their pronounced heterogeneity, further characterization of their surface markers is still inconsistent in the literature. Spectral flow cytometry analysis succeeded in inspecting many key MΦ markers simultaneously to characterize gut MΦ heterogeneity. Eight MΦ subsets were identified as follows: $CD163^+$ MΦ, which were more abundant in the ME layer; $Tim4^+$ and $Lyve1^+$ MΦ, which both expressed MHCII; $CD13^+$, and $CD13^-$ MΦ, which were also described as $MHCII^+$ $Tim4^-Cx3cr1^+$; $MHCII^+Cx3cr1^-$ MΦ, and the two $MHCII^-$ subsets: $MHCII^-Cx3cr1^+$ and $MHCII^-Cx3cr1^-$. In addition to these populations, the ME layer contained the $CD321^+$ subset associated with nerve fibers [50]. The different gut MΦ subpopulations exhibited different phagocytosis capacities with the $Tim4^+Lyve1^+$ being the most phagocytic subset followed by $CD163^+$ MΦ. This comprehensive study on gut MΦ phenotyping enabled studying their specific responses to HSD, including changes in cell count, marker expression, and developmental origin.

The MΦ subpopulations of the different gut regions were analyzed from both sexes for changes in cell count. HSD-fed females had comparable cell counts of MΦ subsets to CD-fed littermates in all different gut regions, indicating that these populations are not numerically

altered—possibly reflecting a degree of protection from HSD-induced depletion or recruitment; however, their origin and functional changes still need to be assessed.

For the male group, the ileum distinctively showed an increase in monocyte counts of lamina propria and muscularis externa layers only upon short-term HSD. This monocyte expansion possibly indicates a transient monocyte recruitment or accumulation of monocytes in response to the early stages of ileum tissue damage. According to previous studies, HSD induces epithelial cells and resident immune cells to secrete chemokines that attract monocytes [246].

Interestingly, the ileal MΦ subset CD13$^-$ with expression profile MHCII$^+$Tim4$^-$Cx3cr1$^+$ in the lamina propria was significantly increased upon long-term HSD, in addition to MHCII$^-$Cx3cr1$^+$ which failed to reach a statistical significance. This specific cell expansion potentially indicates a selective phenotypic shift involved in chronic adaptation to HSD or unresolved inflammation. The fate-mapping model indicated that CD13$^-$ had a significant increase in their monocyte-derived proportion at the expense of fetal-derived one under HSD. This shift was specifically observed in the long-lived monocyte-derived population, while short-lived monocyte-derived cells remained unchanged, suggesting local proliferation of previously recruited monocyte-derived MΦ. This was consistent with the ileal histological changes and the increased intestinal permeability upon long-term HSD.

4.2.4 Ileum MΦ Ontogeny in the Gut Under Long-Term High-Salt Diet

Next, investigating the influence of long-term HSD on gut MΦ developmental origin is crucial for understanding the associated roles of the distinct subsets with high salt intake. The novel double fate-mapping mouse model *Tnfrsf11a^{Cre}; Rosa26$^{LSL\text{-}YFP}$; Ms4a3^{FlpO}; Rosa26$^{LFL\text{-}tdTomato}$* was used to track the developmental origin of MΦ in each gut region separately, by differentially labeling fetal-derived and monocyte-derived MΦ. In this model, long-lived, fetal-derived MΦ are YFP$^+$, freshly recruited/short-lived monocyte-derived MΦ are tdTomato$^+$, and long-lived monocyte-derived MΦ are double positive as they start expressing *Tnfrsf11a* as part of their MΦ core program.

In the ileal lamina propria of HSD-fed male mice, most MΦ subsets showed a significant increase in the proportion of long-lived monocyte-derived cells, while fetal-derived cell proportion decreased. This shift was observed in nearly all subsets except the CD163$^+$ and MHCII$^-$Cx3cr1$^-$ subpopulations. However, the proportion of short-lived monocyte-derived cells remained unchanged between the ileal MΦ subpopulations of CD-fed and HSD-fed mice. The muscularis externa showed the same shift, but only significant in CD13$^-$ MΦ, ensuring their male-specific inflammatory role in the chronic excess salt intake. While the ileum had the most prominent changes in MΦ subsets origin, the duodenum also showed some shifts that align with the findings in the ileum, like decreased fetal-derived cell proportion in the CD13$^-$ subset. Altogether, Long-term HSD promotes the expansion of monocyte-derived over fetal-derived MΦ within the ileum lamina propria tissue over time. This shift may reflect a

long-term remodeling of the MΦ compartment toward a monocyte-derived origin under chronic excess salt exposure.

Along with the transcriptional data showing enhanced pro-inflammatory responses, the increased abundance of specific ileal MΦ subsets—such as $CD31^-$ cells—and their shift toward a bone marrow origin highlight a distinct inflammatory adaptation of ileal MΦ to long-term HSD, potentially contributing to the ileal injury described earlier.

4.2.5 Ileum MΦ FcγR Expression and Clearance Functions under long-term HSD

Studying ileal MΦ phenotype upon HSD in the context of inflammation and tissue remodeling requires conducting functional assays, such as phagocytosis and cytokine release profiling, to provide insight into how these cells contribute to the overall immune response in this model.

FcγRs, a family of receptors, involved in the uptake of IgG-opsonized microorganisms by a process called phagocytosis, in addition to other key MΦ functions like antigen presentation, and cytokine production. Mouse FcγRs comprise four subtypes that differ in their binding affinity to IgG, where FcγRI has high affinity and FcγRIII, FcγRIV, and FcγRIIb have low-to-medium affinity. FcγRIIb also differs in having the immunoreceptor tyrosine-based inhibitory motif (ITIM), while the other FcγRs have the immunoreceptor tyrosine-based activating motif (ITAM) [247]. During immune responses, MΦ modulate the affinity of FcγRs by differential antibody glycosylation and regulation of their expression levels, favoring either activating or inhibitory receptors.

FcγRs gene expression was explored in ileal MΦ following long-term HSD. The slightly enhanced expression of the Fcgr2b gene in $MHCII^+$ and $CD163^+$ MΦ clusters and the decreased expression of Fcgr4 in the $CD163^+$ MΦ cluster upon HSD might imply a potential HSD-driven coordinated response, likely aimed at damping MΦ effector functions [248,249]. Furthermore, further investigating the MΦ FcγRs expression on the protein level and functional assays following HSD is necessary. At the protein level, overexpression of CD32b (FcγRIIb) was detected as early as after short-term HSD in $CD13^-$ MΦ of the $MHCII^+Tim4^-Cx3cr1^+$ profile and persisted after long-term HSD in the same subset, validating the transcriptional findings and potentially suggesting disturbed FcγRIIb-dependent processes, including phagocytosis. Notably, previous work has suggested that the protective effect of IgG in the *C. rodentium* infection model is largely mediated through FcγR-dependent effector functions of myeloid cells (Masuda et al., 2008). Therefore, the impaired clearance of infection under HSD conditions points to blunted MΦ effector functions, indicating that long-term HSD may impair the phagocytic capacity of ileal gut MΦ. This effect may, in part, result from altered IgG-mediated control of infection, consistent with the observed changes in Fc receptor expression levels.

To further assess phagocytic capacity following long-term HSD, ileal MΦ were isolated and cultured *ex-vivo* with IgG-opsonized *C. rodentium*. This assay revealed an enhanced

phagocytic capacity of *C. rodentium* primarily in the ileal Lyve1$^+$ and CD13$^+$ MΦ subsets. In addition to the direct effect of excess NaCl on MΦ effector functions, the HSD-induced dysbiosis and the increased exposure to microbial antigens may promote trained immunity, potentially contributing to enhanced phagocytosis. However, an *in-vivo* phagocytosis assay would be necessary to more accurately evaluate ileal MΦ responses under long-term HSD conditions. Moreover, the mechanisms by which HSD modulates Fcγ receptor (FcγR) expression, and whether driven by sodium, chloride, or both, remain to be elucidated.

4.2.6 Potential Modulation of Apoptotic Cell Clearance Under Long-Term High-Salt Diet

Efferocytosis is the process of removing apoptotic cells, a main component of tissue homeostasis, and is mediated by Mertk, a tyrosine kinase receptor expressed by MΦ. The long-term HSD has been shown to increase *Mertk* gene expression in the MHCII$^+$ MΦ cluster of the ileum. Moreover, this increased *Mertk* gene expression after long-term HSD was also evident in the protein expression, particularly in the CD13$^-$ MΦ subpopulation which positively expresses MHCII. As previously discussed, elevated Mertk expression is associated with enhanced efferocytosis and clearance of dying cells and cellular debris. This suggests a sustained activation of Mertk-dependent efferocytosis at least in the MHCII-expressing CD13$^-$ MΦ subset under long-term high-salt intake. However, a functional assay investigating the impact of HSD on ileal MΦ efferocytosis capacity is necessary to validate this suggestion.

4.2.7 Summary of 4.2

Long-term HSD induced distinct transcriptional changes in ileal MΦ of male mice, notably in ion transport, lipid, and bile acid metabolism, alongside an upregulated pro-inflammatory signature. Dysregulation of Na^+ and Cl^- transporters was associated with disrupted cell volume control mechanisms, leading to MΦ enlargement through *Slc12a2* and Wnk1 that define the Cl-sensing pathway.

HSD also influenced macrophage (MΦ) development and function, specifically in the ileum. Under short-term HSD, monocyte counts in the ileal lamina propria increased without affecting MΦ numbers. In contrast, long-term feeding resulted in unchanged monocyte counts but a selective expansion of the ileal CD13$^-$ MΦ subset. This subset, along with several other MΦ populations, exhibited a shift in origin toward a greater proportion of long-lived, but not short-lived monocyte-derived cells at the expense of fetal-derived MΦ. Thus, long-term HSD suggests a possible local expansion of long-lived monocyte-derived macrophages, replacing fetal-derived counterparts.

Functionally, ileal MΦ may contribute to impaired *C. rodentium infection* clearance following HSD via Fcγ receptor (FcγR)-dependent mechanisms. Upregulation of FcγRs, particularly FcγRIIB, was observed at both transcript and protein levels in MHCII expressing subsets under long-term HSD. The enhanced phagocytic capacity of ileal MΦ toward *C. rodentium* after HSD

further supports a functional modulation, possibly driven by sustained bacterial translocation and FcγRIIB overexpression.

4.2.8 Conclusion

Together with the pathological results of damaged ileal tissue and increased intestinal epithelial permeability upon long-term HSD, these findings suggest a persistent inflammatory condition in the ileum upon long-term HSD, mediated by specific ileal MΦ subpopulation via cellular, morphological, developmental, and functional adaptations.

4.3 Liver MΦ Heterogeneity and Ontogeny in the Gut Following High-Salt Diet

The liver has a central role in the metabolism of carbohydrates, lipids, and proteins. Lipid metabolism is crucial for liver homeostasis, via the production of cholesterol, triacylglycerides (TGs), and other lipids, as well as bile acids [250]. As discussed earlier, long-term HSD induces minor hepatic structural abnormalities and lipid accumulation, that is specific to the intermediate diacylglycerides (DGs), which typically increase in metabolic disorders [251]. As 'leaky gut' has been shown in previous studies to worsen liver inflammation in many contexts [252], the lipid intermediates DGs accumulation was suggested to be driven by the increased intestinal permeability, therefore indirectly disturbing liver homeostasis.

Liver MΦ, mainly Kupffer cells (KCs), are also key regulators of its homeostasis and they respond to the microbe-associated molecular patterns (MAMPs) that arrive from the gut, to balance immune tolerance and inflammation [251]. Thus, Liver MΦ play a major role in the initiation and progression of hepatic inflammation. Upon liver injury, KCs rapidly release pro-inflammatory cytokines such as IL-1β and TNF-α, leading to the recruitment of monocytes that differentiate into pro-inflammatory MΦ [145]. In this study, liver MΦ were characterized by flow cytometry and divided into 3 subpopulations: the tissue-resident KCs which are mostly fetal-derived cells, and Cx3cr1^{+}MHCII^{-}, and Cx3cr1^{+}MHCII^{+} that share both fetal- and monocyte-derived origins and known for their rapid replacement by monocytic-derived cells [253]. Notably, we observed differences in ontogeny of liver MΦ that were gender-specific. While short-term HSD did not alter the total MΦ count in females, it significantly decreased it in males, particularly in KCs. This male-specific reduction in MΦ numbers may indicate an activation of stress pathways in response to the HSD acute effects, including leaky gut, that could happen even at short-term feeding [33,254]. Consequently, though speculative, this may indicate an ongoing apoptotic clearance of KCs, as suggested by Mertk overexpression following short-term HSD, potentially contributing to the observed reduction in MΦ counts. Nevertheless, long-term HSD also led to a reduction in total macrophage numbers in females, most notably in KCs. This effect may reflect KC exhaustion and subsequent replacement by monocyte-derived MΦ, as supported by findings from the double fate-mapping model. In contrast, long-term HSD slightly increased the total MΦ count in male livers, most likely reflecting an expansion of KCs, which showed a trend toward increased numbers, whereas Cx3cr1^{+}MHCII^{-}

and Cx3cr1^{+}MHCII^{+} MΦ remained unchanged. This minor increase could suggest a low-grade inflammation due to the long.-term HSD feeding. These findings suggest a sex-specific effect of both short- and long-term HSD on liver MΦ, particularly KCs. According to previous studies females are more protected to unhealthy dietary interventions than males [255,256]. Therefore, one possible explanation is that adverse effects of HSD, such as oxidative stress, may have been initiated earlier in males, resulting in an initial reduction of MΦ. With prolonged exposure, these cells may have undergone a repopulation phase. In contrast, in females, the detrimental effects have manifested only later during long-term HSD, leading to a delayed depletion of MΦ.

Developmental origin of the Cx3cr1^{+}MHCII^{-} MΦ subpopulation exhibited expansion of short-lived monocyte-derived cells at the expense of fetal-derived cell proportion in both sexes. In a healthy liver, this subset is highly replenished from BM through monocyte differentiation and they mostly located in the liver capsule serving as first-line immune sentinels to defend against peritoneal-derived infections [145,257]. In females, this origin shift is likely a replacement of the decreasing KCs by freshly recruited monocyte-derived cells, which may undergo cell death either directly due to high sodium chloride concentrations or indirectly through exposure to microbiome-derived molecules and altered bile acid metabolites [31,258]. However, KCs numbers were mostly stable in male animals, suggesting the necessity to further study the sex-specific KCs responses to HSD. Nevertheless, the slight increase in the Cx3cr1^{+}MHCII^{-} MΦ subpopulation may result from the recruitment of monocytes that subsequently differentiate into Cx3cr1^{+}MHCII^{-} MΦ.

Monocyte recruitment in the liver can result from injury, inflammation, KC depletion, or increased phagocytic demand [257,259,260]. Long-term HSD appears to induce liver injury or inflammation in males, supported by liver and gut pathology in addition to HSD-driven hepatic inflammation and fibrosis reported in previous studies [261,262]. In contrast, HSD in females was associated with KC depletion. Thus, liver MΦ responses to long-term HSD are sex-dependent, promoting inflammation in males and KC loss in females, yet both converge on monocyte-derived recruitment into the Cx3cr1^{+}MHCII^{-} MΦ subset.

4.4 Liver MΦ Functional Changes Following High-Salt Diet

To test whether HSD could also influence liver MΦ core functions, KC phagocytic activity was assessed. Based on the gut findings, FcγRs play a key role in modulating MΦ phagocytic capacity. Therefore, FcγRs protein expression was initially investigated in males, showing a significant CD32b overexpression (the inhibitory FcγRIIb) in KCs, consistent with its overexpression in the ileal MΦ, potentially hinting towards altered phagocytosis signaling [263]. Thereafter, an *ex-vivo* FcγR-dependent phagocytosis assay targeting male KCs against labeled *C. rodentium* revealed reduced phagocytic capacity of *C. rodentium* after long-term HSD, along with the same trend of CD32b overexpression.

The liver is the key organ for clearing aged platelets through phagocytosis, mainly done by KCs. Owing to that, the phagocytic capacity was also assessed in female mice by using a well-studied immune thrombocytopenia mouse model (ITP). By this model, intra-peritoneal injection with a platelet-specific antibody (6A6) triggers a rapid depletion of IgG-opsonized platelets from the bloodstream mediated by KCs via FcγRs. By this model, long-term HSD revealed ineffective platelet depletion compared to CD-fed mice, resulting in a higher abundance of platelets in the blood. Therefore, blunted KC phagocytosis function after long-term HSD in females was also linked to FcγR modulation. Altogether, male mice showed that HSD-induced CD32b (FcγRIIb) overexpression is highly linked to the impaired KC phagocytic capacity after long-term HSD.

Similarly, Females showed dampened phagocytic capacity after long-term HSD in an FcγR-dependent manner, possibly suggested to be linked to CD32b as well. The HSD-induced exhaustion of KCs and inability to perform their main function of phagocytic activity in both sexes of mice could result in homeostatic imbalance, especially along with their replacement with newly differentiated monocyte-derived MΦ [254]. This impaired KC phagocytosis contrasts with the enhanced phagocytic activity observed in ileal MΦ, highlighting the distinct tissue-specific responses. As a hypothesis, excess NaCl levels generally appear to dampen phagocytosis like in the liver MΦ, however, the HSD-induced leaky gut likely sustains antigenic stimulation in the gut, potentially driving activation of phagocytic pathways [264,265].

As an indicator of MΦ efferocytosis function, Mertk was assessed upon short-term HSD in both mice sexes and upon long-term HSD in only male mice. While no changes in Mertk expression were observed after short-term feeding, long-term HSD feeding increased Mertk expression in the liver KCs upon HSD. Therefore, Mertk overexpression supported the aforementioned suggestion in ileal MΦ, that efferocytosis can be enhanced by the downregulation of Cl^- transporters under HSD [151]. However, functional assays are required to assess MΦ Mertk-dependent efferocytosis. As discussed in subsection 4.2.2 for ileum MΦ changes, while cell volume alone does not define MΦ functions, it contributes to their cellular modulations that accommodate their new roles, perhaps such as enhanced apoptotic clearance by Mertk-dependent efferocytosis.

Overall, long-term HSD induced cellular, developmental, and functional alterations in liver MΦ. Cellular changes were sex-dependent, with a female-specific decrease in KC numbers. Both sexes, however, shared an increase of BM- over fetal-derived cells within the $Cx3cr1^+MHCII^-$ liver MΦ subset. This origin shift supports an active replacement of tissue-resident by newly recruited MΦ from monocytes. Moreover, long-term HSD dampened KC phagocytic activity, possibly mediated by the overexpressed FcγRIIb, and increased expression of efferocytosis receptor Mertk, which may indicate enhanced KC efferocytosis. These findings collectively suggest a response to sustained inflammation or local microenvironmental changes under long-term HSD, likely inducing a functional ‘paralysis’ of phagocytic pathways, including the anti-bacterial FcγR-mediated mechanisms. Besides the cellular and functional

changes of liver MΦ following HSD, KC cell volume and surface were increased upon long-term HSD, aligning with the blood vessel- associated MΦ in the gut, and signifying the possible role of chloride homeostasis in cell volume control and also in influencing MΦ effector functions.

5 Conclusion

High-salt diets have gained significant attention over the past decade due to their impact on blood pressure and related complications. The immune system, particularly MΦ, has emerged as a critical regulator of tissue salt homeostasis. This study highlights how the gut and liver, being the primary interfaces for dietary and microbial exposure, exhibit notable pathological alterations primarily in male mice following three months of HSD. These include gut barrier damage specific to the ileum, microbial dysbiosis, and impaired resolution of infections, in addition to accumulation of lipid intermediates in the liver. These outcomes underscore underappreciated consequences of excessive salt intake and the role of MΦ as possible key mediators.

Among gut regions, the ileum showed notable MΦ adaptations to long-term HSD. Specific MΦ populations in the ileum and liver were differentially affected by short- and long-term HSD in a sex-dependent way. This was highlighted by an increase of the lamina propria $CD13^{-}$ $MHCII^{+}Tim4^{-}Cx3cr1^{+}$ subset in males and decrease in KCs in females. Both gut and liver exhibited enhanced replacement of self-renewing tissue-resident MΦ by monocyte-derived cells—long-lived in the ileum, short-lived in the liver—reflecting tissue-specific responses to excess salt. In contrast to the liver, monocyte-derived cells in the gut more readily acquire long-lived, tissue-integrated identity under both homeostasis and inflammation.

Long-term HSD elevated the expression of Mertk and FcγRIIb, receptors involved in efferocytosis and phagocytosis, respectively in both gut and liver MΦ. In the liver, FcγRIIb overexpression was linked to reduced KC phagocytosis, impairing hepatic stress and infection defenses. Meanwhile, in the gut, HSD-induced FcγRIIb upregulation in ileal MΦ correlated with increased phagocytic activity, reflecting the gut's tissue-specific immune remodeling. Unlike the liver's steady-state environment, the gut operates under physiological low-grade inflammatory tone. The enhanced phagocytic capacity of MHCII expressing ileal MΦ subsets, including $Lyve1^{+}$ and $CD13^{+}$ MΦ upon HSD, along with their transcriptional pro-inflammatory profile, suggests ileal MΦ activation likely driven by gut HSD-induced barrier dysfunction and dysbiosis.

Moreover, the phagocytosis and (potentially) efferocytosis functions modulation in both organs under long-term HSD is suggested to be linked to the increased MΦ cell volume. The transcriptomic analysis suggested a previously unexplored role for Cl^{-}-sensing pathways in modulating MΦ cell volume and consequently enhancing efferocytosis under long-term HSD, potentially influencing other core functions as well.

The HSD-induced MΦ functional alterations in both organs could be linked the increased MΦ cell volume observed upon long-term HSD. This could be explained by the transcriptionally disrupted Wnk1-dependent Cl^{-}-sensing pathway, responsible for regulating MΦ cell volume,

and also mediates consequently enhancing efferocytosis under long-term HSD, potentially influencing other core functions as well.

Additional research is needed to further elucidate mechanisms of MΦ functional changes following HSD and their implications, importantly with understanding to which extent the HSD-induced microbiome dysbiosis contributes to this. A deeper understanding of gut and liver MΦ adaptations to HSD will provide crucial insights into tissue-specific immune regulation and may inform dietary recommendations aimed at mitigating HSD-associated immune dysregulation.

6 References

1. of Medicine, I. *Dietary Reference Intakes for Water, Potassium, Sodium, Chloride, and Sulfate*. (The National Academies Press, Washington, DC, 2005). doi:10.17226/10925.

2. WHO. Guideline: sodium intake for adults and children. https://www.who.int/publications/i/item/9789241504836 (2012).

3. IHME. Global Burden of Disease Study 2019 (GBD 2019) Dietary Risk Exposure Estimates 1990-2019. *Institute for Health Metrics and Evaluation (IHME)* https://ghdx.healthdata.org/record/ihme-data/gbd-2019-dietary-risk-exposure-estimates-1990-2019?utm_source=chatgpt.com (2019).

4. Chia, Y. C. *et al.* Ethnic differences in knowledge, attitudes, and practices related to dietary salt intake and association with hypertension in Malaysia: a multi-centre cross-sectional study. *Hypertension Research* **48**, 131–147 (2024).

5. Leyvraz, M. *et al.* Food consumption, knowledge, attitudes, and practices related to salt in urban areas in five sub-saharan African countries. *Nutrients* **10**, (2018).

6. Strazzullo, P., D'Elia, L., Kandala, N. B. & Cappuccio, F. P. Salt intake, stroke, and cardiovascular disease: Meta-analysis of prospective studies. *BMJ (Online)* **339**, 1296 (2009).

7. Kawakami-Mori, F. *et al.* Aberrant DNA methylation of hypothalamic angiotensin receptor in prenatal programmed hypertension. *JCI Insight* **3**, (2018).

8. Santos-Rocha, J. *et al.* Maternal high-sodium intake affects the offspring' vascular renin-angiotensin system promoting endothelial dysfunction in rats. *Vascul Pharmacol* **115**, 33–45 (2019).

9. Powles, J. *et al.* Global, regional and national sodium intakes in 1990 and 2010: A systematic analysis of 24 h urinary sodium excretion and dietary surveys worldwide. *BMJ Open* **3**, (2013).

10. Titze, J. *et al.* Long-term sodium balance in humans in a terrestrial space station simulation study. *American Journal of Kidney Diseases* **40**, 508–516 (2002).

11. Titze, J. *et al.* Osmotically inactive skin Na+ storage in rats. *Am J Physiol Renal Physiol* **285**, 1108–1117 (2003).

12. MacHnik, A. *et al.* Macrophages regulate salt-dependent volume and blood pressure by a vascular endothelial growth factor-C-dependent buffering mechanism. *Nat Med* **15**, 545–552 (2009).

13. Neubert, P. *et al.* NCX1 represents an ionic Na+ sensing mechanism in macrophages. *PLoS Biol* **18**, e3000722 (2020).

14. Institute for Health Metrics and Evaluation. Diet high in sodium - Level 3 risk |. https://www.healthdata.org/research-analysis/diseases-injuries-risks/factsheets/2021-diet-high-sodium-level-3-risk (2019).

15. Hall, J. E. Kidney Dysfunction Mediates Salt-Induced Increases in Blood Pressure. *Circulation* **133**, 894 (2016).

16. Wang, X. Q., Terry, P. D. & Yan, H. Review of salt consumption and stomach cancer risk: Epidemiological and biological evidence. *World J Gastroenterol* **15**, 2204–2213 (2009).

17. Fonseca-Alaniz, M. H. *et al.* High dietary sodium intake increases white adipose tissue mass and plasma leptin in rats. *Obesity* **15**, 2200–2208 (2007).

18. Weinberger, M. H. Salt sensitivity of blood pressure in humans. *Hypertension* **27**, 481–490 (1996).

19. Hall, J. E. Kidney Dysfunction Mediates Salt-Induced Increases in Blood Pressure. *Circulation* **133**, 894 (2016).

20. Tikellis, C. *et al.* Activation of the renin-angiotensin system mediates the effects of dietary salt intake on atherogenesis in the apolipoprotein E knockout mouse. *Hypertension* **60**, 98–105 (2012).

21. Patik, J. C., Lennon, S. L., Farquhar, W. B. & Edwards, D. G. Mechanisms of Dietary Sodium-Induced Impairments in Endothelial Function and Potential Countermeasures. *Nutrients* **13**, 270 (2021).

22. Ralph, A. F. *et al.* Activation of the Sympathetic Nervous System Promotes Blood Pressure Salt-Sensitivity in C57BL6/J Mice. *Hypertension* **77**, 158–168 (2021).

23. Balan, Y., Packirisamy, R. M. & Mohanraj, P. S. High dietary salt intake activates inflammatory cascades via Th17 immune cells: impact on health and diseases. *Archives of Medical Science* **18**, 459–465 (2022).

24. Faraco, G. *et al.* Dietary salt promotes neurovascular and cognitive dysfunction through a gut-initiated TH17 response. *Nat Neurosci* **21**, 240 (2018).

25. Jung, S. M. *et al.* Sodium Chloride Aggravates Arthritis via Th17 Polarization. *Yonsei Med J* **60**, 88 (2018).

26. Tubbs, A. L., Liu, B., Rogers, T. D., Sartor, R. B. & Miao, E. A. Dietary Salt Exacerbates Experimental Colitis. *The Journal of Immunology* **199**, 1051–1059 (2017).

27. Wu, C. *et al.* Induction of pathogenic TH 17 cells by inducible salt-sensing kinase SGK1. *Nature* **496**, 513–517 (2013).

28. Kleinewietfeld, M. *et al.* Sodium chloride drives autoimmune disease by the induction of pathogenic TH 17 cells. *Nature* **496**, 518–522 (2013).

29. Chen, L. *et al.* Immune Dysregulation Orchestrated by High-Salt Diet: Mechanistic Insights into Disease Pathogenesis. *Nutr Diet Suppl* **16**, 147–164 (2024).

30. Li, X., Alu, A., Wei, Y., Wei, X. & Luo, M. The modulatory effect of high salt on immune cells and related diseases. *Cell Prolif* **55**, e13250 (2022).

31. Wilck, N. *et al.* Salt-responsive gut commensal modulates TH17 axis and disease. *Nature 2017 551:7682* **551**, 585–589 (2017).

32. Zhang, T. *et al.* Excess salt intake promotes M1 microglia polarization via a p38/MAPK/AR-dependent pathway after cerebral ischemia in mice. *Int Immunopharmacol* **81**, 106176 (2020).

33. Zhang, X. *et al.* A High-Salt Diet Exacerbates Liver Fibrosis through Enterococcus-Dependent Macrophage Activation. *Microbiol Spectr* **11**, e03403-22 (2023).

34. Delfini, M., Stakenborg, N., Viola, M. F. & Boeckxstaens, G. Macrophages in the gut: Masters in multitasking. *Immunity* **55**, 1530–1548 (2022).

35. Mowat, A. M. & Agace, W. W. Regional specialization within the intestinal immune system. *Nature Reviews Immunology 2014 14:10* **14**, 667–685 (2014).

36. Rao, J. N. & Wang, J.-Y. Intestinal Architecture and Development. (2010).

37. Young B, O'Dowd G & Woodford P. Gastrointestinal tract. in *Wheater's Functional Histology: a text and colour atlas.* (Churchill Livingston/Elsevier, Philadelphia, PA, 2014).

38. Laurie Kelly McCorry. *Essentials of Human Physiology for Pharmacy - 2nd Edition* -. (2008).

39. Boudry, G., Yang, P.-C. & Perdue, M. H. Small Intestine, Anatomy. *Encyclopedia of Gastroenterology* 404–409 (2004) doi:10.1016/B0-12-386860-2/00648-1.

40. Boron, W. F. & Boulpaep, E. L. *Medical Physiology: A Cellular and Molecular Approach*. (Saunders/Elsevier, 2009).

41. Pawlina W & H. Ross M. Digestive System I & II. in *Histology: A Text and Atlas: With Correlated Cell and Molecular Biology.* vol. 13 76–89 (SE Dnipropetrovsk Medical Academy of Health Ministry of Ukraine, 2019).

42. Beumer, J. & Clevers, H. Cell fate specification and differentiation in the adult mammalian intestine. *Nature Reviews Molecular Cell Biology 2020 22:1* **22**, 39–53 (2020).

43. Noah, T. K., Donahue, B. & Shroyer, N. F. Intestinal development and differentiation. *Exp Cell Res* **317**, 2702 (2011).

44. Gustafsson, J. K. & Johansson, M. E. V. The role of goblet cells and mucus in intestinal homeostasis. *Nat Rev Gastroenterol Hepatol* **19**, 785–803 (2022).

45. Wallaeys, C., Garcia-Gonzalez, N. & Libert, C. Paneth cells as the cornerstones of intestinal and organismal health: a primer. *EMBO Mol Med* **15**, e16427 (2022).

46. Silverman, J. B., Vega, P. N., Tyska, M. J. & Lau, K. S. Intestinal Tuft Cells: Morphology, Function, and Implications for Human Health. *Annu Rev Physiol* **86**, 479–504 (2024).

47. Arbizu, R. & Nurko, S. Colon: Structure and Function. *Encyclopedia of Food and Health* 259–264 (2016) doi:10.1016/B978-0-12-384947-2.00187-2.

48. Furness, J. B. The enteric nervous system. *The Enteric Nervous System* 1–266 (2007) doi:10.1002/9780470988756.

49. Malone, J. C. & Thavamani, A. Physiology, Gastrocolic Reflex. *StatPearls* (2023).

50. Viola, M. F. *et al.* Dedicated macrophages organize and maintain the enteric nervous system. *Nature 2023 618:7966* **618**, 818–826 (2023).

51. Kumar, Vinay., Abbas, A. K. . & Aster, J. C. . Robbins and Cotran Pathologic Basis of Disease. 1413 (2015).

52. Qin, J. *et al.* A human gut microbial gene catalogue established by metagenomic sequencing. *Nature* **464**, 59–65 (2010).

53. Baquero, F. & Nombela, C. The microbiome as a human organ. *Clinical Microbiology and Infection* **18**, 2–4 (2012).

54. Donaldson, G. P., Lee, S. M. & Mazmanian, S. K. Gut biogeography of the bacterial microbiota. *Nature Reviews Microbiology 2015 14:1* **14**, 20–32 (2015).

55. Nicholson, J. K. *et al.* Host-Gut Microbiota Metabolic Interactions. *Science (1979)* **336**, 1262–1267 (2012).

56. Belkaid, Y. & Hand, T. W. Role of the microbiota in immunity and inflammation. *Cell* **157**, 121–141 (2014).

57. Hsu, C. L. & Schnabl, B. The gut–liver axis and gut microbiota in health and liver disease. *Nature Reviews Microbiology 2023 21:11* **21**, 719–733 (2023).

58. Emge, J. R. *et al.* Modulation of the microbiota-gut-brain axis by probiotics in a murine model of inflammatory bowel disease. *Am J Physiol Gastrointest Liver Physiol* **310**, G989–G998 (2016).

59. Segers, M. E. & Lebeer, S. Towards a better understanding of Lactobacillus rhamnosus GG - host interactions. *Microb Cell Fact* **13**, 1–16 (2014).

60. O'Callaghan, A. & van Sinderen, D. Bifidobacteria and their role as members of the human gut microbiota. *Front Microbiol* **7**, 206360 (2016).

61. Kaper, J. B., Nataro, J. P. & Mobley, H. L. T. Pathogenic Escherichia coli. *Nature Reviews Microbiology 2004 2:2* **2**, 123–140 (2004).

62. Theriot, C. M. & Young, V. B. Interactions between the Gastrointestinal Microbiome and Clostridium difficile. *Annu Rev Microbiol* **69**, 445–461 (2015).

63. Jiang, W. *et al.* Dysbiosis gut microbiota associated with inflammation and impaired mucosal immune function in intestine of humans with non-alcoholic fatty liver disease. *Scientific Reports 2015 5:1* **5**, 1–7 (2015).

64. Feng, C., Gao, G., Wu, K. & Weng, X. Causal relationship between gut microbiota and constipation: a bidirectional Mendelian randomization study. *Front Microbiol* **15**, 1438778 (2024).

65. Ren, J. *et al.* Microbial imbalance in Chinese children with diarrhea or constipation. *Scientific Reports 2024 14:1* **14**, 1–11 (2024).

66. Sherwood, L. The Blood Vessels and Blood Pressure. *Human Physiology: From Cells to Systems* 335–379 (2016).

67. Guido, Mch., SCHcognato, S., SacCHi, D. & Ludwig, K. The Anatomy and Histology of the Liver and Biliary Tract. *Pediatric Hepatology and Liver Transplantation* 41–55 (2019) doi:10.1007/978-3-319-96400-3_3.

68. W. Rodwell V. & Murray R. Biochemistry & Medicine. in *Harper's Illustrated Biochemistry* (McGraw Hill Medical, 2018).

69. Szabo, G., Bala, S., Petrasek, J. & Gattu, A. Gut-liver axis and sensing microbes. *Digestive Diseases* **28**, 737–744 (2010).

70. Kumar V., Abbas A. & Aster J. *Robbins Basic Pathology*. (Elsevier Shop, 2017).

71. Krenkel, O. & Tacke, F. Liver macrophages in tissue homeostasis and disease. *Nat Rev Immunol* **17**, 306–321 (2017).

72. Gan, C. *et al.* Liver diseases: epidemiology, causes, trends and predictions. *Signal Transduction and Targeted Therapy 2025 10:1* **10**, 1–36 (2025).

73. Bogdanos, D. P., Gao, B. & Gershwin, M. E. Liver Immunology. *Compr Physiol* **3**, 567 (2013).

74. Pabst, O. *et al.* Gut–liver axis: barriers and functional circuits. *Nature Reviews Gastroenterology & Hepatology 2023 20:7* **20**, 447–461 (2023).

75. Chen, W. *et al.* A Special Network Comprised of Macrophages, Epithelial Cells, and Gut Microbiota for Gut Homeostasis. *Cells* **11**, (2022).

76. Sonnenburg, E. D. *et al.* Diet-induced extinctions in the gut microbiota compound over generations. *Nature* **529**, 212–215 (2016).

77. Vacca, M. *et al.* An unbiased ranking of murine dietary models based on their proximity to human metabolic dysfunction-associated steatotic liver disease (MASLD). *Nature Metabolism 2024 6:6* **6**, 1178–1196 (2024).

78. Zeng, N. *et al.* High-fat diet impairs gut barrier through intestinal microbiota-derived reactive oxygen species. *Sci China Life Sci* **67**, 879–891 (2024).

79. Zhang, Q. *et al.* A high-trans fat, high-carbohydrate, high-cholesterol, high-cholate diet-induced nonalcoholic steatohepatitis mouse model and its hepatic immune response. *Nutr Metab (Lond)* **20**, 1–12 (2023).

80. Wang, J., Chen, W. D. & Wang, Y. D. The Relationship Between Gut Microbiota and Inflammatory Diseases: The Role of Macrophages. *Front Microbiol* **11**, 535016 (2020).

81. Albillos, A., de Gottardi, A. & Rescigno, M. The gut-liver axis in liver disease: Pathophysiological basis for therapy. *J Hepatol* **72**, 558–577 (2020).

82. Rollet, M., Bohn, T. & Vahid, F. Association between Dietary Factors and Constipation in Adults Living in Luxembourg and Taking Part in the ORISCAV-LUX 2 Survey. *Nutrients 2022, Vol. 14, Page 122* **14**, 122 (2021).

83. Aguiar, S. L. F. *et al.* High-salt diet induces IL-17-dependent gut inflammation and exacerbates colitis in mice. *Front Immunol* **8**, 1969 (2018).

84. Birchenough, G. M. H., Johansson, M. E. V., Gustafsson, J. K., Bergström, J. H. & Hansson, G. C. New developments in goblet cell mucus secretion and function. *Mucosal Immunol* **8**, 712–719 (2015).

85. Miranda, P. M. *et al.* High salt diet exacerbates colitis in mice by decreasing Lactobacillus levels and butyrate production. *Microbiome* **6**, 57 (2018).

86. Wang, C. *et al.* High-salt diet has a certain impact on protein digestion and gut microbiota: A sequencing and proteome combined study. *Front Microbiol* **8**, 290188 (2017).

87. Wang, C. *et al.* Role of bile acids in dysbiosis and treatment of nonalcoholic fatty liver disease. *Mediators Inflamm* **2019**, (2019).

88. Metchnikoff, E. J. B. Z. Untersuchungen über die mesodermalen Phagocyten einiger Wirbeltiere. *Biol Zentralbl 3* vol. 560 Preprint at (1883).

89. Merien, F. A Journey with Elie Metchnikoff: From Innate Cell Mechanisms in Infectious Diseases to Quantum Biology. *Front Public Health* **4**, 185770 (2016).

90. Lavin, Y. *et al.* Tissue-resident macrophage enhancer landscapes are shaped by the local microenvironment. *Cell* **159**, 1312–1326 (2014).

91. Mass, E., Nimmerjahn, F., Kierdorf, K. & Schlitzer, A. Tissue-specific macrophages: how they develop and choreograph tissue biology. *Nature Reviews Immunology 2023 23:9* **23**, 563–579 (2023).

92. Chen, S. *et al.* Macrophages in immunoregulation and therapeutics. *Signal Transduction and Targeted Therapy 2023 8:1* **8**, 1–35 (2023).

93. Hoeffel, G. & Ginhoux, F. Ontogeny of tissue-resident macrophages. *Front Immunol* **6**, 162667 (2015).

94. McGrath, K. E., Frame, J. M. & Palis, J. Early hematopoiesis and macrophage development. *Semin Immunol* **27**, 379 (2016).

95. McGrath, K. E. *et al.* Distinct Sources of Hematopoietic Progenitors Emerge before HSCs and Provide Functional Blood Cells in the Mammalian Embryo. *Cell Rep* **11**, 1892–1904 (2015).

96. Mass, E. *et al.* Specification of tissue-resident macrophages during organogenesis. *Science (1979)* **353**, (2016).

97. Mass, E. & Gentek, R. Fetal-Derived Immune Cells at the Roots of Lifelong Pathophysiology. *Front Cell Dev Biol* **9**, (2021).

98. Gomez Perdiguero, E. *et al.* Tissue-resident macrophages originate from yolk-sac-derived erythro-myeloid progenitors. *Nature* **518**, 547–551 (2015).

99. Morrison, S. J. & Scadden, D. T. The bone marrow niche for haematopoietic stem cells. *Nature 2014 505:7483* **505**, 327–334 (2014).

100. Iwasaki, H. & Akashi, K. Myeloid Lineage Commitment from the Hematopoietic Stem Cell. *Immunity* **26**, 726–740 (2007).

101. Osawa, M., Hanada, K. I., Hamada, H. & Nakauchi, H. Long-term lymphohematopoietic reconstitution by a single CD34- low/negative hematopoietic stem cell. *Science (1979)* **273**, 242–245 (1996).

102. Busch, K. *et al.* Fundamental properties of unperturbed haematopoiesis from stem cells in vivo. *Nature* **518**, 542–546 (2015).

103. Hettinger, J. *et al.* Origin of monocytes and macrophages in a committed progenitor. *Nat Immunol* **14**, 821–830 (2013).

104. Viola, M. F. & Boeckxstaens, G. Niche-specific functional heterogeneity of intestinal resident macrophages. *Gut* **70**, 1383–1395 (2021).

105. Dick, S. A. *et al.* Three tissue resident macrophage subsets coexist across organs with conserved origins and life cycles. *Sci Immunol* **7**, (2022).

106. Tan, S. Y. S. & Krasnow, M. A. Developmental origin of lung macrophage diversity. *Development (Cambridge)* **143**, 1318–1327 (2016).

107. De Schepper, S. *et al.* Self-Maintaining Gut Macrophages Are Essential for Intestinal Homeostasis. *Cell* **175**, 400-415.e13 (2018).

108. Liu, Z. *et al.* Fate Mapping via Ms4a3-Expression History Traces Monocyte-Derived Cells. *Cell* **178**, 1509-1525.e19 (2019).

109. Xu, Y., Schrank, P. R. & Williams, J. W. Macrophage Fate Mapping. *Curr Protoc* **2**, e456 (2022).

110. Huang, H. *et al.* Kupffer cell programming by maternal obesity triggers fatty liver disease. *Nature 2025* **5**, 1–9 (2025).

111. Zigmond, E. *et al.* Macrophage-Restricted Interleukin-10 Receptor Deficiency, but Not IL-10 Deficiency, Causes Severe Spontaneous Colitis. *Immunity* **40**, 720–733 (2014).

112. Schridde, A. *et al.* Tissue-specific differentiation of colonic macrophages requires TGFβ receptor-mediated signaling. *Mucosal Immunol* **10**, 1387–1399 (2017).

113. Bain, C. C. *et al.* Resident and pro-inflammatory macrophages in the colon represent alternative context-dependent fates of the same Ly6C hi monocyte precursors. *Mucosal Immunol* **6**, 498–510 (2013).

114. Bain, C. C. & Schridde, A. Origin, Differentiation, and Function of Intestinal Macrophages. *Front Immunol* **9**, 2733 (2018).

115. Gabanyi, I. *et al.* Neuro-immune Interactions Drive Tissue Programming in Intestinal Macrophages. *Cell* **164**, 378–391 (2016).

116. Muller, P. A. *et al.* Crosstalk between muscularis macrophages and enteric neurons regulates gastrointestinal motility. *Cell* **158**, 300–313 (2014).

117. Ma, T. Y. *et al.* TNF-α-induced increase in intestinal epithelial tight junction permeability requires NF-κB activation. *Am J Physiol Gastrointest Liver Physiol* **286**, (2004).

118. Pull, S. L., Doherty, J. M., Mills, J. C., Gordon, J. I. & Stappenbeck, T. S. Activated macrophages are an adaptive element of the colonic epithelial progenitor niche necessary for regenerative responses to injury. *Proc Natl Acad Sci U S A* **102**, 99–104 (2005).

119. Bain, C. C. *et al.* Constant replenishment from circulating monocytes maintains the macrophage pool in the intestine of adult mice. *Nat Immunol* **15**, 929–937 (2014).

120. Shaw, T. N. *et al.* Tissue-resident macrophages in the intestine are long lived and defined by Tim-4 and CD4 expression. *Journal of Experimental Medicine* **215**, 1507–1518 (2018).

121. Viola, M. F. & Boeckxstaens, G. Intestinal resident macrophages: Multitaskers of the gut. *Neurogastroenterology and Motility* **32**, (2020).

122. Chiaranunt, P., Tai, S. L., Ngai, L. & Mortha, A. Beyond Immunity: Underappreciated Functions of Intestinal Macrophages. *Front Immunol* **12**, 749708 (2021).

123. Asano, K. *et al.* Intestinal CD169 + macrophages initiate mucosal inflammation by secreting CCL8 that recruits inflammatory monocytes. *Nat Commun* **6**, (2015).

124. Honda, M. *et al.* Perivascular localization of macrophages in the intestinal mucosa is regulated by Nr4a1 and the microbiome. *Nature Communications 2020 11:1* **11**, 1–17 (2020).

125. Gross-Vered, M. *et al.* Defining murine monocyte differentiation into colonic and ileal macrophages. *Elife* **9**, (2020).

126. Rao, M. & Gershon, M. D. The bowel and beyond: the enteric nervous system in neurological disorders. *Nature Reviews Gastroenterology & Hepatology 2016 13:9* **13**, 517–528 (2016).

127. Stakenborg, N., Viola, M. F. & Boeckxstaens, G. E. Intestinal neuro-immune interactions: focus on macrophages, mast cells and innate lymphoid cells. *Curr Opin Neurobiol* **62**, 68 (2020).

128. Hashimoto, D. *et al.* Tissue-Resident Macrophages Self-Maintain Locally throughout Adult Life with Minimal Contribution from Circulating Monocytes. *Immunity* **38**, 792–804 (2013).

129. Yip, J. L. K., Balasuriya, G. K., Spencer, S. J. & Hill-Yardin, E. L. The Role of Intestinal Macrophages in Gastrointestinal Homeostasis: Heterogeneity and Implications in Disease. *Cell Mol Gastroenterol Hepatol* **12**, 1701 (2021).

130. Asano, K., Kikuchi, K. & Tanaka, M. CD169 macrophages regulate immune responses toward particulate materials in the circulating fluid. *J Biochem* **164**, 77–85 (2018).

131. Asano, K. *et al.* Intestinal CD169+ macrophages initiate mucosal inflammation by secreting CCL8 that recruits inflammatory monocytes. *Nature Communications 2015 6:1* **6**, 1–14 (2015).

132. Sehgal, A. *et al.* The role of CSF1R-dependent macrophages in control of the intestinal stem-cell niche. *Nature Communications 2018 9:1* **9**, 1–17 (2018).

133. Wagner, C. *et al.* Some news from the unknown soldier, the Peyer's patch macrophage. *Cell Immunol* **330**, 159–167 (2018).

134. Kupffer, C. Ueber Sternzellen der Leber - Briefliche Mittheilung an Prof. Waldeyer. *Archiv für Mikroskopische Anatomie* **12**, 353–358 (1876).

135. Bilzer, M., Roggel, F. & Gerbes, A. L. Role of Kupffer cells in host defense and liver disease. *Liver International* **26**, 1175–1186 (2006).

136. Kulle, A., Thanabalasuriar, A., Cohen, T. S. & Szydlowska, M. Resident macrophages of the lung and liver: The guardians of our tissues. *Front Immunol* **13**, 1029085 (2022).

137. Scott, C. L. *et al.* Bone marrow-derived monocytes give rise to self-renewing and fully differentiated Kupffer cells. *Nat Commun* **7**, 10321 (2016).

138. Li, W., Chang, N. & Li, L. Heterogeneity and Function of Kupffer Cells in Liver Injury. *Front Immunol* **13**, 940867 (2022).

139. Zhao, D. *et al.* GDF2 and BMP10 coordinate liver cellular crosstalk to maintain liver health. *Elife* **13**, (2024).

140. De Simone, G. *et al.* Identification of a Kupffer cell subset capable of reverting the T cell dysfunction induced by hepatocellular priming. *Immunity* **54**, 2089-2100.e8 (2021).

141. Blériot, C. *et al.* A subset of Kupffer cells regulates metabolism through the expression of CD36. *Immunity* **54**, 2101-2116.e6 (2021).

142. Guilliams, M. *et al.* Spatial proteogenomics reveals distinct and evolutionarily conserved hepatic macrophage niches. *Cell* **185**, 379-396.e38 (2022).

143. Sierro, F. *et al.* A Liver Capsular Network of Monocyte-Derived Macrophages Restricts Hepatic Dissemination of Intraperitoneal Bacteria by Neutrophil Recruitment. *Immunity* **47**, 374-388.e6 (2017).

144. Scott, C. L. *et al.* The Transcription Factor ZEB2 Is Required to Maintain the Tissue-Specific Identities of Macrophages. *Immunity* **49**, 312-325.e5 (2018).

145. Guilliams, M. & Scott, C. L. Liver macrophages in health and disease. *Immunity* **55**, 1515–1529 (2022).

146. Fabre, T. *et al.* Identification of a broadly fibrogenic macrophage subset induced by type 3 inflammation. *Sci Immunol* **8**, (2023).

147. Timperi, E. *et al.* Lipid-Associated Macrophages Are Induced by Cancer-Associated Fibroblasts and Mediate Immune Suppression in Breast Cancer. *Cancer Res* **82**, 3291–3306 (2022).

148. Wang, H. *et al.* PKC-α contributes to high NaCl-induced activation of NFAT5 (TonEBP/OREBP) through MAPK ERK1/2. *Am J Physiol Renal Physiol* **308**, F140–F148 (2015).

149. MacHnik, A. *et al.* Macrophages regulate salt-dependent volume and blood pressure by a vascular endothelial growth factor-C-dependent buffering mechanism. *Nat Med* **15**, 545–552 (2009).

150. Mayes-Hopfinger, L. *et al.* Chloride sensing by WNK1 regulates NLRP3 inflammasome activation and pyroptosis. *Nature Communications 2021 12:1* **12**, 1–17 (2021).

151. Perry, J. S. A. *et al.* Interpreting an apoptotic corpse as anti-inflammatory involves a chloride sensing pathway. *Nat Cell Biol* **21**, 1532–1543 (2019).

152. Zhang, W. C. *et al.* High salt primes a specific activation state of macrophages, M(Na). *Cell Res* **25**, 893 (2015).

153. Kleinewietfeld, M. *et al.* Sodium chloride drives autoimmune disease by the induction of pathogenic TH 17 cells. *Nature* **496**, 518–522 (2013).

154. Risco, A. *et al.* P38γ and p38δ kinases regulate the Toll-like receptor 4 (TLR4)-induced cytokine production by controlling ERK1/2 protein kinase pathway activation. *Proc Natl Acad Sci U S A* **109**, 11200–11205 (2012).

155. Datta, R. *et al.* PARP-1 deficiency blocks IL-5 expression through calpain-dependent degradation of STAT-6 in a murine asthma model. *Allergy: European Journal of Allergy and Clinical Immunology* **66**, 853–861 (2011).

156. Zhang, W. C. *et al.* Elevated sodium chloride drives type I interferon signaling in macrophages and increases antiviral resistance. *J Biol Chem* **293**, 1030 (2017).

157. Müller, L. *et al.* Differential impact of high-salt levels in vitro and in vivo on macrophage core functions. *Mol Biol Rep* **51**, (2024).

158. Hucke, S. *et al.* Sodium chloride promotes pro-inflammatory macrophage polarization thereby aggravating CNS autoimmunity. *J Autoimmun* **67**, 90–101 (2016).

159. Müller, S. *et al.* Salt-Dependent Chemotaxis of Macrophages. *PLoS One* **8**, (2013).

160. Hansen, J. N. *et al.* MotiQ: an open-source toolbox to quantify the cell motility and morphology of microglia. *Mol Biol Cell* **33**, (2022).

161. Neuberger-Castillo, L. *et al.* Method Validation for Extraction of DNA from Human Stool Samples for Downstream Microbiome Analysis. *Biopreserv Biobank* **18**, 102–116 (2020).

162. Kable, M. E., Chin, E. L., Storms, D., Lemay, D. G. & Stephensen, C. B. Tree-Based Analysis of Dietary Diversity Captures Associations between Fiber Intake and Gut Microbiota Composition in a Healthy US Adult Cohort. *Journal of Nutrition* **152**, 779–788 (2022).

163. Junkins, E. N., McWhirter, J. B., McCall, L.-I. & Stevenson, B. S. Environmental structure impacts microbial composition and secondary metabolism. *ISME Communications 2022 2:1* **2**, 1–10 (2022).

164. Seel, W., Reiners, S., Kipp, K., Simon, M. C. & Dawczynski, C. Role of Dietary Fiber and Energy Intake on Gut Microbiome in Vegans, Vegetarians, and Flexitarians in Comparison to Omnivores—Insights from the Nutritional Evaluation (NuEva) Study. *Nutrients* **15**, (2023).

165. Bolyen, E. *et al.* Reproducible, interactive, scalable and extensible microbiome data science using QIIME 2. *Nat Biotechnol* **37**, 852–857 (2019).

166. Callahan, B. J. *et al.* DADA2: High-resolution sample inference from Illumina amplicon data. *Nat Methods* **13**, 581–583 (2016).

167. Lu, Y. *et al.* MicrobiomeAnalyst 2.0: Comprehensive statistical, functional and integrative analysis of microbiome data. *Nucleic Acids Res* **51**, W310–W318 (2023).

168. Chong, J., Liu, P., Zhou, G. & Xia, J. Using MicrobiomeAnalyst for comprehensive statistical, functional, and meta-analysis of microbiome data. *Nature Protocols 2020 15:3* **15**, 799–821 (2020).

169. Madsen, K. L., Doyle, J. S., Jewell, L. D., Tavernini, M. M. & Fedorak, R. N. Lactobacillus species prevents colitis in interleukin 10 gene-deficient mice. *Gastroenterology* **116**, 1107–1114 (1999).

170. Erben, U. *et al.* A guide to histomorphological evaluation of intestinal inflammation in mouse models. *Int J Clin Exp Pathol* **7**, 4557 (2014).

171. Chen, X. *et al.* Prevent effects of lactobacillus fermentum HY01 on dextran sulfate sodium-induced colitis in mice. *Nutrients* **9**, (2017).

172. Weaver, L. T., Austin, S. & Cole, T. J. Small intestinal length: A factor essential for gut adaptation. *Gut* **32**, 1321–1323 (1991).

173. Arrieta, M. C., Madsen, K., Doyle, J. & Meddings, J. Reducing small intestinal permeability attenuates colitis in the IL10 gene-deficient mouse. *Gut* **58**, 41–48 (2009).

174. Murakami, Y., Tanabe, S. & Suzuki, T. High-fat Diet-induced Intestinal Hyperpermeability is Associated with Increased Bile Acids in the Large Intestine of Mice. *J Food Sci* **81**, H216–H222 (2016).

175. Aguiar, S. L. F. *et al.* High-salt diet induces IL-17-dependent gut inflammation and exacerbates colitis in mice. *Front Immunol* **8**, 1969 (2018).

176. Gomez-Bris, R. *et al.* Segmental Regulation of Intestinal Motility by Colitis and the Adaptive Immune System in the Mouse Ileum and Colon. *Am J Pathol* **195**, 204–220 (2025).

177. Stuart, T. *et al.* Comprehensive Integration of Single-Cell Data. *Cell* **177**, 1888-1902.e21 (2019).

178. McInnes, L., Healy, J., Saul, N. & Großberger, L. UMAP: Uniform Manifold Approximation and Projection. *J Open Source Softw* **3**, 861 (2018).

179. Bording-Jorgensen, M., Armstrong, H., Wickenberg, M., LaPointe, P. & Wine, E. Macrophages and Epithelial Cells Mutually Interact through NLRP3 to Clear Infection and Enhance the Gastrointestinal Barrier. *Immuno* **2**, 13–25 (2022).

180. Takai, T. Roles of Fc receptors in autoimmunity. *Nature Reviews Immunology 2002 2:8* **2**, 580–592 (2002).

181. Rossini, V. *et al.* CX3CR1+ cells facilitate the activation of CD4 T cells in the colonic lamina propria during antigen-driven colitis. *Mucosal Immunology 2014 7:3* **7**, 533–548 (2013).

182. Noel, G. *et al.* A primary human macrophage-enteroid co-culture model to investigate mucosal gut physiology and host-pathogen interactions. *Scientific Reports 2017 7:1* **7**, 1–14 (2017).

183. Anand, R. J. *et al.* Activated macrophages inhibit enterocyte gap junctions via the release of nitric oxide. *Am J Physiol Gastrointest Liver Physiol* **294**, 109–119 (2007).

184. Vavassori, P., Mencarelli, A., Renga, B., Distrutti, E. & Fiorucci, S. The Bile Acid Receptor FXR Is a Modulator of Intestinal Innate Immunity. *The Journal of Immunology* **183**, 6251–6261 (2009).

185. Jin, S., Plikus, M. V. & Nie, Q. CellChat for systematic analysis of cell-cell communication from single-cell and spatially resolved transcriptomics. *bioRxiv* (2023) doi:10.1101/2023.11.05.565674.

186. Richardson, C. J. Z. *et al.* Activation of the thiazide-sensitive Na+-Cl– cotransporter by the WNK-regulated kinases SPAK and OSR1. *J Cell Sci* **121**, 675–684 (2008).

187. McCormick, J. A., Yang, C. L. & Ellison, D. H. WNK kinases and renal sodium transport in health and disease: an integrated view. *Hypertension* **51**, 588 (2008).

188. Tóth, K. *et al.* The NKCC1 ion transporter modulates microglial phenotype and inflammatory response to brain injury in a cell-autonomous manner. *PLoS Biol* **20**, e3001526 (2022).

189. Mutchler, S. M. *et al.* Long-Term High Salt Consumption Decreases Body Weight and Fat Accumulation in Mice in Association with Increased Energy Expenditure and Whole-body Fat Oxidation. *The FASEB Journal* **34**, 1–1 (2020).

190. Patel, S., Rauf, A., Khan, H. & Abu-Izneid, T. Renin-angiotensin-aldosterone (RAAS): The ubiquitous system for homeostasis and pathologies. *Biomedicine & Pharmacotherapy* **94**, 317–325 (2017).

191. Jantsch, J. *et al.* Cutaneous Na+ storage strengthens the antimicrobial barrier function of the skin and boosts macrophage-driven host defense. *Cell Metab* **21**, 493–501 (2015).

192. Rakova, N. *et al.* Long-term space flight simulation reveals infradian rhythmicity in human Na+ balance. *Cell Metab* **17**, 125–131 (2013).

193. Pan, R. *et al.* Imbalances in the gut microbiota and metabolome are associated with functional constipation in pregnancy. *Food Biosci* **59**, 103852 (2024).

194. Stanley, D., Geier, M. S., Chen, H., Hughes, R. J. & Moore, R. J. Comparison of fecal and cecal microbiotas reveals qualitative similarities but quantitative differences. *BMC Microbiol* **15**, 1–11 (2015).

195. Wilck, N. *et al.* Salt-responsive gut commensal modulates TH17 axis and disease. *Nature* **551**, 585 (2017).

196. Alexander, M. & Turnbaugh, P. J. Deconstructing mechanisms of diet-microbiome-immune interactions. *Immunity* **53**, 264 (2020).

197. Volk, J. K. *et al.* The Nlrp6 inflammasome is not required for baseline colonic inner mucus layer formation or function. *J Exp Med* **216**, 2602–2618 (2019).

198. Osborne, G. *et al.* The association between gut microbiome and anthropometric measurements in Bangladesh. *Gut Microbes* **11**, 63–76 (2019).

199. Li, Z. R. *et al.* Sargassum fusiforme polysaccharide partly replaces acarbose against type 2 diabetes in rats. *Int J Biol Macromol* **170**, 447–458 (2020).

200. Zhu, Y. *et al.* Exploration of the *Muribaculaceae* Family in the Gut Microbiota: Diversity, Metabolism, and Function. *Nutrients* **16**, 2660–2660 (2024).

201. Parker, B. J., Wearsch, P. A., Veloo, A. C. M. & Rodriguez-Palacios, A. The Genus Alistipes: Gut Bacteria With Emerging Implications to Inflammation, Cancer, and Mental Health. *Front Immunol* **11**, 522172 (2020).

202. Moschen, A. R. *et al.* Lipocalin 2 Protects from Inflammation and Tumorigenesis Associated with Gut Microbiota Alterations. *Cell Host Microbe* **19**, 455–469 (2016).

203. Hsu, C.-N. *et al.* Altered Gut Microbiota and Its Metabolites in Hypertension of Developmental Origins: Exploring Differences between Fructose and Antibiotics Exposure. *International Journal of Molecular Sciences 2021, Vol. 22, Page 2674* **22**, 2674 (2021).

204. Wu, P. *et al.* Intestinal mucosal and fecal microbiota profiles in Crohn's disease in Chinese children. *Medicine in Microecology* **15**, 100071 (2023).

205. Wei, W. *et al.* Fecal g. Streptococcus and g. Eubacterium_coprostanoligenes_group combined with sphingosine to modulate the serum dyslipidemia in high-fat diet mice. *Clinical Nutrition* **40**, 4234–4245 (2021).

206. Dewei, R., Ling, L., Schwabacher, A. W., Young, J. W. & Beitz, D. C. Mechanism of cholesterol reduction to coprostanol by Eubacterium coprostanoligenes ATCC 51222. *Steroids* **61**, 33–40 (1996).

207. Bolte, L. A. *et al.* Gut microbiota Long-term dietary patterns are associated with pro-inflammatory and anti-inflammatory features of the gut microbiome. *Gut* **0**, 1–12 (2021).

208. Abdulqadir, R., Engers, J. & Al-Sadi, R. Role of Bifidobacterium in Modulating the Intestinal Epithelial Tight Junction Barrier: Current Knowledge and Perspectives. *Curr Dev Nutr* **7**, 102026 (2023).

209. Liu, Z. *et al.* Dachengqi Decoction alleviates intestinal inflammation in ovalbumin-induced asthma by reducing group 2 innate lymphoid cells in a microbiota-dependent manner. *J Tradit Complement Med* **13**, 183–192 (2023).

210. Liong, M. T. & Shah, N. P. Production of organic acids from fermentation of mannitol, fructooligosaccharide and inulin by a cholesterol removing Lactobacillus acidophilus strain. *J Appl Microbiol* **99**, 783–793 (2005).

211. Smet, I. De, Boever, P. De & Verstraete, W. Cholesterol lowering in pigs through enhanced bacterial bile salt hydrolase activity. *Br J Nutr* **79**, 185–194 (1998).

212. Sovijit, W. N. *et al.* Ovarian progesterone suppresses depression and anxiety-like behaviors by increasing the Lactobacillus population of gut microbiota in ovariectomized mice. *Neurosci Res* **168**, 76–82 (2021).

213. Khamoushi, F. *et al.* Association between dietary inflammatory index and musculoskeletal disorders in adults. *Sci Rep* **13**, 20302 (2023).

214. Zheng, D., Wu, Z., Li, L., Cheng, S. & Chang, J. Genetic analysis of the causal relationship between gut microbiota and intervertebral disc degeneration: a two-sample Mendelian randomized study. *European Spine Journal* **33**, 1986–1998 (2024).

215. Thaiss, C. A., Zmora, N., Levy, M. & Elinav, E. The microbiome and innate immunity. *Nature 2016 535:7610* **535**, 65–74 (2016).

216. Stojanović, O. *et al.* Dietary excess regulates absorption and surface of gut epithelium through intestinal PPARα. *Nature Communications 2021 12:1* **12**, 1–15 (2021).

217. Xie, Y. *et al.* Impact of a high-fat diet on intestinal stem cells and epithelial barrier function in middle-aged female mice. *Mol Med Rep* **21**, 1133 (2020).

218. Kalafateli, M., Tourkochristou, E., Tsounis, E. P., Aggeletopoulou, I. & Triantos, C. New Insights into the Pathogenesis of Intestinal Fibrosis in Inflammatory Bowel Diseases: Focusing on Intestinal Smooth Muscle Cells. *Inflamm Bowel Dis* **31**, 579–592 (2025).

219. Powell, D. W., Pinchuk, I. V., Saada, J. I., Chen, X. & Mifflin, R. C. Mesenchymal cells of the intestinal lamina propria. *Annu Rev Physiol* **73**, 213–237 (2011).

220. Park, H. J., Kamm, M. A., Abbasi, A. M. & Talbot, I. C. Immunohistochemical study of the colonic muscle and innervation in idiopathic chronic constipation. *Dis Colon Rectum* **38**, 509–513 (1995).

221. Mishra, S. P. *et al.* A mechanism by which gut microbiota elevates permeability and inflammation in obese/diabetic mice and human gut. *Gut* **72**, 1848 (2023).

222. Mundy, R., MacDonald, T. T., Dougan, G., Frankel, G. & Wiles, S. Citrobacter rodentium of mice and man. *Cell Microbiol* **7**, 1697–1706 (2005).

223. Kamada, N., Chen, G. Y., Inohara, N. & Núñez, G. Control of pathogens and pathobionts by the gut microbiota. *Nat Immunol* **14**, 685–690 (2013).

224. Zhang, X. *et al.* Effects of High-Salt Intake on Glucose Metabolism, Liver Function, and the Microbiome in Rats: Influence of ACE Inhibitors and Angiotensin II Receptor Blockers. *Am J Physiol Cell Physiol* (2025) doi:10.1152/AJPCELL.01036.2024.

225. Zhang, Y. *et al.* Amelioration of hepatic steatosis by dietary essential amino acid-induced ubiquitination. *Mol Cell* **82**, 1528-1542.e10 (2022).

226. Jornayvaz, F. R. & Shulman, G. I. Diacylglycerol Activation of Protein Kinase Cε and Hepatic Insulin Resistance. *Cell Metab* **15**, 574 (2012).

227. Viola, A., Munari, F., Sánchez-Rodríguez, R., Scolaro, T. & Castegna, A. The metabolic signature of macrophage responses. *Front Immunol* **10**, 466337 (2019).

228. A-Gonzalez, N. *et al.* Apoptotic cells promote their own clearance and immune tolerance through activation of the nuclear receptor LXR. *Immunity* **31**, 245–258 (2009).

229. Han, J., Hajjar, D. P., Febbraio, M. & Nicholson, A. C. Native and modified low density lipoproteins increase the functional expression of the macrophage class B scavenger receptor, CD36. *Journal of Biological Chemistry* **272**, 21654–21659 (1997).

230. Javitt, N. B. Bile acid synthesis from cholesterol: regulatory and auxiliary pathways. *The FASEB Journal* **8**, 1308–1311 (1994).

231. Pols, T. W. H. *et al.* TGR5 activation inhibits atherosclerosis by reducing macrophage inflammation and lipid loading. *Cell Metab* **14**, 747–757 (2011).

232. Nowarski, R., Jackson, R. & Flavell, R. A. The Stromal Intervention: Regulation of Immunity and Inflammation at the Epithelial-Mesenchymal Barrier. *Cell* **168**, 362–375 (2017).

233. Zigmond, E. *et al.* Ly6Chi Monocytes in the Inflamed Colon Give Rise to Proinflammatory Effector Cells and Migratory Antigen-Presenting Cells. *Immunity* **37**, 1076–1090 (2012).

234. Latroche, C. *et al.* Coupling between Myogenesis and Angiogenesis during Skeletal Muscle Regeneration Is Stimulated by Restorative Macrophages. *Stem Cell Reports* **9**, 2018–2033 (2017).

235. Kalluri, R. & Weinberg, R. A. The basics of epithelial-mesenchymal transition. *J Clin Invest* **119**, 1420 (2009).

236. Smythies, L. E. *et al.* Human intestinal macrophages display profound inflammatory anergy despite avid phagocytic and bacteriocidal activity. *J Clin Invest* **115**, 66–75 (2005).

237. Van Elsas, M. J. *et al.* Invasive margin tissue-resident macrophages of high CD163 expression impede responses to T cell-based immunotherapy. *J Immunother Cancer* **11**, e006433 (2023).

238. Mori, M. *et al.* CD163+Macrophages Induce Endothelial-to-Mesenchymal Transition in Atheroma. *Circ Res* **135**, e4–e23 (2024).

239. Duggavathi, R. *et al.* The fatty acid binding protein 6 gene (Fabp6) is expressed in murine granulosa cells and is involved in ovulatory response to superstimulation. *J Reprod Dev* **61**, 237 (2015).

240. Wang, F. *et al.* Apolipoprotein A-IV: a protein intimately involved in metabolism. *J Lipid Res* **56**, 1403 (2015).

241. Lennartsson, J. & Rönnstrand, L. Stem cell factor receptor/c-Kit: From basic Science to clinical implications. *Physiol Rev* **92**, 1619–1649 (2012).

242. Takamatsu, H. & Kumanogoh, A. Diverse roles for semaphorin-plexin signaling in the immune system. *Trends Immunol* **33**, 127–135 (2012).

243. Sharpe, A. H. & Freeman, G. J. The B7–CD28 superfamily. *Nature Reviews Immunology 2002 2:2* **2**, 116–126 (2002).

244. Li, M. *et al.* Signaling pathways in macrophages: molecular mechanisms and therapeutic targets. *MedComm (Beijing)* **4**, e349 (2023).

245. Hermiston, M. L., Xu, Z. & Weiss, A. CD45: A critical regulator of signaling thresholds in immune cells. *Annu Rev Immunol* **21**, 107–137 (2003).

246. Zhang, W. C. *et al.* High salt primes a specific activation state of macrophages, M(Na). *Cell Research 2015 25:8* **25**, 893–910 (2015).

247. Nimmerjahn, F. & Ravetch, J. V. Fcγ receptors as regulators of immune responses. *Nature Reviews Immunology 2007 8:1* **8**, 34–47 (2008).

248. Mendoza-Coronel, E. & Ortega, E. Macrophage polarization modulates FcγR- and CD13-mediated phagocytosis and reactive oxygen species production, independently of receptor membrane expression. *Front Immunol* **8**, 252709 (2017).

249. Chuang, H.-J. ; *et al.* The Immunosuppressive Receptor CD32b Regulation of Macrophage Polarization and Its Implications in Tumor Progression. *International Journal of Molecular Sciences 2024, Vol. 25, Page 9737* **25**, 9737 (2024).

250. Rui, L. Energy metabolism in the liver. *Compr Physiol* **4**, 177–197 (2014).

251. Ju, C. & Tacke, F. Hepatic macrophages in homeostasis and liver diseases: from pathogenesis to novel therapeutic strategies. *Cell Mol Immunol* **13**, 316 (2016).

252. Nicoletti, A. *et al.* Intestinal permeability in the pathogenesis of liver damage: From non-alcoholic fatty liver disease to liver transplantation. *World J Gastroenterol* **25**, 4814–4834 (2019).

253. English, K. *et al.* The liver contains distinct interconnected networks of CX3CR1 + macrophages, XCR1 + type 1 and CD301a + type 2 conventional dendritic cells embedded within portal tracts. *Immunol Cell Biol* **100**, 394 (2022).

254. Tacke, F. & Zimmermann, H. W. Macrophage heterogeneity in liver injury and fibrosis. *J Hepatol* **60**, 1090–1096 (2014).

255. Huang, K. P. *et al.* Sex Differences in Response to Short-Term High Fat Diet in Mice. *Physiol Behav* **221**, 112894 (2020).

256. Pettersson, U. S., Waldén, T. B., Carlsson, P. O., Jansson, L. & Phillipson, M. Female Mice are Protected against High-Fat Diet Induced Metabolic Syndrome and Increase the Regulatory T Cell Population in Adipose Tissue. *PLoS One* **7**, e46057 (2012).

257. Tacke, F. & Zimmermann, H. W. Macrophage heterogeneity in liver injury and fibrosis. *J Hepatol* **60**, 1090–1096 (2014).

258. McDonald, B. *et al.* Programing of an Intravascular Immune Firewall by the Gut Microbiota Protects against Pathogen Dissemination during Infection. *Cell Host Microbe* **28**, 660-668.e4 (2020).

259. Feng, D. *et al.* Monocyte-derived macrophages orchestrate multiple cell-type interactions to repair necrotic liver lesions in disease models. *Journal of Clinical Investigation* **133**, (2023).

260. Ramachandran, P. *et al.* Resolving the fibrotic niche of human liver cirrhosis at single-cell level. *Nature 2019 575:7783* **575**, 512–518 (2019).

261. Wang, G. *et al.* Liver Fibrosis Can Be Induced by High Salt Intake through Excess Reactive Oxygen Species (ROS) Production. *J Agric Food Chem* **64**, 1610–1617 (2016).

262. Gao, P. *et al.* Salt-Induced Hepatic Inflammatory Memory Contributes to Cardiovascular Damage through Epigenetic Modulation of SIRT3. *Circulation* **145**, 375–391 (2022).

263. Tridandapani, S. & Anderson, C. L. Regulation of Phagocytosis by FcγRIIb and Phosphatases. (2013).

264. Levy, M., Kolodziejczyk, A. A., Thaiss, C. A. & Elinav, E. Dysbiosis and the immune system. *Nature Reviews Immunology 2017 17:4* **17**, 219–232 (2017).

265. Bain, C. C. & Mowat, A. M. Macrophages in intestinal homeostasis and inflammation. *Immunol Rev* **260**, 102–117 (2014).

266. Titze, J. *et al.* Osmotically inactive skin Na+ storage in rats. *Am J Physiol Renal Physiol* **285**, 1108–1117 (2003).

267. MacHnik, A. *et al.* Macrophages regulate salt-dependent volume and blood pressure by a vascular endothelial growth factor-C–dependent buffering mechanism. *Nature Medicine 2009 15:5* **15**, 545–552 (2009).

268. Müller, S. *et al.* Salt-Dependent Chemotaxis of Macrophages. *PLoS One* **8**, (2013).

Appendix

I. Supplementary methods

a. Na^+ and K^+ measurement in gut and liver

In line with Aim 1 of the study, which investigates the impact of a high-salt diet (HSD) on gut and liver homeostasis, checking sodium and potassium concentrations in these tissues would provide insights into ion accumulation and potential disruptions in osmotic and electrolyte balance that might drive downstream immune or structural changes. After 3 months on a CD or HSD, mice of both sexes were anesthetized and transcardially perfused to remove residual blood from the tissues. Perfusion was performed using 0.29M sucrose solution to preserve osmotic balance in the tissues while. Tissues were then collected and weighted (wet weight) and then frozen at -80°C.

Ashing Procedure and Chemical Analysis was done by Dr. Agnes Schroeder from Jantsch Lab, Institute for Medical Microbiology, Immunology and Hygiene, University of Cologne. The weighted tissued (wet weight) were desiccated at 80°C for 72 hours (dry weight). The difference between wet weight and dry weight was considered as tissue water content. After desiccation, the tissues were ashed at 200°C, 400°C, and 600°C for 24 hours at each temperature level and then dissolved in 5% HNO3. Na^+ and K^+ concentrations were measured by atomic absorption spectrometry [266]. Concentrations of Na^+ and K^+ in the tissues were determined per dry weight (mmol/g), except for Mesenteric lymph nodes, were measured per wet weight (µmol/g).

II. Supplementary results

a. Sodium storage in the gastrointestinal tract and the liver

Previous studies showed that a portion of excess salt intake is stored in the body tissues, specifically in the skin of rat models (Machnik et al., 2009). MΦ accumulate in these high-sodium regions, contributing to pathological responses [268]. Thus far, no research studies have investigated sodium concentration levels in the gut regions, liver, and also brain following HSD. Using mass spectrometry, sodium, and potassium concentrations were analyzed after the long-term HSD in the following tissues: the liver, brain, and gastrointestinal tract regions, including the stomach, duodenum, jejunum, ileum, caecum, colon, and mesenteric lymph nodes (mLN). HSD, despite its high salt content in both food and water, had no significant impact on sodium and potassium concentrations stored in the analyzed tissues compared to CD, as shown in Figures 2 and 3. These findings suggest that excess absorbed Na^+ is directed to the bloodstream without accumulation in the gut or liver, due to their main physiological role in absorption and metabolism, and the lack of sodium-binding matrices as found in the skin and muscles.

b. Liver weight changes after HSD

Liver weights from CD and HSD-fed groups were analyzed, revealing no significant changes in actual liver weight in short- and long-term HSD-fed mice in both sexes (Figure 14 A, C). However, short-term HSD-fed female mice showed an increase in liver weight percentage of body weight (LW/BW) compared to CD-fed mice, though this increase was not observed after the long-term HSD (Figure 14B). Also, no LW/BW changes were observed in HSD-fed male groups, indicating no HSD-induced liver enlargement in males (Figure 14D).

III. Supplementary Figures

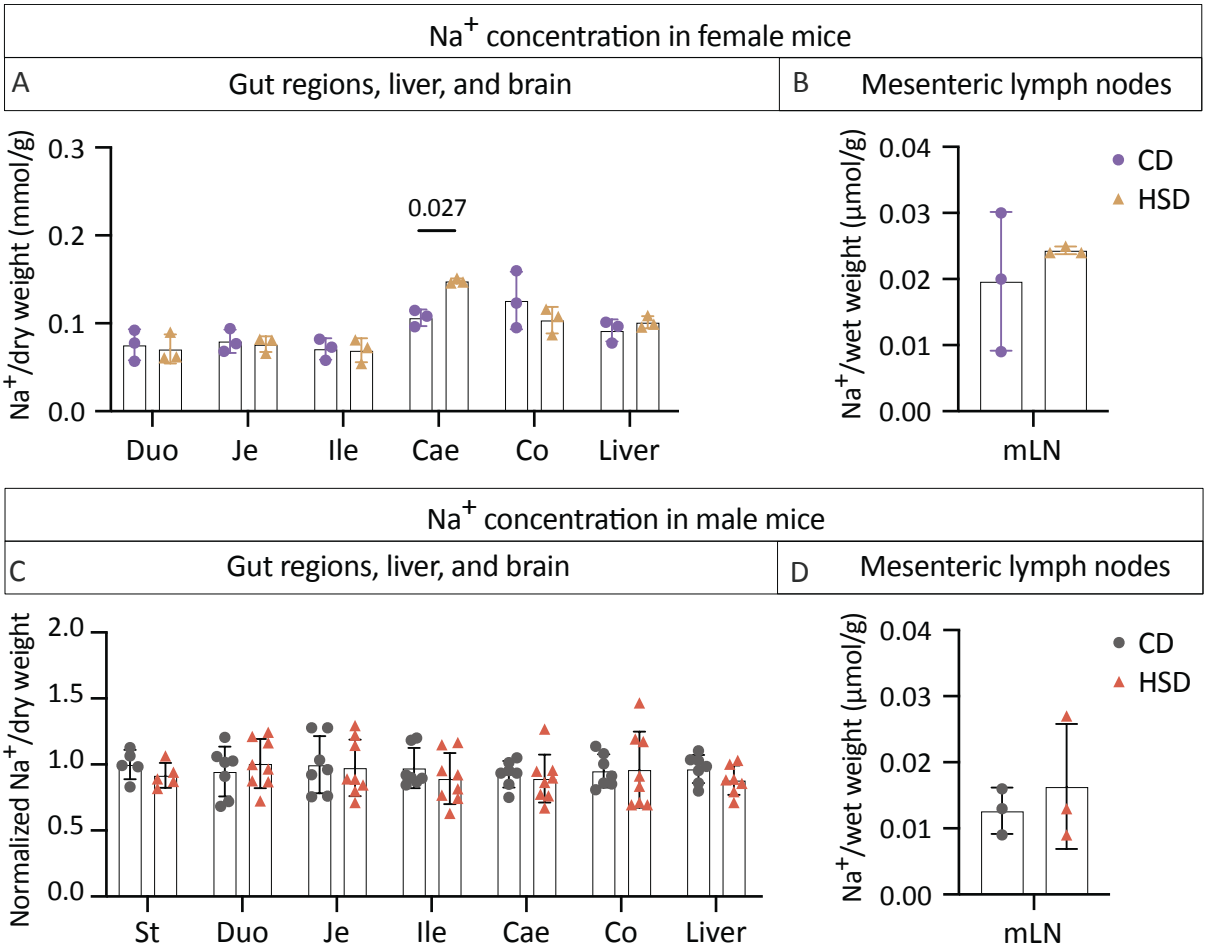

Supplementary Figure 1 Sodium concentration in mice organs upon long-term HSD. 8-week-old mice were fed either CD or HSD for 3 months to achieve long-term HSD treatment. A) Na^+ concentration in female mice gut regions, liver, and B) mesenteric lymph nodes (mLN) (n=3), C) Na^+ concentration in male mice gut regions, liver, and D) mLN (n=8 from 2 experiments, stomach n=5, mLN n=3), t-test for mLN, Two-way ANOVA for the rest. St, Stomach; Duo, Duodenum; Je, Jejunum; Ile, Ileum; Cae, Caecum; Co, Colon, mLN, mesenteric lymph nodes; CD, Control diet; HSD, High salt diet.

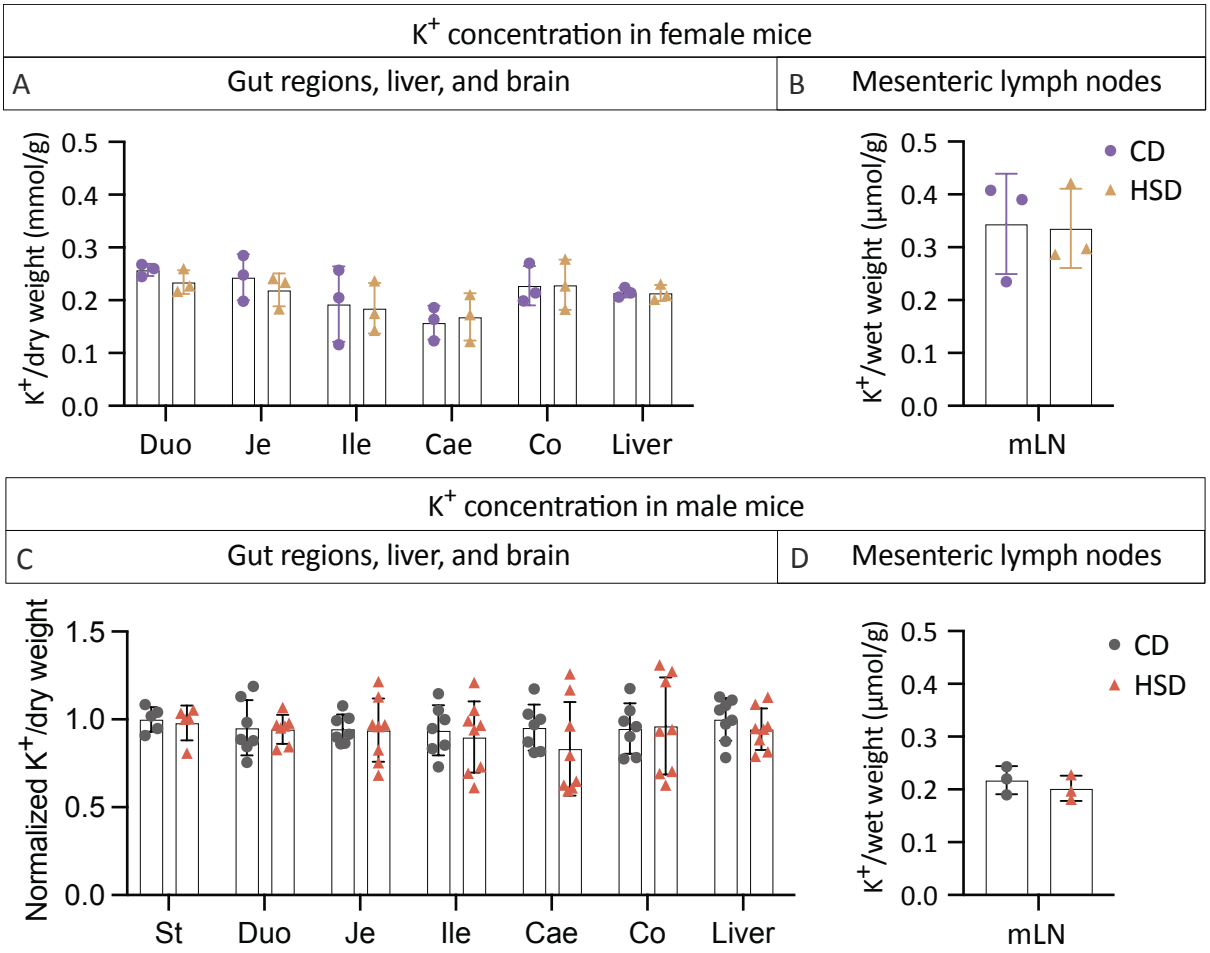

Supplementary Figure 2 Potassium concentration in mice organs upon long-term HSD. 8-week-old mice were fed either CD or HSD for 3 months to achieve long-term HSD treatment. A) K^+ concentration in female mice gut regions, liver, and B) mesenteric lymph nodes (mLN) (n=3), C) K^+ concentration in male mice gut regions, liver (n=8 from 2 experiments, stomach n=5), and D) mesenteric lymph nodes (mLN) (n=3); t-test for mLN, Two-way ANOVA for the rest. St, Stomach; Duo, Duodenum; Je, Jejunum; Ile, Ileum; Cae, Caecum; Co, Colon, MLN, Mesenteric lymph nodes; CD, Control diet; HSD, High salt diet.

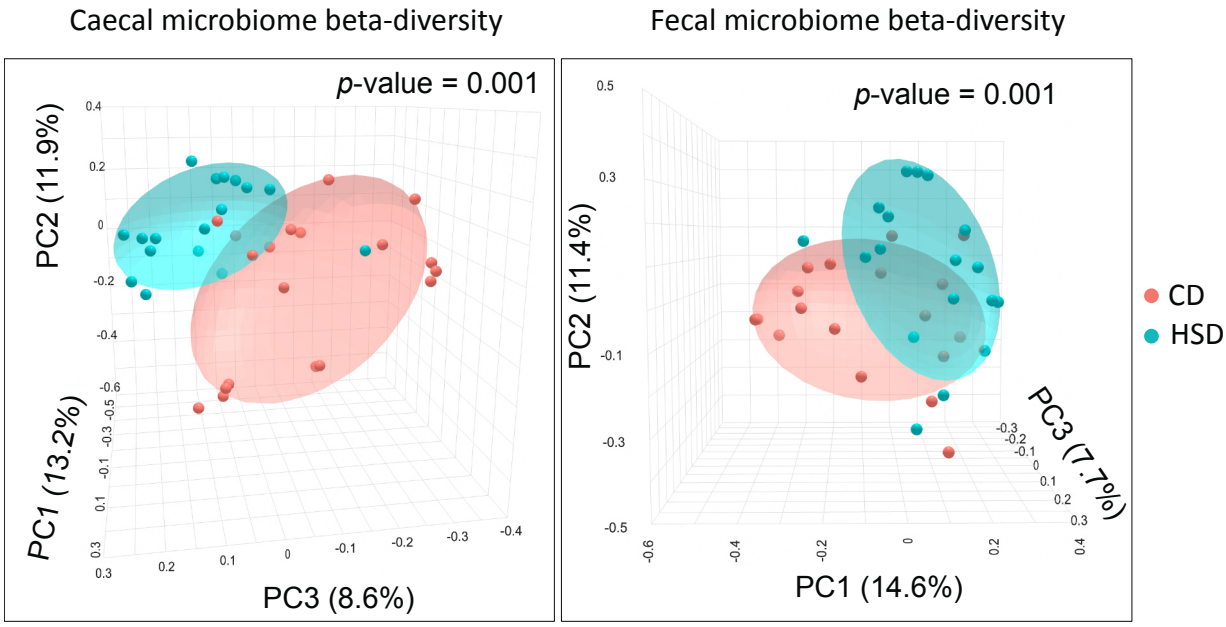

Supplementary Figure 3 3D plot of beta diversity changes of caecal and fecal microbiome in male mice following long-term HSD (distance metric Jaccard, male mice n = 17-19, p-values were obtained using PERMANOVA test).

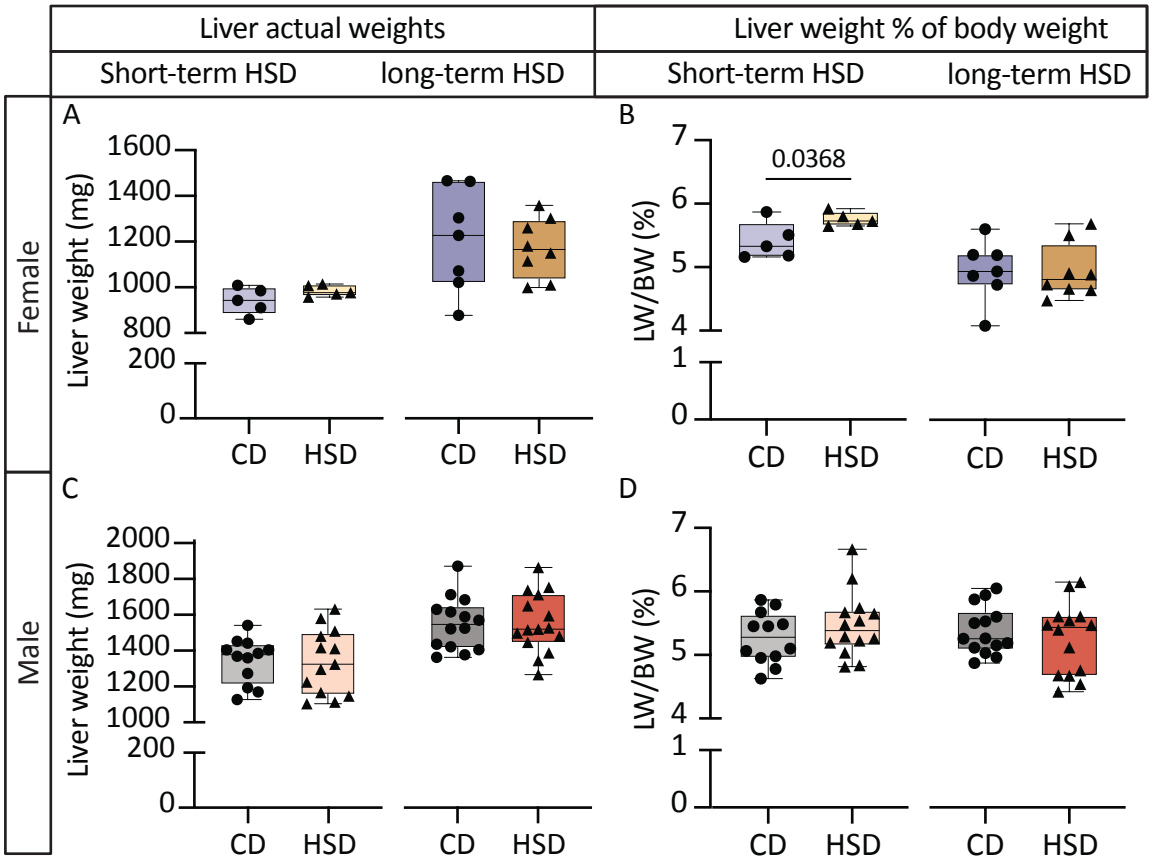

Supplementary Figure 4 Liver weight changes in female and male mice upon short- and long-term HSD. Mice were fed HSD and CD for 3 weeks or 3 months to achieve short- or long-term HSD models.

Livers were collected and weighted directly; Short-term HSD female: n= 5 from one experiment, long-term HSD female: n=7-8 from 2 experiments, males: n=12-1 from 3 experiments, Unpaired t-test.

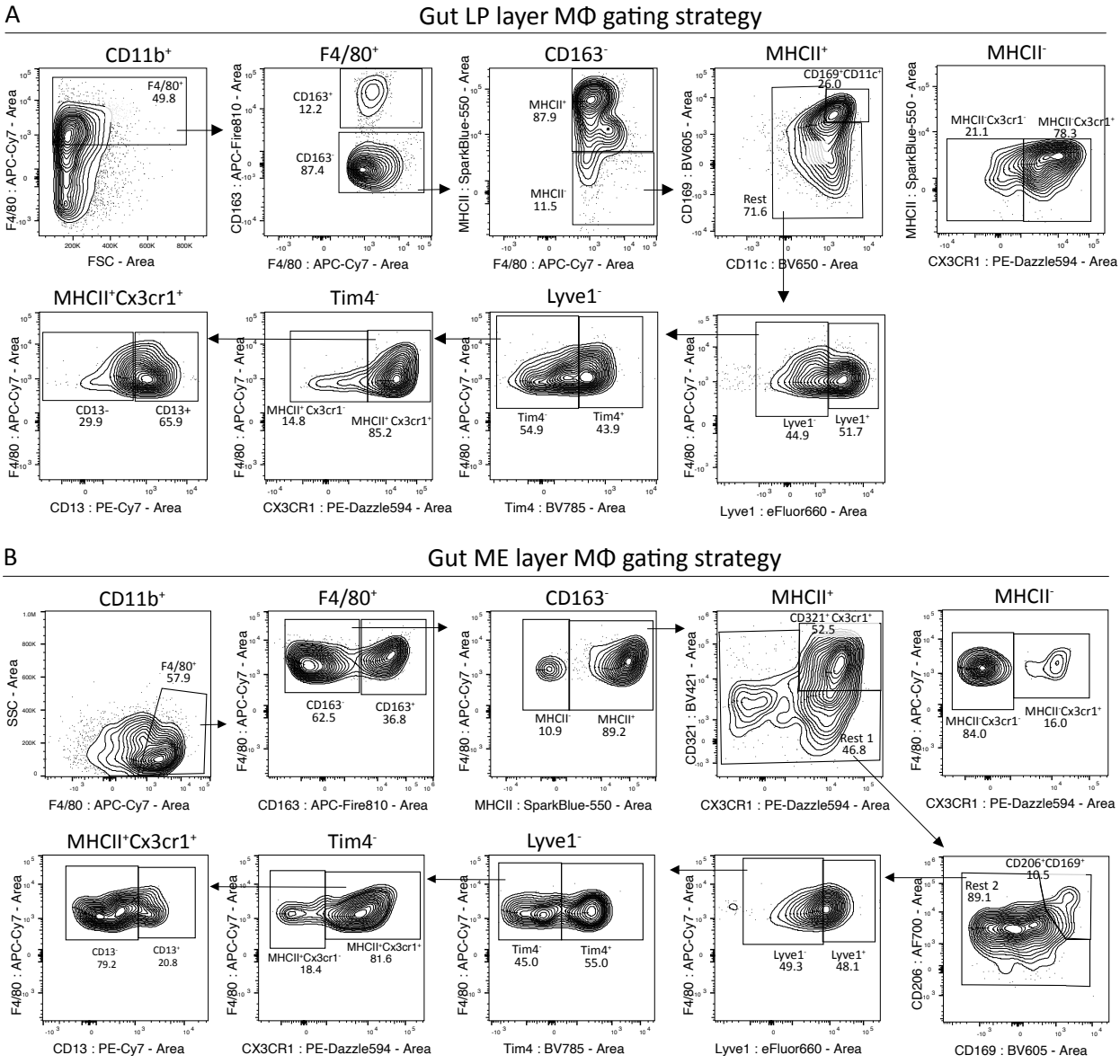

Supplementary Figure 5 Flow cytometry gating strategy of MΦ subpopulations in wildtype mouse gut LP and ME layers. Gut LP and ME layers were separated, underwent mechanical and enzymatic digestion to reach single-cell suspension, and then stained for Flow cytometry analysis.

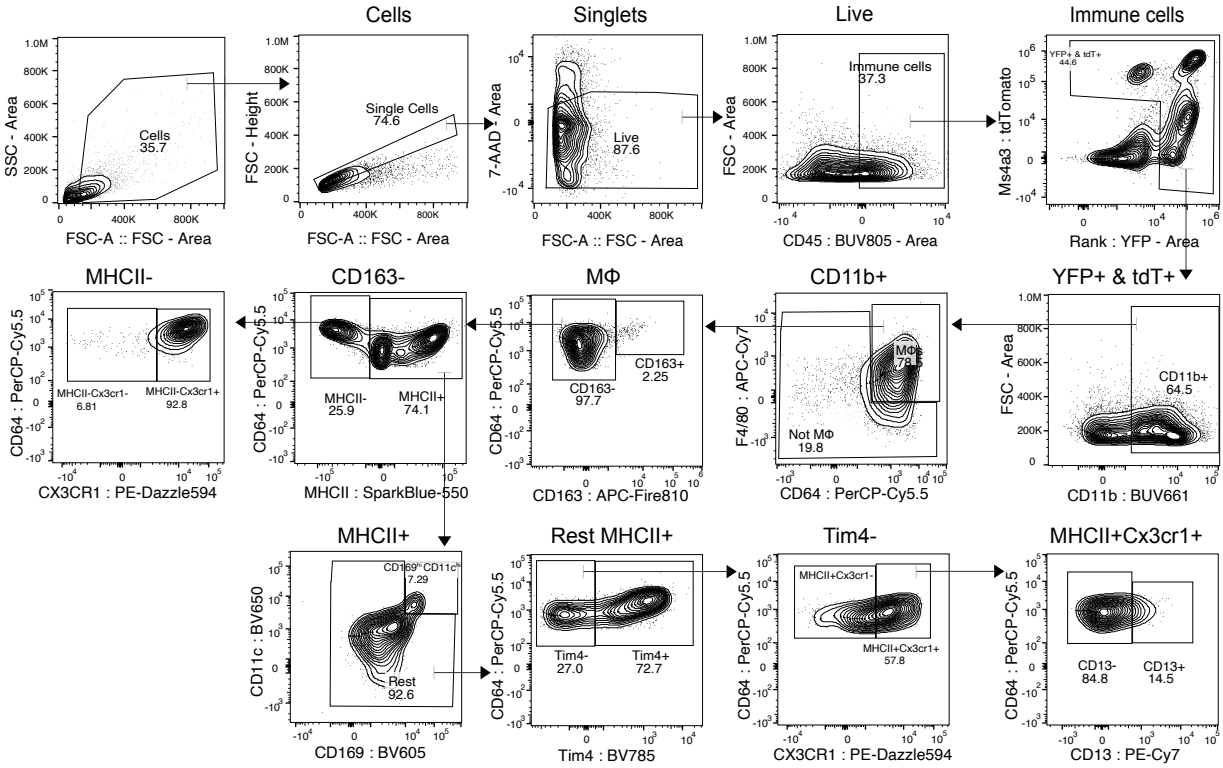

Supplementary Figure 6 Flow cytometry gating strategy of MΦ subpopulations in double fate mapping gut LP and ME layers. Gut LP and ME layers were separated, underwent mechanical and enzymatic digestion to reach single-cell suspension, and then stained for flow cytometry analysis.

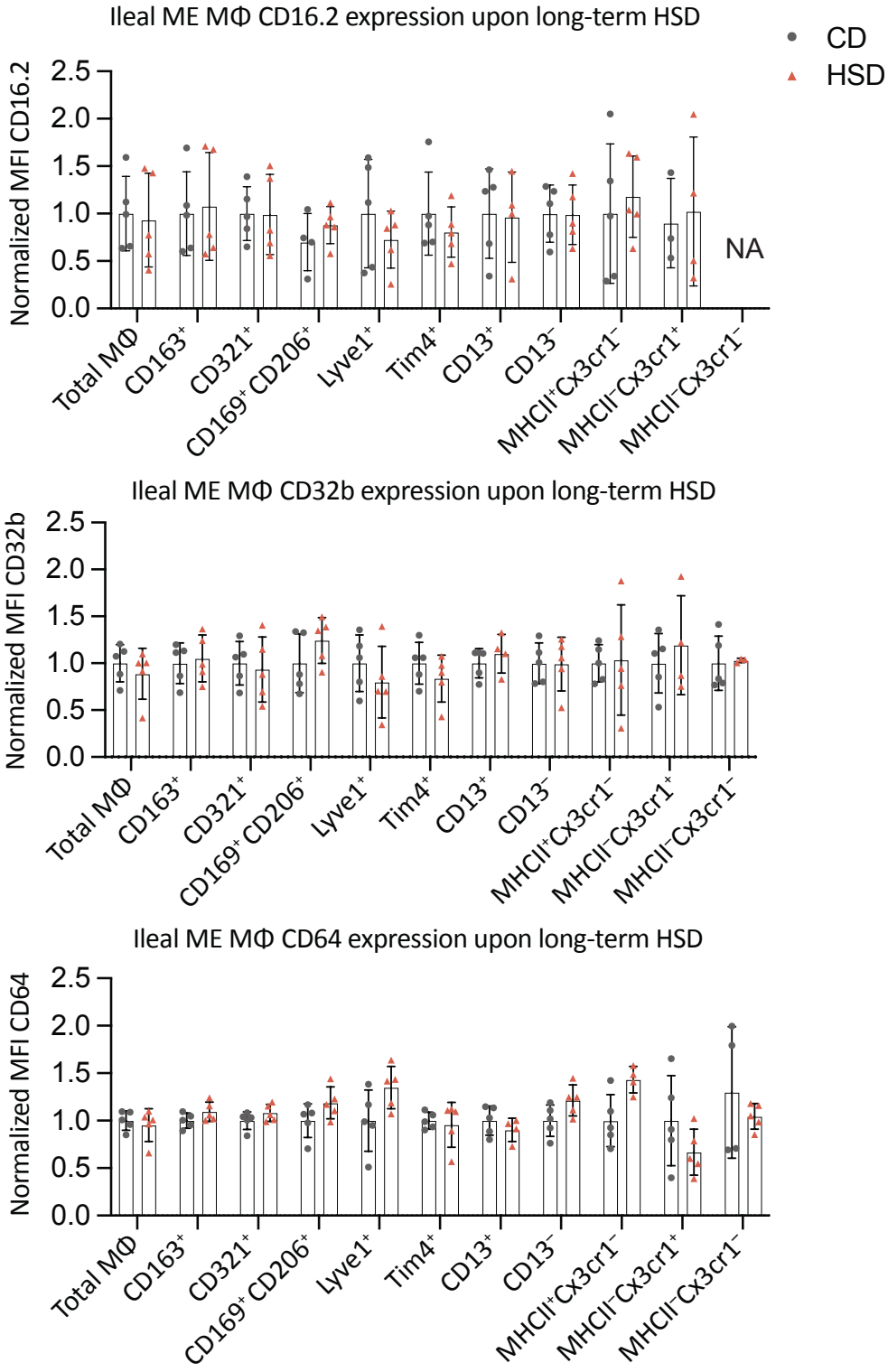

Supplementary Figure 7 FcγRs expression changes in Ileum ME layer after long-term HSD. FcγRs expression is represented by normalized mean fluorescence intensity (MFI) of FcγRs (CD16.2, CD32b, CD64) in ileum ME MΦ subsets upon long-term HSD. Mice were fed CD or HSD for 3 months to achieve a long-term HSD. n = 3-5; data was analyzed using two-way ANOVAs, *p-value < 0.05, ** p-value < 0.01.

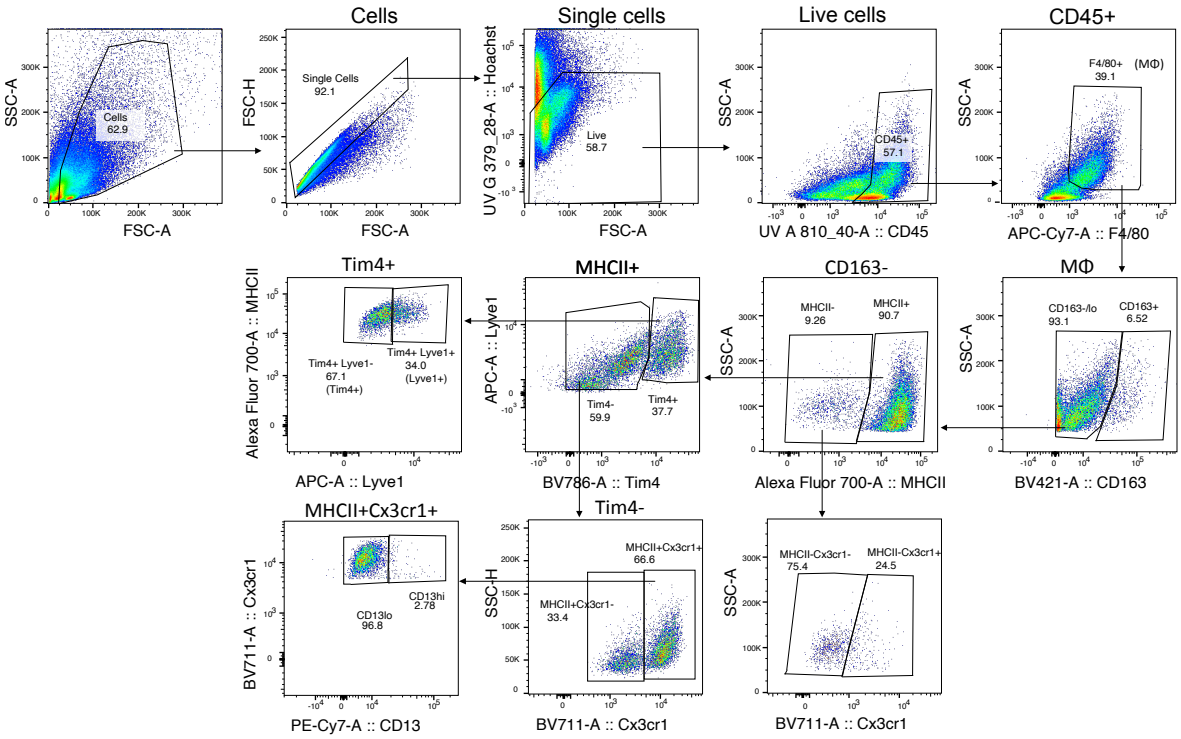

Supplementary Figure 8 MΦ flow cytometry gating strategy for *ex-vivo* phagocytosis assay using *C. rodentium* bacteria. Male mice were fed CD or HSD for 3 months, and then ileum MΦ were isolated, cultured with stained *C. rodentium* for 1h in a ratio 1 MΦ to 160 CFUs, then stained with MΦ markers for flow cytometry analysis.

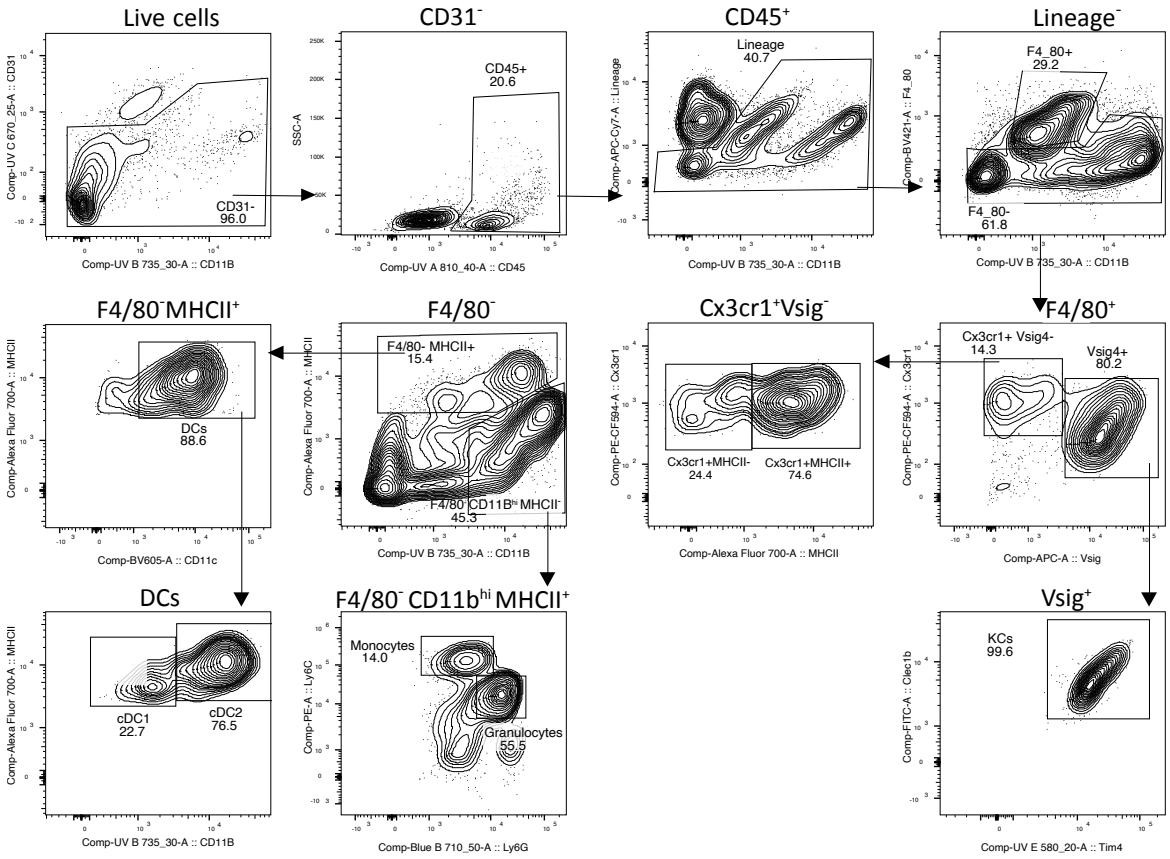

Supplementary Figure 9 Mouse liver Myeloid cells gating strategy. Livers were collected from perfused mice and underwent mechanical and enzymatic digestion to reach liver cell suspension, hepatocytes were mostly discarded by centrifugation, then samples were stained with surface marker antibodies for Flow cytometry analysis. An initial gating strategy was applied to exclude debris, doublets, and dead cells, resulting in a population of live single cells.

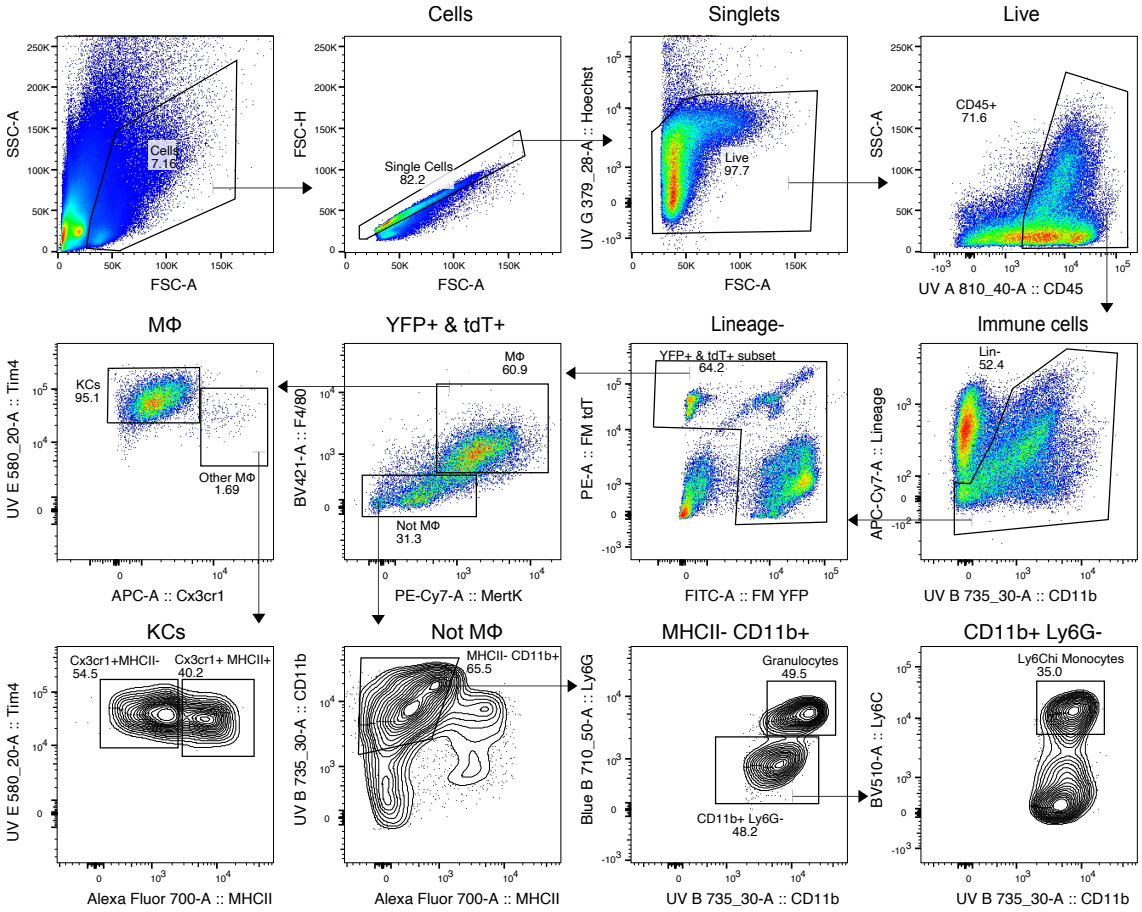

Supplementary Figure 10 Flow cytometry gating strategy of MΦ subpopulations in double fate mapping livers. Liver tissues were collected and subjected to mechanical and enzymatic digestion to obtain a single-cell suspension. Hepatocytes were removed by centrifugation at 50 × g for 3 minutes. The resulting suspension was washed and subsequently stained for flow cytometry analysis.

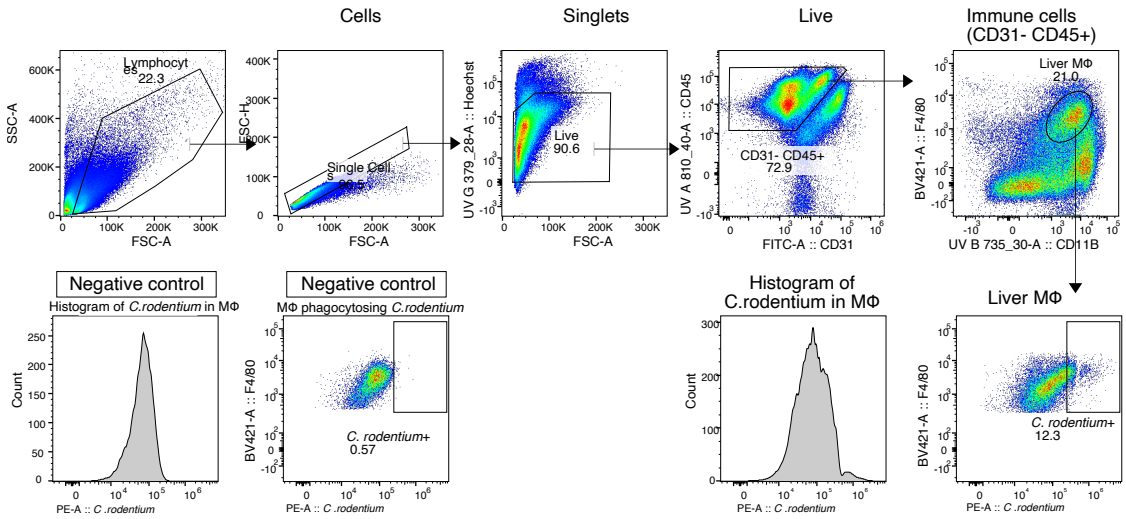

Supplementary Figure 11 Flow cytometry gating strategy of liver MΦ subpopulations for *ex-vivo* phagocytosis assay using *C. rodentium* bacteria. Liver tissues were collected and subjected to mechanical and enzymatic digestion to obtain a single-cell suspension. Hepatocytes were removed by centrifugation at 50 × g for 3 minutes. Liver MΦ were isolated, cultured with stained *C. rodentium* for 1h in a ratio 1 MΦ to 160 CFUs, then stained with MΦ markers for flow cytometry analysis.